# Optimal Weights and Multiple Tracers in Large-Scale Structure

---

**Dissertation**

zur

Erlangung der naturwissenschaftlichen Doktorwürde
(Dr. sc. nat.)

vorgelegt der

Mathematisch-naturwissenschaftlichen Fakultät

der

Universität Zürich

von

## Nico Hamaus

aus

Deutschland

Promotionskomitee

Prof. Dr. Uroš Seljak (Vorsitz)
Prof. Dr. Ben Moore
Prof. Dr. Lucio Mayer

Zürich, 2012

**Nico Hamaus**

Institute for Theoretical Physics
University of Zurich
Winterthurerstrasse 190
CH-8057 Zürich
Switzerland

hamaus@physik.uzh.ch

# Contents

# Preface

This doctoral thesis contains a selection of scientific publications that originated from research projects I was involved in during my PhD studies at the *Institute for Theoretical Physics* (ITP) at the University of Zurich. It is complemented with a general introduction to the field of cosmology, which describes the basic language that is used throughout the professional literature and presents the tools that have been applied to reach the final conclusions. In the end, a brief outlook on possible extensions of the presented research is given.

The general motivation of this thesis is the attempt to model the large-scale structure of the universe with the help of analytical and numerical methods, and the potential application of these models to real observations in order to gain new information on the underlying cosmological framework. Each of the included journal publications deals with different aspects of this framework, the details of which are separately being summarized in each chapter. Additionally, the individual contribution of each author is briefly mentioned. The scientific articles themselves have largely been left unmodified from their published versions so as to make a direct connection to the literature. Each paper comes with a separate bibliography for references used within the article, they should not be confused with the references cited in the remaining part of the thesis, which are listed in the very end of this document.

Zurich, June 2012                                                                                                  Nico Hamaus

8

# Acknowledgments

During the course of my PhD, I appreciated the support of a number of people that enabled me to complete this thesis. First of all, I am grateful to my advisor Uroš Seljak, who gave me the opportunity to join this exciting field of fundamental research and guided me through numerous projects with his expertise. Many thanks to Vincent Desjacques and Robert Smith for assistance with the numerical analysis of their simulations and their expert contributions to my research projects. I also wanna thank the group members Tobias Baldauf, Lucas Lombriser, Zvonimir Vlah, Jaiyul Yoo, Andreu Font and Michael Busha for endless discussions and support. I am grateful to Ben Moore and Lucio Mayer for co-advising my thesis, Regina Schmid-Richmond, Suzanne Wilde and Esther Meier for their assistance in the everyday life at the institute, and all the members of the ITP for discussions, support and making my time in Zurich so worthwhile.

Moreover, I appreciated the hospitality of Lawrence Berkeley National Laboratory, the UC Berkeley Physics Department and the Institute for the Early Universe at Ewha University Seoul, while parts of the research presented in this thesis was conducted, special thanks to Jonathan Blazek and Teppei Okumura for showing me around. Finally, I wanna thank my family and my girlfriend for supporting me throughout my studies and their appreciation for my endeavors.

# Abstract

The past few decades designate a golden age for the science of cosmology. Ground-breaking discoveries and innovative ideas have emerged to form the standard model of cosmology as we know it today. However, major ingredients of this model, such as *dark energy* and *inflation*, are still being disputed and more data is needed to find answers to the open questions. Large-scale structures carry a wealth of information about the cosmological origin and evolution of the universe. They can be explored with the help of redshift surveys that map out the three-dimensional distribution of galaxies within a large fraction of the observable universe. The surveys aim at reconstructing the large-scale distribution of all matter to maximize the statistical significance of the inferred cosmological conclusions. However, there is strong evidence for the fact that galaxies are only the *tracers* of a predominant distribution of *dark matter*, limiting the attainable accuracy on this reconstruction.

On the basis of numerical $N$-body simulations, this thesis presents means to optimize the information content encoded in the statistics of biased tracers of the dark matter density field and investigates their usefulness in cosmological applications. Particular attention is dedicated to an investigation of the stochastic relation between the density fields of halos and dark matter. It is found that the degree of stochasticity decreases as a function of halo mass and that halos of different mass show correlations in their stochastic clustering component. A detailed analysis reveals an *optimal weighting* scheme to minimize the stochasticity of halos with respect to the underlying dark matter density field.

As a matter of fact, the clustering of dark matter is itself characterized by random quantum fluctuations generated in the early universe, so it can only be described in a statistical manner up to an uncertainty referred to as *cosmic variance*. Here, a technique to circumvent cosmic variance is applied by considering multiple tracers of the density field and correlating them against each other. By means of two specific applications, it is demonstrated how in combination with optimal weighting schemes, this approach can improve upon the conventional inference of cosmological parameters from large-scale structure data sets. One such application deals with the signatures of *primordial non-Gaussianity* that can originate in the inflationary phase of the early universe and might still be visible in the clustering statistics of galaxies today. The other one addresses the growth rate of structure that can be constrained from *redshift-space distortions* in the clustering pattern of galaxies. The magnitude of the growth rate is of particular interest in cosmology, as it is very sensitive to the underlying theory of gravity.

# Zusammenfassung

Die vergangenen Jahrzehnte markieren ein goldenes Zeitalter der Kosmologie. Bahnbrechende Entdeckungen und innovative Ideen haben das heutige Standardmodell der Kosmologie hervorgebracht. Zentrale Bestandteile dieses Modells, wie zum Beispiel *dunkle Energie* und *Inflation*, sind jedoch immer noch umstritten und mehr Daten werden benötigt, um Antworten auf die noch ausstehenden Fragen zu finden. Großräumige Strukturen führen eine Fülle an Informationen über den Ursprung und die Entwicklung des Universums mit sich. Man kann sie anhand von Himmelsdurchmusterungen untersuchen, wobei eine dreidimensionale Kartierung eines Großteils aller beobachtbaren Galaxien entsteht. Das Ziel ist, die großräumige Verteilung sämtlicher Materie zu rekonstruieren und so die statistische Aussagekraft daraus gewonnener kosmologischer Schlußfolgerungen zu maximieren. Es gibt allerdings starke Hinweise dafür, dass die Verteilung der Galaxien von einer dominierenden Komponente *dunkler Materie* bestimmt wird, eine Tatsache welche die erzielbare Genauigkeit einer solchen Rekonstruktion erschwert.

Auf der Grundlage von $N$-Teilchen Simulationen werden in dieser Doktorarbeit Methoden entwickelt, um den Informationsgehalt der statistischen Verteilung sogenannter *Tracer* zu optimieren, jener Objekte, die den Anhäufungen der dunklen Materie in gewisser Weise nachfolgen. Der Nutzen dieser Methoden hinsichtlich kosmologischer Anwendungen wird zudem analysiert. Besondere Aufmerksamkeit gilt der Untersuchung der stochastischen Beziehung zwischen den Dichteverteilungen von Halos und dunkler Materie. Es stellt sich heraus, dass das Ausmaß an Zufälligkeit in dieser Beziehung als Funktion der Halomasse abnimmt, und dass Halos verschiedener Massen Korrelationen in ihrer stochastischen Komponente aufweisen. Anhand detaillierter Analysen wird ein *optimales Gewichtungsschema* ermittelt, mit Hilfe dessen diese stochastische Komponente bezüglich der zugrunde liegenden Verteilung dunkler Materie minimiert werden kann.

Tatsächlich ist die Verteilung der dunklen Materie selbst von zufälligen Quantenfluktuationen des frühen Universums bestimmt und kann daher nur auf statistische Weise beschrieben werden, die damit verknüpfte Ungewissheit wird als *kosmische Varianz* bezeichnet. In dieser Arbeit kommt eine Methode zur Anwendung, bei der mehrere Tracer der dunklen Materie berücksichtigt und gegeneinander korreliert werden. Am Beispiel zweier konkreter Anwendungen wird verdeutlicht, wie dies, kombiniert mit optimalen Gewichtungsschemata, die konventionellen Methoden zur Bestimmung kosmologischer Parameter verbessert. Erstere beschäftigt sich mit den Anzeichen *primordialer nicht-Gaußianität*, welche in der inflationären Phase des frühen Universums hervorgerufen werden kann und möglicherweise heute noch in der Statistik von Galaxienansammlungen sichtbar ist. Die zweite Anwendung befasst sich mit der Wachstumsrate von Strukturen im Universum, welche anhand von *Rotverschiebungsverzeichnungen* in den Häufungsmustern von Galaxien ermittelt werden kann. Der Wert dieser Wachstumsrate ist von besonders hohem Interesse für die Kosmologie, da er stark von der zugrunde liegenden Gravitationstheorie abhängt.

"Nature shows us only the tail of the lion. But I do not doubt that the lion belongs to it even though he cannot at once reveal himself because of his enormous size."

*– Albert Einstein*

# 1

## INTRODUCTION

## 1.1. The Homogeneous Cosmos

An important ingredient of contemporary cosmology is the *Copernican Principle*, also known as the *Cosmological Principle*. It states:

> *There is no privileged observer in the universe.*

Although this statement degrades humanity's former vantage point from the center of the world to any insignificant location in the universe, it also implies a promising perspective: observations made from a single location are representative for the entire cosmos. Thus, astronomical observations enable us to reveal the underlying laws of the universe without having to travel far away from our home planet.

The Copernican Principle is based on the assumption of *homogeneity* and *isotropy*, meaning the properties of the universe do neither change with location, nor direction, respectively. Clearly, the immediate world around us looks very distinct from being homogeneous or isotropic, but on very large scales beyond $\sim 100$Mpc most of the astronomical data at hand are in favor of this assumption.

In this section we will focus on those large scales and discuss the properties of a homogeneous and isotropic universe in the framework of General Relativity. This will lead us to the so-called *Standard Model of Cosmology* and its ingredients.

### 1.1.1. Expansion

Edwin Hubble's discovery of a connection between the distance and the color of galaxies [21] initiated the field of observational cosmology as we know it today. In particular, he observed a relative shift $\Delta\lambda$ of the wavelength $\lambda$ towards the red in the spectra of galaxies and found their *redshift* $z \equiv \Delta\lambda/\lambda$ to be proportional to their distance $r$. Thus far this result does not imply any cosmological consequences unless interpreted as a *Doppler shift* originating from the motion of the galaxies away from the observer. In this case the redshift can be expressed as the ratio of the galaxy's velocity to the speed of light, $z \simeq v/c$, and the Hubble law becomes

$$v = Hr \; , \tag{1.1}$$

where $H$ is the so-called *Hubble constant*. It can be shown that the functional form of Hubble's law is the only one that obeys homogeneity and isotropy. In conjunction with the Copernican Principle it yields a seemingly paradoxical conclusion, namely that every observer in the cosmos witnesses all galaxies around him to recede. However, this paradox can be resolved, if we allow the universe itself to have a dynamical character. In this interpretation, it is empty space that is expanding and thus increasing the distance bewteen the galaxies, not the motion of the individual galaxies themselves. The idea was first formulated by Georges Lemaître even before Hubble's discovery [27].

Lemaître's groundbreaking interpretation has another inevitable implication: if the universe is expanding today, it must have been smaller in the past. Assuming the expansion to be monotonic, this leads to the conclusion that the universe must have had a beginning and started out from a point-like object, a so-called *singularity* of spacetime. This evolution is often referred to as the *Big Bang* scenario and works remarkably well in describing the expansion history of the universe.

### 1.1.2. Geometry

General Relativity (GR) relates the distribution of mass and energy to the geometry of spacetime, which is beautifully embodied in Einstein's field equations

$$R_{\mu\nu} - \frac{1}{2}g_{\mu\nu}R = 8\pi T_{\mu\nu} \, , \tag{1.2}$$

with Greek indices representing the four spacetime coordinates $x^{\mu} = (t, x, y, z)$ and $g_{\mu\nu}$ being the metric of spacetime. From here on we will use *Planck units*, setting $c = \hbar = G = k_{\mathrm{B}} = 1$. The *Ricci tensor*

$$R_{\mu\nu} \equiv \frac{\partial \Gamma^{\alpha}_{\mu\nu}}{\partial x^{\alpha}} - \frac{\partial \Gamma^{\alpha}_{\mu\alpha}}{\partial x^{\nu}} + \Gamma^{\alpha}_{\beta\alpha}\Gamma^{\beta}_{\mu\nu} + \Gamma^{\alpha}_{\beta\nu}\Gamma^{\beta}_{\mu\alpha} \tag{1.3}$$

and its contraction $R = g^{\mu\nu}R_{\mu\nu}$ characterizes the curvature of spacetime. It is determined through *Christoffel symbols*

$$\Gamma^{\mu}_{\alpha\beta} = \frac{1}{2}g^{\mu\nu}\left( \frac{\partial g_{\alpha\nu}}{\partial x^{\beta}} + \frac{\partial g_{\beta\nu}}{\partial x^{\alpha}} - \frac{\partial g_{\alpha\beta}}{\partial x^{\nu}} \right) \, , \tag{1.4}$$

which in turn are defined via the metric $g_{\mu\nu}$. The *energy-momentum tensor* $T_{\mu\nu}$ describes any form of mass-energy. To ensure its conservation, the covariant divergence of the energy-momentum tensor must vanish,

$$\nabla_{\nu}T^{\mu\nu} \equiv \frac{\partial T^{\mu\nu}}{\partial x^{\nu}} + \Gamma^{\mu}_{\alpha\nu}T^{\alpha\nu} + \Gamma^{\nu}_{\alpha\nu}T^{\mu\alpha} = 0 \, . \tag{1.5}$$

The same must hold for the left-hand side of Eq. (1.2) and is indeed satisfied as a consequence of the so-called *Bianchi identities* [5].

In order to properly describe the evolution of the universe one needs to find a solution to Eq. (1.2) that obeys homogeneity and isotropy. It can be expressed as a spacetime interval

$$\mathrm{d}s^2 \equiv g_{\mu\nu}\mathrm{d}x^{\mu}\mathrm{d}x^{\nu} = \mathrm{d}t^2 - a^2(t)\left( \frac{\mathrm{d}r^2}{1 - Kr^2} + r^2\mathrm{d}\vartheta^2 + r^2\sin^2\vartheta\mathrm{d}\phi^2 \right) \, , \tag{1.6}$$

and was first derived by Alexander Friedman [16], followed by Lemaître [28], Robertson [41] and Walker [52]. It is composed of the temporal part $\mathrm{d}t$ and the spatial part in the brackets, which is multiplied by the *scale factor* $a(t)$. As the name suggests, $a(t)$ describes the scale of the universe evolving with time. The geometry of space is expressed in spherical coordinates, with radius $r$, polar angle $\vartheta$ and azimuthal angle $\phi$. It can take on three different types of curvature depending on the value of $K$. $K = 0$ describes flat space (no curvature), $K > 0$ a three-dimensional sphere (positive curvature, closed universe) and $K < 0$ a hyperbolic geometry (negative curvature, open universe). Because the magnitude of $K$ can be absorbed in a redefinition of the scale factor $a(t)$, only the sign of $K$ actually matters.

According to Eq. (1.6), physical distances in the universe are proportional to the scale factor $a(t)$, so the Hubble law in Eq. (1.1) can be rewritten as

$$\dot{a} = Ha \, , \tag{1.7}$$

where the dot represents a total time derivative. Moreover, the redshift can be expressed as

$$z = \frac{\Delta\lambda}{\lambda} = \frac{a(t_{\rm re}) - a(t_{\rm em})}{a(t_{\rm em})} = a^{-1} - 1 \, , \tag{1.8}$$

so it is simply a consequence of the expansion of spacetime and determined by the ratio of the scale factor at the time of reception $t_{\rm re}$ and the time of emission $t_{\rm em}$ of light. Since the light is observed today, $t_{\rm re} = t_0$, and we fix $a(t_0) \equiv a_0 = 1$.

Equation (1.6) is a general solution to Eq. (1.2) obeying homogeneity and isotropy without specification of any particular form of energy density $T_{\mu\nu}$. However, we know that the universe is filled with nonrelativistic matter in the form of stars or galaxies, as well as relativistic matter in the form of radiation. On large scales, its distribution is fairly homogeneous and isotropic, so it can be approximated by a perfect fluid with energy-momentum tensor

$$T_{\mu\nu} = (\rho + p) \, u_\mu u_\nu - p g_{\mu\nu} \, , \tag{1.9}$$

of energy density $\rho$ and pressure $p$ moving with four-velocity $u_\mu$. The relation between energy density and pressure is determined by the *equation of state*,

$$p = w\rho \, , \tag{1.10}$$

which for the most common forms of mass-energy can be expressed with is a constant number $w$. Plugging this form of energy-momentum together with the metric from Eq. (1.6) into Einstein's field equations yields two relations for the scale factor of the universe and its matter content. They are known as the *Friedman equations*,

$$\ddot{a} \;\; = -\frac{4\pi}{3} \left( \rho + 3p \right) a \, , \tag{1.11}$$

$$\dot{a}^2 \;\; = \frac{8\pi}{3} \rho a^2 - K \, . \tag{1.12}$$

The first Friedman equation relates the second time-derivative of the scale factor with the energy density and the pressure of the matter in the universe. Assuming cold (non-relativistic) matter with negligible pressure to be dominant, we expect a deceleration of the expansion, $\ddot{a} < 0$. The second Friedman equation reveals another important fact: for a given expansion rate $\dot{a}$ the energy-density of matter determines the geometry of the universe (its curvature $K$). Hence, Eq. (1.12) defines a critical energy-density

$$\rho_{\rm c} \equiv \frac{3H^2}{8\pi} \, , \tag{1.13}$$

which yields a flat geometry of spacetime ($K = 0$). Larger or smaller values of the energy-density implicate a closed or an open geometry, respectively.

### 1.1.3. Inventory

According to the Friedman equations, astronomical observations of the local matter content may reveal geometrical properties of the cosmos as a whole. Vice versa, constraints on the universe's curvature determine its total energy-density budget.

Because there are different forms of matter, it is useful to define a *density parameter*

$$\Omega \equiv \frac{\rho}{\rho_{\rm c}} = \frac{8\pi\rho}{3H^2} \,, \tag{1.14}$$

to distinguish the relative contributions to the energy density of various different components. In terms of today's density parameter $\Omega_{i,0}$ of component $i$, Eq. (1.12) can be recast into

$$\left(\frac{H}{H_0}\right)^2 = \sum_i \Omega_{i,0}a^{\gamma_i} + \Omega_{K,0}a^{-2} \,, \tag{1.15}$$

where $\gamma_i$ is the scaling index of component $i$ and $\Omega_K \equiv -K/H^2a^2 = 1 - \sum_i \Omega_i$ the relative *curvature density*. An index of zero denotes quantities evaluated today ($z = 0$). In the following, some of the most common such components are discussed briefly.

### 1.1.3.1. Dust

Non-relativistic matter is often referred to as *dust*, because it has negligible pressure. Solving the Friedman equations of the flat universe ($K = 0$) for $\rho$ and $a(t)$ assuming $w = 0$ in Eq. (1.10) yields

$$\rho_{\rm m} = \rho_{\rm m,0}a^{-3} \quad , \quad a(t) = \left(\frac{3}{2}H_0t\right)^{2/3} \tag{1.16}$$

and the age of the universe is $t_0 = \frac{2}{3H_0}$. An example for a dust-like fluid is *cold dark matter*, since it mainly interacts gravitationally. On large scales, baryons also behave dust-like, as their electromagnetic interactions can be neglected.

### 1.1.3.2. Radiation

Ultra-relativistic matter has a nonzero pressure with equation of state parameter $w = 1/3$. In a flat radiation-dominated universe the expansion is characterized by

$$\rho_{\rm r} = \rho_{\rm r,0}a^{-4} \quad , \quad a(t) = (2H_0t)^{1/2} \tag{1.17}$$

Hence, compared to the dust-dominated universe, the expansion is slower, yielding an age of merely $t_0 = \frac{1}{2H_0}$. An example for ultra-relativistic matter is electromagnetic radiation or neutrinos.

### 1.1.3.3. Cosmological Constant

The Einstein field equations allow the inclusion of an additional term $\Lambda g_{\mu\nu}$ on the left-hand side of Eq. (1.2), with $\Lambda$ being a so-called *cosmological constant*. When absorbed into $T_{\mu\nu}$ on the right-hand side, it can be interpreted as a form of vacuum energy density with equation of state parameter $w = -1$. Then, the Friedman equations for $K = 0$ yield

$$\rho_\Lambda \equiv \rho_{\Lambda,0} = \frac{\Lambda}{3H_0^2} \quad , \quad a(t) = \exp(H_0t) \tag{1.18}$$

Note that both energy density and Hubble parameter $H \equiv \dot{a}/a$ remain constant in time, so there is no evolution. This kind of solution was first studied by Willem de Sitter [12], it has the remarkable property that it describes the same spacetime for any type of curvature.

### 1.1.3.4. Scalar Field

A more exotic form of matter is a classical scalar field. Unlike baryons, a scalar field only has a single degree of freedom, which is given by its field value $\varphi$. If it is homogeneous, its energy density and pressure can be expressed as

$$\rho_\varphi = \frac{1}{2}\dot{\varphi}^2 + V(\varphi) \quad , \quad p_\varphi = \frac{1}{2}\dot{\varphi}^2 - V(\varphi) \tag{1.19}$$

Thus, the potential $V(\varphi)$ determines its equation of state parameter $w$ and in general

$$\rho_\varphi = \rho_{\varphi,0} a^{-3(1+w)} \quad , \quad a(t) = \left[\frac{3(1+w)}{2} H_0 t\right]^{\frac{2}{3(1+w)}} \tag{1.20}$$

for $w > -1$. If $\dot{\varphi} = 0$, we have $w = -1$ and the properties of a cosmological constant are restored. In principle, $w$ can change as a function of time, the scalar field is then sometimes dubbed *quintessence*.

### 1.1.4. Observational Status

Astronomical observations of the homogeneous universe aim at constraining the free parameters of the cosmological standard model presented above. These are the various energy-density components $\Omega_i$, the effective equation of state parameter $w$ from all components, the relative curvature density $\Omega_K$ and the expansion rate $H_0$.

A measurement of distance and redshift of objects in the universe following the large-scale Hubble flow allows to constrain the cosmic expansion history and thus the parameters that go into it. Although it is generally hard to infer astronomical distances on such large scales, a special class of objects denoted as *standard candles* allow a fairly accurate determination of their absolute luminosity.

The most famous example are supernovae of type Ia that have revealed a late-time acceleration of the universe [37] ($\ddot{a} > 0$), suggesting the energy density today to be dominated by a cosmological constant with $\Omega_{\Lambda,0} \simeq 0.7$ and $w \simeq -1$. Furthermore, the data favor a flat universe with $\Omega_{m,0} \simeq 0.3$ and $\Omega_K$ consistent with zero. The expansion rate today is constrained to be somewhere close to $H_0 \simeq 70$ km s$^{-1}$ Mpc$^{-1}$, which yields the age of the universe to be roughly 14 billion years. Due to degeneracies with other cosmological parameters, the value of $H_0$ is often left unspecified with the dimensionless Hubble parameter

$$h \equiv \frac{H_0}{100 \text{ km s}^{-1} \text{ Mpc}^{-1}} . \tag{1.21}$$

In order to lift degeneracies in the parameter space of the standard model, independent probes of cosmology are necessary. The theory of *nucleosynthesis* and observations of the abundance of light elements in the cosmos is very sensitive to the cosmic

baryon- and photon-content $\Omega_b$ and $\Omega_\gamma$ of the universe, but does neither have strong implications on its dark components, nor on its geometry. The same is true for the theory of *recombination* and observations of the spectrum of the cosmic microwave background (CMB) radiation, first discovered by Penzias and Wilson [36].

However, a sufficiently accurate spatial resolution of the CMB reveals its anisotropy [50] and provides a wealth of new information on cosmology. Similarly, galaxy redshift surveys aiming at reconstructing the fluctuations of the density field of large-scale structure (LSS) achieve a similar goal [11], with the advantage of covering three dimensions instead of only two in the case of CMB observations. In order to exploit the information that is available with these new probes, the theory of perturbations in a slightly inhomogeneous universe is presented in the following section.

## 1.2. The Inhomogeneous Cosmos

The universe we observe in our vicinity (on small scales) is far from homogeneous and isotropic. Conglomerates of galaxies form gravitationally bound systems such as clusters, filaments and walls surrounding large regions of empty space, known as *voids*. This so-called *cosmic web* of structure could not have formed in a perfectly homogeneous universe, initial perturbations must have caused gravitational instabilities leading to its present appearance.

The CMB provides the earliest "snapshot" of perturbations present in the universe and thus the closest connection to what their initial properties must have been. In this section we will briefly sketch the evolution of those perturbations from their creation in the very early universe until today and discuss their properties.

### 1.2.1. Random Fields

The structure of a slightly inhomogeneous universe can be described by a scalar function $f(\mathbf{x})$, representing the energy density, the temperature, or the gravitational potential, for example. For practical reasons it is often useful to consider the Fourier coefficients $f_\mathbf{k}$ of that function. In a finite region of volume $V$, they are defined via

$$f(\mathbf{x}) = \frac{1}{\sqrt{V}} \sum_\mathbf{k} f_\mathbf{k} \exp(i\mathbf{k} \cdot \mathbf{x}) \, , \tag{1.22}$$

where $\mathbf{k}$ is denoted *wavevector*. The inversion of Eq. (1.22) is given by

$$f_\mathbf{k} = \frac{1}{\sqrt{V}} \int_V f(\mathbf{x}) \exp(-i\mathbf{k} \cdot \mathbf{x}) \, \mathrm{d}^3 x \, . \tag{1.23}$$

In general, the Fourier coefficients are complex numbers $f_\mathbf{k} = a_\mathbf{k} + ib_\mathbf{k}$ with real and imaginary parts $a_\mathbf{k}$ and $b_\mathbf{k}$, respectively. Because $f(\mathbf{x})$ is real, the complex conjugate $f_\mathbf{k}^*$ must be equal to $f_{-\mathbf{k}}$ according to Eq. (1.23), so we have $a_{-\mathbf{k}} = a_\mathbf{k}$ and $b_{-\mathbf{k}} = -b_\mathbf{k}$.

Suppose the field $f(\mathbf{x})$ is a realization of a homogeneous and isotropic *Gaussian random process*. Then, the joint probability distribution function for the real and imaginary parts of its Fourier coefficients will be a bivariate Gaussian [32]

$$p(a_\mathbf{k}, b_\mathbf{k}) = \frac{1}{\pi \sigma_k^2} \exp\left(-\frac{a_\mathbf{k}^2}{\sigma_k^2}\right) \exp\left(-\frac{b_\mathbf{k}^2}{\sigma_k^2}\right) \, , \tag{1.24}$$

with variance $\sigma_k^2$ only depending on the magnitude $k \equiv |\mathbf{k}|$ of the wavevector (the wavenumber), not its direction. This means, when two Fourier coefficients of $f(\mathbf{x})$ are correlated by taking the ensemble average $\langle f_\mathbf{k} f_{\mathbf{k}'} \rangle$, this only yields a contribution from the variance of $a_\mathbf{k}$ and $b_\mathbf{k}$ and their covariance vanishes,

$$\langle f_\mathbf{k} f_{\mathbf{k}'} \rangle = \langle a_\mathbf{k} a_{\mathbf{k}'} \rangle - \langle b_\mathbf{k} b_{\mathbf{k}'} \rangle + i \left( \langle a_\mathbf{k} b_{\mathbf{k}'} \rangle + \langle a_{\mathbf{k}'} b_\mathbf{k} \rangle \right) = \sigma_k^2 \delta_{\mathbf{k}, -\mathbf{k}'}^\mathrm{K} \, , \tag{1.25}$$

where $\delta_{\mathbf{k}, -\mathbf{k}'}^\mathrm{K}$ is the *Kronecker symbol*. Hence, real and imaginary parts are statistically independent, just as the coefficients at different wavevectors $\mathbf{k} \neq \mathbf{k}'$. The limit

$V \to \infty$ of Eqs. (1.22) and (1.23) defines the Fourier transform $f(\mathbf{k})$ via the integrals

$$f(\mathbf{x}) = \int f(\mathbf{k}) \exp(i\mathbf{k} \cdot \mathbf{x}) \, \mathrm{d}^3 k \, , \qquad (1.26)$$

$$f(\mathbf{k}) = \frac{1}{(2\pi)^3} \int f(\mathbf{x}) \exp(-i\mathbf{k} \cdot \mathbf{x}) \, \mathrm{d}^3 x \, , \qquad (1.27)$$

and the ensemble average of Eq. (1.25) defines the *power spectrum* $P_f(k)$,

$$\langle f(\mathbf{k}) f(\mathbf{k}') \rangle \equiv P_f(k) \delta^{\mathrm{D}}(\mathbf{k} + \mathbf{k}') \, , \qquad (1.28)$$

where $\delta^{\mathrm{D}}(\mathbf{k} + \mathbf{k}')$ is the *Dirac delta function*. The power spectrum describes the variance of fluctuations in the function $f$ in an infinitesimally thin shell of radius $k$. In the case of a purely Gaussian process, it completely characterizes the properties of the random field, i.e. all higher-order correlations can be expressed in terms of the power spectrum. Since it has the dimension of a volume, it is sometimes convenient to consider the *dimensionless power spectrum*

$$\Delta_f(k) \equiv \frac{k^3}{2\pi^2} P_f(k) \, . \qquad (1.29)$$

Taken in configuration space, the ensemble average from Eq. (1.28) defines the *two-point correlation function* of $f$,

$$\langle f(\mathbf{x}) f(\mathbf{x}') \rangle \equiv \xi_f(\mathbf{x}' - \mathbf{x}) \, . \qquad (1.30)$$

Due to statistical homogeneity and isotropy, $\xi$ only depends on the distance $r \equiv |\mathbf{x}' - \mathbf{x}|$ between any two locations. With Eqs. (1.26) and (1.28) it follows that the correlation function and the power spectrum are Fourier pairs,

$$\xi_f(r) = \int P_f(k) \exp(i\mathbf{k} \cdot \mathbf{r}) \, \mathrm{d}^3 k \, . \qquad (1.31)$$

### 1.2.2. Initial Perturbations

#### 1.2.2.1. Inflation

It is by now widely accepted that the very early universe must have undergone a phase of *inflation*, closely described by an exponentially expanding spacetime as proposed by de Sitter. The main motivation for inflation comes from its solutions to the *horizon-* and the *flatness* problems, as pointed out by Alan Guth [18]. The former arises, because with a decelerating expansion many different regions in the observed universe would have never been in causal contact with each other in the past, posing the question of why then we observe such a high degree of isotropy, for example in the CMB. The latter comes about the question of why the observed curvature of the universe is so small, respectively consistent with zero. In a decelerating universe the initial expansion rate must have been extremely fine-tuned in order to produce the observed flatness.

One way to realize accelerated expansion is to assume a scalar field $\varphi$ that is evolving sufficiently slowly to achieve a negative pressure, see Eq. (1.19). The evolution of a scalar field is dictated by the *Klein-Gordon equation*

$$\frac{1}{\sqrt{-g}}\frac{\partial}{\partial x^\mu}\left(\sqrt{-g}g^{\mu\nu}\frac{\partial\varphi}{\partial x^\nu}\right) + \frac{\partial V}{\partial\varphi} = 0 \ , \tag{1.32}$$

which follows from Eqs. (1.5) and (1.19) with $g \equiv \det g_{\mu\nu}$. From it, the so-called slow-roll conditions for the potential $V(\varphi)$ necessary for inflation can be derived [32],

$$\left(\frac{\partial V/\partial\varphi}{V}\right)^2 \ll 1 \quad , \quad \left|\frac{\partial^2 V/\partial\varphi^2}{V}\right| \ll 1 \ . \tag{1.33}$$

In this regime the scalar field can resemble a cosmological constant with $w \simeq -1$ and yield an exponentially growing scale factor. However, our existence tells us that inflation has to end at some point, so de-Sitter spacetime is only an approximation to the inflationary phase. It comes to an end when the scalar field decays into the minimum of its potential and evolves faster due to oscillations. Then its equation of state changes, because the potential term in Eq. (1.19) can become comparable to the kinetic term $\dot\varphi^2$ and the universe may enter a decelerated phase with $w \simeq 0$.

### 1.2.2.2. Quantum Fluctuations

Considering a mildly inhomogeneous scalar field, we can separate $\varphi$ into a homogeneous part $\varphi_0(t)$ and a linear perturbation $\delta\varphi(\mathbf{x},t)$. These perturbations are generated by *quantum fluctuations* of the scalar field in the very early universe. From *Heisenberg's uncertainty principle* for a massless scalar field it follows that the minimal amplitude of $\delta\varphi(R)$ on a given scale $R$ is inversely proportional to that scale,

$$\delta\varphi(R) \sim 1/R \ . \tag{1.34}$$

In Fourier space, with Eq. (1.22) the typical amplitude of quantum fluctuations of *comoving* wavenumber $k \sim a/R$ becomes

$$|\delta\varphi(k)| \sim k^{-1/2}/a \ . \tag{1.35}$$

Because the creation- and annihilation operators for the field quanta permute for wavemodes with different values of $k$, these wavemodes are independent of each other with random relative phases. Thus, according to the central limit theorem, a superposition of many wavemodes yields a *Gaussian random field* with variance $|\delta\varphi(k)|^2$.

### 1.2.2.3. Primordial Potential

The fluctuations of the scalar field induce perturbations in the metric $g_{\mu\nu}$ from Eq. (1.6), resulting in the so-called *perturbed Friedman metric*. In conformal-Newtonian gauge, it can be expressed as

$$\mathrm{d}s^2 = a^2\left[(1+2\Phi)\mathrm{d}\eta^2 - (1-2\Psi)\delta_{ij}\mathrm{d}x^i\mathrm{d}x^j\right] \ , \tag{1.36}$$

with the scalar perturbations $\Phi$ and $\Psi$ and *conformal time* $\eta$ defined as $\mathrm{d}\eta \equiv \mathrm{d}t/a$. Here, roman indices denote only spatial coordinates and $\delta_{ij}$ is the spatial unit metric. Plugged into Eq. (1.32), this relates the perturbation $\delta\varphi$ and its evolution to the generalized potentials $\Phi$ and $\Psi$, which are identical for a perfect fluid without anisotropic stress. With initial amplitude given in Eq. (1.35), the solution for the perturbation in Fourier space reads [32]

$$\delta\varphi(k) \sim k^{-1/2} \begin{cases} a^{-1}\exp(\pm ik\eta) \,, & \text{for } k \gg Ha \\ \frac{\partial V/\partial\varphi}{V}\left(a^{-1}\frac{V}{\partial V/\partial\varphi}\right)_{k=Ha} \,, & \text{for } k \ll Ha \end{cases} \tag{1.37}$$

On subhorizon scales ($k \gg Ha$), the scalar field perturbation oscillates and its amplitude decays inversely with the scale factor. However, during the inflationary phase $\dot{a} = Ha$ increases with time and a perturbation with given $k$ eventually leaves the horizon. On superhorizon scales ($k \ll Ha$) the perturbation *freezes out* to a roughly constant value. Only when inflation ends and the slow-roll conditions from Eq. (1.33) are violated, $\frac{\partial V/\partial\varphi}{V}$ increases to unity.

Finally, the universe enters the decelerated phase ($\dot{a} < 0$) and wavemodes of a given scale $k$ reenter the horizon. Without an inflationary phase, wavemodes from originally small scales with large amplitude would decay immediately and could not be preserved until today with sufficiently high amplitude (e.g. as observed in the CMB). This is another strong argument for the theory of inflation.

From the solution of Eq. (1.32) we also obtain the potential $\Phi$, which on superhorizon scales becomes

$$\Phi(k) = -\frac{1}{2}\delta\varphi(k)\frac{\partial V/\partial\varphi}{V} \,. \tag{1.38}$$

At the end of inflation we have $\partial V/\partial\varphi \simeq V$ and the dimensionless power spectrum of the potential becomes

$$\Delta_\Phi(k) \simeq \left(H\frac{V}{\partial V/\partial\varphi}\right)^2_{k=Ha} \,. \tag{1.39}$$

Because $H$ is nearly constant during inflation, $\Delta_\Phi$ has very weak scale dependence. In fact, it can be shown that it is logarithmic [33] and within a narrow range of scales is well approximated by a power law with amplitude $A_0$ and *spectral index* $n_S$,

$$\Delta_\Phi \simeq A_0 k^{n_S-1} \,. \tag{1.40}$$

Inflation predicts a slight deviation from a flat spectrum with $n_S = 1$, the so-called *spectral tilt* [33]

$$n_S - 1 \equiv \frac{d\ln\Delta_\Phi}{d\ln k} \simeq -\frac{3}{8\pi}\left(\frac{\partial V/\partial\varphi}{V}\right)^2 + \frac{1}{4\pi}\frac{\partial^2 V/\partial\varphi^2}{V} \,. \tag{1.41}$$

For a massive scalar field with $V \propto \varphi^2$, the result is $n_S \simeq 0.96$. Thus, the considered inflationary scenario makes strong predictions on the properties of the initial fluctuations in our universe: they can be described by a Gaussian random field of adiabatic perturbations with a nearly scale-invariant spectrum. So far, this is in very

good agreement with observations of the CMB [25]. However, if any of these properties can be ruled out by measurement, the theory of single field slow-roll inflation likely has to be extended.

One such possible extension is the introduction of additional inflationary fields and thus entropy perturbations. Couplings between the Fourier modes of different fields can break the Gaussian character of fluctuations and produce so-called *primordial non-Gaussianity* (PNG). This fact makes the detection of PNG a *smoking gun* for inflation.

### 1.2.3. Evolution of Perturbations

The fluctuations of the scalar field produced during the inflationary phase of the universe are not directly observable. We can only observe their relics that have evolved after reentering the horizon in the decelerated phase. The CMB provides the earliest picture of the angular energy density distribution in the universe, when the perturbations are still relatively small and evolve linearly. However, by the time of recombination the initial perturbations have translated into fluctuations in the energy density of various different components, such as dark matter, baryons and radiation.

### 1.2.3.1. Hot Phase

In order to describe their properties at the time of recombination, it is necessary to solve the *Boltzmann equations* for an imperfect fluid with relativistic and nonrelativistic components. Although this cannot be done analytically, numerical methods yield a high accuracy [46]. The solution is usually expressed in the form of a *transfer function* $T(k)$ and the *linear growth factor* $D(t)$ that multiplies the initial fluctuation field $f(k, t_\mathrm{i})$ at the time $t_\mathrm{i}$ when it enters the horizon,

$$f(k, t) = T(k)D(t)f(k, t_\mathrm{i}) . \tag{1.42}$$

For adiabatic perturbations, the asymptotics of $T(k)$ are qualitatively easy to understand. Like in the case of the scalar field, fluctuations in the energy density of both relativistic and nonrelativistic matter are *frozen* (constant) on superhorizon scales. A wavemode entering the horizon during radiation domination grows more slowly compared to a mode entering during dust domination (see below). Therefore, $T(k)$ is suppressed for wavenumbers $kd_\mathrm{eq} \gg 1$, where $d_\mathrm{eq}$ is the comoving horizon at dust-radiation equality. At $kd_\mathrm{eq} \ll 1$ the transfer function approaches a constant value, which is normalized to unity for convenience.

Additionally, the competition between gravity and pressure in the hot plasma of baryons and radiation causes standing waves in their energy density, so-called *acoustic oscillations*. They are only produced within the horizon before dust-radiation equality, so for wavenumbers with $kd_\mathrm{eq} > 1$, and can be directly observed in the radiation component via the CMB [25]. The structure and location of these oscillations is very sensitive to cosmological parameters, such as $\Omega_K$, $\Omega_\mathrm{m}$ and $\Omega_\mathrm{b}$.

### 1.2.3.2. Cold Phase

After recombination, photons propagate freely and the acoustic oscillation signature in the radiation component is washed out. Thanks to gravitational interaction, the oscillations in the baryonic component are carried over to the dominant dark matter distribution and thus survive until the present day. These so-called *baryon acoustic oscillations* (BAO) have been detected recently in galaxy redshift surveys [14] and serve as a *standard ruler* for cosmology.

In order to relate the observed density fluctuations in the present universe to their initial conditions after recombination, one has to understand their gravitational evolution. The dark matter density $\rho_{\mathrm{m}}$, respectively the fluctuation around its mean $\bar{\rho}_{\mathrm{m}}$,

$$\delta(\mathbf{x}, t) \equiv \frac{\rho_{\mathrm{m}}(\mathbf{x}, t) - \bar{\rho}_{\mathrm{m}}(t)}{\bar{\rho}_{\mathrm{m}}(t)} \ , \tag{1.43}$$

is related to the gravitational potential by the *Poisson equation*

$$\Delta \Phi = 4\pi \bar{\rho}_{\mathrm{m}} \delta \ , \tag{1.44}$$

which is only valid on subhorizon scales in the Newtonian regime. In Fourier space with $\Phi$ given by Eq. (1.40), this yields

$$|\delta(k)| = k^2 \frac{\sqrt{A_0}}{4\pi \bar{\rho}_{\mathrm{m}}} k^{\frac{n_S - 1}{2}} \ . \tag{1.45}$$

Taking into account the effects of baryons and radiation described by the transfer function $T(k)$, the dark matter power spectrum at recombination can be written as

$$P_\delta(k, t_{\mathrm{rec}}) = \frac{A_0}{8\bar{\rho}_{\mathrm{m}}^2} D^2(t_{\mathrm{rec}}) T^2(k) k^{n_S} \ . \tag{1.46}$$

Because it only interacts gravitationally, the dark matter density field can be described as a perfect fluid in an expanding background. As long as $\delta \ll 1$, it obeys the linearized *Continuity equation*

$$\frac{\partial \delta}{\partial t} + \frac{\nabla \cdot \mathbf{v}}{a} = 0 \ , \tag{1.47}$$

and *Euler equation*

$$\frac{\partial \mathbf{v}}{\partial t} + H\mathbf{v} + \frac{\nabla \Phi}{a} = 0 \ , \tag{1.48}$$

where $\mathbf{v}$ is the *peculiar velocity field* and derivatives are taken with respect to *Lagrangian coordinates* moving with the Hubble flow. Here, pressure has been neglected, which is a fair approximation on large scales where $|\mathbf{v}| \ll 1$. Together with Eq. (1.44), this yields a closed form differential equation for the dark matter density perturbation,

$$\frac{\partial^2 \delta}{\partial t^2} + 2H \frac{\partial \delta}{\partial t} = 4\pi \bar{\rho}_{\mathrm{m}} \delta \ . \tag{1.49}$$

Its solution can be expressed as

$$\delta = D_+(t) \delta^{(+)}(\mathbf{x}, t_{\mathrm{i}}) + D_-(t) \delta^{(-)}(\mathbf{x}, t_{\mathrm{i}}) \ , \tag{1.50}$$

with the linear growth factors $D_+$ and $D_-$ of the growing and decaying modes, respectively, and the corresponding initial density field configurations $\delta^{(+)}$ and $\delta^{(-)}$. With Eq. (1.47), we can solve for the divergence of the peculiar velocity field

$$\nabla \cdot \mathbf{v} = -aH \left[ f_+ \delta^{(+)}(\mathbf{x}, t_{\mathrm{i}}) + f_- \delta^{(-)}(\mathbf{x}, t_{\mathrm{i}}) \right] \ , \tag{1.51}$$

where $f \equiv \mathrm{d} \ln D / \mathrm{d} \ln a$ is denoted as logarithmic *growth rate*. In the following we can neglect the decaying mode and refer to the growing mode with a single growth factor $D$ and growth rate $f$.

The growth of perturbations depends on the expansion rate of the universe, which in turn is dictated by its constituents. With $H$ taken from Eq. (1.15) and plugged into Eq. (1.49), one can in principle obtain the growth factor and rate for an arbitrary cosmology. While a general analytic solution does not exist, expressions for the following limiting cases can be derived [32]:

(i) Dust domination ($\Omega_{\mathrm{m}} \gg \Omega_{\mathrm{r}}, \Omega_\Lambda, \Omega_k$): $D(t) \propto a(t)$

(ii) Radiation domination ($\Omega_{\mathrm{r}} \gg \Omega_{\mathrm{m}}, \Omega_\Lambda, \Omega_k$): $D(t) \propto \ln a(t)$

(iii) Cosmological constant domination ($\Omega_\Lambda \gg \Omega_{\mathrm{m}}, \Omega_{\mathrm{r}}, \Omega_k$): $D(t) \propto \mathrm{const.}$

Hence, gravity can enhance density perturbations substantially only in the dust-dominated regime, where they grow linearly with the scale factor and the growth rate is close to unity. As soon as a cosmological constant term becomes important in the energy budget of the universe, the growth of perturbations is stalled and the growth rate drops below unity. In a flat universe only filled with dust and cosmological constant, it can be neatly parametrized by

$$f \simeq \Omega_{\mathrm{m}}^\gamma \ , \tag{1.52}$$

with $\gamma \simeq 0.6$ [35] denoted *growth index*. This parametrization turns out to be more general and valid for various different models of dark energy with $\gamma$ still being consistent with the above value [29]. Even modified gravity theories obey Eq. (1.52), but in general predict a growth index distinct from 0.6. This indicates that measurements of peculiar velocities allow tests of general relativity on cosmological scales, which makes them very attractive.

### 1.2.3.3. Nonlinear Regime

When perturbations in the density field reach values of $\delta \sim 1$, higher-order terms such as $\delta^2$ become important and the above linear treatment breaks down. It is very useful to develop a perturbative approach for the evolution of the density field, as it allows to extend analytical predictions into the semilinear regime where $\delta$ approaches unity [3]. However, regions in the universe with $\delta \geq 1$ evolve nonlinearly and become non-perturbative.

A simple example is the collapse of a spherical overdensity $\delta_{\mathrm{sc}}$ of pressureless matter in a flat dust-dominated universe. The overdense region can itself be treated

as a universe with $\Omega_{\mathrm{m}} = 1 + \delta_{\mathrm{sc}} > 1$, implying $\Omega_K < 0$ and thus a positive curvature. In this case, the solution of Eq. (1.12) can be written in parametric form as

$$a(\eta) = \frac{a_{\mathrm{ta}}}{2}(1 - \cos\eta) \quad , \quad t = \frac{t_{\mathrm{ta}}}{\pi}(\eta - \sin\eta) \; , \tag{1.53}$$

where $a_{\mathrm{ta}} \propto \Omega_{\mathrm{m}}/(\Omega_{\mathrm{m}} - 1)$ is the maximal scale factor reached at time $t_{\mathrm{ta}}$, after which the overdense region collapses (*turn-around*). At this time the overdensity reaches its minimal value, which, in order to collapse, must be at least $\delta_{\mathrm{sc}}(t_{\mathrm{ta}}) + 1 = 9\pi^2/16 \simeq 5.55$. After turn-around, the overdensity detaches from the Hubble flow and increases towards a singularity at $t = 2t_{\mathrm{ta}}$. In reality, this singularity is never realized due to deviations from exact spherical symmetry. Instead, by this time the dark matter particles making up the overdense region will form a virialized stable object, denoted *dark matter halo*. Application of the *virial theorem* yields $\delta_{\mathrm{sc}}(2t_{\mathrm{ta}}) + 1 = 18\pi^2 \simeq 178$.

The nonlinear character of Eqs. (1.53) becomes evident when we consider their Taylor expansion only up to linear order. Then, the overdensity at turn-around becomes $\delta_{\mathrm{sc,lin}}(t_{\mathrm{ta}}) \simeq 1.06$ and $\delta_{\mathrm{sc,lin}}(2t_{\mathrm{ta}}) \simeq 1.69$. Hence, when linear theory is applied to evolve the density field, any regions exceeding the critical value $\delta_{\mathrm{c}} \equiv 1.69$ will collapse to form virialized structures.

### 1.2.4. Formation of Large-Scale Structure

Evidently, the formation of structure in the universe is a fairly complex and nonlinear process. The typical amplitude of initial dark matter fluctuations as in Eq. (1.46) increases with $k$, suggesting nonlinear processes to happen earlier on smaller scales. This phenomenon is referred to as *hierarchical clustering* and allows the application of *smoothing*, i.e., the removal of fluctuations below some threshold scale $R$. In Fourier space, the smoothed density field can be expressed as

$$\delta_R(\mathbf{k}) = W(k, R)\delta(\mathbf{k}) \; , \tag{1.54}$$

where $W$ is a *window function* of smoothing scale $R$. Usually, a tophat window in configuration space with Fourier transform

$$W(k, R) = 3\frac{\sin(kR) - kR\cos(kR)}{(kR)^3} \; , \tag{1.55}$$

is used, but depending on the application, a Gaussian window or a tophat window in Fourier space are common, too. The variance of the smoothed field is then determined by applying Eq. (1.31) at $r = 0$,

$$\sigma^2(R) \equiv \langle \delta_R^2(\mathbf{x}) \rangle = \int P_\delta(k)\, |W(k, R)|^2 \, \mathrm{d}^3 k \; , \tag{1.56}$$

it increases with decreasing smoothing scale $R$. Thus, the procedure of smoothing allows to control the degree of nonlinearity in the smoothed field $\delta_R$ by erasing nonlinear structure below that scale.

### 1.2.4.1. Halo Mass Function

Restricting to a range of scales where the probability distribution function of fluctuations is still well described by a Gaussian

$$p(\delta_R) = \frac{1}{\sqrt{2\pi\sigma^2(R)}} \exp\left(-\frac{\delta_R^2}{2\sigma^2(R)}\right) , \qquad (1.57)$$

this allows to estimate the number of collapsed structures in a smoothed field of given $R$ as follows [38]. Regions in the universe whose variance exceeds the critical overdensity for collapse, $\sigma(R) > \delta_c$, form virialized objects of mass $M \propto R^3$. The probability for such a region is obtained by integrating Eq. (1.57),

$$F(\nu) \equiv \int_{\delta_c}^{\infty} p(\delta_R)\, \mathrm{d}\delta_R = \frac{1}{2}\mathrm{erfc}\left(\frac{\nu}{\sqrt{2}}\right) , \qquad (1.58)$$

yielding the *complementary error function*, which depends on the so-called *peak height* $\nu \equiv \delta_c/\sigma(R)$. Thus, the number of collapsed objects between masses $M$ and $M + \mathrm{d}M$ is $n(M)\mathrm{d}M = \frac{\bar{\rho}_m}{M}|\mathrm{d}F(\nu)|$ and with Eq. (1.58) we obtain

$$n(M) = \frac{1}{\sqrt{2\pi}} \frac{\bar{\rho}_m}{M} \frac{\mathrm{d}\nu}{\mathrm{d}M} \exp\left(-\frac{\nu^2}{2}\right) . \qquad (1.59)$$

The typical mass $M_\star$ of halos collapsing at present is defined via $\nu(M_\star) = 1$, respectively $\sigma(M_\star) = \delta_c$. It distinguishes two regimes of the mass function: a power law at $M \ll M_\star$ and an exponential drop-off at $M \gg M_\star$.

Thanks to its simplistic assumptions, this approach yields a qualitatively good description of halo formation, but fails to accurately reproduce the halo mass functions studied in simulations. One caveat is the so-called *cloud-in-cloud problem*, referring to the fact that a spherical region below the threshold of collapse may still virialize when located within a larger region above threshold. Taking this into account amounts to an additional factor of 2 in Eq. (1.59) [6]. Furthermore, the treatment of halos forming from only spherical overdensities can be extended to the more general case of *ellipsoidal collapse*. This results in a collapse threshold that is no longer constant, but a function of the shape of the overdense region and leads to a more accurate halo mass function as compared with simulations [47].

### 1.2.4.2. Halo Bias

To some degree, the large-scale distribution of dark matter halos in the universe can itself be treated as a continuous field, just as the distribution of dark matter particles as in Eq. (1.43). In this case the overdensity of halos is defined as the relative fluctuation in the number of halos around its mean,

$$\delta_h(\mathbf{x}) \equiv \frac{n(\mathbf{x}) - \bar{n}}{\bar{n}} . \qquad (1.60)$$

The spatial variation of $n(\mathbf{x})$ is caused by dark matter density fluctuations $\delta_l$ on large scales, which have not turned nonlinear yet. They can be obtained by smoothing

over a sufficiently large scale by application of Eq. (1.54). Regions with $\delta_l > 0$ will then contain more collapsed objects than slightly underdense regions with $\delta_l < 0$, because nonlinear small-scale perturbations $\delta_s$ reach the collapse threshold $\delta_c$ earlier there. In this manner (referred to as the *peak-background split* formalism [8]), the initial halo density field can be related to the long-wavelength perturbations of the dark matter as

$$n(\mathbf{x}) \simeq \bar{n}\left(1 + b_{\mathrm{L}}\delta_l\right) \;, \tag{1.61}$$

where $b_{\mathrm{L}}$ is a proportionality factor referred to as *linear Lagrangian bias*. With an explicit expression for the mass function, it can be calculated as [31]

$$b_{\mathrm{L}} = \bar{n}^{-1}\frac{\partial n}{\partial \delta_l} \simeq \frac{\nu^2 - 1}{\delta_c} \;, \tag{1.62}$$

where in the second step Eq. (1.59) was approximated to linear order. A better model for the mass function also yields a more accurate formula for $b_{\mathrm{L}}$, for example in the framework of ellipsoidal collapse [48]. Plugged into Eq. (1.60), this reveals that dark matter and halo overdensities are proportional on large scales, $\delta_{\mathrm{h}} = b_{\mathrm{L}}\delta$, and the proportionality constant $b_{\mathrm{L}}$ increases with halo mass. Because a region with positive long-wavelength perturbation $\delta_l$ expands more slowly than the homogeneous background, its final volume becomes smaller, respectively the overdensity of halos larger and vice versa. With the help of Eqs. (1.53), the final halo density field becomes [31]

$$\delta_{\mathrm{h}} = \left(b_{\mathrm{L}} + 1\right)\delta \equiv b\delta \;, \tag{1.63}$$

where $b$ is the so-called *linear Eulerian bias*, according to Eq. (1.62) it is an increasing function of halo mass and redshift. Objects forming at the present epoch with typical mass $M_\star$ have $b(M_\star) = 1$. Because the linear Eulerian bias is independent of scale, Equation (1.63) yields a very simple relation between the clustering statistics of halos and dark matter, both in configuration- and in Fourier space. For instance, to linear order their two-point correlation functions and power spectra are related as

$$\xi_{\delta_{\mathrm{h}}}(r) = b^2 \xi_\delta(r) \quad , \quad P_{\delta_{\mathrm{h}}}(k) = b^2 P_\delta(k) \;. \tag{1.64}$$

When higher orders are considered in the derivation, this relation becomes more complex. More generally, Eq. (1.63) can be written as a Taylor series in the dark matter density [17],

$$\delta_{\mathrm{h}}(\mathbf{x}) = \sum_{i=0}^{\infty} b_i \delta^i(\mathbf{x}) \;, \tag{1.65}$$

with bias parameters $b_i$ for each order $i$, which can be calculated analytically expanding Eq. (1.62) to corresponding order [9]. This ansatz is referred to as the *local bias model*, as the halo overdensity is a function of the dark matter overdensity at the same location in space. Note that higher powers of $\delta$ in Eq. (1.65) correspond to convolutions of $\delta$ in Fourier space, meaning that scales of different size are no longer independent due to *mode coupling*.

### 1.2.4.3. Halo Model

An alternative ansatz to describe the clustering statistics of halos and the dark matter beyond linear order is provided by the *halo model*. The idea is to split the power spectrum into two parts, a *2-halo-* and a *1-halo term* [43],

$$P(k) = P^{2h}(k) + P^{1h}(k) \ . \tag{1.66}$$

The former describes the clustering of different halos within large-scale structure, while the latter only considers the clustering of matter within a single halo, which can still yield contributions on large scales due to mode coupling. For the dark matter power spectrum the two contributions are given by [9]

$$P_\delta^{2h} = \int_0^\infty n(M) \frac{M}{\bar{\rho}_{\mathrm{m}}} U(k|M) \int_0^\infty n(M') \frac{M'}{\bar{\rho}_{\mathrm{m}}} U(k|M') b(M) b(M') P_\delta^{\mathrm{lin}}(k) \ \mathrm{d}M \mathrm{d}M' \ , \tag{1.67}$$

$$P_\delta^{1h} = \int_0^\infty n(M) \left( \frac{M}{\bar{\rho}_{\mathrm{m}}} \right)^2 |U(k|M)|^2 \ \mathrm{d}M \ , \tag{1.68}$$

where $U(k|M)$ is the normalized Fourier space density profile of a dark matter halo with mass $M$ and $P_\delta^{\mathrm{lin}}$ the linear-order dark matter power spectrum as given in Eq. (1.46). For the halo power spectrum the term $M/\bar{\rho}_{\mathrm{m}}$ is exchanged by $1/\bar{n}$ and the integration limits have to be adjusted to the mass range that is considered. The halo model provides a simple phenomenological picture for the clustering statistics of large-scale structure and is able to reproduce simulation results fairly well even in the nonlinear regime [49].

### 1.2.4.4. Stochasticity

The assumption that the distribution of halos can be treated as a continuous field is only accurate in the high number density limit. However, in a given volume $V$ the number of virialized objects above a certain mass is finite, because only regions above threshold will collapse, whereas regions below threshold remain devoid of halos. Therefore, halos sample the dark matter density field in a discrete fashion, resulting in a certain degree of scatter in the relation between their overdensities. For this reason halos are considered being not only biased, but also *stochastic* tracers of the dark matter, and Eq. (1.65) must be complemented with an additional noise field $\epsilon$ [13],

$$\delta_{\mathrm{h}}(\mathbf{x}) = \sum_{i=0}^\infty b_i \delta^i(\mathbf{x}) + \epsilon(\mathbf{x}) \ . \tag{1.69}$$

Since $\epsilon$ is simply defined as a residual of the Taylor series in $\delta$, it is uncorrelated with the latter, i.e. $\langle \epsilon(\mathbf{x}) \delta(\mathbf{x}') \rangle = 0 \quad \forall \ \mathbf{x}, \mathbf{x}'$. Assuming $\epsilon$ to arise from a uniform *Poisson point process* [35], it is also spatially uncorrelated with itself, which means $\langle \epsilon(\mathbf{x}) \epsilon(\mathbf{x}') \rangle = 0 \quad \forall \ \mathbf{x} \neq \mathbf{x}'$. However, the field has a finite variance due to its Poissonian nature for the distribution of $N$ points in a finite volume $V$,

$$\langle \epsilon^2(\mathbf{x}) \rangle = \langle \left( \frac{N - \bar{N}}{\bar{N}} \right)^2 \rangle = \frac{\mathrm{Var}(N)}{\bar{N}^2} = \frac{\bar{N}}{\bar{N}^2} = \frac{1}{\bar{N}} \ . \tag{1.70}$$

This variance is commonly referred to as *Poisson shot noise* and results in an extra contribution in the two-point clustering statistics of halos as in Eq. (1.64),

$$\xi_{\delta_{\mathrm{h}}}(r) = b^2 \xi_\delta(r) + \bar{N}^{-1}\delta^{\mathrm{D}}(r) \quad , \quad P_{\delta_{\mathrm{h}}}(k) = b^2 P_\delta(k) + \bar{n}^{-1} \, , \qquad (1.71)$$

where $\bar{n} = \bar{N}/V$ is the average number density of halos in the considered volume. Thus, Poisson shot noise leads to a scale-independent power with amplitude $\bar{n}^{-1}$ in Fourier space, which is why it is also referred to as *white noise*.

Note that the *1*-halo term of the halo model in Eq. (1.68) already incorporates this behavior on large scales, where $U(k|M) \to 1$. However, for the dark matter power spectrum this is unphysical due to local mass and momentum conservation of the dark matter particles. Suppose a uniform distribution of particles is split into a large number of small cells, such that the particles in each cell will collapse onto a point within the cell's center of mass. Then, a Taylor expansion of the exponential in Eq. (1.23) reveals the lowest non-vanishing order in the Fourier mode of the field to be $\delta_{\mathbf{k}} \propto k^2$, so $P_\delta(k) \propto k^4$ on large scales [35, 53].

### 1.2.4.5. Galaxies

The structure of the universe that we observe today consists of galaxies made from baryonic matter, a fact that has been completely neglected so far. Nevertheless, due to the overabundance of dark matter it seems reasonable to assume baryons to behave as test particles in the gravitational potential of the dark matter and galaxies to form deep inside its potential wells, the dark matter halos [54].

As opposed to halos, the formation of galaxies is subject to electromagnetic interactions among baryons. This causes new physical phenomena to appear, such as star formation, radiation pressure and gas cooling. Thus, a self-consistent analytical treatment of structure formation is much harder to achieve and it is more convenient to resort to semi-analytic models for galaxy formation. One such approach is known as *halo occupation distribution* (HOD) modeling. The idea is to populate dark matter halos with galaxies in a probabilistic fashion, with probability distributions constrained both numerically and observationally.

One generally distinguishes between two such distributions, one for *central galaxies* that reside close to the center of mass of their parent halo, and *satellite galaxies* orbiting the latter. While there is typically one central galaxy in each halo above a given mass threshold, the number of satellites scales with the host-halo mass [58]. Therefore, it is reasonable to describe the clustering of galaxies by means of the halo model, with satellites playing the role of bound dark matter particles in the halo and central galaxies being a proxy for the halo's center of mass.

### 1.2.4.6. Redshift-Space Distortions

A complication in the description of galaxy clustering arises observationally, due to the fact that radial distances of galaxies are inferred via their redshift $z$ and the Hubble law, Eq. (1.1). However, besides their motion within the Hubble flow, galaxies acquire peculiar velocities $\mathbf{v}$ from the mutual gravitational interaction of

their dark matter halos. Neglecting those results in a *redshift-space* coordinate $\mathbf{s}$ that differs from their *real space* coordinate $\mathbf{r}$ by

$$\mathbf{s} = \mathbf{r} + \frac{\hat{\mathbf{r}} \cdot \mathbf{v}}{H} \, \hat{\mathbf{r}} \, , \tag{1.72}$$

where $\hat{\mathbf{r}} \equiv \mathbf{r}/|\mathbf{r}|$ is the unit vector along the line of sight. The volume element in the mapping between the two coordinate frames changes as

$$\mathrm{d}^3 s = \left( 1 + \frac{\hat{\mathbf{r}} \cdot \mathbf{v}}{Hr} \right)^2 \left( 1 + \frac{\mathrm{d}}{\mathrm{d}r} \frac{\hat{\mathbf{r}} \cdot \mathbf{v}}{H} \right) \mathrm{d}^3 r \, , \tag{1.73}$$

but the number of objects is invariant, so $\delta_{\mathrm{g}} \mathrm{d}^3 r = \delta_{\mathrm{g}}^{(s)} \mathrm{d}^3 s$ must hold for the overdensities of galaxies in real- and redshift-space, respectively. To linear order, a plane-wave perturbation with wavevector $\mathbf{k} \parallel \mathbf{v}$ in the distant-observer approximation, i.e. $kr \gg 1$, yields [23]

$$\delta_{\mathrm{g}}^{(s)}(\mathbf{k}, \mu) = \left( b + f\mu^2 \right) \delta(\mathbf{k}) \, , \tag{1.74}$$

where $\mu \equiv \hat{\mathbf{k}} \cdot \hat{\mathbf{r}}$, galaxies are assumed to be linearly biased with respect to the dark matter overdensity field $\delta$ and Eq. (1.51) has been used to relate the velocity perturbation $\mathbf{v}$ with the latter. Therefore, the galaxy redshift-space power spectrum becomes anisotropic and can be written as

$$P_{\delta_{\mathrm{g}}^{(s)}}(k, \mu) = \left( 1 + \beta\mu^2 \right)^2 b^2 P_\delta(k) \, , \tag{1.75}$$

with the observable redshift-space distortion (RSD) parameter $\beta \equiv f/b$. Equations (1.74) and (1.75) are only accurate on linear scales, where peculiar velocities are generated from large-scale flows towards overdense regions (*Kaiser effect*). On nonlinear scales, random motions are generated in the process of virialization which washes out power along the line of sight, the so-called *Finger-of-God effect*. It is often modeled phenomenologically by an additional Gaussian damping factor $\exp(-k^2\mu^2\sigma_v^2/2)$ in Eq. (1.74), with $\sigma_v$ being the velocity dispersion [34].

## 1.3. Scientific Tools

The increasing wealth and complexity of contemporary cosmological data sets requires high logistical demands for their manipulation and analysis. Computers have become inevitable for performing computationally intensive tasks, either for reducing the relevant scientific output from observations to a manageable size, or to reproduce complex experiments in the most realistic way. This section is devoted to the scientific tools that are commonly being utilized in the scientific community for the analysis of large-scale structure.

### 1.3.1. Statistical Techniques

Every observation of nature is affected by uncertainty to some degree, no theory can ever be proven wright, it can only be rejected or updated by a new one. The selection process to find the most accurate description of the observation thus has to be probabilistic, irrespective of the universe's own stochastic nature.

#### 1.3.1.1. Parameter Estimation

In general, a given set of observed data $\mathbf{d}$ is described by a model with parameters $\boldsymbol{\theta}$. The task is to find the posterior probability distribution $p(\boldsymbol{\theta}|\mathbf{d})$ of $\boldsymbol{\theta}$ given the data $\mathbf{d}$ and to extract the most likely value of the parameters including their uncertainties [19]. The model usually provides the opposite quantity $p(\mathbf{d}|\boldsymbol{\theta})$, which is also referred to as the *likelihood* $\mathscr{L}$ of the data, given the model. The two probability distributions are related via *Bayes' Theorem* [2],

$$p(\boldsymbol{\theta}|\mathbf{d}) = \frac{p(\mathbf{d}|\boldsymbol{\theta})p(\boldsymbol{\theta})}{p(\mathbf{d})} \; , \tag{1.76}$$

with so-called *prior* $p(\boldsymbol{\theta})$ and *evidence* $p(\mathbf{d})$. For a given model, the evidence is just a normalization constant and can be ignored. If the prior is assumed to be *flat*, i.e. every parameter value equally likely a priori, then the posterior probability distribution is proportional to the likelihood, $p(\boldsymbol{\theta}|\mathbf{d}) \propto \mathscr{L}(\mathbf{d},\boldsymbol{\theta})$.

In this case, a Taylor expansion of the natural logarithm of the likelihood around the true parameter values $\boldsymbol{\theta}_0$ yields a multivariate Gaussian close to its peak,

$$\mathscr{L}(\mathbf{d},\boldsymbol{\theta}) \simeq \mathscr{L}(\mathbf{d},\boldsymbol{\theta}_0) \exp\left[-\frac{1}{2}\left(\boldsymbol{\theta}-\boldsymbol{\theta}_0\right)^{\mathsf{T}}\mathbf{H}\left(\boldsymbol{\theta}-\boldsymbol{\theta}_0\right)\right] \; , \tag{1.77}$$

where $\mathbf{H}$ is the *Hessian* of the log-likelihood, in index notation $\mathbf{H}_{ij} \equiv -\frac{\partial^2 \ln\mathscr{L}}{\partial\theta_i \partial\theta_j}$. The diagonal elements of this matrix contain the *conditional errors* of the parameters as $\sigma_{\theta_i} = 1/\sqrt{\mathbf{H}_{ii}}$, but in general it also has non-vanishing off-diagonals, meaning different parameters are correlated with each other. Therefore, the *marginal errors* of the parameters are calculated via inversion of the Hessian,

$$\sigma_{\theta_i} = \sqrt{\left(\mathbf{H}^{-1}\right)_{ii}} \; . \tag{1.78}$$

### 1.3.1.2. Error Forecast

With a particular model at hand one can choose fiducial values for its parameters, calculate their likelihood and according to Eq. (1.78) their uncertainties. So before even collecting any data, with a reasonable guess for what the model parameters should roughly be, it is possible to forecast the precision they can be determined with. It can be shown that every unbiased estimator of the parameter $\theta_i$ satisfies the *Cramér-Rao bound* [39]

$$\sigma_{\theta_i} \geq \sqrt{(\mathbf{F}^{-1})_{ii}} \ , \tag{1.79}$$

with the so-called *Fisher information matrix* $\mathbf{F}_{ij}$ [15] defined as the expectation value of the Hessian,

$$\mathbf{F}_{ij} \equiv \langle -\frac{\partial^2 \ln \mathscr{L}}{\partial \theta_i \partial \theta_j} \rangle \ . \tag{1.80}$$

Suppose the likelihood of $N$ measurements is a multivariate Gaussian in the data,

$$\mathscr{L}(\boldsymbol{\theta}, \mathbf{d}) = \frac{1}{(2\pi)^{N/2}\sqrt{\det \mathbf{C}}} \exp \left[ -\frac{1}{2} (\mathbf{d} - \boldsymbol{\mu})^\intercal \, \mathbf{C}^{-1} \, (\mathbf{d} - \boldsymbol{\mu}) \right] \ , \tag{1.81}$$

with mean $\boldsymbol{\mu} \equiv \langle \mathbf{d} \rangle$ and *covariance matrix* $\mathbf{C} \equiv \langle (\mathbf{d} - \boldsymbol{\mu}) (\mathbf{d} - \boldsymbol{\mu})^\intercal \rangle$ depending on the parameters $\boldsymbol{\theta}$. Plugged into Eq. (1.80) with a bit of algebra yields [19]

$$\mathbf{F}_{ij} = \frac{1}{2}\mathrm{Tr} \left( \frac{\partial \mathbf{C}}{\partial \theta_i} \mathbf{C}^{-1} \frac{\partial \mathbf{C}}{\partial \theta_j} \mathbf{C}^{-1} + \mathbf{C}^{-1}\mathbf{M}_{ij} \right) \ , \tag{1.82}$$

where $\mathbf{M}_{ij} \equiv \frac{\partial \boldsymbol{\mu}}{\partial \theta_i} \frac{\partial \boldsymbol{\mu}^\intercal}{\partial \theta_j} + \frac{\partial \boldsymbol{\mu}}{\partial \theta_j} \frac{\partial \boldsymbol{\mu}^\intercal}{\partial \theta_i}$. The Fisher matrix obtained from independent experiments can simply be added, a convenient property reflecting the informational nature of this quantity.

### 1.3.2. Simulations

Numerical simulations have become an inevitable tool for studying the nonlinear regime of structure formation. Thanks to the rapid increase in computer performance and the development of efficient algorithms, substantial progress in the field of numerical cosmology has been achieved in the last two decades.

### 1.3.2.1. Particles

The idea is to solve nonlinear fluid equations with a discretized set of fluid elements, the *particles*. From the classical point of view this is very natural, as baryons and dark matter are described as particles on the fundamental level, as well. However, the actual number of physical particles in the observable universe exceeds the computationally manageable one by many orders of magnitude, which limits the accuracy of these so-called *N-body simulations*.

To set up the initial conditions, particles have to be distributed such as to satisfy the background cosmology and the initial power spectrum of density fluctuations, as in Eq. (1.46). The initial amplitude $A_0$ of these fluctuations is constrained from observations of the CMB, but traditionally it is also common to use $\sigma_8$, the linear

extrapolation of fluctuations to $z = 0$, smoothed according to Eq. (1.54) with $R = 8h^{-1}\text{Mpc}$, to normalize the initial power spectrum. A realization of the latter can be generated by slightly displacing particles on a uniform lattice using the *Zel'dovich approximation* [57], assuming linear growth as in Eqs. (1.50) and (1.51). Extensions to this technique have been developed, utilizing perturbation theory to improve accuracy beyond linear growth [42].

For collisionless particles, such as the dark matter, it is sufficient to evolve them only gravitationally. On sub-horizon scales this amounts to calculating the gravitational forces between each particle and all its neighbors according to Newton's laws and updating their positions and velocities iteratively within an expanding coordinate system [4]. However, the efficiency of this so-called *particle-particle* (PP) method quickly degrades as the number $N_p$ of particles increases: the amount of computing steps scales as $\mathcal{O}(N_p^2)$. The high number of force calculations can be reduced by expanding the potential of extended regions in multipoles hierarchically and truncating the series at sufficient order, resulting in a scaling of $\mathcal{O}(N_p \ln N_p)$ of this so-called *tree method*.

Further improvements, especially in regard of memory consumption, are achieved with the *particle-mesh* (PM) method. Here, particles are interpolated on a mesh with $N_c^3$ cells and the Poisson Eq. (1.44) is solved in $k$-space using a fast Fourier transform (FFT) algorithm. In the next step, forces are interpolated back on the particles, which are moved accordingly, and the whole procedure is reiterated. The scaling of this algorithm is $\mathcal{O}(N_p, N_c^3 \ln N_c)$ and thus allows the highest number of particles of all methods, with the cost of lower spatial resolution due to the mesh interpolation.

A widely used state-of-the-art $N$-body code is is GADGET-2, which uses a combination of the PM method and a tree algorithm to more accurately sample large and small scales, respectively [51]. In addition to collisionless particles, it offers the possibility to evolve gas particles that exhibit heat and pressure, a feature referred to as *smoothed particle hydrodynamics* (SPH).

### 1.3.2.2. Halos

When the dark matter particles in a simulation are evolved deeply into the nonlinear regime, they form a cosmic web of collapsed structures. The classification of these structures into halos, filaments and walls is not unique and many identification schemes have appeared in the literature. Two of the most common ones for halos are the so-called *spherical overdensity* (SO) finder and the *friends-of-friends* (FoF) finder. The former defines halos according to the spherical collapse model, localizing spherical regions with overdensities above some critical threshold [26], while the latter groups particles together that are separated by less than a specified *linking length* [10]. Typically, it is chosen to be 20% of the mean inter-particle distance, yielding a corresponding critical overdensity of $\delta_{\text{c,FoF}} \sim 1/0.2^3 = 125$.

Although neither of these methods guarantees all identified halo particles to be gravitationally bound to a virialized structure, they yield reasonable agreement in identifying halos in the high resolution limit. The SO method tends to miss aspherical objects that are easily identified by the FoF finder. Conversely, the FoF finder may

link adjacent halos with distinct spherical overdensities to a single object. A number of alternatives for defining halos have been proposed to overcome these ambiguities, but a consensus on an optimal identification scheme has not been achieved so far [24].

### 1.3.3. Numerical Analysis

Most of the mathematical operations in the description of large-scale structure assume continuous and differentiable functions of time and space, such as the density fluctuation $\delta(\mathbf{x}, t)$ or the peculiar velocity field $\mathbf{v}(\mathbf{x}, t)$. In numerical simulations however, everything is discretized, so the mathematical operations utilized so far have to be modified accordingly.

### 1.3.3.1. Discrete Fourier Transform

Consider a cubic box of edge length $L$ and volume $L^3$, divided into $N_c^3$ equally sized cubical cells. The discrete analog of Eqs. (1.26) and (1.27) can be formulated as

$$f(\mathbf{x_n}) = \frac{1}{L^{3/2}} \sum_{\mathbf{n'}} f(\mathbf{k_{n'}}) \exp(i\mathbf{k_{n'}} \cdot \mathbf{x_n}) \,, \tag{1.83}$$

$$f(\mathbf{k_n}) = \frac{L^{3/2}}{N_c^3} \sum_{\mathbf{n'}} f(\mathbf{x_{n'}}) \exp(-i\mathbf{k_n} \cdot \mathbf{x_{n'}}) \,, \tag{1.84}$$

where $\mathbf{x_n} = \mathbf{n}\frac{L}{N_c}$ and $\mathbf{k_n} = \mathbf{n}\frac{2\pi}{L}$ with $n_i \in [1, N_c] \; \forall i \in [1, 2, 3]$. The resolution in configuration space is limited by the cell size $L/N_c$, which corresponds to the *Nyquist wavenumber* $k_{\mathrm{N}} \equiv \pi N_c / L$ in Fourier space.

### 1.3.3.2. Mesh Interpolation

The overdensity field of $N_p$ point particles can formally be written as a superposition of Dirac delta functions

$$\delta(\mathbf{x}) = \frac{1}{N_p} \sum_{i=0}^{N_p} \delta^{\mathrm{D}}(\mathbf{x} - \mathbf{x}_i) - 1 \,, \tag{1.85}$$

where at the location $\mathbf{x}_i$ of particle $i$, $\delta$ is infinite. In order to manipulate $\delta(\mathbf{x})$ using mathematical operations involving derivatives, it has to be interpolated on a mesh. This corresponds to a smoothing procedure as in Eq. (1.54) with a suitable window function. A common choice is the so-called *cloud-in-cell* (CIC) window [20]

$$W_{\mathrm{CIC}}(\mathbf{x} - \mathbf{x_n}) = \begin{cases} 1 - \frac{|\mathbf{x} - \mathbf{x_n}|}{L/N_c} & \text{, if } |\mathbf{x} - \mathbf{x_n}| \leq L/N_c \\ 0 & \text{, otherwise} \end{cases} \tag{1.86}$$

which is being convolved with the point distribution from Eq. (1.85) over the whole volume $V = L^3$ in configuration space,

$$\delta(\mathbf{x_n}) = \int_V \delta(\mathbf{x}) W_{\mathrm{CIC}}(\mathbf{x} - \mathbf{x_n}) \, \mathrm{d}^3x = \frac{1}{N_p} \sum_{i=1}^{N_p} W_{\mathrm{CIC}}(\mathbf{x}_i - \mathbf{x_n}) \,. \tag{1.87}$$

In Fourier space, the CIC window function of Eq. (1.86) reads

$$W_{\mathrm{CIC}}(\mathbf{k_n}) = \prod_{i=1}^{3} \frac{\sin^2\left(\pi n_i/N_c\right)}{\left(\pi n_i/N_c\right)^2} \; , \tag{1.88}$$

so the structure introduced in the particle density field caused by the mesh interpolation can be easily corrected for by simply dividing out the window function in Fourier space as suggested by Eq. (1.54). Due to discreteness this is not exact, but an accurate correction can be achieved iteratively [22].

### 1.3.3.3. Estimators

With the interpolated overdensity field $\delta(\mathbf{k_n})$ in Fourier space, it is straight-forward to compute an estimator $\hat{P}$ for its power spectrum via shell averaging,

$$\hat{P}_\delta(k) = \frac{1}{N_k} \sum_{\Delta k} \delta(\mathbf{k_n})\delta^*(\mathbf{k_n}) \; , \tag{1.89}$$

where $\Delta k$ denotes a shell in Fourier space containing all wavevectors $\mathbf{k_n}$ with lengths $|\mathbf{k_n}| - \Delta k \leq |\mathbf{k_n}| < |\mathbf{k_n}| + \Delta k$. This amounts to a number of $N_k \simeq \frac{4\pi k^2 \Delta k}{(2\pi/L)^3}$ independent Fourier modes in a bin of average wavenumber $k = \frac{1}{N_k}\sum_{\Delta k}|\mathbf{k_n}|$.
Likewise, the estimator for the two-point correlation function of $\delta(\mathbf{x_n})$ can be determined as

$$\hat{\xi}_\delta(r) = \frac{1}{N_r} \sum_{\Delta r} \frac{1}{N_c^3} \sum_{\mathbf{n}'} \delta(\mathbf{x_{n'}})\delta(\mathbf{x_{n'}} + \mathbf{r_n}) \; , \tag{1.90}$$

where all cells of mutual distance $\mathbf{r_n}$ within the interval $|\mathbf{r_n}| - \Delta r \leq |\mathbf{r_n}| < |\mathbf{r_n}| + \Delta r$ are summed over. Here, the normalization is given by the number of cells $N_r \simeq \frac{L^3}{4\pi r^2 \Delta r}$ in the bin of average separation $r = \frac{1}{N_r}\sum_{\Delta r}|\mathbf{r_n}|$. The Fourier-pair relationship between the power spectrum and the two-point correlation function from Eq. (1.31) is only restored for their estimators in the limit $\Delta k, \Delta r \to 0$ and $N_c \to \infty$.

# 2

## PAPER I

**Summary**   The following letter describes a curious feature of dark matter halos in $N$-body simulations: As opposed to the Poisson assumption, the shot noise of halos is found to be dependent on the mass of the considered halos, with values ranging from below to above the expected inverse halo number density $1/\bar{n}$. Moreover, weighting each halo in the simulation by its *mass* (number of dark matter particles) yields a considerable reduction to the shot noise measured in the unweighted halo density field. The paper presents the results for various halo samples of different mass range and number density and finds even higher suppression in shot noise feasible with slightly modified weights. As a physical explanation it is argued that local mass and momentum conservation of the halos is responsible for the observed effects. Although strictly obeyed only by the dark matter particles themselves, mass and momentum conservation may, to some degree, also apply to central galaxies in halos. It is argued that a proper implementation of the weighting scheme in current and future galaxy surveys may have the potential to significantly improve on parameter constraints in cosmology. A number of possible applications are mentioned, such as measurements of baryon acoustic oscillations, the dark energy equation of state, primordial non-Gaussianity and redshift-space distortions.

The input for this article was contributed by a collaboration of three authors. Uroš Seljak initiated a project to study the stochasticity of halos in $N$-body simulations and proposed the presented estimator for the shot noise. He also suggested the use of weights to observe how this estimator is affected. The numerical analysis was carried out by myself on the basis of $N$-body simulations and halo catalogs provided by Vincent Desjacques. The main part of the manuscript was written by Uroš Seljak, I provided the figures. It got published in August 2009 in *Physical Review Letters* (vol. 103, ID 091303, arXiv:0904.2963).

# How to Suppress the Shot Noise in Galaxy Surveys

Uroš Seljak,[1, 2, 3] Nico Hamaus,[1] and Vincent Desjacques[1]

[1]*Institute for Theoretical Physics, University of Zurich, 8057 Zurich, Switzerland*
[2]*Physics Department, Astronomy Department and Lawrence Berkeley National Laboratory,*
*University of California, Berkeley, California 94720, USA*
[3]*Ewha University, Seoul 120-750, S. Korea*
(Dated: August 26, 2009)

Galaxy surveys are one of the most powerful means to extract cosmological information and for a given volume the attainable precision is determined by the galaxy shot noise $\sigma_n^2$ relative to the power spectrum $P$. It is generally assumed that shot noise is white and given by the inverse of the number density $\bar{n}$. In this Letter we argue one may considerably improve upon this due to mass and momentum conservation. We explore this idea with N-body simulations by weighting central halo galaxies by halo mass and find that the resulting shot noise can be reduced dramatically relative to expectations, with a 10-30 suppression at $\bar{n} = 4 \times 10^{-3}(h/\mathrm{Mpc})^3$. These results open up new opportunities to extract cosmological information in galaxy surveys and may have important consequences for the planning of future redshift surveys.

Galaxy clustering has been one of the leading methods to measure the clustering of dark matter in the past and with upcoming redshift surveys such as SDSS-III and JDEM/EUCLID this will continue to be the case in the future. Galaxies are easily observed and by measuring their redshift one can determine their three-dimensional distribution. This is currently the only large scale structure method that provides three-dimensional information. On large scales galaxies trace the dark matter up to a constant of proportionality called bias $b$, so the galaxy power spectrum can be directly related to the dark matter power spectrum shape, which contains a wealth of information such as the scale dependence of primordial fluctuations, signatures of massive neutrinos and matter density, etc. In recent years the baryonic acoustic oscillations (BAO) feature in the power spectrum has been emphasized, which can be used as a standard ruler and in combination with cosmic microwave background anisotropies can provide a redshift distance test [1].

For the power spectrum measurement there are two sources of error: one is the sampling (sometimes called cosmic) variance, the fact that each mode is a Gaussian random realization and all the cosmological information lies in its variance, which cannot be well determined on the largest scales because the number of modes is finite. Second source of noise is the shot noise due to the discrete sampling of galaxies, $\sigma_n^2$, which under the standard assumptions of Poisson sampling equals the inverse of the number density $\bar{n}$. The total error on the power spectrum $P$ is $\sigma_P/P = (2/N)^{1/2}(1+\sigma_n^2/P)$, where $N$ is the number of modes measured and scales linearly with the volume of the survey. While the above expression suggests there is not much benefit in reducing the shot noise to $\sigma_n^2/P \ll 1$ since sampling variance error remains, recent work suggests there are potential gains in that limit, since we may be able to reduce the damping of the BAO better [2].

Recently a new multitracer method has been developed where by comparing two differently biased tracers of the same structure one can extract cosmological information in a way that the sampling variance error cancels out [3]. There are several applications of this method, such as measuring the primordial non-Gaussianity [3], redshift-space distortion parameter $\beta$ [4] or relation between the Hubble parameter and the angular diameter distance [4]. In all these applications one can achieve significant gains in the error of the extracted cosmological parameters if $\sigma_n^2/P \ll 1$. Thus in all of these applications the galaxy shot noise relative to the power spectrum is the key quantity that controls the ultimate level of cosmological precision one can achieve with galaxy surveys.

The relation between the galaxy and the dark matter clustering can be understood with the halo model [5–7], where all of the dark matter is divided into collapsed halos of varying mass. There are two contributions to the dark matter clustering: first is the correlation between two separate halos, which is assumed to be proportional to the linear theory spectrum times the product of the two halo biases, while the second contribution is the one halo term which includes the clustering contributions from the individual halo itself. One obtains the dark matter power spectrum prediction by adding up the contributions from all the halos. Since galaxies are assumed to form inside the halos one can write analogous expressions for galaxy clustering power spectra once one specifies the occupation distribution of galaxies as a function of halo mass.

One consequence of the halo model is that the one halo term is dominated by the most massive halos and reduces to white noise $k^0$ for very small wave-mode amplitude $k \ll R^{-1}$, where $R$ is the size of the largest halos. For galaxies this is believed to be a valid description of the shot noise amplitude in the low $k$ limit. It distinguishes

between the galaxy and the halo number density, but for a typical survey the fraction of halos with more than one galaxy in it is small, 5-30% [8], and here we will ignore this distinction and assume for simplicity there is only one galaxy in each halo at its center.

For the dark matter, the nonlinear evolution of structure requires local mass and momentum conservation and as a result the low $k$ limit of nonlinear contribution is predicted to scale as $k^4$ and not $k^0$ [9]. This is indeed seen in simulations [10], making the prediction of the halo model invalid. While this is often seen as a deficiency of the halo model, here we take it as an opportunity: if the dark matter has no white noise tail in the $k \to 0$ limit then in the context of the halo model where all the dark matter is in the halos and the halo size becomes irrelevant in the $k \ll R^{-1}$ limit it should be possible to achieve the same effect with galaxies, if one can enforce local mass and momentum conservation. The most natural possibility is to weight the galaxies by the halo mass.

The purpose of this Letter is to explore this idea with numerical simulations. We employ a suite of large N-body simulations using the Gadget II code, which include four simulations with $1024^3$ particles in a $(1.6h^{-1}\text{Gpc})^3$ box and one simulation with $1536^3$ particles in a $(1.3h^{-1}\text{Gpc})^3$ box. The fiducial cosmological model has a scale invariant spectrum with amplitude $\sigma_8 = 0.81$, matter density $\Omega_m = 0.28$ and Hubble parameter $H_0 = 70$km/s/Mpc. We ran a Friends of Friends halo finder and kept all the halos with more than 20 particles, with the lowest halo mass of $6 \times 10^{12} h^{-1} M_\odot$ and $10^{12} h^{-1} M_\odot$, respectively.

If a tracer has an overdensity $\delta_h$ with a bias $b_h$, then the relation to the dark matter overdensity $\delta_m$ in Fourier space can be written as $\delta_h = b_h \delta_m + n$, where $n$ is shot noise with a power spectrum $\langle n^2 \rangle = \sigma_n^2$ and we assume it is uncorrelated with the signal, i.e. $\langle \delta_m n \rangle = 0$ (the operations should be taken separately on real and imaginary components of the Fourier modes). Thus we define $\sigma_n^2 = \langle (\delta_h - b_h \delta_m)^2 \rangle$ and bias is $b_h = (P_{hh}/P_{mm})^{1/2} = P_{hm}/P_{mm}$, where $P_{hh} = \langle \delta_h^2 \rangle - \sigma_n^2$, $P_{hm} = \langle \delta_m \delta_h \rangle$ and $P_{mm} = \langle \delta_m^2 \rangle$. This is equivalent to choosing $\sigma_n^2$ such that the cross correlation coefficient is unity, $r \equiv P_{hm}/(P_{hh}P_{mm})^{1/2} = 1$. Thus our definition of the shot noise includes all sources of stochasticity between the halos and the dark matter, so it is the most conservative. This can be done as a function of $k$ and so allows for a possibility that noise is not white. We do not assume a constant bias, although we find that for $k \ll 0.1h$/Mpc this is generally true. Another way to define the shot noise is through the power spectrum fluctuations, $\langle (\delta_h^2 - P_{hh} - \sigma_n^2)^2 \rangle = (2/N)(P_{hh}^2 + (\sigma_n^2)^2)$. We find this definition in general has larger variance, but is on average in agreement with the definition above, which
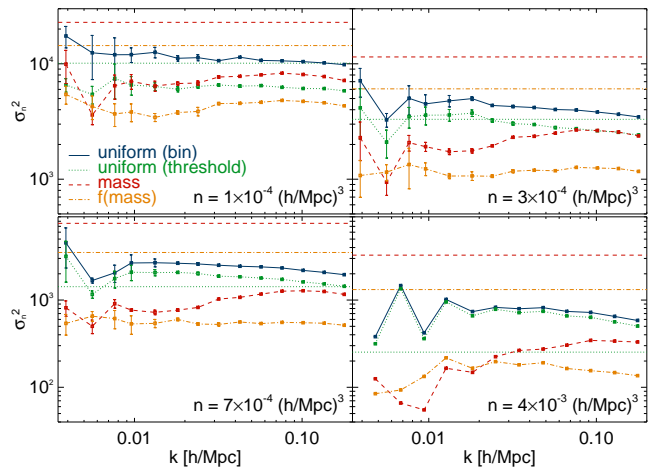


FIG. 1. Shot noise power spectrum $\sigma_n^2$ measured in simulations for uniform weighting of halos in a mass bin and mass threshold, mass weighting and $f(M) = M/[1 + (M/10^{14}h^{-1}M_\odot)^{0.5}]$ weighting, for several different abundances, corresponding at $z = 0$ to mass thresholds of $4 \times 10^{13} h^{-1} M_\odot$, $1.4 \times 10^{13} h^{-1} M_\odot/h$, $6 \times 10^{12} h^{-1} M_\odot$ and $10^{12} h^{-1} M_\odot/h$, from the lowest to the highest abundance, respectively. Straight lines (same color or line style) are the expected shot noise $\sigma_e^2$ for each of the weightings (equal for the mass bin and mass threshold with uniform weighting).

we will use in the following.

We begin by first investigating the shot noise when each halo has equal weight. The simplest case is that of a mass threshold, where all of the halos above a certain minimum cutoff are populated. Second possibility is that of a bin in halo mass, for which we remove the top 10% of the most massive halos in a simulation and take the remaining ones to match a given abundance. As shown in Fig. 1 this leads to a larger shot noise than the mass threshold case, neither of which in general agrees with the prediction $\sigma_n^2 = \bar{n}^{-1}$. The latter can dramatically underestimate the shot noise at higher abundances, by a factor of 3 for our highest number density of $\bar{n} = 4 \times 10^{-3} (h/\text{Mpc})^3$. The standard error analysis assumes $\sigma_n^2 = \bar{n}^{-1}$ and may be overly optimistic: shot noise should be a free parameter determined from the data itself.

Next we investigate the shot noise for nonuniform halo dependent weighting $w_i$ for the same mass threshold sample. We compare the simulations to the expectation $\sigma_e^2 = V \sum_i w_i^2 / (\sum_i w_i)^2$, where $V$ is the volume and the sum is over all the halos. At a given number density this expression is minimized for uniform weighting (where it equals $\bar{n}^{-1}$), so nonuniform weighting generally increases the expected shot noise. As argued above $w_i = M_i$, where $M_i$ is the halo mass, is the natural implementation of the idea to enforce mass and momen-

tum conservation for the halos. The results are shown in Fig. 1. We see that the predicted and measured shot noise amplitudes differ significantly and the difference reaches a factor of 10-30 at the highest abundance in our simulations, $\bar{n} = 4 \times 10^{-3}(h/\mathrm{Mpc})^3$. This demonstrates that this is not a simple Poisson sampling of the field and that mass and momentum conservation work to suppress the shot noise relative to expectations.

Other weightings may also improve the results relative to naive expectations and may work even better for specific applications. For example, weighting by $f(M) = M/[1 + (M/10^{14}h^{-1}M_\odot)^{0.5}]$, shown in Fig. 1, improves upon the mass weighting. This weighting equals the halo mass weighting over the mass range of $M < 10^{14}h^{-1}M_\odot$, while giving a lower weight to the higher mass halos relative to the mass weighting. Weighting by the halo mass gives a very large weight to the most massive halos and this non-uniform weighting leads to a significant increase in the naive shot noise prediction $\sigma_e^2$ relative to the number density of halos. Therefore, if the conservation of mass and momentum is not perfect for the most massive halos the residual shot noise may still be large, which may explain why downweighting high mass halos may work better. On the other hand, simply eliminating the halos above $10^{14}h^{-1}M_\odot$ while preserving mass weighting below that mass completely erased any advantages. We also tried weighting by the halo bias $b$, which was argued to minimize $\sigma^2/P$ [11], and found no improvements relative to uniform weighting, as expected since it is close to uniform weighting for most of the halos and therefore does not implement the mass and momentum conservation efficiently. It is possible that one may be able to further improve the signal to noise by optimizing the weights, but the optimization will depend on the specific application one has in mind (e.g. non-Gaussianity, redshift-space distortions, BAO etc.) and is beyond the scope of this Letter.

For actual applications we want to minimize $\sigma_n^2/P$. Figure 2 shows the results for the same cases as in Fig. 1. We see there are significant improvements in $\sigma_n^2/P$ relative to the uniform weighting and that mass and modified mass give comparable results, with improvements in excess of 10 possible relative to the uniform weighting. While these results are all at $z = 0$ where we have the highest density of halos, we also computed them at higher redshifts. At $z = 0.5$ and $\bar{n} = 3 \times 10^{-4}(h/\mathrm{Mpc})^3$, target density for SDSS-III, we find a factor of 3-10 improvement at the BAO scale in mass weighting relative to the uniform, comparable to the $z = 0$ case at the same number density. This means that the achievable error on cosmological parameters from BAO can be improved significantly for the same number of objects measured. Alternatively, a significantly lower number of objects may be needed to achieve the same precision and one can re-
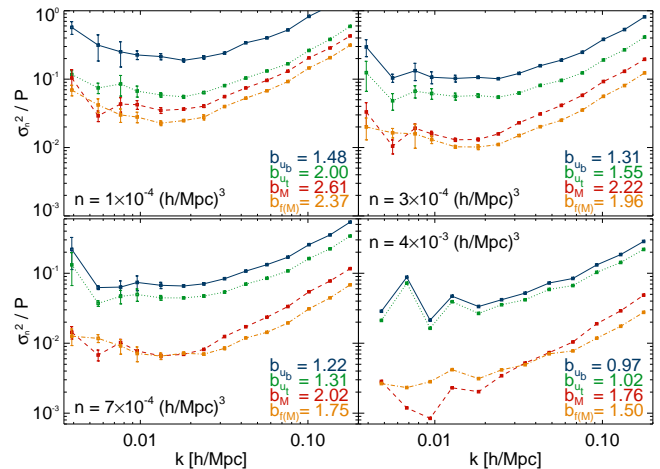


FIG. 2. Same as Fig. 1, but for $\sigma_n^2/P$. Also shown are the bias values $b$ for the different cases, which affect $\sigma_n^2/P$, since $P = b^2 P_{mm}$, where $P_{mm}$ is the matter power spectrum.
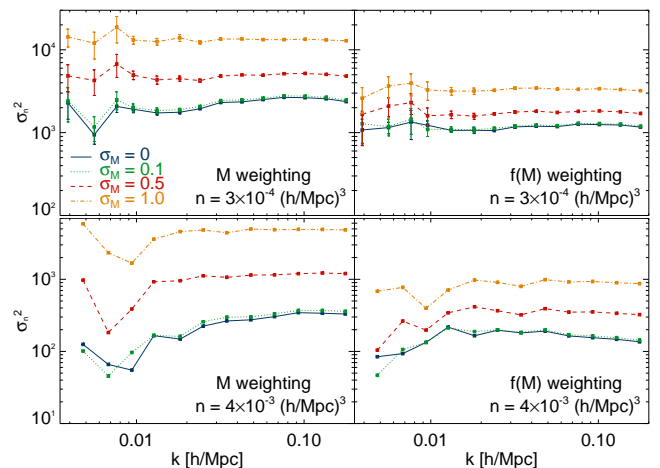


FIG. 3. Effects of log-normal scatter $\sigma$ in halo mass observable on the shot noise $\sigma_n^2$ for mass and $f(M) = M/[1 + (M/10^{14}h^{-1}M_\odot)^{0.5}]$ weights, for $\bar{n} = 3 \times 10^{-4}(h/\mathrm{Mpc})^3$ and $\bar{n} = 4 \times 10^{-3}(h/\mathrm{Mpc})^3$. Scatter hardly affects the bias, so the relative effects of scatter are the same for $\sigma_n^2/P$ and we do not show them here.

duce the target number density by nearly a factor of 3. Note that SDSS-III plans to oversample the galaxies at the BAO scale and to use reconstruction to reduce the damping of BAO, which can be done better if the shot noise is lower. It is also possible that imposing the local mass and momentum conservation will minimize systematic shifts in the BAO position relative to the dark matter that may otherwise be problematic [12], but we leave this investigation for the future.

So far we ignored the real world complications such as the imprecise knowledge of the halo mass. To investi-

gate this we add a log-normal scatter with rms variance $\sigma$ to each halo mass and recompute the analysis. Figure 3 shows the results for mass and modified mass $f(M)$ weighting: for the latter we see that a scatter of 50% in mass increases $\sigma_n^2/P$ by about 50% for lower abundance and a factor of 2 for higher abundance. Since this is a realistic scatter for optically selected clusters [13] there is thus realistic possibility that we can apply such analysis to the real data and achieve these gains. In practical applications one would try to identify the best halo mass tracer as a function of halo mass, for example, central galaxy luminosity in the galactic halos and richness or total luminosity for the cluster halos. In order to minimize the scatter one must understand the relation between the galaxy observables and the underlying halos, so progress in galaxy formation studies will be needed to maximize the gains. We find that for the mass weighting, scatter has a larger effect, such that for $\sigma = 0.5$ the degradation in $\sigma_n^2/P$ is a factor of 2-3. Once the scatter becomes too large there is no longer any local mass and momentum conservation and we find that for $\sigma = 1$ the shot noise is worse than for uniform weighting. Another potential complication is the effect of redshift-space distortions, since the observed radial distance is a sum of the true radial distance and peculiar velocity (divided by the Hubble parameter). We find a modest (50%) increase in $\sigma_n^2/P$, where $P$ in redshift space is the spherically averaged (i.e. monopole) power spectrum. Since redshift space contains much more information than just the monopole it is possible that one may be able to use the additional information to reduce this degradation and we leave this for a future investigation.

These results are particularly relevant for the multitracer methods where the data are analyzed in terms of ratios of different tracers and for which the sampling variance error cancels, such as those recently proposed for non-Gaussianity [3], redshift-space distortions and Hubble versus angular distance relation [4]. For these there is no lower limit on the achievable error, as long as $\sigma_n^2/P$ decreases and the method proposed here could lead to a significant reduction of errors relative to previous expectations. We see from Fig. 2 that for mass weighting at $\bar{n} = 4 \times 10^{-3}(h/\text{Mpc})^3$, $\sigma_n^2/P \sim 10^{-3}$ on large scales, so this could give a signal to noise of 30 for a single mode, compared to 0.7 for the single tracer method, equivalent to 3 orders of magnitude reduction in volume needed to reach the same precision. Note that this is not unreachable, since the existing SDSS survey achieves $\bar{n} \sim 10^{-2}(h/\text{Mpc})^3$ for the redshift survey of the main sample.

Equally impressive improvements may be possible for future redshift surveys such as JDEM/EUCLID or Big-BOSS, which are expected to operate at redshifts up to $z \sim 2$. Their target number density could be as high as $\bar{n} \sim 10^{-3}(h/\text{Mpc})^3$ or higher, and the method proposed here could lead to a dramatic reduction of errors or, equivalently, to a several-fold reduction in the number of measured redshifts required to reach the target precision, with potentially important implications for the design of these missions. The weights can be further optimized for specific applications, specially for the multitracer methods that cancel out the sampling variance error. This approach holds the promise to become the most accurate method to extract both the primordial non-Gaussianity and the dark energy equation of state and its full promise should be explored further with more realistic simulations. In parallel we should develop our understanding of galaxy formation better to relate the galaxy observables to the underlying halo mass with as little scatter as possible.

---

[1] D. J. Eisenstein, I. Zehavi, D. W. Hogg, R. Scoccimarro, M. R. Blanton, R. C. Nichol, R. Scranton, H.-J. Seo, M. Tegmark, Z. Zheng, et al., ApJ **633**, 560 (2005), arXiv:astro-ph/0501171.

[2] D. J. Eisenstein, H.-J. Seo, E. Sirko, and D. N. Spergel, ApJ **664**, 675 (2007), arXiv:astro-ph/0604362.

[3] U. Seljak, Physical Review Letters **102**, 021302 (2009), 0807.1770.

[4] P. McDonald and U. Seljak, J. Cosmology Astropart. Phys. **10**, 7 (2009), 0810.0323.

[5] J. A. Peacock and R. E. Smith, MNRAS **318**, 1144 (2000), arXiv:astro-ph/0005010.

[6] U. Seljak, MNRAS **318**, 203 (2000), arXiv:astro-ph/0001493.

[7] R. Scoccimarro, R. K. Sheth, L. Hui, and B. Jain, ApJ **546**, 20 (2001), arXiv:astro-ph/0006319.

[8] R. Mandelbaum, U. Seljak, G. Kauffmann, C. M. Hirata, and J. Brinkmann, MNRAS **368**, 715 (2006), arXiv:astro-ph/0511164.

[9] P. J. E. Peebles, *The large-scale structure of the universe* (1980).

[10] M. Crocce and R. Scoccimarro, Phys. Rev. D **77**, 023533 (2008), 0704.2783.

[11] W. J. Percival, L. Verde, and J. A. Peacock, MNRAS **347**, 645 (2004), arXiv:astro-ph/0306511.

[12] R. E. Smith, R. Scoccimarro, and R. K. Sheth, Phys. Rev. D **77**, 043525 (2008), arXiv:astro-ph/0703620.

[13] E. Rozo, E. S. Rykoff, A. Evrard, M. Becker, T. McKay, R. H. Wechsler, B. P. Koester, J. Hao, S. Hansen, E. Sheldon, et al., ApJ **699**, 768 (2009), 0809.2794.

# 3

## PAPER II

**Summary**   The next article is a more detailed follow-up study on the results found in the previous paper. The stochasticity of halos is being studied in a more general way by defining the so-called *shot noise matrix*. Here, all the halos in a large sample of $N$-body simulations are split up into equal number-density mass bins and the shot noise is calculated from all auto- and cross power spectra between the bins. It is found that low mass halos exhibit more-, and high mass halos less stochasticity than expected from the Poisson sampling model. Moreover, non-vanishing off-diagonal elements in the shot noise matrix are detected, implying both correlations and anti-correlations in the shot noise of halos of different mass. An eigendecomposition of the shot noise matrix reveals two eigenmodes that are distinct from Poisson sampling, a super- and a sub-Poissonian one. The latter provides an optimal weighting function to suppress the shot noise in the halo density field. This function is found to scale linearly with mass at high masses, and saturate towards a constant value at low masses, determined by the mass resolution of the simulation. It is demonstrated how an application of this weighting scheme can significantly reduce the shot noise of halos, even more than the previously studied weights. In realistic observations the halo masses may be poorly constrained, the influence of scatter in the mass-observable relation is therefore examined. In consideration of the halo model, the properties of the shot noise matrix can be described remarkably well, providing an analytical expression for the optimal weighting function. Finally, it is shown how the scale dependence of the halo bias emerges in this model.

# Minimizing the Stochasticity of Halos in Large-Scale Structure Surveys

Nico Hamaus,[1, *] Uroš Seljak,[1, 2, 3, †] Vincent Desjacques,[1] Robert E. Smith,[1] and Tobias Baldauf[1]

[1] *Institute for Theoretical Physics, University of Zurich, 8057 Zurich, Switzerland*
[2] *Physics Department, Astronomy Department and Lawrence Berkeley National Laboratory,*
*University of California, Berkeley, California 94720, USA*
[3] *Ewha University, Seoul 120-750, S. Korea*
(Dated: August 13, 2010)

In recent work (Seljak, Hamaus and Desjacques 2009) it was found that weighting central halo galaxies by halo mass can significantly suppress their stochasticity relative to the dark matter, well below the Poisson model expectation. This is useful for constraining relations between galaxies and the dark matter, such as the galaxy bias, especially in situations where sampling variance errors can be eliminated. In this paper we extend this study with the goal of finding the optimal mass-dependent halo weighting. We use $N$-body simulations to perform a general analysis of halo stochasticity and its dependence on halo mass. We investigate the stochasticity matrix, defined as $C_{ij} \equiv \langle (\delta_i - b_i \delta_m)(\delta_j - b_j \delta_m) \rangle$, where $\delta_m$ is the dark matter overdensity in Fourier space, $\delta_i$ the halo overdensity of the $i$-th halo mass bin, and $b_i$ the corresponding halo bias. In contrast to the Poisson model predictions we detect nonvanishing correlations between different mass bins. We also find the diagonal terms to be sub-Poissonian for the highest-mass halos. The diagonalization of this matrix results in one large and one low eigenvalue, with the remaining eigenvalues close to the Poisson prediction $1/\bar{n}$, where $\bar{n}$ is the mean halo number density. The eigenmode with the lowest eigenvalue contains most of the information and the corresponding eigenvector provides an optimal weighting function to minimize the stochasticity between halos and dark matter. We find this optimal weighting function to match linear mass weighting at high masses, while at the low-mass end the weights approach a constant whose value depends on the low-mass cut in the halo mass function. This weighting further suppresses the stochasticity as compared to the previously explored mass weighting. Finally, we employ the halo model to derive the stochasticity matrix and the scale-dependent bias from an analytical perspective. It is remarkably successful in reproducing our numerical results and predicts that the stochasticity between halos and the dark matter can be reduced further when going to halo masses lower than we can resolve in current simulations.

## I. INTRODUCTION

The large-scale structure (LSS) of the Universe carries a wealth of information about the physics that governs cosmological evolution. By measuring LSS we can attempt to answer such fundamental questions as what the Universe is made of, what the initial conditions for the structure in the Universe were, and what its future will be. Traditionally, the easiest way to observe it is by measuring galaxy positions and redshifts, which provides the 3D spatial distribution of LSS via so-called redshift surveys (e.g., [1, 2]).

However, dark matter dominates the evolution and relation to fundamental cosmological parameters, while galaxies are only biased, stochastic tracers of this underlying density field. On large scales, this bias is expected to be a constant offset in clustering amplitude relative to the dark matter, which can be removed to reconstruct the dark matter power spectrum [3]. Nevertheless, this reconstruction is hampered due to a certain degree of randomness in the distribution of galaxies, which is based

on the nonlinear and stochastic relation between galaxies and the dark matter. In the simplest model one describes this stochasticity with the Poisson model of *shot noise*. Shot noise constitutes a source of error in the power spectrum [4] and therefore limits the accuracy of cosmological constraints. The Poisson model predicts it to be determined by the inverse of the galaxy number density, assuming galaxies to be random and pointlike tracers. However, galaxies are born inside dark matter halos and for these extended, gravitationally interacting objects, the shot noise model is harder to describe. It is thus desirable to develop estimators that are least affected by this source of stochasticity.

In Fourier space the stochasticity of galaxies is usually described by the *cross-correlation coefficient*

$$ r_{gm} \equiv \frac{P_{gm}}{\sqrt{\hat{P}_{gg} P_{mm}}} , \qquad (1) $$

where $\hat{P}_{gg}$ is the measured galaxy autopower spectrum, $P_{mm}$ the dark matter autopower spectrum, and $P_{gm}$ the cross-power spectrum of the two components. The cross-correlation coefficient $r_{gm}$ can be related to the shot noise power $\sigma^2$, which is commonly defined via the decomposition $\hat{P}_{gg} = P_{gg} + \sigma^2$, with $P_{gg} = b^2 P_{mm}$ and the bias

defined as $b = P_{gm}/P_{mm}$. This yields

$$\frac{\sigma^2}{P_{gg}} = \frac{1 - r_{gm}^2}{r_{gm}^2} \ .\qquad(2)$$

Thus, the lower the shot noise, the smaller the stochasticity, i.e., the deviation of the cross-correlation coefficient from unity. Minimizing this stochasticity is important if one attempts to determine the relation between galaxies and the underlying dark matter. One example of such an application is correlating the weak lensing signal, which traces dark matter, to properly radially weighted galaxies [5]: an accurate determination of the galaxy bias can be combined with a 3-dimensional galaxy redshift survey to greatly reduce the statistical errors relative to the corresponding 2-dimensional weak lensing survey.

The ultimate precision on how accurate the galaxy bias can be estimated from such methods is determined by the cross-correlation coefficient and previous work has shown that it can deviate significantly from unity for uniformly weighted galaxies or halos [4]. However, it was demonstrated recently that weighting halos by mass considerably reduces the stochasticity between halos and the dark matter [6]. The purpose of this paper is to explore this more systematically and to develop an optimal weighting method that achieves the smallest possible stochasticity.

Our definition of the shot noise above is relevant for the methods that attempt to cancel sampling variance (or *cosmic variance*) [7, 8] and this will be our primary motivation in this paper. Alternatively, the shot noise is often associated with its contribution to the error in the power spectrum determination, this error usually being decomposed into sampling variance and shot noise. Sampling variance refers to the fact that in a given volume $V$ the number $N_k$ of observable Fourier modes of a given wave vector amplitude is finite. In the case of a Gaussian random field the relative error in the measured galaxy power spectrum $\hat{P}_{gg}$ due to the sum of the two errors is given by $\sigma_{\hat{P}_{gg}}/\hat{P}_{gg} = 1/\sqrt{N_k}$ (each complex Fourier mode has two independent realizations and we only count modes with positive wave vector components). Using the above decomposition of the measured power $\hat{P}_{gg}$ into intrinsic power $P_{gg}$ and shot noise $sigma^2$, one finds

$$\frac{\sigma_{P_{gg}}}{P_{gg}} = \frac{1}{\sqrt{N_k}} \left( 1 + \frac{\sigma^2}{P_{gg}} \right) \ .\qquad(3)$$

This definition is ambiguous, since it leaves the decomposition of the measured power into shot noise and shot noise subtracted power unspecified. Most of the analyses so far have simply assumed the Poisson model, where the shot noise is given by the inverse of the number density of galaxies, $\sigma^2 = 1/\bar{n}$. A second possibility is to define the shot noise such that the galaxy bias estimator $\sqrt{P_{gg}/P_{mm}}$ becomes as scale independent as possible. The third way is to define it via the stochasticity between

halos and the dark matter, i.e., the cross-correlation coefficient $r_{gm}$ as in Eq. (2). We choose the third definition, but will comment on the relations to the other two methods as well.

It is important to emphasize here that the first two definitions are not directly related to the applications where the sampling variance error can be eliminated, since they do not include correlations between tracers (where the dark matter itself can also be seen as a tracer). While in this paper we focus on minimizing the error on the bias estimation using the sampling variance canceling method, there are other applications where correlating dark matter and galaxies, or two differently biased galaxy samples, allows us to reduce the sampling variance error [7–9]. In such cases the stochasticity, or the shot noise to power ratio as defined in Eq. (2), is the dominant source of error and methods capable of reducing it offer the potential to further advance the precision of cosmological tests. Indeed, since the error on the power spectrum as in Eq. (3) contains two contributions, in the past there was not much interest in investigating the situation where the shot noise is much smaller than sampling variance. It is the situations where the sampling variance error vanishes that are most relevant for our study.

In this paper we will focus on the relation between halos and the underlying dark matter, using two-point correlations in Fourier space (i.e. the power spectrum) as a statistical estimator. A further step to connect halos to observations of galaxies can be accomplished by specification of a halo occupation distribution for galaxies [10], but we do not investigate this in any detail. Alternatively, one can think of the halos as a sample of central halo galaxies from which satellites have been removed.

## II. SHOT NOISE MATRIX

The term shot noise is usually related to the fact that the sampling of a continuous field with a finite number of objects yields a spurious contribution of power to its autopower spectrum. In the Poisson model the contribution to the autopower spectrum is $1/\bar{n}$, where $\bar{n} = N/V$ is the mean number density of objects sampling the continuous field, whereas the cross-power spectrum of two distinct samples of objects is not affected (see, e.g., [11, 12]). However, in cosmology one studies galaxies residing in dark matter halos, which are not a random subsample of the dark matter particles. The Poisson model does not account for that fact.

In recent work it has been argued that there are other nonlinear terms that appear like white noise terms in the power spectrum of halos and so a more general approach is needed to determine the shot noise [13]. In order to account for this fact we define the shot noise more generally as the two-point correlation matrix

$$C_{ij} \equiv \langle (\delta_i - b_i \delta_m)(\delta_j - b_j \delta_m) \rangle \ .\qquad(4)$$

Here the subscripts $i$ and $j$ refer to specific subsamples of the halo density field with overdensities $\delta_i$ and $\delta_j$ and corresponding scale-independent bias $b_i$ and $b_j$, respectively. The dark matter density fluctuation is denoted by $\delta_m$ and the angled brackets denote an ensemble average. We work in Fourier space and the $\delta$'s are the complex Fourier components of the density field,

$$\delta(\mathbf{k}) = \frac{1}{\sqrt{V}} \int \delta(\mathbf{x}) e^{-i\mathbf{k}\cdot\mathbf{x}} \mathrm{d}^3 x \ . \tag{5}$$

However, we handle the complex density modes $\delta$ as real quantities, since their real and imaginary parts are uncorrelated and one can treat them as two independent modes. Further, we assume the overdensity of a particular halo sample $i$ to be composed of two terms [4]:

$$\delta_i = b_i \delta_m + \epsilon_i \ , \tag{6}$$

where $\epsilon_i$ is a random variable of zero mean assumed to be uncorrelated with the signal, i.e., $\langle \epsilon_i \delta_m \rangle = 0$. It follows that the bias parameter $b_i$ can be obtained from cross correlation with the dark matter,

$$b_i = \frac{\langle \delta_i \delta_m \rangle}{\langle \delta_m^2 \rangle} \ , \tag{7}$$

and the shot noise matrix can be written as $C_{ij} = \langle \epsilon_i \epsilon_j \rangle$. With these definitions the cross-correlation coefficient between any given halo bin $i$ and the dark matter,

$$r_{im} \equiv \frac{\langle \delta_i \delta_m \rangle}{\sqrt{\langle \delta_i^2 \rangle \langle \delta_m^2 \rangle}} \ , \tag{8}$$

becomes unity when we subtract the shot noise component $C_{ii}$ from $\langle \delta_i^2 \rangle$. We thus recover the shot noise definition from Eq. (2) and define $P_{ii} \equiv \langle \delta_i^2 \rangle - C_{ii}$ to be the halo autopower spectrum (shot noise subtracted), $P_{im} = \langle \delta_i \delta_m \rangle$ the halo-matter cross-power spectrum, and $P_{mm} = \langle \delta_m^2 \rangle$ the matter autopower spectrum (we assume the shot noise of the matter auto-, as well as the halo-matter cross-power spectrum to vanish). Note that these relations are still self-consistent if we allow the bias $b_i$ to be scale dependent. Here we will, however, explore the simpler case assuming scale-independent bias, which is a good approximation on large scales.

In the Poisson model the shot noise matrix $C_{ij}$ is diagonal, but this is not necessarily the case in our definition. The objective of this paper is to study all the components of this matrix using $N$-body simulations. In particular we divide the halos into bins of different mass, but equal number density. A diagonalization of the shot noise matrix will then provide its eigenvalues and eigenvectors, which contain important information about the stochastic properties of the halo density field.

## III.   SIMULATIONS

We use the zHORIZON simulations [12], 30 realizations of numerical $N$-body simulations with $750^3$ particles of mass $5.55 \times 10^{11} h^{-1} \mathrm{M}_\odot$ and a box-size of $1.5 h^{-1} \mathrm{Gpc}$ (total effective volume of $V_{\mathrm{tot}} = 101.25 h^{-3} \mathrm{Gpc}^3$) to accurately sample the density field of cold dark matter. The simulations were performed at the University of Zurich supercomputers zBOX2 and zBOX3 with the GADGET II code [14]. We chose the cosmological parameters to be close to the outcome of the WMAP5 data release [15], namely $\Omega_m = 0.25$, $\Omega_\Lambda = 0.75$, $\Omega_b = 0.04$, $\sigma_8 = 0.8$, $n_s = 1.0$ and $h = 0.7$. The transfer function was computed with the CMBFAST code [16] and the initial conditions were set up at redshift $z = 50$ with the 2LPT initial conditions generator [17, 18].

We applied the friends-of-friends (FoF) algorithm B-FOF by V. Springel with a linking length of 20% of the mean interparticle distance and a minimum of 30 particles per halo to generate halo catalogs. The resulting catalogs contain about $1.3 \times 10^6$ halos ($\bar{n} \simeq 3.7 \times 10^{-4} h^3 \mathrm{Mpc}^{-3}$) with masses between $M_{\min} \simeq 1.1 \times 10^{13} h^{-1} \mathrm{M}_\odot$ and $M_{\max} \simeq 3.1 \times 10^{15} h^{-1} \mathrm{M}_\odot$. In order to investigate the influence of the mass resolution on our results, we employ another set of 5 $N$-body simulations [19] of box-size $1.6 h^{-1} \mathrm{Gpc}$ with $1024^3$ particles of mass $3.0 \times 10^{11} h^{-1} \mathrm{M}_\odot$, resolving halos down to $M_{\min} \simeq 5.9 \times 10^{12} h^{-1} \mathrm{M}_\odot$ ($\bar{n} \simeq 7.0 \times 10^{-4} h^3 \mathrm{Mpc}^{-3}$). All other parameters of this simulation are similar to the one above, namely $\Omega_m = 0.279$, $\Omega_\Lambda = 0.721$, $\Omega_b = 0.046$, $\sigma_8 = 0.81$, $n_s = 0.96$, $h = 0.7$. One further realization with these parameters was generated with an even higher mass resolution, namely $1536^3$ particles of mass $4.7 \times 10^{10} h^{-1} \mathrm{M}_\odot$ in a box of $1.3 h^{-1} \mathrm{Gpc}$, resolving halos down to $M_{\min} \simeq 9.4 \times 10^{11} h^{-1} \mathrm{M}_\odot$ ($\bar{n} \simeq 4.0 \times 10^{-3} h^3 \mathrm{Mpc}^{-3}$).

The density fields of dark matter and halos in configuration space were computed via interpolation of the particles onto a cubical mesh with $512^3$ grid points using a cloud-in-cell mesh assignment algorithm [20]. We then applied fast Fourier transforms to compute the modes of the fields in $k$-space. All our results are presented at $z = 0$ and we do not explore the redshift dependence, because at higher redshifts the halo number density is lower and we wish to explore the stochastic properties of halos in the high density limit.

## IV.   ANALYSIS

### A.   Estimators for the binned halo density field

The shot noise matrix from Eq. (4) is calculated by plugging in the Fourier modes provided by our simulations and averaging over a range of wave numbers. The bias is determined via the ratio in Eq. (7), we thus neglect any shot noise contribution in this expression. In Eq. (4)

we use the scale-independent bias, which is obtained by averaging over the range $k \leq 0.024 \ h\mathrm{Mpc}^{-1}$, corresponding to our first four $k$-bins. This range of wave numbers is least affected by scale dependence, as apparent from the middle panel of Fig. 1.

For the division into subsamples we bin the full halo catalog into bins of different mass, keeping the number density of each bin constant. This is done by sorting the halos according to their mass and then dividing this sorted array into subarrays with an equal number of halos. We use 10 bins for most of the plots presented here, since more bins make them increasingly hard to read. For some plots we also show the results with 30 and 100 bins to provide a more accurate sampling of halo masses. A convergence of the results can only be reached with infinitely many bins, which is numerically impossible to accomplish. However, using linear mass weighting of the halos within each bin makes the results converge faster, as will be justified later. We apply this technique to our 100 halo mass bins, as shown in some of the following plots.

### 1. Power spectrum, bias and cross-correlation coefficient

We start by looking at the autopower spectrum of the halos in each mass bin as shown in the top panel of Fig. 1, using our lower resolution simulation with average halo number density of $\bar{n} \simeq 3.7 \times 10^{-4} h^3 \mathrm{Mpc}^{-3}$. The halo autopower spectra have been subtracted by $C_{ii}$, the diagonal elements of the shot noise matrix from Eq. (4), depicted below in Fig. 2. The halo subsamples increasingly gain power with higher mass due to their enhanced bias, which is plotted in the middle panel of Fig. 1. This plot shows the bias obtained from Eq. (7) as a function of $k$. The scale-independent bias is drawn as straight dotted lines for comparison. On large scales, roughly below $k \simeq 0.015 \ h\mathrm{Mpc}^{-1}$, sampling variance makes the curves appear more noisy, while on smaller scales, $k \gtrsim 0.04 \ h\mathrm{Mpc}^{-1}$, possibly nonlinear evolution of the density field or higher-order bias corrections set in causing the halo bias to pick up a scale dependence [21]. This scale dependence is most pronounced for the highest-mass bin.

The degree of halo stochasticity can also be assessed in the cross-correlation coefficient between halos and the dark matter, as depicted in the bottom panel of Fig. 1. We see that the more massive halos are a *less stochastic* tracer of the dark matter. Note that subtracting our definition of the shot noise from the autocorrelation of halos makes the cross-correlation coefficient become unity. It has the nice property that the bias determined from halo auto-correlation and from halo-matter cross-correlation is identical by definition.
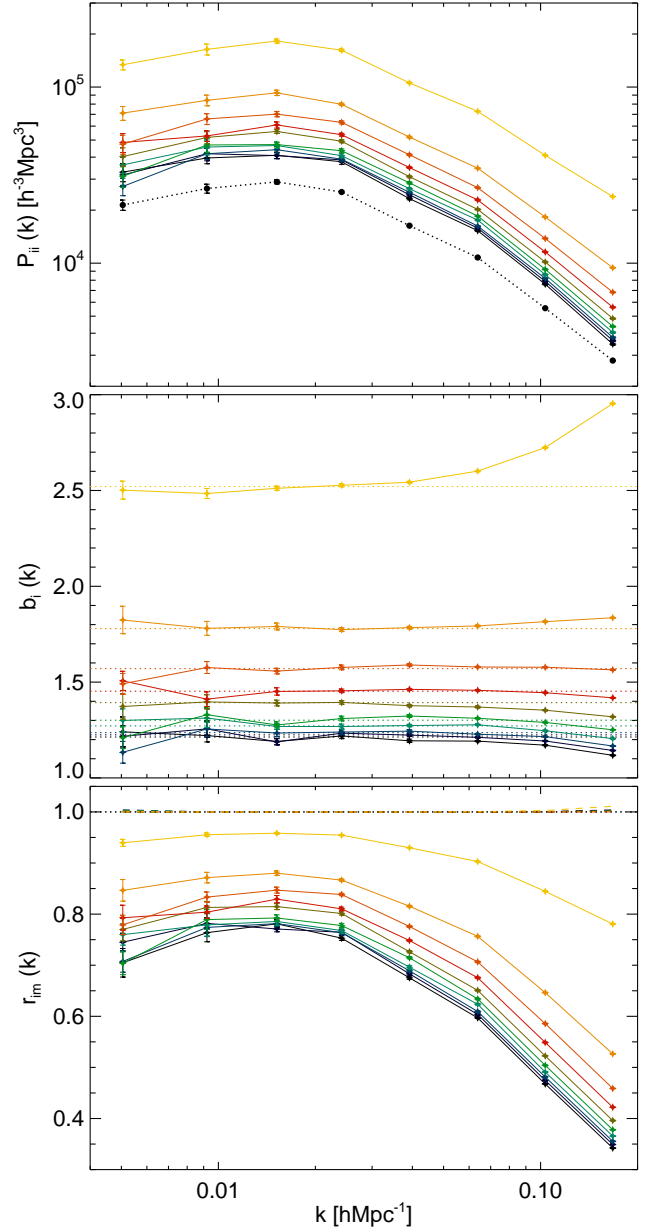


FIG. 1. TOP: Autopower spectra for 10 consecutive halo mass bins (solid colored lines) and the dark matter (dotted black line). MIDDLE: Bias of the 10 halo bins determined from the cross power with the dark matter, the dotted lines show the scale-independent bias. BOTTOM: Cross-correlation coefficients of the 10 halo bins with the dark matter (solid colored lines) without shot noise subtraction. When the shot noise $C_{ii}$ is subtracted from $\langle \delta_i^2 \rangle$, by definition the cross-correlation coefficient becomes unity (dashed lines). For reference, the value $r = 1$ is plotted (dotted black line). The error bars on all three plots were computed from the ensemble of the 30 independent realizations of our simulations. They show the standard deviation on the mean of each quantity shown.

## 2. Shot noise matrix

We now turn to the calculation of the shot noise matrix for the 10 halo mass bins. Figure 2 shows each element of $C_{ij}$ plotted against the wave number. As expected, the diagonal components of the shot noise (solid lines) are dominant. They all show essentially no scale dependence and match the usual expectation of $1/\bar{n}_i$ very well (where $\bar{n}_i$ is the mean number density of halos in bin $i$), except for the highest-mass bin (solid, black line), which is suppressed by about a factor of 2. The conventional expression for the shot noise breaks down for the highest-mass halos. This sub-Poissonian behavior of the shot noise at high masses has been found in simulations before [22, 23].

Moreover we find both negative and positive elements in the off-diagonal parts of the shot noise matrix. In the case of $N$ halo bins, in total there are $N(N + 1)/2$ independent elements, since $C_{ij}$ is a symmetric matrix. These are composed of $N$ diagonal and $N(N - 1)/2$ off-diagonal elements. Hence, in the case of $N = 10$, there are 45 off-diagonal elements and we find 33 of them to be positive (dashed lines), while 12 are negative (dotted lines). While all off-diagonal elements are white noise like, i.e., scale independent, most of the negative components have a higher magnitude than the positive ones. The former correspond to the cross correlations of any given halo mass bin with the highest-mass halos.

This finding is rather surprising, because shot noise cross correlations are usually being neglected. Since there appear to be negative off-diagonal components in the shot noise matrix and their magnitude exceeds the positive ones, one might expect that a suitable linear combination of the halo bins can reduce the total shot noise, as found in [6]. In the subsequent section we will show that this expectation is indeed fulfilled.

### B. Eigensystem of the shot noise matrix

In order to find the principal components of the shot noise matrix we have to diagonalize it by determining its eigenvalues $\lambda^{(l)}$ and eigenvectors $V^{(l)}$, defined via

$$\sum_j C_{ij} V_j^{(l)} = \lambda^{(l)} V_i^{(l)} . \tag{9}$$

The superscript $(l)$ is used to enumerate the eigenvalues and eigenvectors, while the subscripts $i$ and $j$ refer to the components of the vectors and matrices. We use routines from [24] to do the calculations.

#### 1. Eigenvalues

The left panel of Fig. 3 shows the eigenvalues $\lambda^{(l)}$ of the shot noise matrix from Fig. 2 for the 10 halo bins as
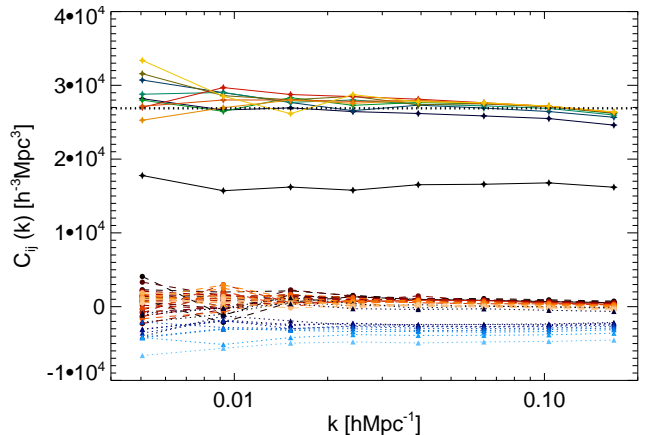


FIG. 2. Elements of the shot noise matrix as defined in Eq. (4) with 10 halo mass bins. Most of the diagonal components (solid lines with stars) agree with Poisson white noise, i.e., $C_{ii} = 1/\bar{n}_i$ (dotted black line on top), except the highest-mass bin which is clearly suppressed (solid black line). There are both positive (dashed lines with circles, scaled in red) and negative (dotted lines with triangles, scaled in blue) off-diagonal components.

a function of $k$. The eigenvalues are computed separately for every $k$-bin and then ordered by their magnitude. As apparent from the figure, we find two eigenvalues to differ significantly from all the others. One of them is enhanced by roughly a factor of 1.5 and one is suppressed by a factor of about 2.5 compared to the other ones that lie close to the value $1/\bar{n}_i$. The spread of the curves at low $k$ is likely due to the low number of modes available there, making the eigenvalue determination inaccurate.

This result reveals the fact that one of the eigenvectors, which represents a particular linear combination of the halo mass bins, yields a very low shot noise level. This shot noise level is determined by the lowest eigenvalue of the shot noise matrix, which we will denote as $\lambda^-$. Increasing the number of halo bins we find an even stronger suppression of $\lambda^-$ compared to the expectation of $1/\bar{n}_i$ (see Sec. IV C).

The other eigenvalue that differs from the value $1/\bar{n}_i$ represents the highest shot noise level. We designate this eigenvalue $\lambda^+$. Since it does not carry much information (see below) we do not investigate it further in this paper beyond noticing that it is likely to be connected to the second-order bias. We note that had we investigated the halo covariance matrix $\langle \delta_i \delta_j \rangle$, we would not have been able to reveal the lowest eigenvalue as cleanly, because it would have been swamped by sampling variance. Indeed, previous work focused its attention mostly on the largest eigenvalues of $\langle \delta_i \delta_j \rangle$ [25].
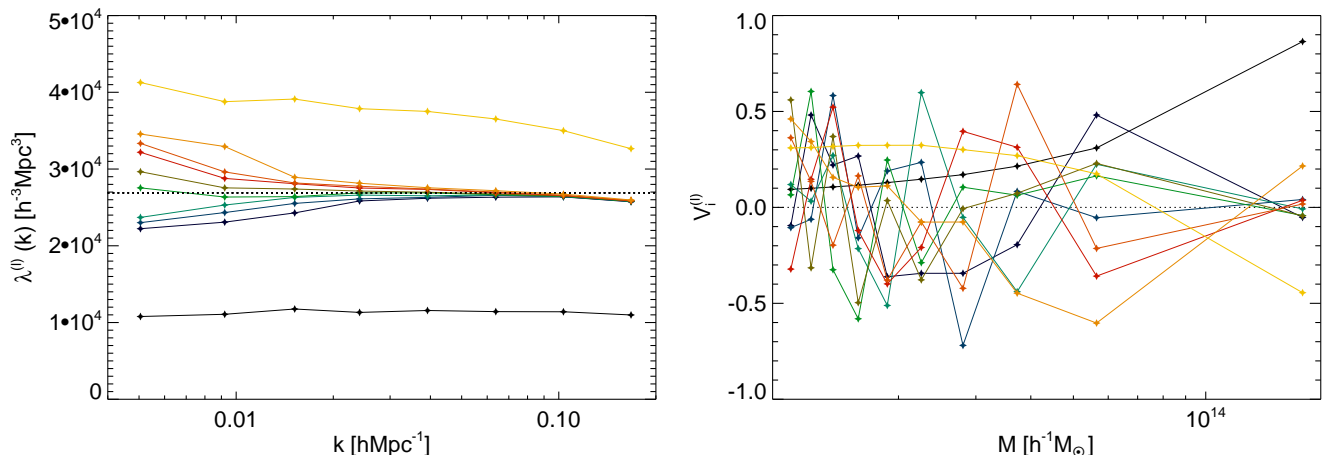
FIG. 3. The 10 eigenvalues (left) and eigenvectors (right) of the shot noise matrix from Fig. 2 in corresponding colors. The black dotted line shows the value $1/\bar{n}_i$. The eigenvectors are averaged over the entire $k$-range.

### 2. Eigenvectors

Every eigenvector $V_i^{(l)}$ is a function of the wave number, just like the eigenvalues. However, as can be seen from Figs. 2 and 3, over a reasonable range of wave numbers this dependence can be ignored and we average the eigenvectors over the entire $k$-range. We also divide each eigenvector by its length $|V_i| = (\sum_i V_i^2)^{1/2}$ to normalize it.

The right panel of Fig. 3 displays the 10 eigenvectors corresponding to the 10 eigenvalues in the left panel. Each component of an eigenvector corresponds to one halo mass bin. Since we have equal number densities per bin, the mass range per bin gets wider with increasing mass due to the rapid decline of the halo mass function. Every data point in the figure is plotted at the respective average mass of each halo bin. Only one eigenvector shows exclusively positive components, while at least one negative component can be found in the remaining eigenvectors. It is this eigenvector that corresponds to the lowest eigenvalue $\lambda^-$ and we will denote it as $V_i^-$. Its components continuously increase with mass. The eigenvector $V_i^+$ corresponding to the largest eigenvalue $\lambda^+$ also shows a monotonic behavior, but its components decrease with mass and turn negative at the high-mass end (similarly to the second-order halo bias with an opposite sign).

One can think of the eigenvectors as weighting functions for the halos, since each component acts as a weight for the associated halo mass bin. Hence, the weighted halo density field $\delta_w(\mathbf{x})$ in configuration space can be written as a weighted sum over the halo mass bins, normalized by the sum of the weights,

$$\delta_w^{(l)}(\mathbf{x}) = \frac{\sum_i V_i^{(l)} \delta_i(\mathbf{x})}{\sum_i V_i^{(l)}} \ . \tag{10}$$

We specifically want to investigate the eigenvector $V_i^-$, since it yields the lowest eigenvalue of the shot noise matrix, $\lambda^-$. In Fig. 4 we plot the components of $V_i^-$ in a log-log plot to investigate this eigenvector in more detail and compare to the results with 30 and 100 mass bins. The components of $V_i^-$ increase linearly with mass above $M \simeq 10^{14} h^{-1} \mathrm{M}_\odot$, while at lower masses the slope tends to become shallower. We compare this eigenvector to two different smooth weighting functions for the halo density field. The first weighting function simply takes the halo mass as a weight for each halo, $w(M) = M$, we will denote it as *linear mass weighting*. However, as apparent from the dotted lines in Fig. 4, it only matches the components of $V_i^-$ at high mass. In order to account for the saturation effect at low masses, we consider a second weighting function that mimics this behavior,

$$w(M) = M + M_0 \ . \tag{11}$$

The free parameter $M_0$ determines the shape of this weighting function, it specifies the mass threshold where the saturation sets in. For $M \ll M_0$, Eq. (11) approaches uniform weighting, whereas in the limit $M \gg M_0$ it matches linear mass weighting. We call this weighting scheme *modified mass weighting*, it is shown as a dashed curve in Fig. 4 and obviously provides a much better fit to $V_i^-$ than linear mass weighting. The fit is shown for each case of our mass binning. The best-fit value for $M_0$ increases with the number of bins and in the case of 100 mass-weighted bins becomes $M_0 \simeq 1.7 \times 10^{13} h^{-1} \mathrm{M}_\odot$. Note that for visibility reasons this eigenvector is shifted downwards by a factor of 2 in the plot.

Similar weighting schemes have already been applied to the halo density field in [6], where a significant reduction of the stochasticity between halos and the dark matter could be achieved. In particular, a trial weighting function also denoted as modified mass weighting was
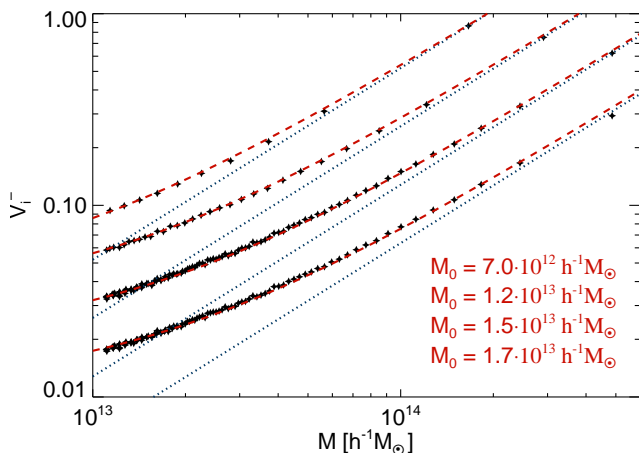
FIG. 4. The normalized eigenvector $V_i^-$, corresponding to the lowest shot noise eigenvalue $\lambda^-$, computed for 10, 30, 100 uniformly weighted bins and 100 mass-weighted bins (from top to bottom). The latter was shifted downwards by a factor of 2 for visibility. The dotted (blue) and the dashed (red) lines represent linear and modified mass weighting, respectively. The best-fit values for $M_0$ are given in the bottom right for the respective cases.

shown to improve on linear mass weighting. However, in that paper the functional form was found empirically and was not demonstrated to be optimal. In this work we show why modified mass weighting as defined in Eq. (11) is the optimal weighting to suppress the stochasticity in halos: in the limit of many halo mass bins it converges to the components of $V_i^-$, the eigenvector of the shot noise matrix with the lowest eigenvalue. What remains to be shown is what determines the value of $M_0$: we will argue it depends on the lower boundary of the halo mass function considered.

These results also justify why applying linear mass weighting to the halos *within* each bin leads to a better convergence of the eigenvector towards a smooth weighting with infinitely many bins: linear mass weighting already reduces the stochasticity of each bin as compared to the uniformly weighted case (see [6]). The resulting eigenvector is then determined more accurately, corresponding to an effectively higher sampling with more bins. This mainly has an effect on the highest-mass bins, since they have the broadest range in mass. At low masses the bins are increasingly narrow, so uniform and linear mass weighting become increasingly similar within a given bin.

Other attempts to find an optimal weighting scheme for the halo (galaxy) density field found the halo bias to yield the best constraining power on dark matter statistics and cosmological parameters when used as weighting function [25–27]. We have tried using only $b(M)$ as a weighting function, but found less suppression in halo stochasticity as compared to modified mass weighting.

## C. Signal-to-noise

While we have demonstrated that it is possible to suppress the stochasticity of a given halo density field using a single linear combination of halo bins, it remains to be shown how the information content in this single eigenmode compares to the complete information content. We cannot answer this question in general, since it depends not only on the property of the shot noise matrix, but also on derivatives of the halo density field with respect to the cosmological parameters one wants to estimate. Those two ingredients depend on halo mass and determine the Fisher information content of the halo density field. We will not explore the general case here and instead focus on the simple case where the information content is expressed via the ratio of the autopower spectrum to the shot noise of a particular tracer (signal-to-noise ratio per mode). Its inverse appears in Eqs. (2) and (3). We compute it for the weighted halo density field,

$$\frac{S}{N} \equiv \frac{P_w}{\sigma_w^2} = \frac{b_w^2}{\sigma_w^2} P_{mm} = \frac{r_{wm}^2}{1 - r_{wm}^2} \ . \tag{12}$$

$P_w$ denotes the autopower spectrum of the weighted halo density field, $\sigma_w^2$ its shot noise, $b_w$ the corresponding weighted bias and $r_{wm}$ the cross-correlation coefficient between the fields $\delta_w$ and $\delta_m$ as defined in Eq. (8). The weighted bias can be computed from the halo bins via

$$b_w = \frac{\langle \delta_w \delta_m \rangle}{\langle \delta_m^2 \rangle} = \frac{\sum_i V_i b_i}{\sum_i V_i} \ . \tag{13}$$

It is clear from this expression that in order to maximize the signal, the eigenvector components should all be of equal sign, since otherwise different halo bins cancel each others signal. Using Eq. (4) to express $\sigma_w^2$ in terms of the weighted density field $\delta_w$ and Eq. (10) for the definition of $\delta_w$ (we omit the superscripts for clarity), we have

$$\sigma_w^2 \equiv \langle (\delta_w - b_w \delta_m)^2 \rangle = \left\langle \left( \frac{\sum_i V_i \delta_i}{\sum_i V_i} - \frac{\sum_i V_i b_i}{\sum_i V_i} \delta_m \right)^2 \right\rangle =$$
$$= \frac{\sum_{i,j} V_i V_j C_{ij}}{\sum_{i,j} V_i V_j} = \lambda \frac{\sum_i V_i^2}{(\sum_i V_i)^2} \ , \tag{14}$$

where $\sum_i V_i^2 = 1$ in case the eigenvectors are normalized. Hence, the signal-to-noise ratio becomes

$$\frac{S}{N} = \frac{(\sum_i V_i b_i)^2}{\lambda \sum_i V_i^2} P_{mm} = \frac{b_w^2}{\lambda} \frac{(\sum_i V_i)^2}{\sum_i V_i^2} P_{mm} \ . \tag{15}$$

Note that this is only the signal-to-noise ratio for one particular weighting of the halo density field, corresponding to one eigenmode of the shot noise matrix. The complete information content of the halos is calculated by summing up all $N$ contributions,

$$\frac{S}{N} = \sum_{l=1}^{N} \left( \frac{b_w^{(l)}}{\sigma_w^{(l)}} \right)^2 P_{mm} \ . \tag{16}$$

However, since we find one very low eigenvalue of the shot noise, most of the signal will be contained in the halos weighted by $V_i^-$. Adding up the denominators of Eq. (16) and taking the inverse yields the total noise contribution of the halos. We call it the *reduced* shot noise,

$$\sigma_r^2 = \frac{1}{\sum_l (1/\sigma_w^{(l)})^2} \ . \tag{17}$$

Alternatively, the signal-to-noise ratio of the halo density field can be derived from a $\chi^2$ distribution. Since the modes of the halo bins are assumed to be independent, normally distributed variables, the expression

$$\chi^2 \equiv \sum_{i,j,k} (\delta_i - b_i \delta_m) \, C_{ij}^{-1} \, (\delta_j - b_j \delta_m) \tag{18}$$

follows a $\chi^2$ distribution. Here, $C_{ij}^{-1}$ refers to the $i$-$j$ component of the inverse shot noise matrix and the index $k$ connotes a summation over all Fourier modes. The derivative of the $\chi^2$ distribution with respect to the inferred dark matter density field $\delta_m$ must vanish, $\partial \chi^2 / \partial \delta_m = 0$. This yields

$$\delta_m = \frac{\sum_{i,j,k} C_{ij}^{-1} b_i \delta_j}{\sum_{i,j,k} C_{ij}^{-1} b_i b_j} \ . \tag{19}$$

Here, the vector $\sum_i C_{ij}^{-1} b_i$ conducts a weighting of the halo mass bins again. The difference to the weighting with one particular eigenvector of $C_{ij}$ is that this vector contains the complete information of all eigenmodes and thus provides an optimal estimator for the dark matter density field. However, as can be seen in Fig. 5, it has a very similar shape as $V_i^-$ and modified mass weighting provides an equally thorough fit to this vector. The only difference is a slight increase in the best-fit value for the parameter $M_0$.

The second derivative of the $\chi^2$ distribution leads to the signal-to-noise ratio of the halo density field,

$$\frac{S}{N} \equiv \frac{S}{2N_k} \frac{\partial^2 \chi^2}{\partial \delta_m^2} = \sum_{i,j} C_{ij}^{-1} b_i b_j P_{mm} \ , \tag{20}$$

This expression is equivalent to the Fisher information on the dark matter density mode $\delta_m$. Here, the reduced shot noise is simply computed as

$$\sigma_r^2 = \frac{1}{\sum_{i,j} C_{ij}^{-1}} \ . \tag{21}$$

We first show the $V_i^{(l)}$-weighted bias for the 10 halo bins in the left panel of Fig. 6. The highest bias, $b_w \simeq 2$, is achieved by weighting with $V_i^-$, as expected, since its components are all positive and give the largest weight to the highest halo masses. All the other eigenvectors produce lower values of the bias, distributed around unity.
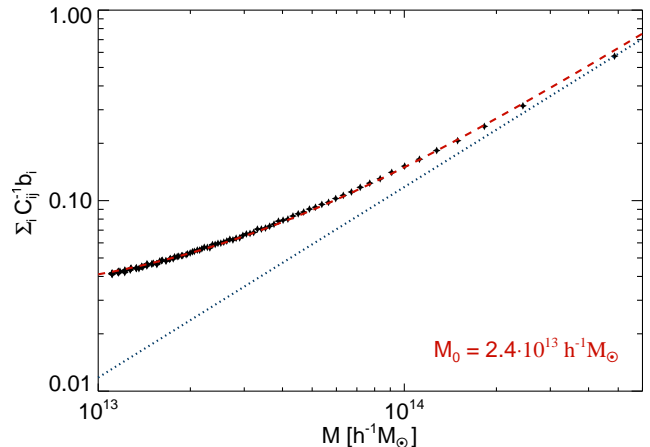


FIG. 5. The normalized vector $\sum_i C_{ij}^{-1} b_i$ that provides an optimal estimator for the dark matter, computed for 100 uniformly weighted mass bins. Since this vector is very similar to $V_i^-$, modified mass weighting (dashed red line) still yields a reasonable fit with a slightly higher value of $M_0$ (bottom right).

Note, however, that the weighted bias alone is not sufficient to describe the complete information content of the weighted halo density field. It is given by the signal-to-noise ratio in Eq. (15), which contains the weighted bias, the eigenvalue and the sums over the eigenvector components.

The total signal-to-noise ratio of the 10 eigenmodes is shown in the right panel of Fig. 6. This panel also shows the sum of all signal-to-noise ratios of each eigenmode, i.e. Eq. (16), and the signal-to-noise ratio as defined in Eq. (20) as a cross-check. Clearly, the weighting with $V_i^-$ dominates the signal-to-noise ratio. The eigenvector corresponding to the largest eigenvalue yields the second largest contribution, which may appear surprising since its effective bias is around unity and its eigenvalue is by far the largest. However, the sum of this eigenvector's components is large, which makes its signal-to-noise ratio dominant in comparison to the other eigenmodes. Still, it is suppressed by roughly 1 order of magnitude compared to the weighting with $V_i^-$ and can be safely ignored. This fact can be cross-checked when we compare the vector $\sum_i C_{ij}^{-1} b_i$ appearing in Eq. (19) to $V_i^-$. We found no mentionable discrepancy between the two. Thus, the main conclusion from this analysis is that the lowest eigenvalue contains most of the information and the other eigenmodes can be neglected.

So far we explored the signal-to-noise ratio of only 10 eigenmodes, a relatively sparse mass binning of the halo density field. Do these results converge with increasing the number of halo mass bins? It is interesting to plot the inverse signal-to-noise ratio, since it appears in Eq. (3) and thus determines the relative error on the power spectrum. We display it in the left panel of Fig. 7, where the
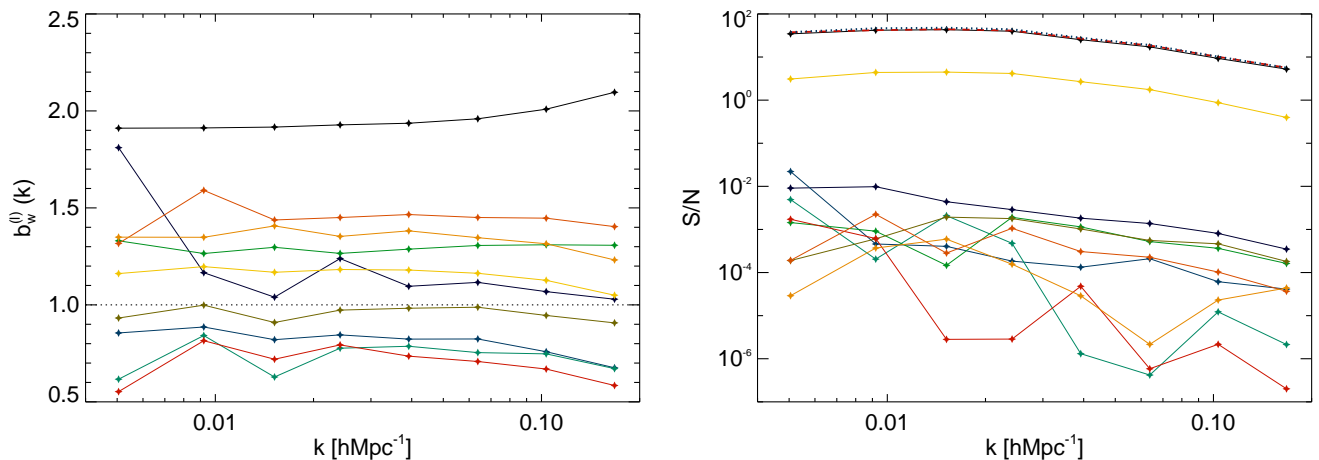
FIG. 6. Weighted bias (left) and signal-to-noise ratios (right) of the 10 $V^{(l)}$-weighted halo density fields. Colors correspond to the eigenvalues and eigenvectors of Fig. 3. The sum of all 10 signal-to-noise ratios is plotted as a dotted (blue) curve. The dashed (red) curve shows the signal-to-noise ratio as defined in Eq. (20).

results for different numbers of halo bins are presented. Increasing the number of halo bins improves the signal-to-noise ratio. In the limit of a large number of bins this should be equivalent to applying the smooth weighting function we found from the eigenvector $V_i^-$ (modified mass weighting) to each halo individually. We thus compute the inverse signal-to-noise ratio from the *smoothly* weighted halo density field, defined as

$$\delta_w(\mathbf{x}) = \frac{\sum_i w(M_i)\delta_i(\mathbf{x})}{\sum_i w(M_i)} \ . \qquad (22)$$

In practice, for every halo of mass $M$ in the simulation we assign a weight $w(M)$ according to the smooth weighting function of Eq. (11). Summing over all such weighted halo overdensities and normalizing yields the smoothly weighted halo density field $\delta_w$.

Its inverse signal-to-noise ratio results in the lowest (solid black line) curve in the left panel of Fig. 7. We also compare to the case when we assume all off-diagonal elements of the shot noise matrix to vanish (long dashed blue line). Clearly, a lot of information is lost when doing so and any improvements compared to uniform weighting (dotted black line) are canceled: we find roughly a factor of 5 improvement in the best case compared to uniform weighting. We optimized the value for $M_0$ by iteration to reach a minimal shot noise level and find $M_0 \simeq 3.4 \times 10^{13}h^{-1}M_\odot$, larger than our best-fit values for the highest resolution eigenvector from Fig. 4 and the vector from Fig. 5. This is expected, since we only tested up to 100 halo mass bins and have not fully converged yet ($M_0$ increases with the number of bins). However, the results from 100 mass-weighted halo bins closely approach the results obtained from smoothly weighting the halo density field (solid black lines in Fig. 7).

Looking at the reduced shot noise, we see a similar be-

havior. The right panel of Fig. 7 shows the same improvements when accounting for the off-diagonal elements of the shot noise matrix and increasing the number of bins. The shot noise of the halo density field can drastically be reduced using the appropriate weighting, on average by a factor of 4 in this case. Since the bias increases with our weighting, the improvement in the inverse signal-to-noise ratio is more striking, though.

This is well in agreement with the results in [6], where we applied linear and a different kind of modified mass weighting to halo density fields with different abundances. The modified mass-weighting function we applied there was rather a trial function that happened to suppress the shot noise better than linear mass weighting, and we did not derive it via any formal procedure like we do here. In order to directly compare to these older results, we apply modified mass weighting to one of the simulations presented in that paper. In particular, we use the simulation with $1024^3$ dark matter particles and a mean halo number density of $\bar{n} \simeq 7.0 \times 10^{-4}h^3\mathrm{Mpc}^{-3}$, resolving halos down to $M_{\min} \simeq 5.9 \times 10^{12}h^{-1}\mathrm{M}_\odot$. This yields the inverse signal-to-noise ratio and the reduced shot noise presented in Fig. 8. We also show the results from the binned halo density field, as before. Note that the strong decline of the curves corresponding to 100 bins is likely due to noise at low $k$. It is the same effect present already in our first simulation, however it is pronounced here, since the number of modes per $k$-bin is lowered by a factor of 6. Compared to the best case shown in Fig. 2 of [6], we managed to further reduce the inverse signal-to-noise ratio by an additional factor of 2.

The overall improvement compared to uniform weighting is even more striking, about a factor of 10 on average in signal-to-noise and roughly a factor of 4-5 in shot noise. Hence, owing to the higher mass resolution of this simula-
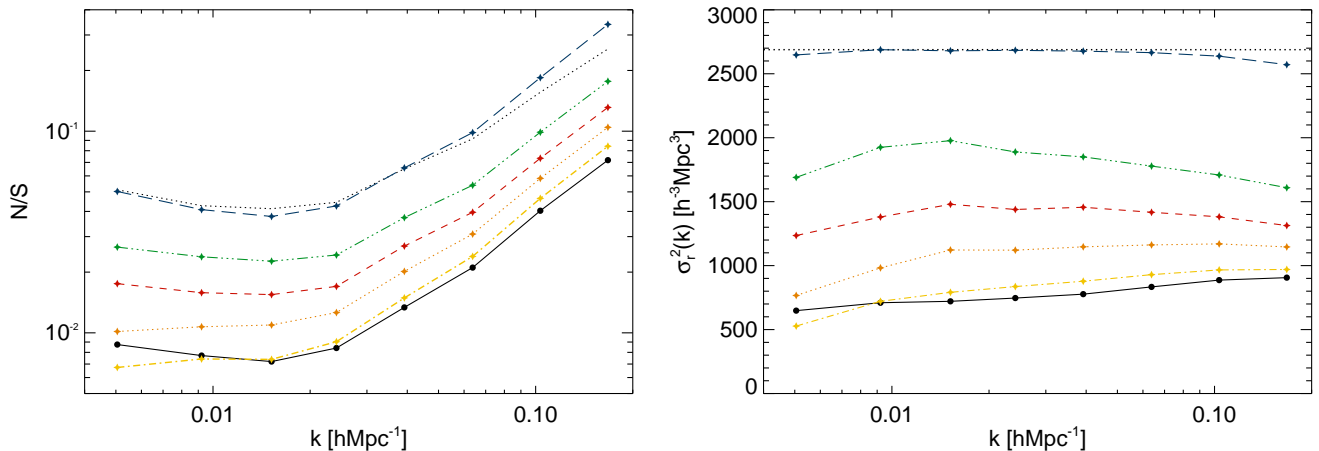
FIG. 7. Inverse signal-to-noise ratio (left) and reduced shot noise (right) of the halo density field, sliced into 10 (dot-dot-dashed green line), 30 (dashed red line), 100 uniformly weighted (dotted orange line) and 100 mass-weighted (dot-dashed yellow line) mass bins. The upper curves (long dashed blue line) show the results when neglecting the off-diagonal elements of the shot noise matrix. They agree well with uniform weighting (dotted black line, left panel) and the value $1/\bar{n}$ (dotted black line, right panel), respectively. The lowest curves (solid black line) display the results obtained from weighting the halo density field with the smooth function $w(M) = M + M_0$.
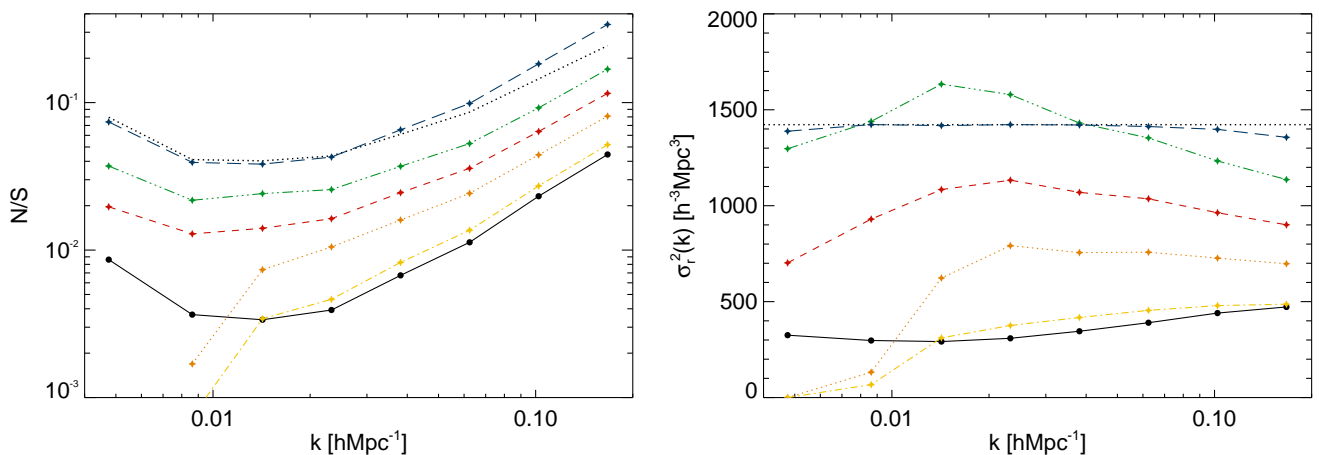


FIG. 8. Same as Fig. 7, computed from our higher resolution simulation with $1024^3$ particles and a mean halo number density of $\bar{n} \simeq 7.0 \times 10^{-4} h^3 \mathrm{Mpc}^{-3}$, resolving halos down to $M_{\min} \simeq 5.9 \times 10^{12} h^{-1} \mathrm{M}_\odot$.

tion, we include many more low-mass halos and therefore roughly double the signal. Via iteration we find the value $M_0 \simeq 1.7 \times 10^{13} h^{-1} \mathrm{M}_\odot$ to yield the lowest shot noise level. Comparing to the value we found in the previous simulation, $M_0 \simeq 3.4 \times 10^{13} h^{-1} \mathrm{M}_\odot$, it is roughly half as large. In our lower resolution simulation the lowest halo mass we can resolve is $M_{\min} \simeq 1.1 \times 10^{13} h^{-1} \mathrm{M}_\odot$, while in the higher resolution simulation it is $M_{\min} \simeq 5.9 \times 10^{12} h^{-1} \mathrm{M}_\odot$.

The decline of $M_0$ with the increase in the resolved halo mass fraction is expected, since one needs to account for the unresolved halos in the simulations. The relation between $M_0$ and $M_{\min}$ should be monotonic: in

the limit of perfect mass resolution we would expect all the dark matter to be in halos of a certain mass. Weighting all these halos by their mass should then recover the statistics of the dark matter density field without shot noise, at least on large scales. Within the tested domain of our simulations we find the relation $M_0 \simeq 3M_{\min}$ to be a good approximation in order to determine the appropriate choice for $M_0$ given $M_{\min}$.
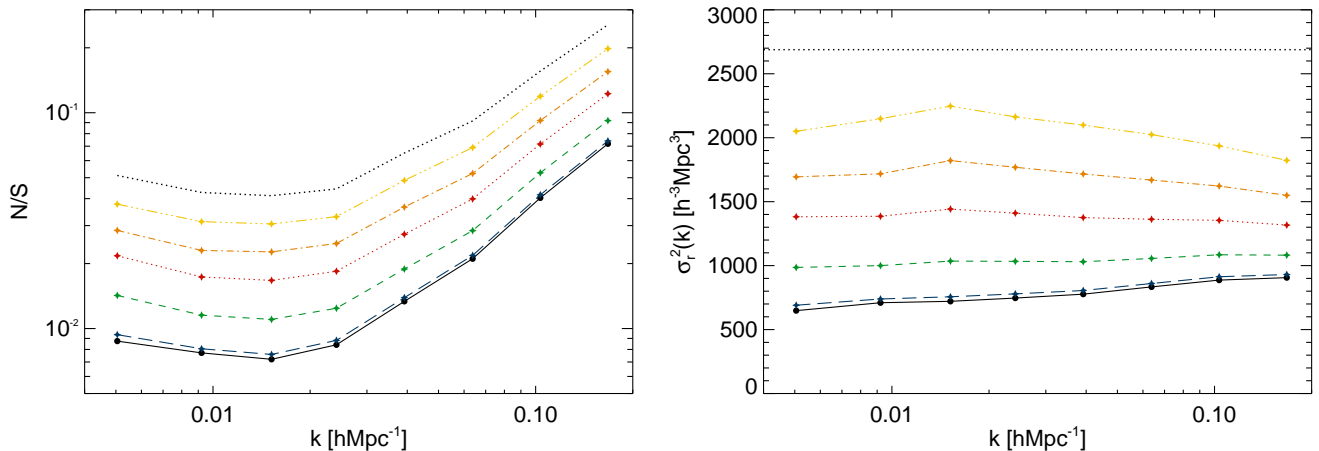
FIG. 9. Inverse signal-to-noise ratio (left) and reduced shot noise (right) of halos with a log-normal mass scatter of $\sigma_{\ln M} = 0,\ 0.1,\ 0.3,\ 0.5,\ 0.8 \to 0.4$ and $1.0$ (bottom to top), weighted by $w(M) = M + M_0$. The dotted (black) lines show the results from uniform weighting.

## D. Mass uncertainty

Up to now we have always been assuming to precisely know the mass of each halo (up to the sampling variance of the halo finder). However, in realistic observations the halo mass can only be determined with a limited accuracy. Commonly, the uncertainty is expressed as a log-normal scatter in halo mass. We can mimic this uncertainty by adding a Gaussian random variable $\mathcal{G}$ with zero mean and unit variance, scaled by $\sigma_{\ln M}$, to the exponent of the mass,

$$\tilde{M} = M \exp(\sigma_{\ln M}\, \mathcal{G} - \sigma_{\ln M}^2/2)\,. \tag{23}$$

This yields the noisier mass $\tilde{M}$, which then follows a log-normal distribution. The value $\sigma_{\ln M}$ is the log-normal scatter and the term $\sigma_{\ln M}^2/2$ is subtracted to maintain the same mean. For optical tracers of clusters $\sigma_{\ln M}$ is about 0.5 [28] and is expected to be much lower for SZ or X-ray proxies, such as $Y_X$ [29]. At the lower mass end the log-normal scatter is, however, poorly constrained. For simplicity, we will consider a constant log-normal scatter for all halos and apply the values of $\sigma_{\ln M} = 0.1,\ 0.3,\ 0.5,\ 1.0$. As a more complicated model we vary the scatter linearly with mass, with $\sigma_{\ln M} = 0.8$ at $M = 10^{12}h^{-1}\mathrm{M}_\odot$ and $\sigma_{\ln M} = 0.4$ at $M = 10^{15}h^{-1}\mathrm{M}_\odot$ (abbreviated as $\sigma_{\ln M} = 0.8 \to 0.4$).

We again apply modified mass weighting to construct the smoothly weighted density field as in Eq. (22) and compute the inverse signal-to-noise ratio as well as the reduced shot noise from it. For each case we adjust the value for $M_0$ in the weighting function separately by iteration. The results are depicted in Fig. 9. When using modified mass weighting, a 50% log-normal scatter in halo mass still yields about half the shot noise level of what is expected from uniform weighting. Even

our model with linearly decreasing $\sigma_{\ln M}$ from 0.8 to 0.4 and the high value of $\sigma_{\ln M} = 1.0$ yields inverse signal-to-noise ratios and shot noise levels that are below common expectations. The optimal values for $M_0$ increase with higher mass scatter. We find $M_0 \simeq 3.5 \times 10^{13},\ 5.1 \times 10^{13},\ 9.0 \times 10^{13},\ 4.4 \times 10^{14}h^{-1}\mathrm{M}_\odot$ for the cases of $\sigma_{\ln M} = 0.1,\ 0.3,\ 0.5,\ 1.0$.

Figure 10 shows the resulting eigenvector $V_i^-$ when applying a log-normal scatter with $\sigma_{\ln M} = 0.5,\ 0.8 \to 0.4$ and $1.0$ to the halo masses. In this case we only present it with uniformly weighted bins, since due to the


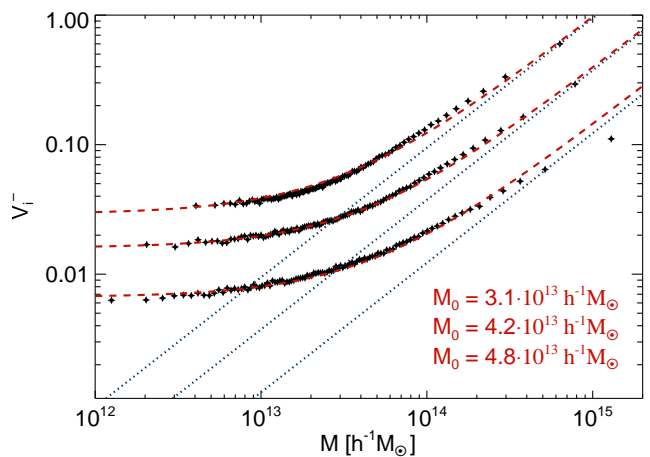
FIG. 10. The normalized eigenvector $V_i^-$ computed for 100 uniformly weighted bins with a log-normal scatter of $\sigma_{\ln M} = 0.5,\ 0.8 \to 0.4$ and $1.0$ added to the halo masses (top to bottom). For visibility, the lower two eigenvectors are shifted downwards by a factor of 2 and 5. The dotted (blue) and the dashed (red) lines represent linear and modified mass weighting, respectively.

scatter, mass weighting the bins does not improve on the results. Clearly, the saturation effect at low masses is more pronounced the stronger the scatter, resulting in an increase of the value for $M_0$. Also the halo mass range becomes wider. However, the smooth function for modified mass weighting still fits the data well. The only impact that mass scatter has on the eigenvector $V_i^-$ is to raise its saturation tail and thus the value of $M_0$. This is even the case for our model of linearly varying $\sigma_{\ln M}$ with mass: modified mass weighting still provides a reasonable fit to the simulation data.

## V. HALO MODEL APPROACH

In order to interpret our results, let us consider the *halo model* [21, 30–36]. The basic assumption of this model is that the power spectra of either dark matter or halos can be written as the sum of a *one-halo* term $P^{1\mathrm{H}}$ and a *two-halo* term $P^{2\mathrm{H}}$. The former describes the clustering of substructure within one single halo, whereas the latter represents the clustering among different halos. Moreover, it is assumed that all the dark matter is confined within virialized halos. The two terms can be expressed analytically via the halo mass function $\frac{\mathrm{d}n}{\mathrm{d}M}(M)$, the normalized Fourier transform of the halo profile $u(k, M)$, the analytic bias $b(M)$, the linear power spectrum $P_{\mathrm{lin}}(k)$, and the mean density of dark matter $\bar{\rho}_m$. Considering all the possibilities of auto- and cross-power spectra between halos in distinct mass bins $i$ and $j$ and the dark matter, the halo model for uniform weighting yields:

$$P_{ij}^{2\mathrm{H}}(k) = \frac{1}{\bar{n}_i \bar{n}_j} \iint \frac{\mathrm{d}n}{\mathrm{d}M}(M)\frac{\mathrm{d}n}{\mathrm{d}M}(M')b(M)b(M')\Theta(M, M_i)\Theta(M', M_j)P_{\mathrm{lin}}(k)\mathrm{d}M\mathrm{d}M' = b_i b_j P_{\mathrm{lin}}(k) \tag{24}$$

$$P_{im}^{2\mathrm{H}}(k) = \frac{1}{\bar{n}_i \bar{\rho}_m} \iint \frac{\mathrm{d}n}{\mathrm{d}M}(M)\frac{\mathrm{d}n}{\mathrm{d}M}(M')b(M)b(M')M'\Theta(M, M_i)P_{\mathrm{lin}}(k)\mathrm{d}M\mathrm{d}M' = b_i P_{\mathrm{lin}}(k) \tag{25}$$

$$P_{mm}^{2\mathrm{H}}(k) = \frac{1}{\bar{\rho}_m^2} \iint \frac{\mathrm{d}n}{\mathrm{d}M}(M)\frac{\mathrm{d}n}{\mathrm{d}M}(M')b(M)b(M')MM'P_{\mathrm{lin}}(k)\mathrm{d}M\mathrm{d}M' = P_{\mathrm{lin}}(k) \tag{26}$$

$$P_{ij}^{1\mathrm{H}}(k) = \frac{1}{\bar{n}_i \bar{n}_j} \int \frac{\mathrm{d}n}{\mathrm{d}M}(M)\Theta(M, M_i)\Theta(M, M_j)\mathrm{d}M = \frac{1}{\bar{n}_i}\delta_{ij}^{\mathrm{K}} \tag{27}$$

$$P_{im}^{1\mathrm{H}}(k) = \frac{1}{\bar{n}_i \bar{\rho}_m} \int \frac{\mathrm{d}n}{\mathrm{d}M}(M)M\Theta(M, M_i)\mathrm{d}M = \frac{M_i}{\bar{\rho}_m} \tag{28}$$

$$P_{mm}^{1\mathrm{H}}(k) = \frac{1}{\bar{\rho}_m^2} \int \frac{\mathrm{d}n}{\mathrm{d}M}(M)M^2\mathrm{d}M \equiv \frac{\langle nM^2\rangle}{\bar{\rho}_m^2} \ . \tag{29}$$

Here we assume the large-scale limit for the halo profile, i.e., $u(k \to 0, M) = 1$. Moreover, $\delta_{ij}^{\mathrm{K}}$ denotes the Kronecker symbol and $\Theta$ a product of two Heaviside step functions $\vartheta$:

$$\Theta(M, M_i) \equiv \vartheta(M - M_i)\vartheta(M_{i+1} - M) \ . \tag{30}$$

Since the integrals all go from $0$ to $\infty$, this function selects the considered halo bin $i$ with mass range $M_i < M < M_{i+1}$. The corresponding average halo mass of that bin is simply denoted as $M_i$, whereas for an average over all halos we omit the index.

In the simple approach adopted here the halo model predicts a white noise term not only for the autopower spectrum of halos, but also for the halo-matter cross- and the matter autopower spectra. However, simulations have shown that the low-$k$ behavior of the dark matter one-halo term is incorrect: subtracting off the component correlated with the linear power spectrum [which is approximately $P_{\mathrm{lin}}(k)$ at large scales] from the simulated one indeed yields a $k^4$-scaling instead of a constant white noise in the residual power (mode-coupling power) [34, 37]. This $k^4$-tail is a consequence of local mass and momentum conservation of the dark matter on

small scales and the same conservation laws should also apply to halo-matter correlations. We defer further discussions of this point to a future publication, where we show that a proper implementation of mass conservation in the $k = 0$ limit still yields similar results to those presented here.

The shot noise matrix as defined in Eq. (4) can be written as

$$C_{ij} = \langle\delta_i\delta_j\rangle - b_i\langle\delta_j\delta_m\rangle - b_j\langle\delta_i\delta_m\rangle + b_ib_j\langle\delta_m^2\rangle \ . \tag{31}$$

Plugging in the sum of the corresponding one- and two-halo terms for each of the angled brackets, we see that the two-halo terms cancel each other and we are left with

$$C_{ij} = \frac{\delta_{ij}^{\mathrm{K}}}{\bar{n}_i} - b_i\frac{M_j}{\bar{\rho}_m} - b_j\frac{M_i}{\bar{\rho}_m} + b_ib_j\frac{\langle nM^2\rangle}{\bar{\rho}_m^2} \ . \tag{32}$$

Our lower resolution simulation determines the dark matter one-halo term to be $\langle nM^2\rangle/\bar{\rho}_m^2 \simeq 428h^{-3}\mathrm{Mpc}^3$. Note that this value is by almost 2 orders of magnitude smaller than the first term in Eq. (32). However, for highly biased halo bins it can become important in the off-diagonal terms of $C_{ij}$. The same applies to the one-

halo term of the halo-matter cross-power spectrum, because it scales with the mean halo mass of each bin. For example, it yields $M_1/\bar{\rho}_m \simeq 164h^{-3}\mathrm{Mpc}^3$ for the lowest, and $M_{10}/\bar{\rho}_m \simeq 2394h^{-3}\mathrm{Mpc}^3$ for the highest of our 10 mass bins. In Fig. 11 we compare each matrix element of Eq. (32) to the numerically determined shot noise matrix (from Fig. 2). The model yields a good agreement with the data, especially the observed sub-Poissonian shot noise power of the highest-mass halos, as well as the negative off-diagonal components are nicely reproduced. The off-diagonal elements with low power are more affected by scatter and therefore show stronger deviations from the theory.

For the comparison of our model to the numerical data it is, however, more convenient to look at the eigenvectors and eigenvalues of the shot noise matrix, since they describe the complete information on halo stochasticity in a more concise manner. Let us redefine the halo mass as

$$\mathcal{M}_i \equiv M_i - b_i \frac{\langle nM^2 \rangle}{2\bar{\rho}_m} \ . \tag{33}$$

Now, Eq. (32) can be written more succinctly:

$$C_{ij} = \frac{\delta_{ij}^{\mathrm{K}}}{\bar{n}_i} - b_i \frac{\mathcal{M}_j}{\bar{\rho}_m} - b_j \frac{\mathcal{M}_i}{\bar{\rho}_m} \ . \tag{34}$$

It is straightforward to work out the eigenvalues and eigenvectors of this matrix. For $d > 2$ mass bins, there are $d - 2$ degenerate eigenvalues with the value $\lambda = 1/\bar{n}_i$. The two remaining eigenvalues with corresponding eigenvectors are

$$\lambda^{\pm} = \frac{1}{\bar{n}_i} - \frac{1}{\bar{\rho}_m} \sum_i \mathcal{M}_i b_i \pm \frac{1}{\bar{\rho}_m} \sqrt{\sum_i \mathcal{M}_i^2 \sum_i b_i^2} \ , \tag{35}$$

$$V_i^{\pm} = \frac{\mathcal{M}_i}{\sqrt{\sum_i \mathcal{M}_i^2}} \mp \frac{b_i}{\sqrt{\sum_i b_i^2}} \ . \tag{36}$$

They are shown in Fig. 12 for the case of 10 halo bins. It is remarkable how well the halo model reproduces the distribution of eigenvalues we found in our numerical analysis. The mass dependence of the eigenvectors also shows a good agreement. This can be seen when we renormalize $V_i^{\pm}$ by multiplication with $\sqrt{\sum_i \mathcal{M}_i^2}$ in Eq. (36), we get

$$V_i^{\pm} = M_i \mp b_i \tilde{M}_0^{\pm} \ , \tag{37}$$

with

$$\tilde{M}_0^{\pm} \equiv \frac{\sqrt{\sum_i \mathcal{M}_i^2}}{\sqrt{\sum_i b_i^2}} \pm \frac{\langle nM^2 \rangle}{2\bar{\rho}_m} \ . \tag{38}$$

In other words, $V_i^{\pm}$ is nothing else than a superposition of mass and bias weighting. The relative weight
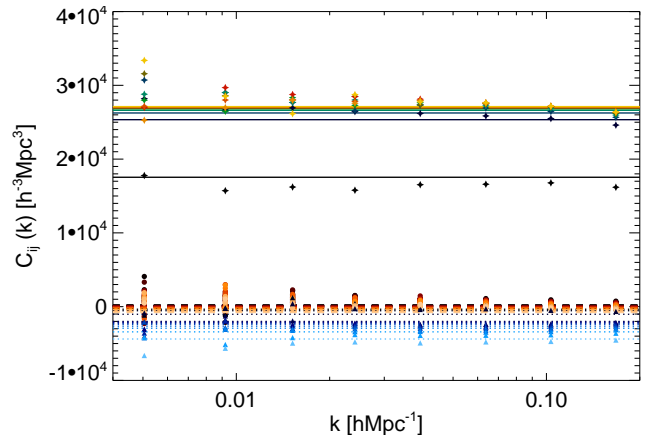


FIG. 11. Elements of the shot noise matrix as described by the halo model in Eq. (32), compared to the simulation results taken from Fig. 2 (symbols). The diagonal components (solid lines) monotonously decrease from the lowest (yellow) to the highest-mass bin (black), in good agreement with the numerical data. The halo model also reproduces both the positive (dashed lines, scaled in red) and the negative (dotted lines, scaled in blue) off-diagonal elements of the shot noise matrix fairly well.

between the two is determined by $\tilde{M}_0^{\pm}$. Equation (37) has a very similar form as the modified mass-weighting fitting function from Eq. (11). Evaluating Eq. (38) using $b_i$ and $M_i$ from the simulation with 10 mass bins yields $M_0^- \simeq 1.2 \times 10^{13}h^{-1}\mathrm{M}_\odot$. At the high-mass end, i.e., $M \simeq 10^{15}h^{-1}\mathrm{M}_\odot$, the second term in Eq. (37) is negligible compared to the first one, since $b_i \lesssim 10$ in this regime. However, at lower masses the two terms become closer in magnitude and finally the second term dominates at the low-mass end, i.e., $M \simeq 10^{13}h^{-1}\mathrm{M}_\odot$. In this regime the bias is a slowly varying function of mass and thus well approximated by a constant. Hence, the analytical form of $V_i^-$ predicted by the halo model agrees well with the functional form for modified mass weighting that we found earlier.

In order to check our model more quantitatively, we compare its predictions directly to our numerical results in Fig. 12. Here we focus on the nontrivial eigenvalues $\lambda^{\pm}$ and eigenvectors $V_i^{\pm}$, since only they contain information on the halo statistics. The agreement between simulation and theory is remarkable, only for the eigenvalue $\lambda^+$ we find a stronger discrepancy, but since it shows a slight scale dependence it probably involves more detailed modeling. We did the same comparison for the case of 30 and 100 mass bins and find the agreement in the eigenvectors to become even better. The offset in $\lambda^+$ however does not vanish with an increasing number of bins.

One might argue that the way we estimate the bias from the simulation in Eq. (7) is not correct in this approach, since the halo model predicts a nonzero white

FIG. 12. The eigenvalues $\lambda^{\pm}$ (left) and eigenvectors $V_i^{\pm}$ (right) from Fig. 3 compared to the predictions of the halo model (dashed red line). The dotted line in the left panel shows the value $1/\bar{n}_i$.

noise term for both the halo-matter cross, as well as the dark matter autopower spectrum. We repeated the same analysis with a shot noise corrected halo bias defined as

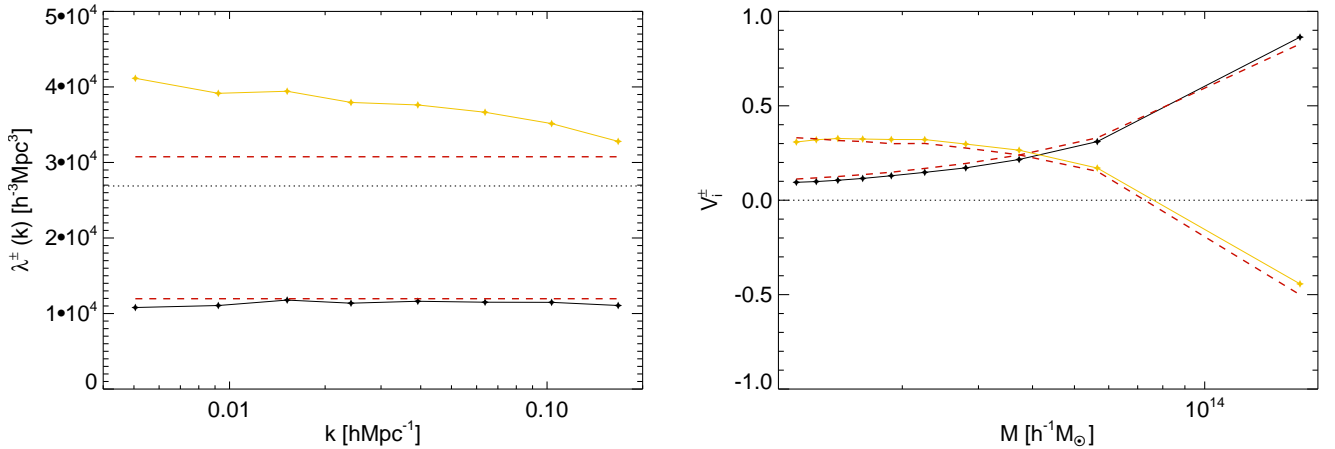$$b_i = \frac{\langle \delta_i \delta_m \rangle - \frac{M_i}{\bar{\rho}_m}}{\langle \delta_m^2 \rangle - \frac{\langle nM^2 \rangle}{\bar{\rho}_m^2}} \; . \tag{39}$$

However, we find essentially no differences in the shot noise matrix and its eigenvalues and eigenvectors. As can be seen in Eq. (31), this is because small changes in the bias are compensated by terms of opposite sign. For the same reason it does not matter much whether we use the scale-dependent or scale-independent bias in our analysis.

Another way to compare our model to the simulations is to look at the estimators for the halo bias itself,

$$\frac{\langle \delta_i \delta_m \rangle}{\langle \delta_m^2 \rangle} \quad \text{and} \quad \sqrt{\frac{\langle \delta_i^2 \rangle}{\langle \delta_m^2 \rangle}} \; . \tag{40}$$

Since the halo model yields white noise terms for all three correlators appearing in these estimators, this can partly account for their scale dependence. We get

$$\frac{\langle \delta_i \delta_m \rangle}{\langle \delta_m^2 \rangle} = \frac{b_i P_{\mathrm{lin}}(k) + \frac{M_i}{\bar{\rho}_m}}{P_{\mathrm{lin}}(k) + \frac{\langle nM^2 \rangle}{\bar{\rho}_m^2}} \; , \tag{41}$$

$$\frac{\langle \delta_i^2 \rangle}{\langle \delta_m^2 \rangle} = \frac{b_i^2 P_{\mathrm{lin}}(k) + \frac{1}{\bar{n}_i}}{P_{\mathrm{lin}}(k) + \frac{\langle nM^2 \rangle}{\bar{\rho}_m^2}} \; , \tag{42}$$

where we take $b_i$ as an average over large scales from Eq. (39) or compute it from the halo mass function via the peak-background split formalism [3]. The simulation results for both estimators are shown in Fig. 13 for the case of 10 mass bins. The halo model reproduces the numerical results very well up to scales of $k \simeq 0.1\ h\mathrm{Mpc}^{-1}$.

The deviation on smaller scales is expected, since higher-order bias effects, the nonlinear evolution of the density field [34, 38], and the detailed shape of the halo profile begin to matter [33].

The figure also shows the result of the two estimators when accounting for all of the halos in the simulation. In the case of uniform weighting (dashed lines) they both agree on large scales, but show a different scale dependence towards higher $k$-modes. With modified mass weighting (dotted lines) however, both estimators agree even up to smaller scales, a consequence of the small stochasticity in this estimator. Note that for a weighted field we need to account for the weights in the averaged quantities, so in Eqs. (41) and (42) we have to exchange $M_i$ by the weighted mean halo mass $M_w$, $b_i$ by the weighted bias $b_w$, and $1/\bar{n}_i$ by $1/\bar{n} \times \langle w^2 \rangle / \langle w \rangle^2$, with

$$\bar{n} = \int \frac{\mathrm{d}n}{\mathrm{d}M}(M)\, \mathrm{d}M \; , \tag{43}$$

$$\langle w \rangle = \frac{1}{\bar{n}} \int \frac{\mathrm{d}n}{\mathrm{d}M}(M) w(M)\, \mathrm{d}M \; , \tag{44}$$

$$\langle w^2 \rangle = \frac{1}{\bar{n}} \int \frac{\mathrm{d}n}{\mathrm{d}M}(M) w^2(M)\, \mathrm{d}M \; , \tag{45}$$

$$M_w = \frac{1}{\bar{n}} \int \frac{\mathrm{d}n}{\mathrm{d}M}(M) w(M) M\, \mathrm{d}M \; , \tag{46}$$

$$b_w = \frac{1}{\bar{n}} \int \frac{\mathrm{d}n}{\mathrm{d}M}(M) w(M) b(M)\, \mathrm{d}M \; , \tag{47}$$

where we integrate over all resolved halo masses.

Last but not least we can utilize the halo model to determine the reduced shot noise as a function of mass resolution. For this we need analytic expressions for the halo mass function $\frac{\mathrm{d}n}{\mathrm{d}M}(M)$ and the halo bias $b(M)$ to compute the eigenvalues and eigenvectors of the shot noise matrix. We use the functional forms of Sheth-Tormen [3] with the parameters given in [39]. For infinitesimal bins,
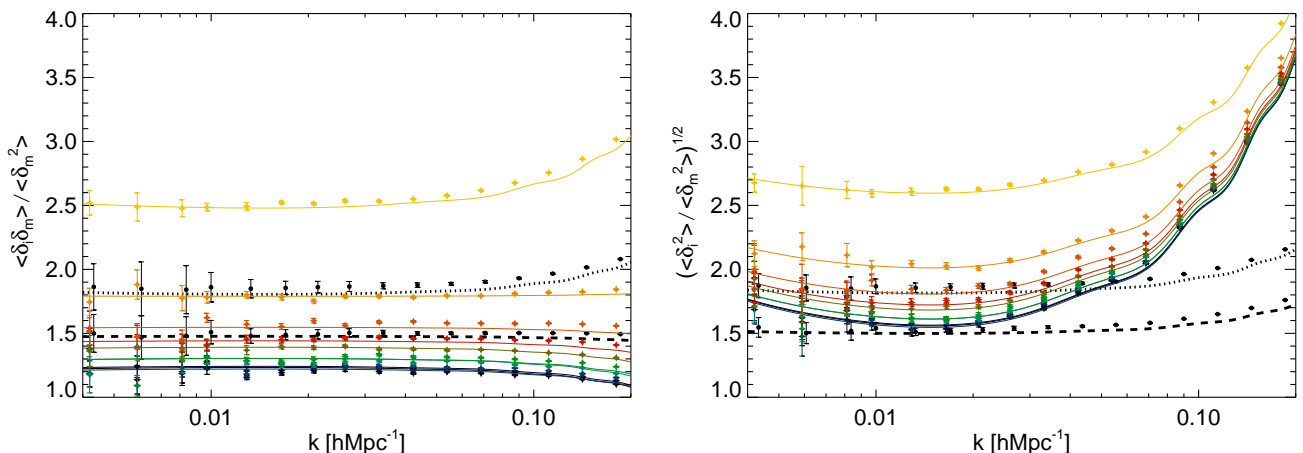
FIG. 13. Scale-dependent bias estimators from halo-matter cross correlation (left panel) and halo-auto correlation (right panel) as predicted by the halo model. The simulation results from 10 mass bins are shown as crosses with error bars (in color); the solid lines show the halo model results. The black dots with error bars show the results for only one mass bin (all halos) for both uniform and modified mass weighting, with the halo model prediction overplotted in dashed and dotted, respectively.

Eqs. (35) and (36) can be rewritten as

$$\lambda^{\pm} = \frac{1}{\mathrm{d}n} - \frac{1}{\bar{\rho}_m}\langle \mathcal{M}b\rangle \pm \frac{1}{\bar{\rho}_m}\sqrt{\langle \mathcal{M}^2\rangle\langle b^2\rangle} \,, \qquad (48)$$

$$V^{\pm}(M) = \frac{\mathcal{M}}{\sqrt{\langle \mathcal{M}^2\rangle}} \mp \frac{b}{\sqrt{\langle b^2\rangle}} \,, \qquad (49)$$

with

$$\langle \mathcal{M}b\rangle = \frac{1}{\bar{n}}\int \frac{\mathrm{d}n}{\mathrm{d}M}(M)\mathcal{M}b\,\mathrm{d}M \,, \qquad (50)$$

$$\langle \mathcal{M}^2\rangle = \frac{1}{\bar{n}}\int \frac{\mathrm{d}n}{\mathrm{d}M}(M)\mathcal{M}^2\,\mathrm{d}M \,, \qquad (51)$$

$$\langle b^2\rangle = \frac{1}{\bar{n}}\int \frac{\mathrm{d}n}{\mathrm{d}M}(M)b^2\,\mathrm{d}M \,. \qquad (52)$$

The integrals run from $M_{\min}$ to $\infty$ and we can compute the reduced shot noise $\sigma_r^2$ of the weighted halo density field for various values of $M_{\min}$ using Eqs. (14) and (17) in their infinitesimal form:

$$\sigma_w^2(M_{\min}) = \lambda \frac{\frac{1}{\bar{n}}\int \frac{\mathrm{d}n}{\mathrm{d}M}(M)V^2(M)\,\mathrm{d}M}{\left(\frac{1}{\bar{n}}\int \frac{\mathrm{d}n}{\mathrm{d}M}(M)V(M)\,\mathrm{d}M\right)^2} \,. \qquad (53)$$

We neglect all eigenmodes except $\lambda^{\pm}$ and $V^{\pm}$ for this calculation, since they have the largest contribution in signal-to-noise. This yields

$$\sigma_r^2(M_{\min}) = \left(\frac{1}{\sigma_{w^+}^2} + \frac{1}{\sigma_{w^-}^2}\right)^{-1} \,. \qquad (54)$$

The result can then be compared to the expected shot noise from uniform weighting, which, according to the
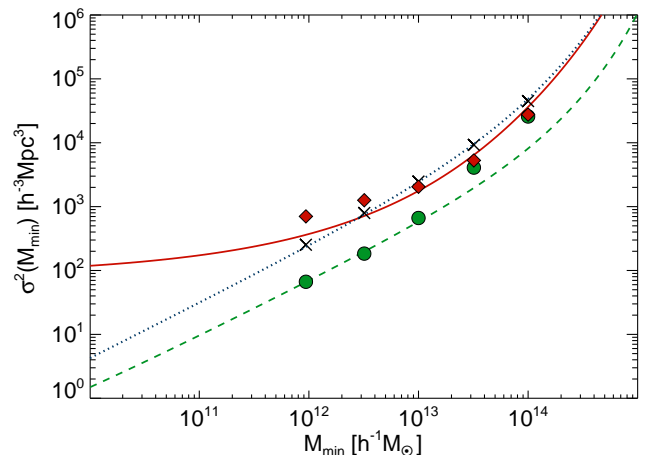


FIG. 14. Stochasticity between halos and the dark matter as a function of mass resolution as predicted by the halo model for the cases of uniform ($\sigma_u^2$, solid red line) and modified mass weighting ($\sigma_r^2$, dashed green line). The dotted (blue) line shows the Poisson prediction $1/\bar{n}$. The results from our highest resolution simulation are overplotted as red diamonds (uniform weighting) and green circles (modified mass weighting) for five different low-mass cuts. The black crosses show the corresponding values of $1/\bar{n}$ taken from the simulation.

halo model, is given by

$$\sigma_u^2(M_{\min}) = \frac{1}{\bar{n}} - 2b\frac{M}{\bar{\rho}_m} + b^2\frac{\langle nM^2\rangle}{\bar{\rho}_m^2} \,, \qquad (55)$$

where $\bar{n}$, $M$ and $b$ depend on $M_{\min}$ and can be computed from Eqs. (43), (46) and (47) using uniform weights, i.e. $w(M) = 1$. The functions $\sigma_u^2(M_{\min})$ and $\sigma_r^2(M_{\min})$ are depicted in Fig. 14. Apparently, at low resolution (high

$M_{\min}$), the improvement due to modified mass weighting is quite modest. However, for $M_{\min} \lesssim 10^{12} h^{-1} \mathrm{M}_\odot$ the function $\sigma_u^2(M_{\min})$ approaches a constant, while $\sigma_r^2(M_{\min})$ still decreases linearly with $M_{\min}$. This linear trend leads to a suppression of stochasticity by almost 2 orders of magnitude if one can resolve halos down to $M_{\min} = 10^{10} h^{-1} \mathrm{M}_\odot$.

In order to cross-check these results we computed the $k$-averaged shot noise (shown as filled symbols) for various low-mass cuts from our highest resolution simulation consisting of $1536^3$ particles resolving halos down to $M_{\min} \simeq 9.4 \times 10^{11} h^{-1} \mathrm{M}_\odot$. Taking into account all halos in this simulation we obtain a minimal shot noise level when applying modified mass weighting with $M_0 \simeq 3.1 \times 10^{12} h^{-1} \mathrm{M}_\odot$, which again satisfies the anticipated relation $M_0 \simeq 3 M_{\min}$.

Overall, the agreement between the simulations and the halo model is reasonable, but not perfect. At low $M_{\min}$ the halo model underestimates the shot noise of the uniformly weighted halo density field and the shot noise suppression due to modified mass weighting relative to uniform weighting is even larger than predicted by the model. At high $M_{\min}$ the shot noise in the simulation is not perfectly scale independent anymore and since we are taking the average over the whole $k$-range the result becomes more inaccurate.

## VI. CONCLUSIONS

In a previous paper [6] it was shown that weighting dark matter halos by their mass can lead to a suppression of stochasticity between halos and the dark matter relative to naive expectations. In this work we investigated the shot noise matrix, defined as the two-point correlator $C_{ij} \equiv \langle (\delta_i - b_i \delta_m)(\delta_j - b_j \delta_m) \rangle$ in Fourier space, split into equal number density mass bins. The eigensystem of this matrix reveals two nontrivial eigenvalues, one of them being enhanced, the other suppressed compared to the Poisson model expectation. It is the latter that leads to a reduced stochasticity. The optimal estimator of the dark matter and the eigenvector corresponding to the lowest eigenvalue are very similar and the latter dominates the signal-to-noise ratio of the halo density field. We fit both vectors by a smooth function of mass which we denote *modified mass weighting*. It is proportional to halo mass at the high-mass end and approaches a constant towards lower masses which is determined by the minimum halo mass resolved in the simulations. This constant is roughly 3 times the minimum halo mass over the range of masses we explored.

Applying this function to weight the halo density field results in a field that is more correlated with the dark matter with a suppressed shot noise component, improving upon previous results [6] by a factor of 2 in signal-to-noise. We investigate the effect of uncertainty in halo mass, finding that it does not change our fundamental conclusions, even if it weakens the strength of the method: a realistic amount of log-normal scatter in mass at the level of 0.5 increases the shot noise by a about a factor of 2. Our results can directly be applied to methods that attempt to eliminate sampling variance by investigating the relation between galaxies and the dark matter both tracing the same LSS. In this case the error is determined by the stochasticity between the two and reducing it can improve the ultimate reach of these methods [4, 5].

Considering the halo model as a theoretical approach to describe the shot noise matrix, we find analytical expressions for its eigenvalues and eigenvectors. In particular, the two nontrivial eigenvectors can be written as a linear combination of halo bias and halo mass, which yields a considerable agreement with our simulation results. Furthermore, the two estimators of the scale-dependent bias, $\langle \delta_h \delta_m \rangle / \langle \delta_m^2 \rangle$ and $\sqrt{\langle \delta_h^2 \rangle / \langle \delta_m^2 \rangle}$, are well reproduced. However, our model suffers from the lack of mass and momentum conservation: its implementation, together with higher-order perturbation theory and halo exclusion, further improves the agreement and will be presented elsewhere.

The halo model suggests the stochasticity between modified mass-weighted halos and the dark matter to decrease linearly with mass resolution below $M \simeq 10^{12} h^{-1} \mathrm{M}_\odot$, yielding a suppression by almost 2 orders of magnitude at $M_{\min} \simeq 10^{10} h^{-1} \mathrm{M}_\odot$ as compared to uniformly weighted halos. While we focused on the question of how well halos can reconstruct the dark matter, our analysis is also applicable to the study of stochasticity between halos themselves. Indeed, reducing the stochasticity between different halo tracers by optimal weighting techniques, while at the same time canceling sampling variance, should be possible even if the dark matter field is not measured. This will be addressed in more detail in a future work.

Specific applications are the best way to test the efficiency of our method. There is probably not much advantage in applying it to the standard power spectrum determination, where the sampling variance error dominates the error budget in the limit of small stochasticity, while in the opposite limit of rare halos, when the shot noise power is comparable to the intrinsic halo power, we do not see much gain (as demonstrated by the fact that all the points in Fig. 14 overlap for the highest $M_{\min}$, which corresponds to halos with the lowest number density). More promising applications are those where the sampling variance error is eliminated and the error budget is dominated by stochasticity, or the ratio of shot noise power to the halo power.

In this paper we have focused on the bias determination from galaxy and dark matter correlations [5] as a specific application, but other applications are possible, such as constraining $f_{\mathrm{NL}}$ from non-Gaussianity [27, 40]

and the redshift-space parameter $\beta$ from redshift-space distortions [8, 41], to name a few. Upcoming surveys like SDSS-III [42], JDEM/EUCLID [43, 44] or BigBOSS [45] and LSST [46] will increase the available number of galaxies significantly, providing both 3D galaxy maps and 2D to 3D dark matter maps (via weak lensing techniques, enhanced by lensing tomography).

Our results suggest that correlating modified halo mass-weighted galaxies against the dark matter has the potential to lead to dramatic improvements in the precision of cosmological parameter estimation. We will explore more explicit demonstrations of the above mentioned applications in future work.

## ACKNOWLEDGMENTS

[1] M. Tegmark, D. J. Eisenstein, M. A. Strauss, D. H. Weinberg, M. R. Blanton, J. A. Frieman, M. Fukugita, J. E. Gunn, A. J. S. Hamilton, G. R. Knapp, et al., Phys. Rev. D **74**, 123507 (2006), arXiv:astro-ph/0608632.

[2] B. A. Reid, W. J. Percival, D. J. Eisenstein, L. Verde, D. N. Spergel, R. A. Skibba, N. A. Bahcall, T. Budavari, J. A. Frieman, M. Fukugita, et al., MNRAS **404**, 60 (2010), 0907.1659.

[3] R. K. Sheth and G. Tormen, MNRAS **308**, 119 (1999), arXiv:astro-ph/9901122.

[4] U. Seljak and M. S. Warren, MNRAS **355**, 129 (2004), arXiv:astro-ph/0403698.

[5] U. Pen, MNRAS **350**, 1445 (2004), arXiv:astro-ph/0402008.

[6] U. Seljak, N. Hamaus, and V. Desjacques, Phys. Rev. Lett. **103**, 091303 (2009), 0904.2963.

[7] U. Seljak, Physical Review Letters **102**, 021302 (2009), 0807.1770.

[8] P. McDonald and U. Seljak, J. Cosmology Astropart. Phys. **10**, 7 (2009), 0810.0323.

[9] H. Gil-Marín, C. Wagner, L. Verde, R. Jimenez, and A. F. Heavens, MNRAS **407**, 772 (2010), 1003.3238.

[10] A. A. Berlind and D. H. Weinberg, ApJ **575**, 587 (2002), arXiv:astro-ph/0109001.

[11] P. J. E. Peebles, *Principles of Physical Cosmology* (1993).

[12] R. E. Smith, MNRAS **400**, 851 (2009), 0810.1960.

[13] P. McDonald, Phys. Rev. D **75**, 043514 (2007), arXiv:astro-ph/0606028.

[14] V. Springel, MNRAS **364**, 1105 (2005), arXiv:astro-ph/0505010.

[15] E. Komatsu, J. Dunkley, M. R. Nolta, C. L. Bennett, B. Gold, G. Hinshaw, N. Jarosik, D. Larson, M. Limon, L. Page, et al., ApJS **180**, 330 (2009), 0803.0547.

[16] U. Seljak and M. Zaldarriaga, ApJ **469**, 437 (1996), arXiv:astro-ph/9603033.

[17] R. Scoccimarro, MNRAS **299**, 1097 (1998), arXiv:astro-ph/9711187.

[18] M. Crocce, S. Pueblas, and R. Scoccimarro, MNRAS **373**, 369 (2006), arXiv:astro-ph/0606505.

[19] V. Desjacques, U. Seljak, and I. T. Iliev, MNRAS **396**, 85 (2009), 0811.2748.

[20] R. W. Hockney and J. W. Eastwood, *Computer simulation using particles* (1988).

[21] R. E. Smith, R. Scoccimarro, and R. K. Sheth, Phys. Rev. D **75**, 063512 (2007), arXiv:astro-ph/0609547.

[22] R. Casas-Miranda, H. J. Mo, R. K. Sheth, and G. Boerner, MNRAS **333**, 730 (2002), arXiv:astro-ph/0105008.

[23] M. Manera and E. Gaztañaga, MNRAS **415**, 383 (2011), 0912.0446.

[24] W. H. Press, S. A. Teukolsky, W. T. Vetterling, and B. P. Flannery, *Numerical recipes in FORTRAN. The art of scientific computing* (1992).

[25] S. Bonoli and U. L. Pen, MNRAS **396**, 1610 (2009), 0810.0273.

[26] W. J. Percival, L. Verde, and J. A. Peacock, MNRAS **347**, 645 (2004), arXiv:astro-ph/0306511.

[27] A. Slosar, J. Cosmology Astropart. Phys. **3**, 4 (2009), 0808.0044.

[28] E. Rozo, E. S. Rykoff, A. Evrard, M. Becker, T. McKay, R. H. Wechsler, B. P. Koester, J. Hao, S. Hansen, E. Sheldon, et al., ApJ **699**, 768 (2009), 0809.2794.

[29] A. V. Kravtsov, A. Vikhlinin, and D. Nagai, ApJ **650**, 128 (2006), arXiv:astro-ph/0603205.

[30] J. A. Peacock and R. E. Smith, MNRAS **318**, 1144 (2000), arXiv:astro-ph/0005010.

[31] U. Seljak, MNRAS **318**, 203 (2000), arXiv:astro-ph/0001493.

[32] R. Scoccimarro, R. K. Sheth, L. Hui, and B. Jain, ApJ **546**, 20 (2001), arXiv:astro-ph/0006319.

[33] A. Cooray and R. Sheth, Phys. Rep. **372**, 1 (2002), arXiv:astro-ph/0206508.

[34] M. Crocce and R. Scoccimarro, Phys. Rev. D **77**, 023533 (2008), 0704.2783.

[35] J. Hamann, S. Hannestad, A. Melchiorri, and Y. Y. Y. Wong, J. Cosmology Astropart. Phys. **7**, 17 (2008), 0804.1789.

[36] F. Bernardeau, S. Colombi, E. Gaztañaga, and R. Scoccimarro, Phys. Rep. **367**, 1 (2002), arXiv:astro-ph/0112551.

[37] R. E. Smith, J. A. Peacock, A. Jenkins, S. D. M. White, C. S. Frenk, F. R. Pearce, P. A. Thomas, G. Efstathiou, and H. M. P. Couchman, MNRAS **341**, 1311 (2003), arXiv:astro-ph/0207664.

[38] M. Crocce and R. Scoccimarro, Phys. Rev. D **73**, 063519 (2006), arXiv:astro-ph/0509418.

[39] R. Mandelbaum, A. Tasitsiomi, U. Seljak, A. V. Kravtsov, and R. H. Wechsler, MNRAS **362**, 1451 (2005), arXiv:astro-ph/0410711.

[40] A. Slosar, C. Hirata, U. Seljak, S. Ho, and N. Padmanabhan, J. Cosmology Astropart. Phys. **8**, 31 (2008), 0805.3580.

[41] U. Seljak, MNRAS **325**, 1359 (2001), arXiv:astro-ph/0009016.

[42] N. Ross, E. S. Sheldon, A. D. Myers, C. Yeche, G. T. Richards, R. G. McMahon, J. F. Hennawi, K. Lee, W. M. Wood-Vasey, A. Weyant, et al., in *American Astronomical Society Meeting Abstracts #215* (2010), vol. 42 of *Bulletin of the American Astronomical Society*, p. #471.04.

[43] N. Gehrels, in *American Astronomical Society Meeting Abstracts #215* (2010), vol. 42 of *Bulletin of the American Astronomical Society*, p. #380.01.

[44] A. Refregier, A. Amara, T. D. Kitching, A. Rassat, R. Scaramella, J. Weller, and f. t. Euclid Imaging Consortium, ArXiv e-prints (2010), 1001.0061.

[45] D. J. Schlegel, C. Bebek, H. Heetderks, S. Ho, M. Lampton, M. Levi, N. Mostek, N. Padmanabhan, S. Perlmutter, N. Roe, et al., ArXiv e-prints (2009), 0904.0468.

[46] Z. Ivezic, J. A. Tyson, E. Acosta, R. Allsman, S. F. Anderson, J. Andrew, R. Angel, T. Axelrod, J. D. Barr, A. C. Becker, et al., ArXiv e-prints (2008), 0805.2366.

# 4

# PAPER III

**Summary**   One promising application of the previous findings is the search for primordial non-Gaussianity (PNG) in the clustering of galaxies. It has been shown that certain types of PNG induce a scale-dependent correction to the halo bias, which grows towards larger scales. When multiple tracers of the dark matter density field are considered, such as halos of different mass, the relative bias between the tracers is not as severely affected by cosmic variance as the power spectrum of each tracer. In this case, the accuracy is limited by the shot noise of the tracers only. In the following paper, optimal weighting techniques are applied to improve the measurement of a scale-dependent component of the halo bias arising in simulations with non-Gaussian initial conditions. On the basis of a Fisher matrix analysis, it is shown that the signatures of PNG are more likely to be found when multiple tracers are considered, due to the cancellation of cosmic variance. If, in addition, the dark matter density field itself is available, it is shown how the previously derived optimal weights can help improve upon current constraints on PNG by more than an order of magnitude. Utilizing the halo model to extrapolate our numerical results to higher mass resolution suggests that the same gains can be expected even without observations of the dark matter density field, by considering a wide enough mass range of halos split into multiple tracers.

# Optimal Constraints on Local Primordial Non-Gaussianity from the Two-Point Statistics of Large-Scale Structure

Nico Hamaus,[1, *] Uroš Seljak,[1, 2, 3] and Vincent Desjacques[1]

[1]*Institute for Theoretical Physics, University of Zurich, 8057 Zurich, Switzerland*
[2]*Physics Department, Astronomy Department and Lawrence Berkeley National Laboratory,*
*University of California, Berkeley, California 94720, USA*
[3]*Ewha University, Seoul 120-750, S. Korea*
(Dated: October 10, 2011)

One of the main signatures of primordial non-Gaussianity of the local type is a scale-dependent correction to the bias of large-scale structure tracers such as galaxies or clusters, whose amplitude depends on the bias of the tracers itself. The dominant source of noise in the power spectrum of the tracers is caused by sampling variance on large scales (where the non-Gaussian signal is strongest) and shot noise arising from their discrete nature. Recent work has argued that one can avoid sampling variance by comparing multiple tracers of different bias, and suppress shot noise by optimally weighting halos of different mass. Here we combine these ideas and investigate how well the signatures of non-Gaussian fluctuations in the primordial potential can be extracted from the two-point correlations of halos and dark matter. On the basis of large $N$-body simulations with local non-Gaussian initial conditions and their halo catalogs we perform a Fisher matrix analysis of the two-point statistics. Compared to the standard analysis, optimal weighting and multiple-tracer techniques applied to halos can yield up to 1 order of magnitude improvements in $f_{\mathrm{NL}}$-constraints, even if the underlying dark matter density field is not known. In this case one needs to resolve all halos down to $10^{10}h^{-1}\mathrm{M}_\odot$ at $z = 0$, while with the dark matter this is already achieved at a mass threshold of $10^{12}h^{-1}\mathrm{M}_\odot$. We compare our numerical results to the halo model and find satisfactory agreement. Forecasting the optimal $f_{\mathrm{NL}}$-constraints that can be achieved with our methods when applied to existing and future survey data, we find that a survey of $50h^{-3}\mathrm{Gpc}^3$ volume resolving all halos down to $10^{11}h^{-1}\mathrm{M}_\odot$ at $z = 1$ will be able to obtain $\sigma_{f_{\mathrm{NL}}} \sim 1$ (68% cl), a factor of $\sim 20$ improvement over the current limits. Decreasing the minimum mass of resolved halos, increasing the survey volume or obtaining the dark matter maps can further improve these limits, potentially reaching the level of $\sigma_{f_{\mathrm{NL}}} \, sim 0.1$. This precision opens up the possibility to distinguish different types of primordial non-Gaussianity and to probe inflationary physics of the very early Universe.

## I. INTRODUCTION

A detection of primordial non-Gaussianity has the potential to test today's standard inflationary paradigm and its alternatives for the physics of the early Universe. Measurements of the CMB bispectrum furnish a direct probe of the nature of the initial conditions (see, e.g., [1–5] and references therein), but are limited by the two-dimensional nature of the CMB and its damping on small scales. However, the non-Gaussian signatures imprinted in the initial fluctuations of the potential gravitationally evolve into the large-scale structure (LSS) of the Universe, which can be observed in all three dimensions and whose statistical properties can be constrained with galaxy clustering data (for recent reviews, see [6, 7]).

One of the cleanest probes is the galaxy (or, more generally, any tracer of LSS including clusters, etc.) two-point correlation function (in configuration space) or power spectrum (in Fourier space), which develops a characteristic scale dependence on large scales in the presence of primordial non-Gaussianity of the local

type [8]. The power spectrum picks up an additional term proportional to $f_{\mathrm{NL}}(b_{\mathrm{G}} - 1)$, where $b_{\mathrm{G}}$ is the Gaussian bias of the tracer and $f_{\mathrm{NL}}$ is a parameter describing the strength of the non-Gaussian signal. However, the precision to which we can constrain $f_{\mathrm{NL}}$ is limited by sampling variance on large scales: each Fourier mode is an independent realization of a (nearly) Gaussian random field, so the ability to determine its rms-amplitude from a finite number of modes is limited. Recent work has demonstrated that it is possible to circumvent sampling variance by comparing two different tracers of the same underlying density field [9–12]. The idea is to take the ratio of power spectra from two tracers to (at least partly) cancel out the random fluctuations, leaving just the signature of primordial non-Gaussianity itself.

Another important limitation arises from the fact that galaxies are discrete tracers of the underlying dark matter distribution. Therefore, with a finite number of observable objects, the measurement of their power spectrum is affected by shot noise. Assuming galaxies are sampled from a Poisson process, this adds a constant contribution to their power spectrum, it is given by the inverse tracer number density $1/\bar{n}$. This is particularly important for massive tracers such as clusters, since their number density is very low. Yet they are strongly biased and there-

fore very sensitive to a potential non-Gaussian signal. Recent work has demonstrated the Poisson shot noise model to be inadequate [13–15]. In particular, [13, 14] have shown that a mass-dependent weighting can considerably suppress the stochasticity between halos and the dark matter and thus reduce the shot noise contribution. In view of constraining primordial non-Gaussianity from LSS, this can be a very helpful tool to further reduce the error on $f_{\rm NL}$.

Both of these methods (sampling variance cancellation and shot noise suppression) have so far been discussed separately in the literature. In this paper we combine the two to derive optimal constraints on $f_{\rm NL}$ that can be achieved from two-point correlations of LSS. We show that dramatic improvements are feasible, but we do not imply that two-point correlations achieve optimal constraints in general: further gains may be possible when considering higher-order correlations, starting with the bispectrum analysis [16] (three-point correlations).

This paper is organized as follows: Sec. II briefly reviews the impact of local primordial non-Gaussianity on the halo bias, and the calculation of the Fisher information content on $f_{\rm NL}$ from two-point statistics in Fourier space is presented in Sec. III. In Sec. IV we apply our weighting and multitracer methods to dark matter halos extracted from a series of large cosmological $N$-body simulations and demonstrate how we can improve the $f_{\rm NL}$-constraints. These results are confronted with the halo model predictions in Sec. V before we finally summarize our findings in Sec. VI.

## II. NON-GAUSSIAN HALO BIAS

Primordial non-Gaussianity of the local type is usually characterized by expanding Bardeen's gauge-invariant potential $\Phi$ about the fiducial Gaussian case. Up to second order, it can be parametrized by the mapping [17–20]

$$\Phi(\mathbf{x}) = \Phi_{\rm G}(\mathbf{x}) + f_{\rm NL}\Phi_{\rm G}^2(\mathbf{x}) \;, \qquad (1)$$

where $\Phi_{\rm G}(\mathbf{x})$ is an isotropic Gaussian random field and $f_{\rm NL}$ a dimensionless phenomenological parameter. Ignoring smoothing (we will consider scales much larger than the Lagrangian size of a halo), the linear density perturbation $\delta_0$ is related to $\Phi$ through the Poisson equation in Fourier space,

$$\delta_0(\mathbf{k}, z) = \frac{2}{3}\frac{k^2 T(k)D(z)c^2}{\Omega_{\rm m}H_0^2}\Phi(\mathbf{k}) \;, \qquad (2)$$

where $T(k)$ is the matter transfer function and $D(z)$ is the linear growth rate normalized to $1 + z$. Applying the peak-background split argument to the Gaussian piece of Bardeen's potential, one finds a scale-dependent correction to the linear halo bias [8, 21, 22]:

$$b(k, f_{\rm NL}) = b_{\rm G} + f_{\rm NL}(b_{\rm G} - 1)u(k, z) \;, \qquad (3)$$

where $b_{\rm G}$ is the scale-independent linear bias parameter of the corresponding Gaussian field ($f_{\rm NL} = 0$) and

$$u(k, z) \equiv \frac{3\delta_{\rm c}\Omega_{\rm m}H_0^2}{k^2 T(k)D(z)c^2} \;. \qquad (4)$$

Here, $\delta_{\rm c} \simeq 1.686$ is the linear critical overdensity for spherical collapse. Corrections to Eq. (3) beyond linear theory have already been worked out and agree reasonably well with numerical simulations [23–26]. Also, the dependence of the halo bias on merger history and halo formation time affects the amplitude of the non-Gaussian corrections in Eq. (3) [22, 27–29], which we will neglect here.

## III. FISHER INFORMATION FROM THE TWO-POINT STATISTICS OF LSS

It is believed that all discrete tracers of LSS, such as galaxies and clusters, reside within dark matter halos, collapsed nonlinear structures that satisfy the conditions for galaxy formation. The analysis of the full complexity of LSS is therefore reduced to the information content in dark matter halos. In this section we introduce our model for the halo covariance matrix and utilize it to compute the Fisher information content on $f_{\rm NL}$ from the two-point statistics of halos and dark matter in Fourier space. We separately consider two cases: first halos only and second halos combined with dark matter. While the observation of halos is relatively easy with present-day galaxy redshift surveys, observing the underlying dark matter is hard, but not impossible: weak-lensing tomography is the leading candidate to achieve that.

### A. Covariance of Halos

#### 1. Definitions

We write the halo overdensity in Fourier space as a vector whose elements correspond to $N$ successive bins

$$\boldsymbol{\delta}_{\rm h} \equiv (\delta_{\rm h_1}, \delta_{\rm h_2}, \ldots, \delta_{\rm h_N})^{\sf T} \;. \qquad (5)$$

In this paper we will only consider a binning in halo mass, but the following equations remain valid for any quantity that the halo density field depends on (e.g., galaxy-luminosity, etc.). The covariance matrix of halos is defined as

$$\mathbf{C}_{\rm h} \equiv \langle \boldsymbol{\delta}_{\rm h}\boldsymbol{\delta}_{\rm h}^{\sf T} \rangle \;, \qquad (6)$$

i.e., the outer product of the vector of halo fields averaged within a $k$-shell in Fourier space. Assuming the halos to be locally biased and stochastic tracers of the dark matter density field $\delta$, we can write

$$\boldsymbol{\delta}_{\rm h} = \boldsymbol{b}\delta + \boldsymbol{\epsilon} \;, \qquad (7)$$

and we define

$$\boldsymbol{b} \equiv \frac{\langle \boldsymbol{\delta}_{\mathrm{h}} \delta \rangle}{\langle \delta^2 \rangle} \qquad (8)$$

as the *effective bias*, which is generally scale-dependent and non-Gaussian. $\boldsymbol{\epsilon}$ is a residual noise-field with zero mean and we assume it to be uncorrelated with the dark matter, i.e., $\langle \boldsymbol{\epsilon} \delta \rangle = 0$ [30].

In each mass bin, the effective bias $\boldsymbol{b}$ shows a distinct dependence on $f_{\mathrm{NL}}$. In what follows, we will assume that $\boldsymbol{b}$ is linear in $f_{\mathrm{NL}}$, as suggested by Eq. (3):

$$\boldsymbol{b}(k, f_{\mathrm{NL}}) = \boldsymbol{b}_{\mathrm{G}} + f_{\mathrm{NL}} \boldsymbol{b}'(k) . \qquad (9)$$

Here, $\boldsymbol{b}_{\mathrm{G}}$ is the Gaussian effective bias and $\boldsymbol{b}' \equiv \partial \boldsymbol{b} / \partial f_{\mathrm{NL}}$. Finally, we write $P \equiv \langle \delta^2 \rangle$ for the nonlinear dark matter power spectrum and assume $\partial P / \partial f_{\mathrm{NL}} = 0$. This is a good approximation on large scales [31–33]. Thus, the model from Eq. (7) yields the following halo covariance matrix:

$$\mathbf{C}_{\mathrm{h}} = \boldsymbol{b} \boldsymbol{b}^{\mathsf{T}} P + \boldsymbol{\mathcal{E}} , \qquad (10)$$

where the *shot noise matrix* $\boldsymbol{\mathcal{E}}$ was defined as

$$\boldsymbol{\mathcal{E}} \equiv \langle \boldsymbol{\epsilon} \boldsymbol{\epsilon}^{\mathsf{T}} \rangle . \qquad (11)$$

In principle, $\boldsymbol{\mathcal{E}}$ can contain other components than pure Poisson noise, for instance higher-order terms from the bias expansion [34–36]. Here and henceforth, we will define $\boldsymbol{\mathcal{E}}$ as the residual from the effective bias term $\boldsymbol{b} \boldsymbol{b}^{\mathsf{T}} P$ in $\mathbf{C}_{\mathrm{h}}$, and allow it to depend on $f_{\mathrm{NL}}$. Thus, with Eqs. (8) and (10) the shot noise matrix can be written as

$$\boldsymbol{\mathcal{E}} = \langle \boldsymbol{\delta}_{\mathrm{h}} \boldsymbol{\delta}_{\mathrm{h}}^{\mathsf{T}} \rangle - \frac{\langle \boldsymbol{\delta}_{\mathrm{h}} \delta \rangle \langle \boldsymbol{\delta}_{\mathrm{h}}^{\mathsf{T}} \delta \rangle}{\langle \delta^2 \rangle} . \qquad (12)$$

This agrees precisely with the definition given in [14] for the Gaussian case, however it also takes into account the possibility of a scale-dependent effective bias in non-Gaussian scenarios, such that the effective bias term $\boldsymbol{b} \boldsymbol{b}^{\mathsf{T}} P$ always cancels in this expression [37].

Reference [10] already investigated the Fisher information content on primordial non-Gaussianity for the idealized case of a purely Poissonian shot noise component in the halo covariance matrix. In [15], the halo covariance was suggested to be of a similar simple form, albeit with a modified definition of halo bias and a diagonal shot noise matrix. In this work we will consider the more general model of Eq. (10) without assuming anything about $\boldsymbol{\mathcal{E}}$. Instead we will investigate the shot noise matrix with the help of $N$-body simulations.

The Gaussian case has already been studied in [14]. Simulations revealed a very simple eigenstructure of the shot noise matrix: for $N > 2$ mass bins of equal number density $\bar{n}$ it exhibits a $(N - 2)$-dimensional degenerate subspace with eigenvalue $\lambda_{\mathrm{P}}^{(N-2)} = 1/\bar{n}$, which is the

expected result from Poisson sampling. Of the two remaining eigenvalues $\lambda_{\pm}$, one is enhanced $(\lambda_{+})$ and one suppressed $(\lambda_{-})$ with respect to the value $1/\bar{n}$. The shot noise matrix can thus be written as

$$\boldsymbol{\mathcal{E}} = \bar{n}^{-1} \mathbf{I} + (\lambda_{+} - \bar{n}^{-1}) \boldsymbol{V}_{+} \boldsymbol{V}_{+}^{\mathsf{T}} + (\lambda_{-} - \bar{n}^{-1}) \boldsymbol{V}_{-} \boldsymbol{V}_{-}^{\mathsf{T}} , \quad (13)$$

where $\mathbf{I}$ is the $N \times N$ identity matrix and $\boldsymbol{V}_{\pm}$ are the normalized eigenvectors corresponding to $\lambda_{\pm}$. Its inverse takes a very similar form

$$\boldsymbol{\mathcal{E}}^{-1} = \bar{n} \mathbf{I} + (\lambda_{+}^{-1} - \bar{n}) \boldsymbol{V}_{+} \boldsymbol{V}_{+}^{\mathsf{T}} + (\lambda_{-}^{-1} - \bar{n}) \boldsymbol{V}_{-} \boldsymbol{V}_{-}^{\mathsf{T}} . \quad (14)$$

The halo model [38] can be applied to predict the functional form of $\lambda_{\pm}$ and $\boldsymbol{V}_{\pm}$ (see [14] and Sec. V). This approach is however not expected to be exact, as it does not ensure mass- and momentum conservation of the dark matter density field and leads to white-noise-like contributions in both the halo-matter cross and the matter auto power spectra which are not observed in simulations [39]. Yet, the halo model is able to reproduce the eigenstructure of $\boldsymbol{\mathcal{E}}$ fairly well [14] and we will use it for making predictions beyond our $N$-body resolution limit.

In the Gaussian case one can also relate the dominant eigenmode $\boldsymbol{V}_{+}$ with corresponding eigenvalue $\lambda_{+}$ to the second-order term arising in a local bias-expansion model [34, 35], where the coefficients $\boldsymbol{b}_i$ are determined analytically from the peak-background split formalism given a halo mass function [40, 41]. In non-Gaussian scenarios this can be extended to a multivariate expansion in dark matter density $\delta$ and primordial potential $\Phi$ including bias coefficients for both fields [16, 23]. For the calculation of $\boldsymbol{\mathcal{E}}$ we will however restrict ourselves to the Gaussian case and later compare with the numerical results of non-Gaussian initial conditions to see the effects of $f_{\mathrm{NL}}$ on $\boldsymbol{\mathcal{E}}$ and its eigenvalues. The suppressed eigenmode $\boldsymbol{V}_{-}$ with eigenvalue $\lambda_{-}$ can also be explained by a halo-exclusion correction to the Poisson-sampling model for halos, as studied in [33].

In what follows, we will truncate the local bias expansion at second order. Therefore, we shall assume the following model for the halo overdensity in configuration space

$$\boldsymbol{\delta}_{\mathrm{h}}(\mathbf{x}) = \boldsymbol{b}_1 \delta(\mathbf{x}) + \boldsymbol{b}_2 \delta^2(\mathbf{x}) + \boldsymbol{n}_{\mathrm{P}}(\mathbf{x}) + \boldsymbol{n}_{\mathrm{c}}(\mathbf{x}) . \qquad (15)$$

Here, $\boldsymbol{n}_{\mathrm{P}}$ is the usual Poisson noise and $\boldsymbol{n}_{\mathrm{c}}$ a correction to account for deviations from the Poisson-sampling model. In Fourier space, this yields

$$\boldsymbol{\delta}_{\mathrm{h}}(\mathbf{k}) = \boldsymbol{b}_1 \delta(\mathbf{k}) + \boldsymbol{b}_2 (\delta * \delta)(\mathbf{k}) + \boldsymbol{n}_{\mathrm{P}}(\mathbf{k}) + \boldsymbol{n}_{\mathrm{c}}(\mathbf{k}) , \quad (16)$$

where the asterisk-symbol denotes a convolution. The Poisson noise $\boldsymbol{n}_{\mathrm{P}}$ arises from a discrete sampling of the field $\boldsymbol{\delta}_{\mathrm{h}}$ with a finite number of halos, it is uncorrelated with the underlying dark matter density, $\langle \boldsymbol{n}_{\mathrm{P}} \delta \rangle = 0$, and its power spectrum is $\langle \boldsymbol{n}_{\mathrm{P}} \boldsymbol{n}_{\mathrm{P}}^{\mathsf{T}} \rangle = 1/\bar{n}$ (Poisson white

noise). We further assume $\langle \boldsymbol{n}_{\mathrm{P}} \boldsymbol{n}_{\mathrm{c}}^{\mathsf{T}} \rangle = \langle \boldsymbol{n}_{\mathrm{c}} \delta \rangle = 0$, which leads to

$$\boldsymbol{b} = \boldsymbol{b}_1 + \boldsymbol{b}_2 \frac{\langle (\delta * \delta) \, \delta \rangle}{\langle \delta^2 \rangle} \, , \qquad (17)$$

$$\begin{aligned} \mathbf{C}_{\mathrm{h}} &= \boldsymbol{b}_1 \boldsymbol{b}_1^{\mathsf{T}} \langle \delta^2 \rangle + (\boldsymbol{b}_1 \boldsymbol{b}_2^{\mathsf{T}} + \boldsymbol{b}_2 \boldsymbol{b}_1^{\mathsf{T}}) \langle (\delta * \delta) \, \delta \rangle \\ &\quad + \boldsymbol{b}_2 \boldsymbol{b}_2^{\mathsf{T}} \langle (\delta * \delta)^2 \rangle + \langle \boldsymbol{n}_{\mathrm{P}} \boldsymbol{n}_{\mathrm{P}}^{\mathsf{T}} \rangle + \langle \boldsymbol{n}_{\mathrm{c}} \boldsymbol{n}_{\mathrm{c}}^{\mathsf{T}} \rangle \, , \qquad (18) \end{aligned}$$

$$\boldsymbol{\mathcal{E}} = \bar{n}^{-1} \mathbf{I} + \boldsymbol{b}_2 \boldsymbol{b}_2^{\mathsf{T}} \left[ \langle (\delta * \delta)^2 \rangle - \frac{\langle (\delta * \delta) \, \delta \rangle^2}{\langle \delta^2 \rangle} \right] + \langle \boldsymbol{n}_{\mathrm{c}} \boldsymbol{n}_{\mathrm{c}}^{\mathsf{T}} \rangle \, . \qquad (19)$$

Hence, we can identify the normalized vector $\boldsymbol{b}_2 / |\boldsymbol{b}_2|$ with the eigenvector $\boldsymbol{V}_+$ of Eq. (13) with corresponding eigenvalue

$$\lambda_+ = \boldsymbol{b}_2^{\mathsf{T}} \boldsymbol{b}_2 \mathcal{E}_{\delta^2} + \bar{n}^{-1} \, , \qquad (20)$$

where we define

$$\mathcal{E}_{\delta^2} \equiv \langle (\delta * \delta)^2 \rangle - \frac{\langle (\delta * \delta) \, \delta \rangle^2}{\langle \delta^2 \rangle} \, . \qquad (21)$$

In [36] this term is absorbed into an effective shot noise power, since it behaves like white noise on large scales and arises from the peaks and troughs in the dark matter density field being nonlinearly biased by the $b_2$-term [42]. We evaluated $\mathcal{E}_{\delta^2}$ along with the expressions that appear in Eq. (21) with the help of our dark matter $N$-body simulations for Gaussian and non-Gaussian initial conditions (for details about the simulations, see Sec. IV).

The results are depicted in Fig. 1. $\mathcal{E}_{\delta^2}$ obviously shows a slight dependence on $f_{\mathrm{NL}}$, but it remains white-noise-like even in the non-Gaussian cases. The $f_{\mathrm{NL}}$-dependence of this term has not been discussed in the literature yet, but it can have a significant impact on the power spectrum of high-mass halos which have a large $b_2$-term; see Eq. (20). A discussion of the numerical results for halos, specifically the $f_{\mathrm{NL}}$-dependence of $\lambda_+$, is conducted later in this paper. It is also worth noticing the $f_{\mathrm{NL}}$-dependence of $\langle (\delta * \delta)^2 \rangle$ and $\langle (\delta * \delta) \, \delta \rangle$. The properties of the squared dark matter field $\delta^2(\mathbf{x})$ are similar to the ones of halos, namely, the $k^{-2}$-correction of the effective bias in Fourier space, which in this case is defined as $b_{\delta^2} \equiv \langle (\delta * \delta) \, \delta \rangle / \langle \delta^2 \rangle$ and appears in Eq. (17).

The last term in Eq. (19) corresponds to the suppressed eigenmode of the shot noise matrix. Both its eigenvector and eigenvalue can be described reasonably well by the halo model [14]. The argument of [33] based on halo exclusion yields a similar result while providing a more intuitive explanation for the occurrence of such a term.

### 2. Likelihood and Fisher information

In order to find the *best unbiased estimator* for $f_{\mathrm{NL}}$, we have to maximize the likelihood function. Although
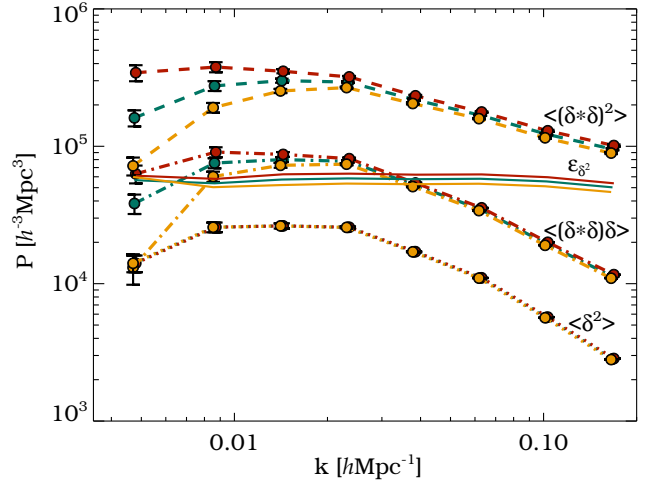


FIG. 1. Shot noise $\mathcal{E}_{\delta^2}$ of the squared dark matter density field $\delta^2$ as defined in Eq. (21) with both Gaussian (solid green) and non-Gaussian initial conditions with $f_{\mathrm{NL}} = +100$ (solid red) and $f_{\mathrm{NL}} = -100$ (solid yellow) from $N$-body simulations at $z = 0$. Clearly, $\mathcal{E}_{\delta^2}$ is close to white-noise like in all three cases. The auto power spectrum $\langle (\delta * \delta)^2 \rangle$ of $\delta^2$ in Fourier space (dashed), its cross power spectrum $\langle (\delta * \delta) \, \delta \rangle$ with the ordinary dark matter field $\delta$ (dot-dashed), as well as the ordinary dark matter power spectrum $\langle \delta^2 \rangle$ (dotted) are overplotted for the corresponding values of $f_{\mathrm{NL}}$. The squared dark matter field $\delta^2$ can be interpreted as a biased tracer of $\delta$ and therefore shows the characteristic $f_{\mathrm{NL}}$-dependence of biased fields (like halos) on large scales.

we are dealing with non-Gaussian statistics of the density field, deviations from the Gaussian case are usually small in practical applications (e.g., [22, 43, 44]), so we will consider a multivariate Gaussian likelihood

$$\mathscr{L} = \frac{1}{(2\pi)^{N/2} \sqrt{\det \mathbf{C}_{\mathrm{h}}}} \exp \left( -\frac{1}{2} \boldsymbol{\delta}_{\mathrm{h}}^{\mathsf{T}} \mathbf{C}_{\mathrm{h}}^{-1} \boldsymbol{\delta}_{\mathrm{h}} \right) \, . \qquad (22)$$

Maximizing this likelihood function is equivalent to minimizing the following chi-square,

$$\chi^2 = \boldsymbol{\delta}_{\mathrm{h}}^{\mathsf{T}} \mathbf{C}_{\mathrm{h}}^{-1} \boldsymbol{\delta}_{\mathrm{h}} + \ln (1 + \alpha) + \ln (\det \boldsymbol{\mathcal{E}}) \, , \qquad (23)$$

where we dropped the irrelevant constant $N \ln(2\pi)$ and used

$$\det \mathbf{C}_{\mathrm{h}} = \det \left( \boldsymbol{b} \boldsymbol{b}^{\mathsf{T}} P + \boldsymbol{\mathcal{E}} \right) = (1 + \alpha) \det \boldsymbol{\mathcal{E}} \, , \qquad (24)$$

with $\alpha \equiv \boldsymbol{b}^{\mathsf{T}} \boldsymbol{\mathcal{E}}^{-1} \boldsymbol{b} P$. For a single mass bin, Eq. (23) simplifies to

$$\chi^2 = \frac{\delta_{\mathrm{h}}^2}{b^2 P + \mathcal{E}} + \ln \left( b^2 P + \mathcal{E} \right) \, . \qquad (25)$$

The Fisher information matrix [45] for the parameters $\theta_i$ and $\theta_j$ and the random variable $\boldsymbol{\delta}_{\mathrm{h}}$ with covariance $\mathbf{C}_{\mathrm{h}}$,

as derived from a multivariate Gaussian likelihood [46, 47], reads

$$F_{ij} \equiv \frac{1}{2}\mathrm{Tr}\left(\frac{\partial \mathbf{C}_\mathrm{h}}{\partial \theta_i}\mathbf{C}_\mathrm{h}^{-1}\frac{\partial \mathbf{C}_\mathrm{h}}{\partial \theta_j}\mathbf{C}_\mathrm{h}^{-1}\right) . \qquad (26)$$

With the above assumptions, the derivative of the halo covariance matrix with respect to the parameter $f_\mathrm{NL}$ is

$$\frac{\partial \mathbf{C}_\mathrm{h}}{\partial f_\mathrm{NL}} = \left(\boldsymbol{b}\boldsymbol{b}'^\mathsf{T} + \boldsymbol{b}'\boldsymbol{b}^\mathsf{T}\right)P + \boldsymbol{\mathcal{E}}' , \qquad (27)$$

with $\boldsymbol{\mathcal{E}}' \equiv \partial \boldsymbol{\mathcal{E}}/\partial f_\mathrm{NL}$. The inverse of the covariance matrix can be obtained by applying the *Sherman-Morrison* formula [48, 49]

$$\mathbf{C}_\mathrm{h}^{-1} = \boldsymbol{\mathcal{E}}^{-1} - \frac{\boldsymbol{\mathcal{E}}^{-1}\boldsymbol{b}\boldsymbol{b}^\mathsf{T}\boldsymbol{\mathcal{E}}^{-1}P}{1+\alpha} , \qquad (28)$$

where again $\alpha \equiv \boldsymbol{b}^\mathsf{T}\boldsymbol{\mathcal{E}}^{-1}\boldsymbol{b}P$. On inserting the two previous relations into Eq. (26), we eventually obtain the full expression for $F_{f_\mathrm{NL}f_\mathrm{NL}}$ in terms of $\boldsymbol{b}$, $\boldsymbol{b}'$, $\boldsymbol{\mathcal{E}}$, $\boldsymbol{\mathcal{E}}'$ and $P$ (see Appendix A for the derivation of Eq. (A11)). Neglecting the $f_\mathrm{NL}$-dependence of $\boldsymbol{\mathcal{E}}$, i.e., setting $\boldsymbol{\mathcal{E}}' \equiv 0$, the Fisher information on $f_\mathrm{NL}$ becomes

$$F_{f_\mathrm{NL}f_\mathrm{NL}} = \frac{\alpha\gamma + \beta^2 + \alpha\left(\alpha\gamma - \beta^2\right)}{(1+\alpha)^2} , \qquad (29)$$

with $\alpha \equiv \boldsymbol{b}^\mathsf{T}\boldsymbol{\mathcal{E}}^{-1}\boldsymbol{b}P$, $\beta \equiv \boldsymbol{b}^\mathsf{T}\boldsymbol{\mathcal{E}}^{-1}\boldsymbol{b}'P$ and $\gamma \equiv \boldsymbol{b}'^\mathsf{T}\boldsymbol{\mathcal{E}}^{-1}\boldsymbol{b}'P$. For a single mass bin, Eq. (A11) simplifies to Eq. (A12),

$$F_{f_\mathrm{NL}f_\mathrm{NL}} = 2\left(\frac{bb'P + \mathcal{E}'/2}{b^2P + \mathcal{E}}\right)^2 . \qquad (30)$$

This implies that even in the limit of a very well-sampled halo density field ($\bar{n} \to \infty$) with negligible shot noise power $\mathcal{E}$ (and neglecting $\mathcal{E}'$) the Fisher information content on $f_\mathrm{NL}$ that can be extracted per mode from a single halo mass bin is limited to the value $2\left(b'/b\right)^2$. This is due to the fact that we can only constrain $f_\mathrm{NL}$ from a change in the halo bias relative to the Gaussian expectation, not from a measurement of the effective bias itself. The latter can only be measured directly if one knows the dark matter distribution, as will be shown in the subsequent paragraph. However, the situation changes for several halo mass bins (multiple tracers as in [9]). In this case, the Fisher information content from Eqs. (A11) and (29) can exceed the value $2\left(b'/b\right)^2$ (see Sec. IV and V).

### B. Covariance of Halos and Dark Matter

#### 1. Definitions

We will now assume that we possess knowledge about the dark matter distribution in addition to the halo density field. In practice one may be able to achieve this by

combining galaxy redshift surveys with lensing tomography [50], but the prospects are somewhat uncertain. We will simply add the dark matter overdensity mode $\delta$ to the halo overdensity vector $\boldsymbol{\delta}_\mathrm{h}$, defining a new vector

$$\boldsymbol{\delta} \equiv (\delta, \delta_{\mathrm{h}_1}, \delta_{\mathrm{h}_2}, \ldots, \delta_{\mathrm{h}_N})^\mathsf{T} . \qquad (31)$$

In analogy with the previous section, we define the covariance matrix as $\mathbf{C} \equiv \langle\boldsymbol{\delta}\boldsymbol{\delta}^\mathsf{T}\rangle$ and write

$$\mathbf{C} = \begin{pmatrix} \langle\delta^2\rangle & \langle\boldsymbol{\delta}_\mathrm{h}^\mathsf{T}\delta\rangle \\ \langle\boldsymbol{\delta}_\mathrm{h}\delta\rangle & \langle\boldsymbol{\delta}_\mathrm{h}\boldsymbol{\delta}_\mathrm{h}^\mathsf{T}\rangle \end{pmatrix} = \begin{pmatrix} P & \boldsymbol{b}^\mathsf{T}P \\ \boldsymbol{b}P & \mathbf{C}_\mathrm{h} \end{pmatrix} . \qquad (32)$$

#### 2. Likelihood and Fisher information

Upon inserting the new covariance matrix into the Gaussian likelihood as defined in Eq. (22), we find the chi-square to be

$$\chi^2 = \boldsymbol{\delta}^\mathsf{T}\mathbf{C}^{-1}\boldsymbol{\delta} + \ln\left(\det\boldsymbol{\mathcal{E}}\right) , \qquad (33)$$

where we used

$$\det\mathbf{C} = \det\mathbf{C}_\mathrm{h}\det\left(P - \boldsymbol{b}^\mathsf{T}\mathbf{C}_\mathrm{h}^{-1}\boldsymbol{b}P^2\right) = P\det\boldsymbol{\mathcal{E}} , \quad (34)$$

and we still assume $P$ to be independent of $f_\mathrm{NL}$ and therefore drop the term $\ln\left(P\right)$ in Eq. (33). In terms of the halo and dark matter overdensities, the chi-square can also be expressed as

$$\chi^2 = \left(\boldsymbol{\delta}_\mathrm{h} - \boldsymbol{b}\delta\right)^\mathsf{T}\boldsymbol{\mathcal{E}}^{-1}\left(\boldsymbol{\delta}_\mathrm{h} - \boldsymbol{b}\delta\right) + \ln\left(\det\boldsymbol{\mathcal{E}}\right) , \qquad (35)$$

which is equivalent to the definition in [14] (where the last term was neglected). The corresponding expression for a single halo mass bin reads

$$\chi^2 = \frac{(\delta_\mathrm{h} - b\delta)^2}{\mathcal{E}} + \ln\left(\mathcal{E}\right) . \qquad (36)$$

For the derivative of $\mathbf{C}$ with respect to $f_\mathrm{NL}$ we get

$$\frac{\partial \mathbf{C}}{\partial f_\mathrm{NL}} = \begin{pmatrix} 0 & \boldsymbol{b}'^\mathsf{T}P \\ \boldsymbol{b}'P & \boldsymbol{b}\boldsymbol{b}'^\mathsf{T}P + \boldsymbol{b}'\boldsymbol{b}^\mathsf{T}P + \boldsymbol{\mathcal{E}}' \end{pmatrix} . \qquad (37)$$

Performing a block inversion, we readily obtain the inverse covariance matrix,

$$\mathbf{C}^{-1} = \begin{pmatrix} (1+\alpha)P^{-1} & -\boldsymbol{b}^\mathsf{T}\boldsymbol{\mathcal{E}}^{-1} \\ -\boldsymbol{\mathcal{E}}^{-1}\boldsymbol{b} & \boldsymbol{\mathcal{E}}^{-1} \end{pmatrix} . \qquad (38)$$

As shown in Appendix B, the Fisher information content on $f_\mathrm{NL}$ now becomes

$$F_{f_\mathrm{NL}f_\mathrm{NL}} = \gamma + \tau , \qquad (39)$$

with $\gamma \equiv \boldsymbol{b}'^\mathsf{T}\boldsymbol{\mathcal{E}}^{-1}\boldsymbol{b}'P$ and $\tau \equiv \frac{1}{2}\mathrm{Tr}\left(\boldsymbol{\mathcal{E}}'\boldsymbol{\mathcal{E}}^{-1}\boldsymbol{\mathcal{E}}'\boldsymbol{\mathcal{E}}^{-1}\right)$. For a single halo mass bin this further simplifies to

$$F_{f_\mathrm{NL}f_\mathrm{NL}} = \frac{b'^2P}{\mathcal{E}} + \frac{1}{2}\left(\frac{\mathcal{E}'}{\mathcal{E}}\right)^2 . \qquad (40)$$

It is worth noting that, in contrast to Eq. (30), the Fisher information from one halo mass bin with knowledge of the dark matter becomes infinite in the limit of vanishing $\mathcal{E}$. In this limit the effective bias can indeed be determined exactly, allowing an exact measurement of $f_{\rm NL}$ [9].

## IV. APPLICATION TO N-BODY SIMULATIONS

We employ numerical $N$-body simulations with both Gaussian and non-Gaussian initial conditions to find signatures of primordial non-Gaussianity in the two-point statistics of the final density fields in Fourier space. More precisely, we consider an ensemble of 12 realizations of box-size $1.6h^{-1}{\rm Gpc}$ (this yields a total effective volume of $V_{\rm eff} \simeq 50h^{-3}{\rm Gpc}^3$). Each realization is seeded with both Gaussian ($f_{\rm NL} = 0$) and non-Gaussian ($f_{\rm NL} = \pm100$) initial conditions of the local type [31], and evolves $1024^3$ particles of mass $3.0 \times 10^{11}h^{-1}{\rm M}_\odot$. The cosmological parameters are $\Omega_{\rm m} = 0.279$, $\Omega_\Lambda = 0.721$, $\Omega_{\rm b} = 0.046$, $\sigma_8 = 0.81$, $n_{\rm s} = 0.96$, and $h = 0.7$, consistent with the WMAP5 [51] best-fit constraint. Additionally, we consider one realization with each $f_{\rm NL} = 0, \pm50$ of box-size $1.3h^{-1}{\rm Gpc}$ with $1536^3$ particles of mass $4.7 \times 10^{10}h^{-1}{\rm M}_\odot$ to assess a higher-resolution regime. The simulations were performed on the supercomputer ZBOX3 at the University of Zürich with the GADGET II code [52]. The initial conditions were laid down at redshift $z = 100$ by perturbing a uniform mesh of particles with the Zel'dovich approximation.

To generate halo catalogs, we employ a friends-of-friends (FOF) algorithm [53] with a linking length equal to 20% of the mean interparticle distance. For comparison, we also generate halo catalogs using the AHF halo finder developed by [54], which is based on the spherical overdensity (SO) method [55]. In this case, we assume an overdensity threshold $\Delta_{\rm c}(z)$ being a decreasing function of redshift, as dictated by the solution to the spherical collapse of a tophat perturbation in a $\Lambda$CDM Universe [56]. In both cases, we require a minimum of 20 particles per halo, which corresponds to a minimum halo mass $M_{\rm min} \simeq 5.9 \times 10^{12}h^{-1}{\rm M}_\odot$ for the simulations with $1024^3$ particles. For Gaussian initial conditions the resulting total number density of halos is $\bar{n} \simeq 7.0 \times 10^{-4}h^3{\rm Mpc}^{-3}$ and $4.2 \times 10^{-4}h^3{\rm Mpc}^{-3}$ for the FOF and SO catalogs, respectively. Note that the FOF mass estimate is on average 20% higher than the SO mass estimate. For our $1536^3$-particles simulation we obtain $M_{\rm min} \simeq 9.4 \times 10^{11}h^{-1}{\rm M}_\odot$ and $\bar{n} \simeq 4.0 \times 10^{-3}h^3{\rm Mpc}^{-3}$ resulting from the FOF halo finder.

The binning of the halo density field into $N$ consecutive mass bins is done by sorting all halos by increasing mass and dividing this ordered array into $N$ bins with an equal number of halos. The halos of each bin $i \in [1 \dots N]$ are selected separately to construct the halo density field $\delta_{\rm h_i}$. The density fields of dark matter and halos are first com-

puted in configuration space via interpolation of the particles onto a cubical mesh with $512^3$ grid points using a cloud-in-cell mesh assignment algorithm [57]. We then perform a fast fourier transform to compute the modes of the fields in $k$-space.

For each of our Gaussian and non-Gaussian realizations, we match the total number of halos to the one realization with the least amount of them by discarding halos from the low-mass end. This *abundance matching* technique ensures that we eliminate any possible signature of primordial non-Gaussianity induced by the unobservable $f_{\rm NL}$-dependence of the halo mass function. It guarantees a constant value $1/\bar{n}$ of the Poisson noise for both Gaussian and non-Gaussian realizations. A dependence of the Poisson noise on $f_{\rm NL}$ would complicate the interpretation of the Fisher information content. Note also that, in order to calculate the derivative of a function $\mathcal{F}$ with respect to $f_{\rm NL}$, we apply the linear approximation

$$\frac{\partial \mathcal{F}}{\partial f_{\rm NL}} \simeq \frac{\mathcal{F}(f_{\rm NL} = +100) - \mathcal{F}(f_{\rm NL} = -100)}{2 \times 100} , \quad (41)$$

which exploits the statistics of all our non-Gaussian runs. All the error bars quoted in this paper are computed from the variance amongst our 12 realizations.

### A. Effective bias and shot noise

At the two-point level and in Fourier space, the clustering of halos as described by Eq. (10) is determined by two basic components: effective bias and shot noise. Since the impact of primordial non-Gaussianity on the nonlinear dark matter power spectrum $P$ is negligible on large scales (see Fig. 1), the dependence of both $\boldsymbol{b}$ and $\boldsymbol{\mathcal{E}}$ on $f_{\rm NL}$ must be known if one wishes to constrain the latter. In the following sections, we will examine this dependence in our series of $N$-body simulations.

#### 1. Effective bias

In the top left panel of Fig. 2, the effective bias $\boldsymbol{b}$ in the fiducial Gaussian case ($f_{\rm NL} = 0$) is shown for 30 consecutive FOF halo mass bins as a function of wave number. In the large-scale limit $k \to 0$, the measurements are consistent with being scale-independent, as indicated by the dotted lines which show the average of $\boldsymbol{b}(k, f_{\rm NL} = 0)$ over all modes with $k \leq 0.032h{\rm Mpc}^{-1}$, denoted $\boldsymbol{b}_{\rm G}$. At larger wave numbers, the deviations can be attributed to higher-order bias terms, which are most important at high mass. Relative to the low-$k$ averaged, scale-independent Gaussian bias $\boldsymbol{b}_{\rm G}$, these corrections tend to suppress the effective bias at low mass, whereas they increase it at the very high-mass end (see Eq. (17)). The right panel of Fig. 2 shows the large-scale average $\boldsymbol{b}_{\rm G}$ as a function of halo mass, as determined
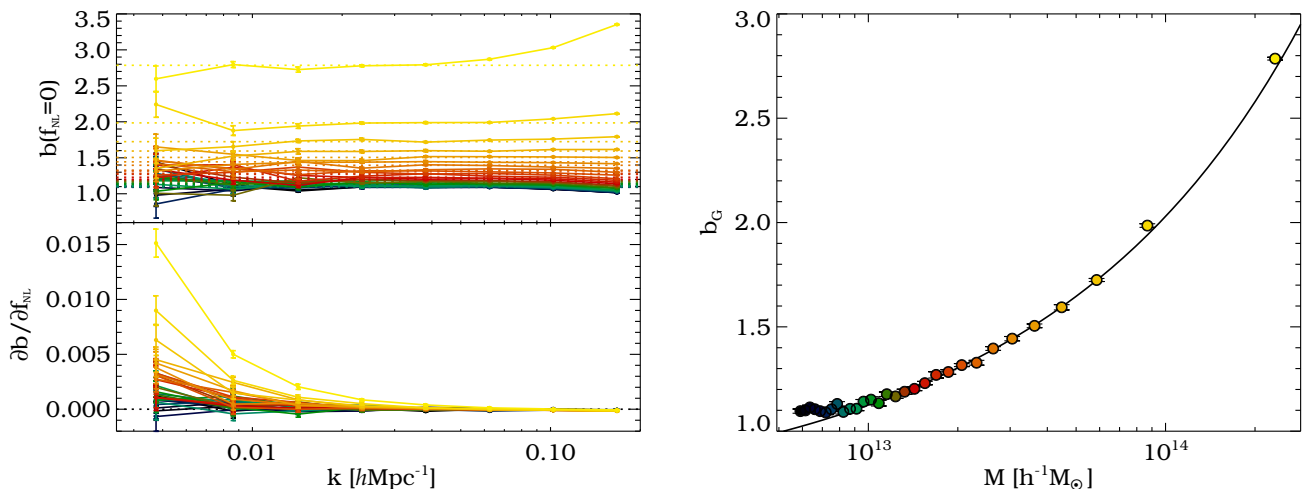
FIG. 2. LEFT: Gaussian effective bias (top) and its derivative with respect to $f_{\rm NL}$ (bottom) for the case of 30 mass bins. The scale-independent part $\boldsymbol{b}_{\rm G}$ is plotted in dotted lines for each bin; it was obtained by averaging all modes with $k \leq 0.032h{\rm Mpc}^{-1}$. RIGHT: Large-scale averaged Gaussian effective bias $\boldsymbol{b}_{\rm G}$ from the left panel (dotted lines) plotted against mean halo mass. The solid line depicts the linear-order bias derived from the peak-background split formalism. All error bars are obtained from the variance of our 12 boxes to their mean. Results are shown for FOF halos at $z = 0$.

from 30 halo mass bins, each with a number density of $\bar{n} \simeq 2.3 \times 10^{-5}h^3{\rm Mpc}^{-3}$. The solid line is the linear-order bias as derived from the peak-background split formalism [40, 41]. We find a good agreement with our $N$-body data, only at masses below $\sim 8 \times 10^{12}h^{-1}{\rm M}_\odot$ deviations appear for halos with less than $\sim 30$ particles [58].

The bottom left panel of Fig. 2 depicts the derivative of $\boldsymbol{b}$ with respect to $f_{\rm NL}$ for each of the 30 mass bins. The behavior is well described by the linear theory prediction of Eq. (3), leading to a $k^{-2}$-dependence on large scales which is more pronounced for more massive halos (for quantitative comparisons with simulations, see [31, 32, 59]). Thus, the amplitude of this effect gradually diminishes towards smaller scales and even disappears around $k \sim 0.1h{\rm Mpc}^{-1}$. Note that [31] argued for an additional non-Gaussian bias correction which follows from the $f_{\rm NL}$-dependence of the mass function. This $k$-independent contribution should in principle be included in Eq. (3). However, as can be seen in the lower left plot, it is negligible in our approach (i.e., all curves approach zero at high $k$) owing to the matching of halo abundances between our Gaussian and non-Gaussian realizations.

### 2. Shot noise matrix

The shot noise matrix $\boldsymbol{\mathcal{E}}$ has been studied using simulations with Gaussian initial conditions in [14]. Figure 3 displays the eigenstructure of this matrix for $f_{\rm NL} = 0$ (solid curves) and $f_{\rm NL} = \pm 100$ (dashed and dotted curves). The left panel depicts all the eigenvalues (top) and their derivatives with respect to $f_{\rm NL}$ (bottom), while

the right panel shows the two important eigenvectors $\boldsymbol{V}_+$ and $\boldsymbol{V}_-$ (top) along with their derivatives (bottom). The eigenstructure of $\boldsymbol{\mathcal{E}}$ is accurately described by Eq. (13), even in the non-Gaussian case. Namely, we still find one enhanced eigenvalue $\lambda_+$ and one suppressed eigenvalue $\lambda_-$. The remaining $N - 2$ eigenvalues $\lambda_{\rm P}^{(N-2)}$ are degenerate with the value $1/\bar{n}$, the Poisson noise expectation. This means that our Gaussian bias-expansion model from Eq. (16) still works to describe $\boldsymbol{\mathcal{E}}$ in the weakly non-Gaussian regime.

Note however that, owing to sampling variance, the decomposition into eigenmodes becomes increasingly noisy towards larger scales. This leads to an artificial breaking of the eigenvalue degeneracy which manifests itself as a scatter around the mean value $1/\bar{n}$. This scatter is the major contribution of sampling variance in the halo covariance matrix $\mathbf{C}_{\rm h}$. Although we can eliminate most of it by setting $\lambda_{\rm P}^{(N-2)} \equiv 1/\bar{n}$, a residual degree of sampling variance will remain in $\lambda_+$ and $\lambda_-$, as well as in $\boldsymbol{b}$ and $P$.

As is apparent from the left panel in Fig. 3, the dominant eigenvalue $\lambda_+$ exhibits a small, but noticeable $f_{\rm NL}$-dependence similar to that of $\mathcal{E}_{\delta^2}$ in Fig. 1, which is about 2% in this case. Its derivative, $\partial\lambda_+/\partial f_{\rm NL}$, clearly dominates the derivative of all other eigenvalues (which are all consistent with zero due to matched abundances). Only the derivative of the suppressed eigenvalue $\lambda_-$ shows a similar $f_{\rm NL}$-dependence of $\sim 2\%$, albeit at a much lower absolute amplitude. To check the convergence of our results, we repeated the analysis with 100 and 200 bins and found both derivatives of $\lambda_+$ and $\lambda_-$ to increase, supporting an $f_{\rm NL}$-dependence of these eigenvalues.

By contrast, the eigenvectors $\boldsymbol{V}_+$ and $\boldsymbol{V}_-$ shown in
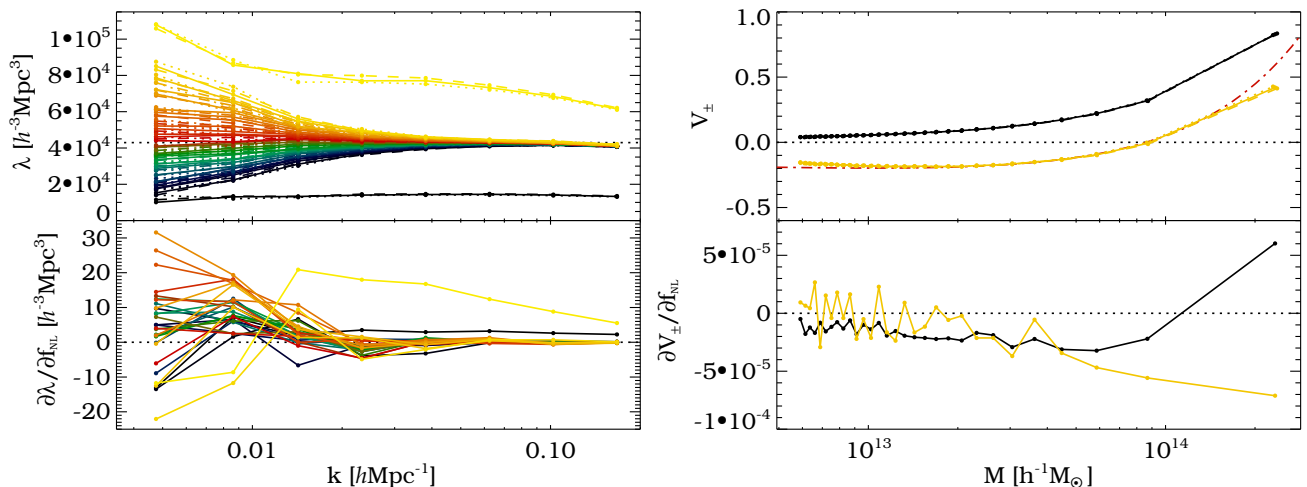
FIG. 3. Eigenvalues (left panel) and eigenvectors (right panel) of the shot noise matrix $\boldsymbol{\mathcal{E}}$ for $f_{\mathrm{NL}} = 0$ (solid), $+100$ (dashed) and $-100$ (dotted) in the case of 30 mass bins. Their derivatives with respect to $f_{\mathrm{NL}}$ are plotted underneath. For clarity, only the two eigenvectors $\boldsymbol{V}_{\pm}$ along with their derivatives are shown in the right panel. The straight dotted line in the upper left panel depicts the value $1/\bar{n}$ and the red (dot-dashed) curve in the top right panel shows $b_2(M)$ computed from the peak-background split formalism, scaled to the value of $\boldsymbol{V}_+$ at $M \simeq 3 \times 10^{13} h^{-1}\mathrm{M}_\odot$. Results are shown for FOF halos at $z = 0$.

the right panel of Fig. 3 exhibit very little dependence on $f_{\mathrm{NL}}$ (the different lines are all on top of each other). The derivatives of $\boldsymbol{V}_+$ and $\boldsymbol{V}_-$ with respect to $f_{\mathrm{NL}}$ shown in the lower panel reveal a very weak sensitivity to $f_{\mathrm{NL}}$ which is less than 0.5% for most of the mass bins (for the most massive bin it reaches up to 1%). We repeated the same analysis with 100 and 200 mass bins and found that the relative differences between the measurements in Gaussian and non-Gaussian simulations further decrease. We thus conclude that the eigenvectors $\boldsymbol{V}_+$ and $\boldsymbol{V}_-$ can be assumed independent of $f_{\mathrm{NL}}$ to a very high accuracy.

Our findings demonstrate that the two-point statistics of halos are sensitive to primordial non-Gaussianity beyond the linear-order effect of Eq. (3) derived in [8, 21, 22]. However, the corrections are tiny if one considers a single bin containing many halos of very different mass (see [37]) due to mutual cancellations from $b_2$-terms of opposite sign. Only two specific eigenmodes of the shot noise matrix (corresponding to two different weightings of the halo density field) inherit a significant dependence on $f_{\mathrm{NL}}$. This is most prominently the case for the eigenmode corresponding to the highest eigenvalue $\lambda_+$. Its eigenvector, $\boldsymbol{V}_+$, is shown to be closely related to the second-order bias $\boldsymbol{b}_2$ in Eq. (19). As can be seen in the upper right panel of Fig. 3, $\boldsymbol{V}_+$ measured from the simulations, and the function $b_2(M)$ calculated from the peak-background split formalism [40, 41], agree closely ( note that $b_2(M)$ has been rescaled to match the normalized vector $\boldsymbol{V}_+$).

In the continuous limit this implies that weighting the halo density field with $b_2(M)$ selects the eigenmode with eigenvalue $\lambda_+$ given in Eq. (20). Since $\lambda_+$ depends on $f_{\mathrm{NL}}$ through the quantity $\mathcal{E}_{\delta^2}$ defined in Eq. (21), the result-

ing weighted field will show the same $f_{\mathrm{NL}}$-dependence. However, this $f_{\mathrm{NL}}$-dependence cannot immediately be exploited to constrain primordial non-Gaussianity, because the Fourier modes of $\mathcal{E}_{\delta^2}$ are heavily correlated due to the convolution of $\delta$ with itself in Eq. (21), and thus do not contribute to the Fisher information independently. The bottom line is that for increasingly massive halo bins with large $b_2$, the term $\mathcal{E}_{\delta^2}$ makes an important contribution to the halo power spectrum *and* shows a significant dependence on $f_{\mathrm{NL}}$. It is important to take into account this dependence when attempting to extract the best-fit value of $f_{\mathrm{NL}}$ from high-mass clusters, so as to avoid a possible measurement bias. Although it provides some additional information on $f_{\mathrm{NL}}$, we will ignore it in the following and quote only lower limits on the Fisher information content.

## B. Constraints from Halos and Dark Matter

Let us first assume the underlying dark matter density field $\delta$ is available in addition to the galaxy distribution. Although this can in principle be achieved with weak-lensing surveys using tomography, the spatial resolution will not be comparable to that of galaxy surveys. To mimic the observed galaxy distribution we will assume that each dark matter halo (identified in the numerical simulations) hosts exactly one galaxy. A further refinement in the description of galaxies can be accomplished with the specification of a halo occupation distribution for galaxies [15, 60], but we will not pursue this here. Instead, we can think of the halo catalogs as a sample

of central halo galaxies from which satellites have been removed. We also neglect the effects of baryons on the evolution of structure formation, which are shown to be marginally influenced by primordial non-Gaussianity at late times [61].

### 1. Single tracer: uniform weighting

In the simplest scenario we only consider one single halo mass bin. In this case, all the observed halos (galaxies) of a survey are correlated with the underlying dark matter density field in Fourier space to determine their scale-dependent effective bias, which can then be compared to theoretical predictions. In practice, this translates into fitting our theoretical model for the scale-dependent effective bias, Eq. (3), to the Fourier modes of the density fields and extracting the best fitting value of $f_{\rm NL}$ together with its uncertainty. For a single halo mass bin, we can employ Eq. (36) and sum over all the Fourier modes.

In the Gaussian simulations, we measure the scale-independent effective bias $b_{\rm G}$ via the estimator $\langle \delta_{\rm h} \delta \rangle / \langle \delta^2 \rangle$ and the shot noise $\mathcal{E}$ via $\langle (\delta_{\rm h} - b_{\rm G} \delta)^2 \rangle$, and average over all modes with $k \leq 0.032 h {\rm Mpc}^{-1}$. In practice, $b_{\rm G}$ and $\mathcal{E}$ are not directly observable, but a theoretical prediction based on the peak-background split [40, 41] and the halo model [14] provides a reasonable approximation to the measured $b_{\rm G}$ and $\mathcal{E}$, respectively, (see Sec. V). Note that for bins covering a wide range of halo masses, the $f_{\rm NL}$-dependence of the shot noise is negligible [37] and it is well approximated by its Gaussian expectation.

Figure 4 shows the best fits of Eq. (3) to the simulations with $f_{\rm NL} = 0, \pm 100$ using all the halos of our FOF (left panel) and SO catalogs (right panel). In order to highlight the relative influence of $f_{\rm NL}$ on the effective bias, we normalize the measurements by the large-scale Gaussian average $b_{\rm G}$ and subtract unity. The resulting best-fit values of $f_{\rm NL}$ along with their one-sigma errors are quoted in the lower right for each case of initial conditions. The 68%-confidence region is determined by the condition $\Delta\chi^2(f_{\rm NL}) = 1$. Note that we include only Fourier modes up to $k \simeq 0.032 h {\rm Mpc}^{-1}$ in the fit, as linear theory begins to break down at higher wave numbers.

Obviously, the best-fit values for $f_{\rm NL}$ measured from the FOF halo catalogs are about 20% below the input values. A suppression of the non-Gaussian correction to the bias of FOF halos has already been reported by [32, 59]. These authors showed that the replacement $\delta_{\rm c} \to q\delta_{\rm c}$ with $q = 0.75$ in Eq. (3) yields a good agreement with their simulation data. In our framework, including this "q-factor" is equivalent to exchanging $f_{\rm NL} \to f_{\rm NL}/q$ and $\sigma_{f_{\rm NL}} \to \sigma_{f_{\rm NL}}/q$, owing to the linear scaling of Eq. (3) with $\delta_{\rm c}$. Repeating the chi-square minimization with $q = 0.75$ yields best-fit values that are consistent with our input values, namely $f_{\rm NL} = +107.0 \pm 8.3, +1.8 \pm 8.7$ and

$-104.0 \pm 8.5$. In fact, the closest match to the input $f_{\rm NL}$-values is obtained for a slightly larger $q$ of $\simeq 0.8$.

Note that [59] attributed this suppression to ellipsoidal collapse. However, this conclusion seems rather unlikely since ellipsoidal collapse increases the collapse threshold or, equivalently, implies $q > 1$ [62]. A more sensible explanation arises from the fact that a linking length of 0.2 times the mean interparticle distance can select regions with an overdensity as low as $\Delta \sim 1/0.2^3 = 125$ (with respect to the mean background density $\bar\rho_{\rm m}$), which is much less than the virial overdensity $\Delta_{\rm c}(z = 0) \simeq 340$ associated with a linear overdensity $\delta_{\rm c}$ (see [56, 63, 64]). Therefore, we may reasonably expect that, on average, FOF halos with this linking length trace linear overdensities of height less than $\delta_{\rm c}$.

In the case of SO halos, however, we observe the opposite trend. As is apparent in the right panel of Fig. 4, the model from Eq. (3) overestimates the amplitude of primordial non-Gaussianity by roughly 40%. This is somewhat surprising since the overdensity threshold $\Delta_c \simeq 340$ used to identify the SO halos at $z = 0$ is precisely the virial overdensity predicted by the spherical collapse of a linear perturbation of height $\delta_{\rm c}$. As we will see shortly, however, an optimal weighting of halos can remove this overshoot and therefore noticeably improve the agreement between model and simulations.

### 2. Single tracer: optimal weighting

As demonstrated in [14], the shot noise matrix $\mathcal{E}$ exhibits nonzero off-diagonal elements from correlations between halos of different mass. Thus, in order to extract the full information on halo statistics, it is necessary to include these correlations into our analysis. For this purpose, we must employ the more general chi-square of Eq. (35). The halo density field is split up into $N$ consecutive mass bins in order to construct the vector $\boldsymbol{\delta}_{\rm h}$, and the full shot noise matrix $\mathcal{E}$ must be considered.

However, this approach can be simplified, since we know that $\mathcal{E}$ exhibits one particularly low eigenvalue $\lambda_-$. Because the Fisher information content on $f_{\rm NL}$ from Eq. (39) is proportional to the inverse of $\mathcal{E}$ (this is true at least for the dominant part $\gamma$), it is governed by the eigenmode corresponding to this eigenvalue. In [14] it has been shown that this eigenmode dominates the clustering signal-to-noise ratio. In the continuous limit (infinitely many bins), it can be projected out by performing an appropriate weighting of the halo density field. The corresponding weighting function, denoted as *modified mass weighting* with functional form

$$w(M) = M + M_0 , \qquad (42)$$

was found to minimize the stochasticity of halos with respect to the dark matter. Here, $M$ is the individual halo mass and $M_0$ a constant whose value depends on
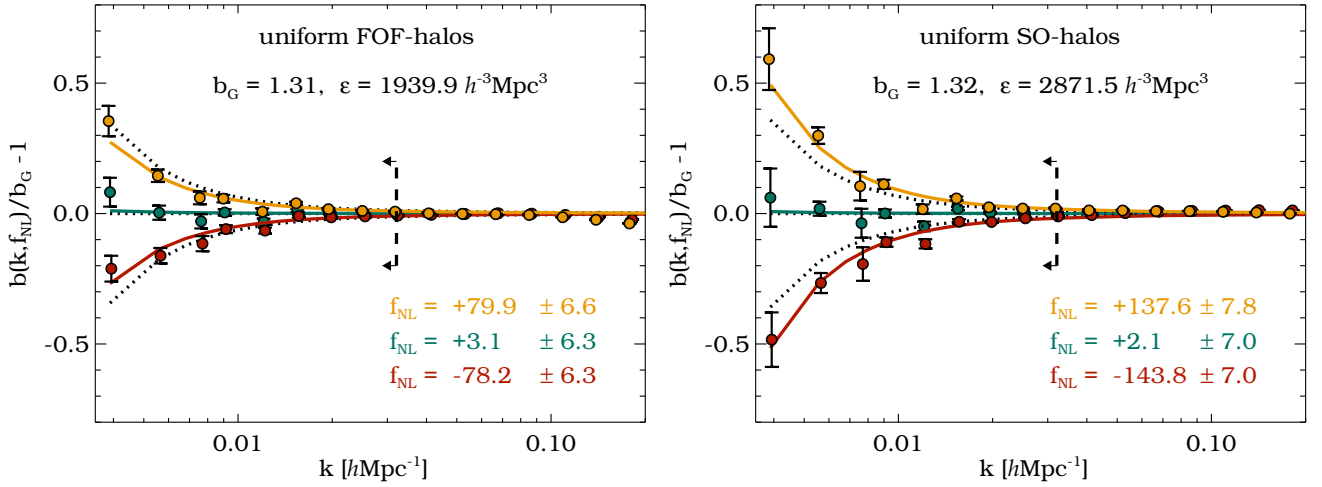
FIG. 4. Relative scale dependence of the effective bias from all FOF (left panel) and SO halos (right panel) resolved in our N-body simulations ($M_{\min} \simeq 5.9 \times 10^{12} h^{-1} M_\odot$), which are seeded with non-Gaussian initial conditions of the local type with $f_{\rm NL} = +100, 0, -100$ (solid lines and data points from top to bottom). The solid lines show the best fit to the linear theory model of Eq. (3), taking into account all the modes to the left of the arrow. The corresponding best-fit values are quoted in the bottom right of each panel. The dotted lines show the model evaluated at the input values $f_{\rm NL} = +100, 0, -100$. The results assume knowledge of the dark matter density field and an effective volume of $V_{\rm eff} \simeq 50 h^{-3} {\rm Gpc}^3$ at $z = 0$.
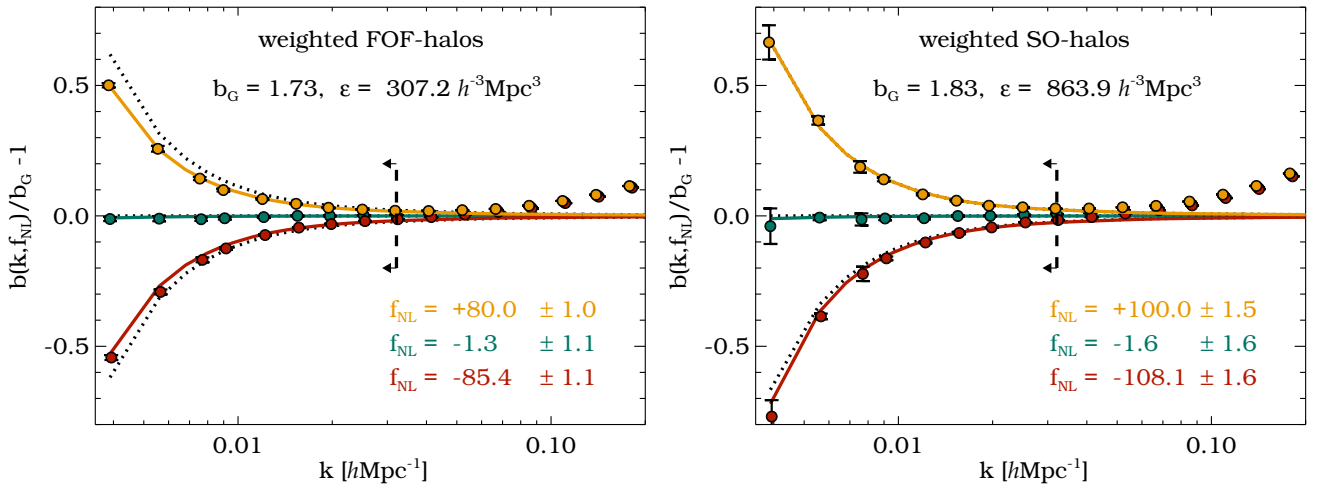


FIG. 5. Same as Fig. 4, but for weighted halos that have minimum stochasticity relative to the dark matter. Note that the one-sigma errors on $f_{\rm NL}$ are reduced by a factor of $\sim 5$ compared to uniform weighting. In the case of SO halos the input values for $f_{\rm NL}$ are well recovered by the best-fit, while FOF halos still show a suppression of $\sim 20\%$ ($q \simeq 0.8$) in the best-fit $f_{\rm NL}$.

the resolution of the simulation. It is approximately 3 times the minimum resolved halo mass $M_{\min}$, so in this case $M_0 \simeq 1.8 \times 10^{13} h^{-1} M_\odot$. The weighted halo density field is computed as

$$\delta_w = \frac{\sum_i w(M_i) \delta_{{\rm h}_i}}{\sum_i w(M_i)} \equiv \frac{\boldsymbol{w}^{\mathsf{T}} \boldsymbol{\delta}_{\rm h}}{\boldsymbol{w}^{\mathsf{T}} \mathbb{1}} , \qquad (43)$$

where we have combined the weights of the individual mass bins into a vector $\boldsymbol{w}$ in the last expression. Because the chi-square in Eq. (35) is dominated by only one

eigenmode, it simplifies to the form of Eq. (36) with the halo field $\delta_{\rm h}$ being replaced by the weighted halo field $\delta_w$. Note also that $b_{\rm G}$ and $\mathcal{E}$ have to be replaced by the corresponding weighted quantities (see [14]).

The results are shown in Fig. 5 for both FOF and SO halos. We observe a remarkable reduction in the error on $f_{\rm NL}$ by a factor of $\sim 4 - 6$ (depending on the halo finder) when replacing the uniform sample used in Fig. 4 by the optimally weighted one. While for the FOF halos the predicted amplitude of the non-Gaussian correction

to the halo bias still shows the 20% suppression (again, this can be taken into account by introducing a $q$-factor into our fit), for the SO halos the best-fit values of $f_{NL}$ now agree much better with the input values, i.e., $q \simeq 1$.

Therefore, the large discrepancy seen in Fig. 4 presumably arises from noise in the SO mass assignment at low mass. To ascertain whether this is the case, we repeat the analysis, increasing the threshold for the minimum number of particles per halo and discarding all halos below that threshold. If this threshold reaches 40 particles per halo, we find the best-fit $f_{NL}$ to be much closer to the input values, namely $f_{NL} = +102.6 \pm 4.6$, $+2.1 \pm 4.5$ and $-103.5 \pm 4.4$. This suggests that most of the discrepancy seen in the right panel of Fig. 4 is due to poorly resolved halos of mass $M \lesssim 2M_{min}$ [58]. However, modified mass weighting removes this discrepancy since halos at low mass are given less weight.

Our findings are consistent with the ones of [31], where the non-Gaussian bias of SO halos has been measured also at higher redshifts and mass thresholds, and the results of [65], where the fractional deviation from the Gaussian mass function for both FOF and SO halos was presented (see their Fig. 5). The remarkable improvement in the constraints on $f_{NL}$ follows from the fact that the stochasticity (shot noise) of the optimally weighted halo density field is strongly suppressed with respect to the dark matter [14]. This means that the fluctuations of the halo and the dark matter overdensity fields are more tightly correlated and the variance of the estimator $\langle \delta_h \delta \rangle / \langle \delta^2 \rangle$ for the effective bias is minimized. Also, cosmic variance fluctuations inherent in both $\delta$ and $\delta_h$ are canceled in this ratio (see Appendix C). Since the scale dependence of this estimator is a direct probe of primordial non-Gaussianity, the error on $f_{NL}$ is significantly reduced. At the same time, modified mass weighting increases the magnitude of $b_G$. We will show below that the constraints on $f_{NL}$ are indeed optimized with this approach.

Finally, we can test our assumption about the likelihood function as defined in Eq. (22) being of a Gaussian form and thus yielding the correct Fisher information. Non-Gaussian corrections could arise from correlated $k$-modes in the covariance matrix (as present in the eigenmode $\lambda_+$ of the shot noise matrix), preventing the Fisher information from being a single integral over $k$. The error $\sigma_b$ on the effective bias in Figs. 4 and 5 is determined from the variance amongst our sample of 12 realizations and thus provides an independent way of testing the value for $\sigma_{f_{NL}}$: from Eq. (3) we can determine $\sigma_{f_{NL}} = \sigma_b/(b_G - 1)u(k, z)$ and compare it to the value obtained from the chi-square fit with Eq. (35). Applying the two methods, we find no significant differences in $\sigma_{f_{NL}}$, so at least up to the second moment of the likelihood function, the assumption of it being Gaussian seems reasonable for the considered values of $f_{NL}$.

### 3. Multiple tracers

Let us now estimate the minimal error on $f_{NL}$ achievable with a given galaxy survey for the general case, dividing halos into multiple mass bins. The Fisher information is given by Eq. (39) or (29), depending on whether the dark matter density field is known or not, and the minimal error on $f_{NL}$ is determined via integration over all observed modes in the volume $V$,

$$\sigma_{f_{NL}}^{-2} = \frac{V}{2\pi^2} \int_{k_{min}}^{k_{max}} F_{f_{NL} f_{NL}}(k) \, k^2 \mathrm{d}k . \qquad (44)$$

The largest modes with wave number $k_{min} = 2\pi/L_{box} \simeq 0.0039h\mathrm{Mpc}^{-1}$ available from our $N$-body simulations are smaller than the largest modes in a survey of $50h^{-3}\mathrm{Gpc}^3$ volume ($k_{min} \simeq 0.0017h\mathrm{Mpc}^{-1}$), since we only obtain an *effective* volume by considering 12 smaller simulation boxes. Because the signal from $f_{NL}$ is strongest at low $k$, our results slightly underestimate the total Fisher information. However, we can roughly estimate that on larger scales ($k_{min} < 0.0039h\mathrm{Mpc}^{-1}$), $F_{f_{NL} f_{NL}}(k) \sim u^2(k)P(k) \sim k^{-4}k^{n_s}$ [see Eqs. (4), (29) and (39), as well as Figs. 6 and 8], and thus $\sigma_{f_{NL}} \sim \ln{(k_{max}/k_{min})}^{-1/2}$ assuming $n_s \simeq 1$, a relatively weak dependence on $k_{min}$. In our case this amounts to an overestimation of $\sigma_{f_{NL}}$ by roughly 20%.

Note that we only consider the $f_{NL}$-$f_{NL}$-element of the Fisher matrix. In principle we would have to consider various other parameters of our cosmology and then marginalize over them, i.e., compute $(F^{-1})_{f_{NL} f_{NL}}$ [66]. However, any degeneracy with cosmological parameters is largely eliminated when multiple tracers are considered, since the underlying dark matter density field mostly cancels out in this approach [9]. A mathematical demonstration of this fact is presented in Appendix C.

Recent studies have developed a gauge-invariant description of the observable large-scale power spectrum consistent with general relativity [67–73]. In particular, it has been noted that the general relativistic corrections to the usually adopted Newtonian treatment leave a signature in the galaxy power spectrum that is very similar to the one caused by primordial non-Gaussianity of the local type [74–76]. However, in a multitracer analysis the two effects can be distinguished sufficiently well, so that the ability to detect primordial non-Gaussianity is little compromised in the presence of general relativistic corrections [77].

In order to make the most conservative estimates we will discard all the terms featuring $\mathcal{E}'$ in the Fisher matrix, since it is not obvious how much information on $f_{NL}$ can actually be extracted from the shot noise matrix. $\mathcal{E}$ is indeed close to a pure white-noise quantity and we find its Fourier modes to be highly correlated. Therefore, in order to extract residual information on $f_{NL}$, one would have to decorrelate those modes through an in-
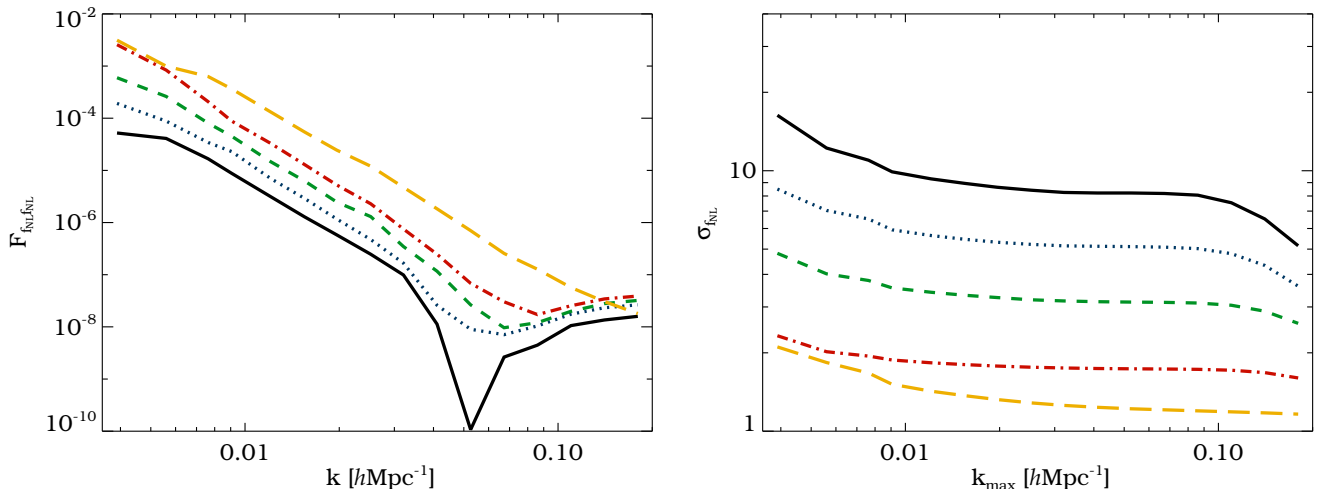
FIG. 6. Fisher information (left panel) and one-sigma error on $f_{\mathrm{NL}}$ (right panel, $k_{\mathrm{min}} = 0.0039h\mathrm{Mpc}^{-1}$, $V_{\mathrm{eff}} \simeq 50h^{-3}\mathrm{Gpc}^3$) from simulations of FOF halos and dark matter at $z = 0$. The lines show the results for 1 (solid black), 3 (dotted blue), 10 (dashed green) and 30 (dot-dashed red) uniform halo mass bins, as well as for 1 weighted bin (long-dashed yellow).

version of the correlation matrix among $k$-bins (see [78]). However, in light of the limited volume of our simulations this can be a fairly noisy procedure, especially when the halo distribution is additionally split into narrow mass bins. Hence, for the Fisher information content on $f_{\mathrm{NL}}$ assuming knowledge of both halos and dark matter, we will retain only the first term in Eq. (39) and provide a lower limit:

$$F_{f_{\mathrm{NL}}f_{\mathrm{NL}}} \geq \gamma \equiv \boldsymbol{b}'^{\mathsf{T}} \boldsymbol{\mathcal{E}}^{-1} \boldsymbol{b}' P \ . \tag{45}$$

To calculate $F_{f_{\mathrm{NL}}f_{\mathrm{NL}}}$, we measure the functions $\boldsymbol{b}(k)$, $\boldsymbol{b}'(k)$, $\boldsymbol{\mathcal{E}}(k)$ and $P(k)$ from our $N$-body simulations (see Figs. 1, 2 and 3). In order to mitigate sampling variance in the multibin case, we then use Eq. (13) to recalculate the shot noise matrix. Namely, we set all the eigenvalues $\lambda_{\mathrm{P}}^{(N-2)}$ equal to the average value $1/\bar{n}$, and measure $\lambda_+$, $\lambda_-$, as well as $\boldsymbol{V}_+$ and $\boldsymbol{V}_-$ directly from the numerical eigendecomposition of $\boldsymbol{\mathcal{E}}$.

Figure 6 depicts $F_{f_{\mathrm{NL}}f_{\mathrm{NL}}}(k)$ and $\sigma_{f_{\mathrm{NL}}}(k_{\mathrm{max}})$ with fixed $k_{\mathrm{min}} = 0.0039h\mathrm{Mpc}^{-1}$ for the cases of 1, 3, 10 and 30 halo mass bins. Clearly, the finer the sampling into mass bins, the higher the information content on $f_{\mathrm{NL}}$. The weighted halo density field with minimal stochasticity relative to the dark matter (corresponding to a continuous sampling of infinitely many bins) yields more than a factor of 6 reduction in $\sigma_{f_{\mathrm{NL}}}$ when compared to a single mass bin of uniformly weighted halos. This improvement agrees reasonably well with that seen in Figs. 4 and 5, although the estimates for $\sigma_{f_{\mathrm{NL}}}$ are slightly larger than those we obtained from the fitting procedure. This may be expected, since we only obtain an upper limit on $\sigma_{f_{\mathrm{NL}}}$ from Eqs. (44) and (45).

The inflection around $k \sim 0.1h\mathrm{Mpc}^{-1}$ in $F_{f_{\mathrm{NL}}f_{\mathrm{NL}}}$ and $\sigma_{f_{\mathrm{NL}}}$ marks a breakdown of the linear model from

Eq. (9). We should not trust our results too much at high wave number, where higher-order contributions to the non-Gaussian effective bias may become important. It should also be noted that the inflection disappears for the weighted field, suggesting numerical issues to be less problematic in that case.

Further improvements can be achieved when going to lower halo masses (see Sec. V): the error on $f_{\mathrm{NL}}$ is proportional to the shot noise of the halo density field (Eq. (40)), which itself is a function of the minimum halo mass $M_{\mathrm{min}}$. References [14, 15] numerically investigated the extent to which the shot noise depends on $M_{\mathrm{min}}$ and proposed a method based on the halo model for extrapolating it to lower mass. It predicts the shot noise of the weighted halo density field to decrease linearly with $M_{\mathrm{min}}$, anticipating about 2 orders of magnitude further reduction in $\mathcal{E}$ when resolving halos down to $M_{\mathrm{min}} \simeq 10^{10}h^{-1}\mathrm{M}_\odot$. In terms of $f_{\mathrm{NL}}$-constraints this is however somewhat mitigated by the fact that the Gaussian bias also decreases with $M_{\mathrm{min}}$, so the non-Gaussian correction to the effective bias in Eq. (3) gets smaller. Furthermore, [14] studied the effect of adding random noise to the halo mass (to mimic scatter between halo mass and the observables such as galaxy luminosity), while [15] explored the redshift dependence of the optimally weighted halo density field and extended the method to halo occupation distributions for galaxies.

## C. Constraints from Halos

The scenario described above is optimistic in the sense that it assumes the dark matter density field is available. In the following section we will show that it is possible to
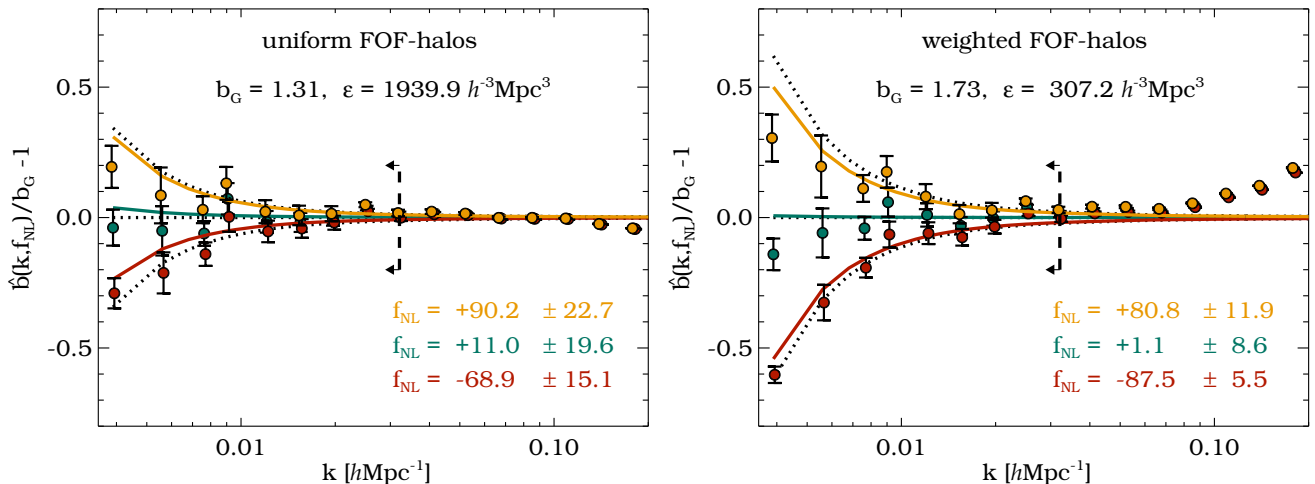
FIG. 7. Relative scale dependence of the effective bias $\hat{b}$ estimated from all uniform (left panel) and weighted FOF halos (right panel) resolved in our N-body simulations ($M_{\min} \simeq 5.9 \times 10^{12} h^{-1} M_\odot$), which are seeded with non-Gaussian initial conditions of the local type with $f_{\rm NL} = +100, 0, -100$ (solid lines and data points from top to bottom). The solid lines show the best fit to the linear theory model of Eq. (3), taking into account all the modes to the left of the arrow. The corresponding best-fit values are quoted in the bottom right of each panel. The dotted lines show the model evaluated at the input values $f_{\rm NL} = +100, 0, -100$. The results assume no knowledge of the dark matter density field and an effective volume of $V_{\rm eff} \simeq 50 h^{-3} {\rm Gpc}^3$ at $z = 0$.

considerably improve the constraints on $f_{\rm NL}$ even without this assumption. This is perhaps not surprising in light of the results in [14, 15], where it was argued that halos can be used to reconstruct the dark matter to arbitrary precision, as long as they are resolved down to the required low-mass threshold.

### 1. Single tracer

Considering a single halo mass bin, we must again sum over all the Fourier modes in Eq. (25) and minimize this chi-square with respect to $f_{\rm NL}$. Although we pretend to have no knowledge of the dark matter distribution, we determine $b_{\rm G}$ and $\mathcal{E}$ from our simulations. In realistic applications, however, these quantities will have to be accurately modeled. In addition, we use the linear power spectrum $P_0(k)$ instead of the simulated nonlinear dark matter power spectrum $P(k)$ in Eq. (25).

Since, in this case, we cannot determine the scale-dependent effective bias directly from the estimator $\langle \delta_{\rm h} \delta \rangle / \langle \delta^2 \rangle$, we define the new estimator

$$\hat{b} \equiv \sqrt{\frac{\langle \delta_{\rm h}^2 \rangle - \mathcal{E}}{P_0}}, \qquad (46)$$

which solely depends on the two-point statistics of halos. In Fig. 7 we plot this estimator together with the best-fit solutions for the scale-dependent effective bias obtained from the chi-square fit of Eq. (25). The left panel depicts the results obtained for uniform FOF halos. Compared

to the previous case with dark matter, we observe the constraints on $f_{\rm NL}$ to be weaker by a factor of $\sim 3$. The main reason for this difference is the fact that sampling variance inherent in $\delta_{\rm h}$ is not canceled out by subtracting $\delta$, as is done in Eq. (36). This can also be seen in the estimator $\hat{b}$, where a division of the smooth linear power spectrum $P_0$ does not cancel the cosmic variance inherent in $\langle \delta_{\rm h}^2 \rangle$. Hence, $\hat{b}$ shows significantly stronger fluctuations than $b = \langle \delta_{\rm h} \delta \rangle / \langle \delta^2 \rangle$, which demonstrates how well the basic idea of sampling variance cancellation works.

Exchanging the uniform halo field $\delta_{\rm h}$ with the weighted one, $\delta_w$, the constraints on $f_{\rm NL}$ improve by about a factor of $2 - 3$, as can be seen in the right panel of Fig. 7. However, this improvement is mainly due to the larger value of $b_{\rm G}$ of the weighted sample, since the relative scatter among the data points remains unchanged. This is expected, because we do not consider a second tracer (e.g., the dark matter) in this case, and therefore do not cancel cosmic variance.

Comparing the uncertainty on $f_{\rm NL}$ obtained from Eq. (23) with the one determined via the variance of $\hat{b}$ amongst our 12 realizations, we can check once more the assumption of a Gaussian likelihood as given in Eq. (22). Again, we find both methods to yield consistent values for $\sigma_{f_{\rm NL}}$, suggesting any non-Gaussian corrections to the likelihood function to be negligible at this order.
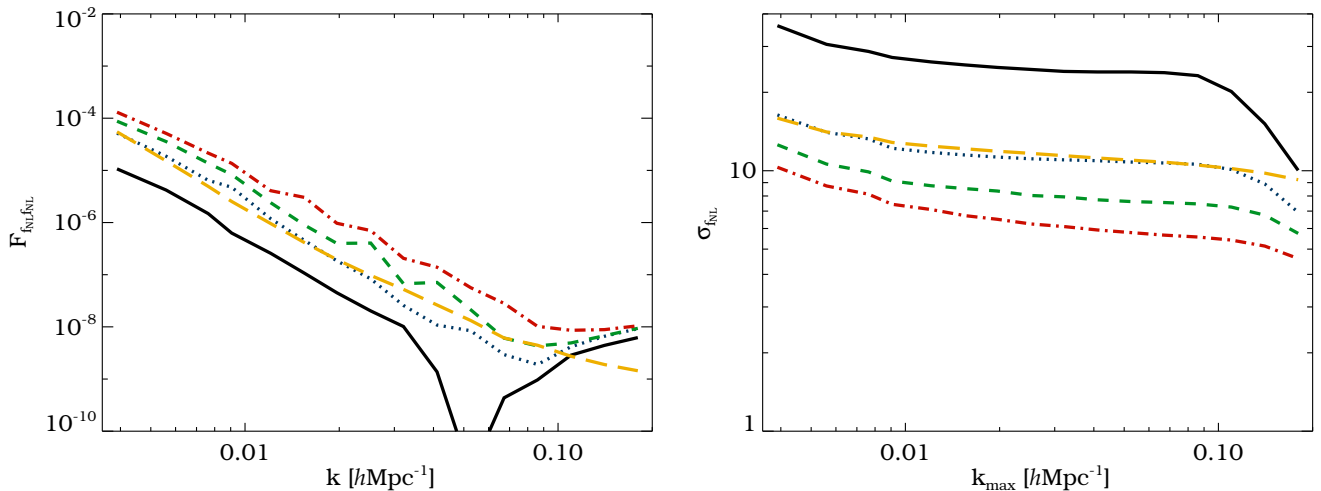
FIG. 8. Fisher information (left panel) and one-sigma error on $f_{\mathrm{NL}}$ (right panel, $k_{\min} = 0.0039h\mathrm{Mpc}^{-1}$, $V_{\mathrm{eff}} \simeq 50h^{-3}\mathrm{Gpc}^3$) from simulations of FOF halos only ($z = 0$). The lines show the results for 1 (solid black), 3 (dotted blue), 10 (dashed green) and 30 (dot-dashed red) uniform halo mass bins, as well as for 1 weighted bin (long-dashed yellow).

### 2. Multiple tracers

If we want to exploit the gains from sampling variance cancellation in the case where the dark matter density field is not available, we have to perform a multitracer analysis of halos (see Appendix C), which is the focus of this section. We now consider Eq. (23) for the chi-square fit. In order to calculate the Fisher information, we use Eq. (29) and thus neglect any possible contribution emerging from the $f_{\mathrm{NL}}$-dependence of the shot noise matrix $\boldsymbol{\mathcal{E}}$.

Numerical results for the Fisher information content and the one-sigma error on $f_{\mathrm{NL}}$ are shown in Fig. 8 for 1, 3, 10 and 30 uniform FOF halo mass bins, as well as for 1 weighted bin. Clearly, the cases of 10 and 30 uniform bins outperform a single bin of the weighted field in terms of Fisher information. This suggests that further improvements compared to the single weighted halo field can be achieved when all the correlations of sufficiently many halo mass bins are taken into account.

In principle, we want to split the halo density field into as many mass bins as possible and extrapolate the results to the limit of infinitely many bins (continuous limit). Note that in the high-sampling limit of $\bar{n} \to \infty$, $F_{f_{\mathrm{NL}}f_{\mathrm{NL}}}$ from Eq. (30) is limited to $2(b'/b)^2$, whereas the same quantity for several mass bins, Eq. (29), may surpass this bound (see Sec. V). In Sec. IV B we showed that a single optimally weighted halo sample combined with the dark matter reaches the continuous limit in $F_{f_{\mathrm{NL}}f_{\mathrm{NL}}}$, which corresponds to a splitting into infinitely many bins in the multitracer approach. It is unclear, whether a similar goal can be achieved from halos alone, e.g., by considering two differently weighted tracers that would preserve all

of the information on $f_{\mathrm{NL}}$, because we do not know the continuous limit of the Fisher information in that case. We will therefore turn to theoretical predictions by the halo model in the following paragraph.

## V. HALO MODEL PREDICTIONS

A useful theoretical framework for the description of dark matter and halo clustering is given by the halo model (see, e.g., [38]). Despite its limitations [39], the halo model achieves remarkable agreement with the results from $N$-body simulations [14, 38]. In particular, it provides an analytical expression for the shot noise matrix in the fiducial Gaussian case, given by

$$\boldsymbol{\mathcal{E}} = \bar{n}^{-1}\mathbf{I} - \boldsymbol{b}\boldsymbol{\mathcal{M}}^{\mathsf{T}} - \boldsymbol{\mathcal{M}}\boldsymbol{b}^{\mathsf{T}} \, , \qquad (47)$$

where $\boldsymbol{\mathcal{M}} \equiv \boldsymbol{M}/\bar{\rho}_{\mathrm{m}} - \boldsymbol{b}\langle nM^2\rangle/2\bar{\rho}_{\mathrm{m}}^2$ and $\boldsymbol{M}$ is a vector containing the mean halo mass of each bin (see [14] for the derivation). The Poisson model is recovered when we set $\boldsymbol{\mathcal{M}} = 0$. Here, $\boldsymbol{b}$ can be determined by integrating the peak-background split bias $b(M)$ over the Sheth-Tormen halo mass function $dn/dM$ [40] in each mass bin. The expression $\langle nM^2\rangle/\bar{\rho}_{\mathrm{m}}^2$ originates from the dark matter one-halo term, so it does not depend on halo mass and from our suite of simulations we determine its Gaussian value to be $\simeq 418h^{-3}\mathrm{Mpc}^3$ at $z = 0$ and $\simeq 45h^{-3}\mathrm{Mpc}^3$ at $z = 1$. In the case of one single mass bin, Eq. (47) reduces to $\mathcal{E} = \bar{n}^{-1} - 2bM/\bar{\rho}_{\mathrm{m}} + b^2\langle nM^2\rangle/\bar{\rho}_{\mathrm{m}}^2$, while if we project out the lowest eigenmode $\boldsymbol{V}_-$ and normalize, we obtain the weighted shot noise

$$\mathcal{E}_w \equiv \frac{\boldsymbol{V}_-^{\mathsf{T}}\boldsymbol{\mathcal{E}}\boldsymbol{V}_-}{\left(\boldsymbol{V}_-^{\mathsf{T}}\mathbb{1}\right)^2} = \lambda_- \frac{\boldsymbol{V}_-^{\mathsf{T}}\boldsymbol{V}_-}{\left(\boldsymbol{V}_-^{\mathsf{T}}\mathbb{1}\right)^2} \, . \qquad (48)$$
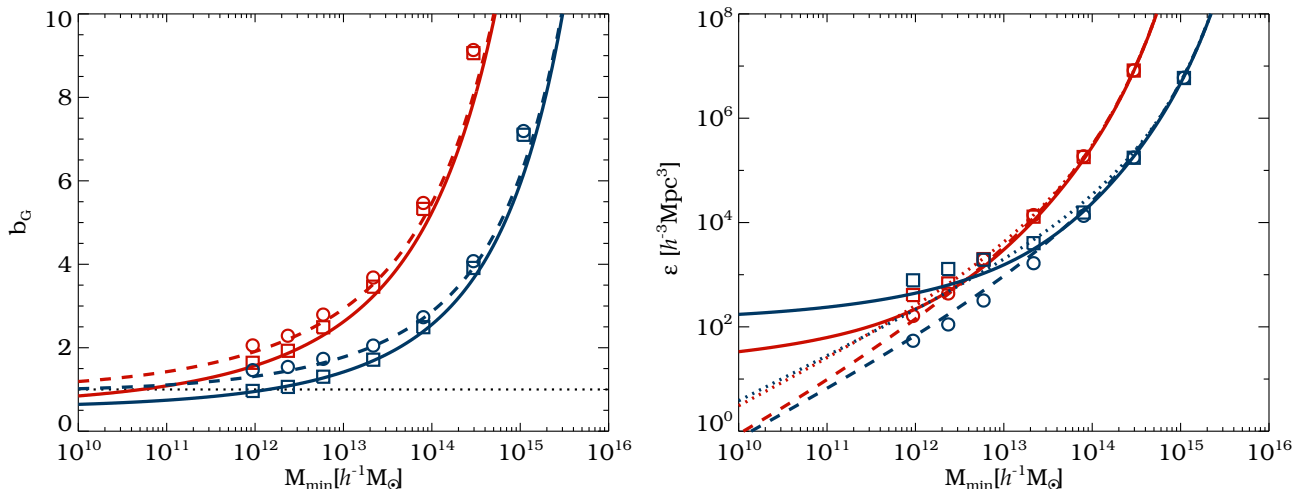
FIG. 9. Halo model predictions for the mean scale-independent Gaussian bias (left panel) and shot noise (right panel) as a function of minimum halo mass from uniform- (solid lines) and weighted halos (dashed lines) from a single mass bin at $z = 0$ (blue) and $z = 1$ (red). $N$-body simulation results are overplotted, respectively, as squares and circles for different low-mass cuts. The dotted line in the left panel depicts $b_G = 1$, the ones in the right panel show the Poisson-model shot noise $\bar{n}_{tot}^{-1}$.

The eigenvalues $\lambda_\pm$ with eigenvectors $\boldsymbol{V}_\pm$ can be found from Eq. (47),

$$\lambda_\pm = \bar{n}^{-1} - \boldsymbol{\mathcal{M}}^\mathsf{T}\boldsymbol{b} \pm \sqrt{\boldsymbol{\mathcal{M}}^\mathsf{T}\boldsymbol{\mathcal{M}}\,\boldsymbol{b}^\mathsf{T}\boldsymbol{b}}\,, \qquad (49)$$

$$\boldsymbol{V}_\pm = \mathcal{N}_\pm^{-1}\left(\boldsymbol{\mathcal{M}}\Big/\sqrt{\boldsymbol{\mathcal{M}}^\mathsf{T}\boldsymbol{\mathcal{M}}} \mp \boldsymbol{b}\Big/\sqrt{\boldsymbol{b}^\mathsf{T}\boldsymbol{b}}\right)\,, \qquad (50)$$

where

$$\mathcal{N}_\pm \equiv \sqrt{2 \mp 2\boldsymbol{\mathcal{M}}^\mathsf{T}\boldsymbol{b}\Big/\sqrt{\boldsymbol{\mathcal{M}}^\mathsf{T}\boldsymbol{\mathcal{M}}\,\boldsymbol{b}^\mathsf{T}\boldsymbol{b}}} \qquad (51)$$

is a normalization constant to guarantee $\boldsymbol{V}_\pm^\mathsf{T}\boldsymbol{V}_\pm = 1$. It is easily verified that $\boldsymbol{V}_\pm^\mathsf{T}\boldsymbol{V}_\mp = 0$, i.e., they are orthogonal. In the continuous limit of infinitely many bins ($N \to \infty$) we can replace $\boldsymbol{V}_\pm$ by the smooth function

$$V_\pm = \mathcal{N}_\pm^{-1}\left(\mathcal{M}\Big/\sqrt{\langle\mathcal{M}^2\rangle} \mp b\Big/\sqrt{\langle b^2\rangle}\right)\,, \qquad (52)$$

and obtain

$$\mathcal{E}_w = \left(\bar{n}_{tot}^{-1} - \langle\mathcal{M}b\rangle - \sqrt{\langle\mathcal{M}^2\rangle\langle b^2\rangle}\right)\frac{\langle V_-^2\rangle}{\langle V_-\rangle^2}\,, \qquad (53)$$

$$b_w = \frac{\langle V_- b\rangle}{\langle V_-\rangle}\,, \qquad (54)$$

where $b_w$ is the weighted effective bias and we exchanged the vector products by integrals over the mass function:

$$\boldsymbol{x}^\mathsf{T}\boldsymbol{y} \longrightarrow \frac{N}{\bar{n}_{tot}}\int_{M_{min}}^{M_{max}}\frac{dn}{dM}(M)x(M)y(M)\,dM \equiv N\langle xy\rangle\,, \qquad (55)$$

$$\bar{n}_{tot} = \int_{M_{min}}^{M_{max}}\frac{dn}{dM}(M)\,dM \equiv N\bar{n}\,. \qquad (56)$$

Figure 9 depicts the halo model prediction for the scale-independent Gaussian bias $b_G$ and shot noise $\mathcal{E}$ as a function of minimum halo mass $M_{min}$ at $z = 0$ and $z = 1$ for both the uniform and the weighted case of a single mass bin. Simulation results are overplotted as symbols for a few $M_{min}$ [we approximate the weighting function $V_-(M)$ by $w(M)$ from Eq. (42) in the simulations]. Obviously, modified mass weighting increases $b_G$, especially when going to lower halo masses. It is also worth noticing that in contrast to the uniform case, $b_G$ is always greater than unity when weighted by $w(M)$ (at least in the considered mass range). Going to higher redshift further increases $b_G$ at any given $M_{min}$.

For the shot noise we observe the opposite behavior: modified mass weighting leads to a suppression of $\mathcal{E}$, which is increasingly pronounced towards lower halo masses. Moreover, it is always below the Poisson-model prediction of $\bar{n}_{tot}^{-1}$. Our $N$-body simulation results generally confirm this trend (at least down to our resolution limit), although the halo model slightly underestimates the suppression of shot noise between uniform and weighted halos at lower $M_{min}$. At higher redshifts, this suppression becomes smaller at given $M_{min}$, but the magnitude of $\mathcal{E}_w$ at $z = 1$ approaches the one at $z = 0$ towards low $M_{min}$ and is still small compared to the Poisson-model prediction of $\bar{n}_{tot}^{-1}$.

## A. Single tracer

With predictions for $b_G$ and $\mathcal{E}$ at hand, we can directly compute the expected Fisher information content on $f_{NL}$ from a single halo mass bin. If the dark mat-
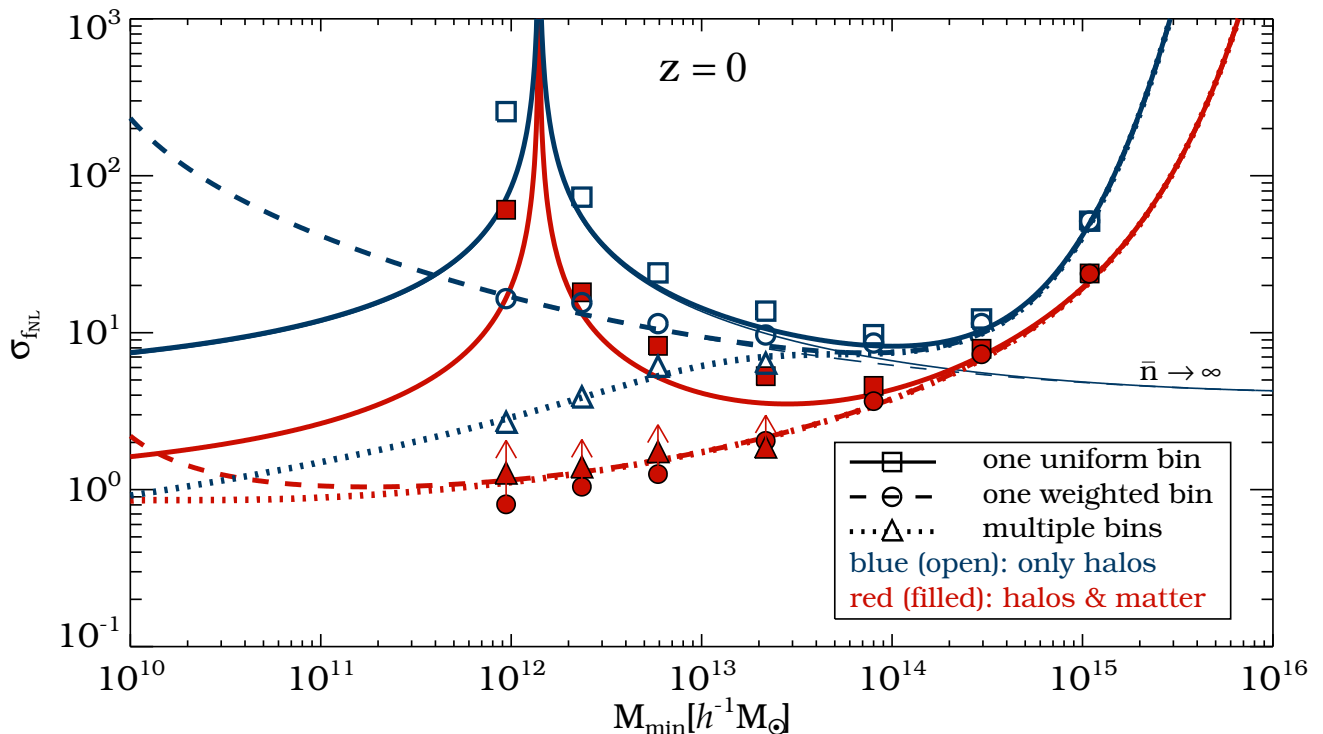
FIG. 10. Halo model predictions for the one-sigma error on $f_{\rm NL}$ (inferred from an effective volume of $V_{\rm eff} \simeq 50h^{-3}{\rm Gpc}^3$, taking into account all modes with $0.0039h{\rm Mpc}^{-1} \leq k \leq 0.032h{\rm Mpc}^{-1}$ at $z = 0$) as a function of minimum halo mass from uniform- (solid lines) and weighted halos (dashed lines) from a single mass bin. The $N$-body simulation results are overplotted, respectively, as squares and circles for different low-mass cuts. Results that assume knowledge of halos and the dark matter are plotted in red (filled symbols), those that only consider halos are depicted in blue (open symbols). The dotted lines (triangles) show the results from splitting the halo catalog into multiple mass bins and taking into account the full halo covariance matrix in calculating $F_{f_{\rm NL} f_{\rm NL}}$. The high-sampling limit for one mass bin ($\bar{n} \to \infty$, $F_{f_{\rm NL} f_{\rm NL}} = 2\left(b'/b\right)^2$) is overplotted for the uniform- (thin solid line) and the weighted case ( thin dashed line). Arrows show the effect of adding a log-normal scatter of $\sigma_{\ln M} = 0.5$ to all halo masses, they are omitted in all cases where the scatter has negligible impact.

ter density field is known we apply Eq. (40), if it is not we use Eq. (30). In order to obtain most conservative results, we neglect terms featuring derivatives of the shot noise with respect to $f_{\rm NL}$. We then apply Eq. (44) with $k_{\rm min} = 0.0039h{\rm Mpc}^{-1}$, $k_{\rm max} = 0.032h{\rm Mpc}^{-1}$ and $V \simeq 50h^{-3}{\rm Gpc}^3$ to compute the one-sigma error forecast for $f_{\rm NL}$.

Results are shown in Fig. 10 for $z = 0$. When the dark matter density field is available (red lines and filled symbols), weighting the halos (red dashed lines and filled circles) is always superior to the conventional uniform case (red solid lines and filled squares), especially when going to lower halo masses. In particular, $\sigma_{f_{\rm NL}}$ substantially decreases with decreasing $M_{\rm min}$ in the weighted case, while for uniform halos it shows a spike at $M_{\rm min} \simeq 1.4 \times 10^{12}h^{-1}{\rm M}_\odot$. This happens when $b_{\rm G}$ becomes unity and the non-Gaussian correction to the halo bias in Eq. (3) vanishes, leaving no signature of $f_{\rm NL}$ in the effective bias. Since in the weighted case $b_{\rm G} > 1$ for all considered $M_{\rm min}$, this spike does not appear, although

we notice that the error on $f_{\rm NL}$ begins to increase below $M_{\rm min} \sim 10^{11}h^{-1}{\rm M}_\odot$.

The simulation results are overplotted as symbols for a few values of $M_{\rm min}$, the agreement with the halo model predictions is remarkable. Note that the first two data-points at $M_{\rm min} = 9.4 \times 10^{11}h^{-1}{\rm M}_\odot$ and $M_{\rm min} = 2.35 \times 10^{12}h^{-1}{\rm M}_\odot$ resulting from our high-resolution simulation were scaled to the effective volume of our 12 low-resolution boxes. The simulations yield a minimum error of $\sigma_{f_{\rm NL}} \simeq 0.8$ at $M_{\rm min} \simeq 10^{12}h^{-1}{\rm M}_\odot$ in the optimally weighted case with the dark matter available. This value is even lower than what is anticipated by the halo model ($\sigma_{f_{\rm NL}} \simeq 1$).

The results without the dark matter are shown as blue lines and open symbols. $\sigma_{f_{\rm NL}}$ exhibits a minimum at $M_{\rm min} \simeq 10^{14}h^{-1}{\rm M}_\odot$ with $\sigma_{f_{\rm NL}} \sim 10$ for both uniform and weighted halos. Thus, weighting the halos does not decrease the lowest possible error on $f_{\rm NL}$ from the uniform case, as expected. This suggests that only the highest-mass halos (clusters at $z = 0$) need to be consid-
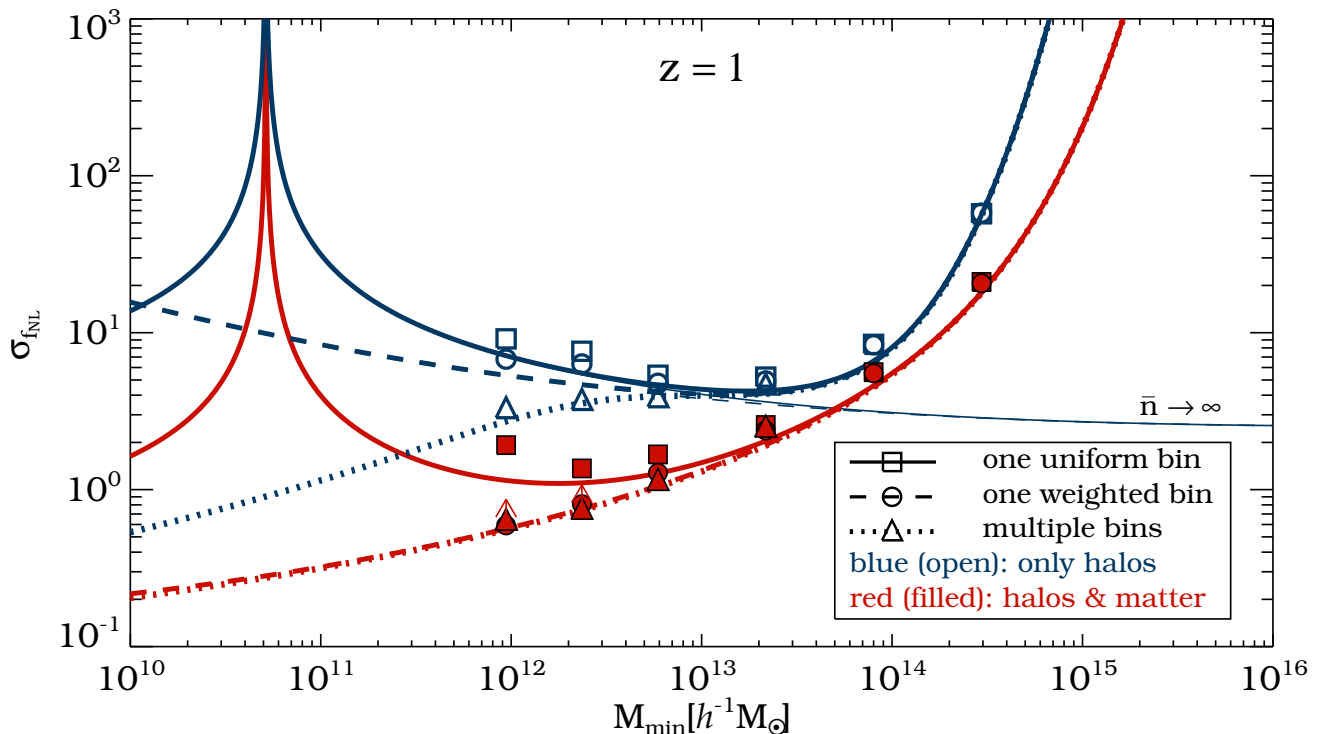
FIG. 11. Same as Fig. 10 at $z = 1$.

ered to optimally constrain $f_{\mathrm{NL}}$ from a single-bin survey without observations of the dark matter.

In the limit of $\bar{n} \to \infty$, $F_{f_{\mathrm{NL}} f_{\mathrm{NL}}} \to 2 \left( b'/b \right)^2$. Then, according to Eq. (3) for high $M_{\mathrm{min}}$, $b' \to b_{\mathrm{G}} u$, and hence $F_{f_{\mathrm{NL}} f_{\mathrm{NL}}} \to 2 u^2$ becomes independent of $M_{\mathrm{min}}$. The corresponding $\sigma_{f_{\mathrm{NL}}}$ in the limit $\bar{n} \to \infty$ is plotted in Fig. 10 for both uniform- (thin blue solid line) and weighted halos (thin blue dashed line) and it indeed approaches a constant value at high $M_{\mathrm{min}}$. It is about a factor of 2 below the minimum in $\sigma_{f_{\mathrm{NL}}}$ without setting $\bar{n} \to \infty$.

The results for redshift $z = 1$ are presented in Fig. 11. In comparison to Fig. 10 one can observe that all the curves are shifted towards the lower left of the plot, i.e., the constraints on $f_{\mathrm{NL}}$ improve with increasing redshift. This is mainly due to the increase of the Gaussian effective bias $b_{\mathrm{G}}$ with $z$, as evident from the left panel of Fig. 9. For example, the location of the spikes in $\sigma_{f_{\mathrm{NL}}}(M_{\mathrm{min}})$ requires $b_{\mathrm{G}} = 1$. At $z = 1$ this condition is fulfilled at lower $M_{\mathrm{min}}$ ($\simeq 5 \times 10^{10} h^{-1} \mathrm{M}_{\odot}$) than at $z = 0$, thus shifting the spikes to the left. Further, since the Fisher information from Eqs. (30) and (40) increases with $b_{\mathrm{G}}$, $\sigma_{f_{\mathrm{NL}}}(M_{\mathrm{min}})$ decreases, especially at low $M_{\mathrm{min}}$.

In the case of optimally weighted halos with knowledge of the dark matter, our simulations suggest $\sigma_{f_{\mathrm{NL}}} \simeq 0.6$ when reaching $M_{\mathrm{min}} \simeq 10^{12} h^{-1} \mathrm{M}_{\odot}$ at $z = 1$, in good agreement with the halo model. It even forecasts $\sigma_{f_{\mathrm{NL}}} \simeq 0.2$ when including halos down to $M_{\mathrm{min}} \simeq 10^{10} h^{-1} \mathrm{M}_{\odot}$.

### B. Multiple tracers

The more general strategy for constraining $f_{\mathrm{NL}}$ from a galaxy survey is to consider all auto- and cross-correlations between tracers of different mass, namely, the halo covariance matrix $\mathbf{C}_{\mathrm{h}}$. If the dark matter density field is known, one can add the correlations with this field and determine $\mathbf{C}$. The Fisher information on $f_{\mathrm{NL}}$ is then given by Eq. (29) and Eq. (39), respectively. Again, the halo model can be applied to make predictions on the Fisher information content. In Appendix D, the analytical expressions for $\alpha$, $\beta$ and $\gamma$ are derived for arbitrarily many mass bins and the continuous limit of infinite bins.

The dotted lines in Fig. 10 show the halo model predictions at $z = 0$ in this continuous limit of infinitely many mass bins. When the dark matter is available (red dotted line), $\sigma_{f_{\mathrm{NL}}}$ coincides with the results from the optimally weighted one-bin case (dashed red lines). This confirms our claim that with the dark matter density field at hand, modified mass weighting is the optimal choice for constraining $f_{\mathrm{NL}}$ and yields the maximal Fisher information content. Only below $M_{\mathrm{min}} \sim 10^{12} h^{-1} \mathrm{M}_{\odot}$ the optimally weighted halo field becomes slightly inferior to the case of infinite bins.

From multiple bins of halos without the dark matter (blue dotted line) we observe a different behavior. While at high $M_{\mathrm{min}}$ the error on $f_{\mathrm{NL}}$ still matches the results
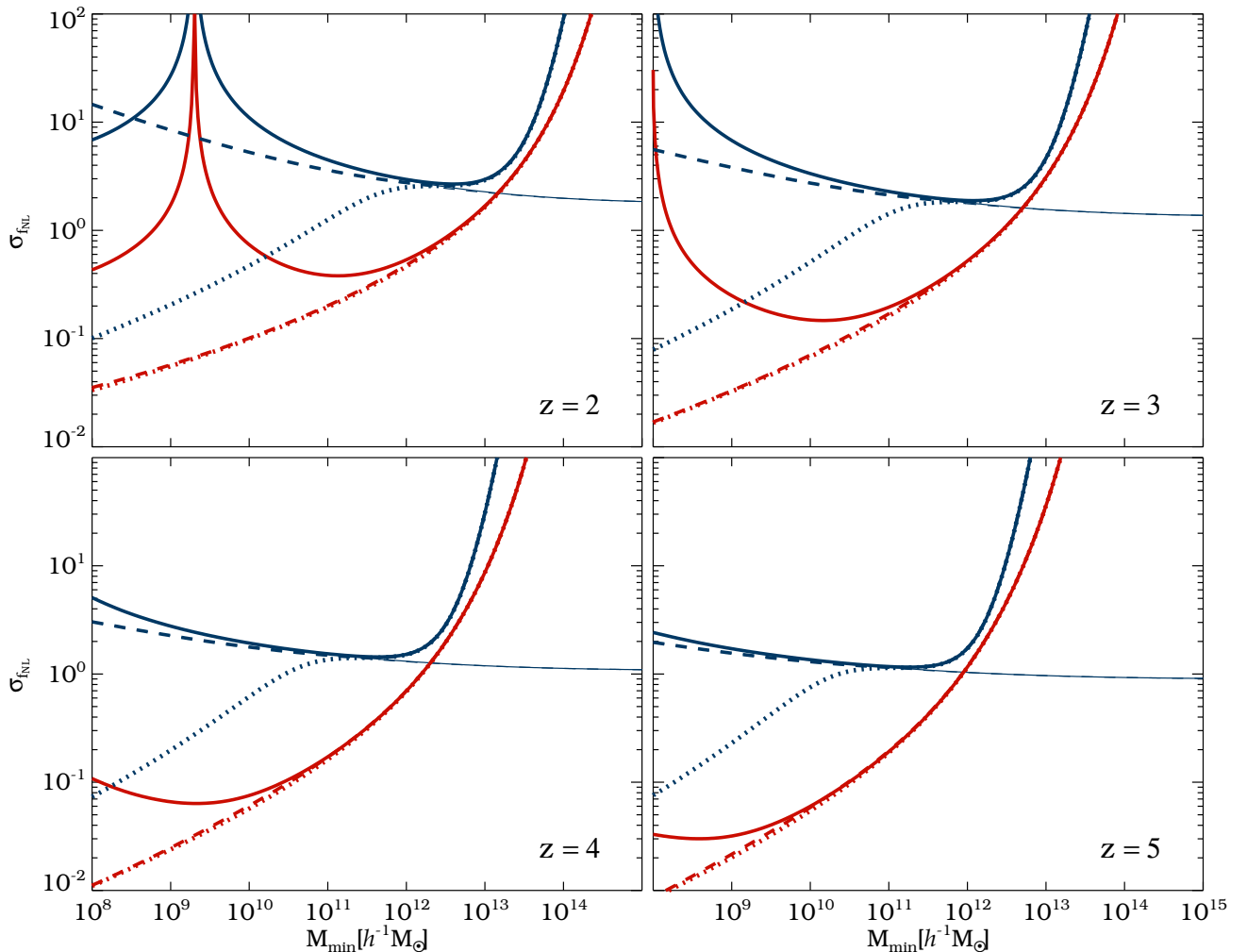
FIG. 12. Same as Figs. 10 and 11 at higher redshifts, as indicated in the bottom right of each panel. Here, only the halo model predictions are shown.

from one mass bin, either uniform (blue solid line) or weighted (blue dashed line), below $M_{\rm min} \sim 10^{14}h^{-1}{\rm M}_\odot$ it departs towards lower values and finally reaches the same continuous limit as in the case where the dark matter is available at $M_{\rm min} \sim 10^{10}h^{-1}{\rm M}_\odot$. Thus, galaxies in principle suffice to yield optimal constraints on $f_{\rm NL}$, however, one has to go to very low halo mass.

Our simulation results for multiple bins (triangles in Fig. 10) support this conclusion. Although we can only consider a limited number of mass bins in the numerical analysis (we used $N = 30$ for our 12 low-res boxes and $N = 10$ for our high-res box), the continuous limit of the halo model can be approached closely. However, note that residuals of sampling variance in the numerical determination of $\mathcal{E}$, as described in Sec. IV B and shown in Fig. 3, can result in an overestimation of $F_{f_{\rm NL}f_{\rm NL}}$. This is especially the case when the number of mass bins $N$ is

high, resulting in a low halo number density per bin $\bar{n}$. Hence, we chose $N$ such that the influence of sampling variance on our results is negligible, and yet clear improvements compared to the single-tracer case are established.

One concern in practical applications is scatter in the halo mass estimation. Although X-ray cluster-mass proxies show very tight correlations with halo mass with a log-normal scatter of $\sigma_{\ln M} \lesssim 0.1$ [79, 80], optical mass-estimators are more likely to have $\sigma_{\ln M} \simeq 0.5$ [81]. We applied a log-normal mass scatter of $\sigma_{\ln M} = 0.5$ to all of our halo masses and repeated the numerical analysis for all the cases (symbols) shown in Fig. 10. The arrows in that figure show the effect of adding the scatter, pointing to the new (higher) value of $\sigma_{f_{\rm NL}}$. We find the effect of the applied mass scatter to be negligible in most of the considered cases (arrows omitted). Only in the case of

one weighted halo bin with knowledge of the dark matter (red filled circles) we observe a moderate weakening in $f_{\mathrm{NL}}$-constraints, especially towards lower $M_{\min}$. This is expected, since we make most heavy use of the halo masses when applying modified mass weighting. Yet, the improvement compared to the uniform one-bin case remains substantial, so the method is still beneficial in the presence of mass scatter.

At higher redshifts, we observe the same characteristics as in the single-tracer case: the $\sigma_{f_{\mathrm{NL}}}$-curves are shifted towards the lower left of the plot in Fig. 11, due to the increase in the effective bias with $z$. Moreover, the impact of mass scatter on $\sigma_{f_{\mathrm{NL}}}$ becomes less severe at higher redshifts, as evident from the smaller arrows in Fig. 11 as compared to Fig. 10. High-redshift data are therefore more promising for constraining $f_{\mathrm{NL}}$. This is good news, since the relatively large effective volume assumed in the current analysis ($V_{\mathrm{eff}} \simeq 50 h^{-3} \mathrm{Gpc}^3$) can only be reached in practical applications when going to $z \sim 1$ or higher.

On the other hand, the convergence of the constraints obtained with and without the dark matter is pushed to even lower halo masses at higher redshifts. This can be seen in Fig. 12, where we show the halo model predictions for even higher redshifts, going up to $z = 5$. With a mass threshold of $M_{\min} = 10^{10} h^{-1} \mathrm{M}_\odot$, the optimal constraints on $f_{\mathrm{NL}}$ from only halos start to saturate above $z \simeq 2$, where $\sigma_{f_{\mathrm{NL}}} \simeq 0.5$. This is however not the case when the dark matter is available: the error on $f_{\mathrm{NL}}$ decreases monotonically up to $z = 5$ reaching $\sigma_{f_{\mathrm{NL}}} \simeq 0.06$, although for practical purposes it will be difficult to achieve this limit. Yet, reaching $\sigma_{f_{\mathrm{NL}}} \sim 1$ at $z = 1$ and $M_{\min} \sim 10^{11} h^{-1} \mathrm{M}_\odot$ with a survey volume of about $50 h^{-3} \mathrm{Gpc}^3$ seems realistic.

## VI.  CONCLUSIONS

The aim of this work is to assess the amount of information on primordial non-Gaussianity that can be extracted from the two-point statistics of halo- and dark matter large-scale structure in light of shot noise suppression and sampling variance cancellation techniques that have been suggested in the literature. For this purpose we developed a theoretical framework for calculating the Fisher information content on $f_{\mathrm{NL}}$ that relies on minimal assumptions for the covariance matrix of halos in Fourier space. The main ingredients of this model are the *effective bias* and the *shot noise matrix*, both of which we measure from $N$-body simulations and compare to analytic predictions. Our results can be summarized as follows:

(i) On large scales the effective bias agrees well with linear theory predictions from the literature, while towards smaller scales, it shows deviations that can be explained by the local bias-expansion model.

The shot noise matrix exhibits two nontrivial eigenvalues $\lambda_+$ and $\lambda_-$, both of which show a considerable dependence on $f_{\mathrm{NL}}$. We further show that the eigenvector $\boldsymbol{V}_+$ is closely related to the second-order bias and that the corresponding eigenvalue $\lambda_+$ depends on the shot noise of the squared dark matter density field $\mathcal{E}_{\delta^2}$, which itself depends on $f_{\mathrm{NL}}$ weakly. This property can become important when constraining $f_{\mathrm{NL}}$ from very high-mass halos (clusters). However, since the Fourier modes of $\mathcal{E}_{\delta^2}$ are highly correlated, it is questionable how much information on primordial non-Gaussianity can be gained from the $f_{\mathrm{NL}}$-dependence of the shot noise matrix. We demonstrate, though, that for the considered values of $f_{\mathrm{NL}}$ the assumption of a Gaussian form of the likelihood function is sufficient to determine the correct Fisher information.

(ii) With the help of $N$-body simulations we demonstrate how the parameter $f_{\mathrm{NL}}$ can be constrained and its error reduced relative to traditional methods by applying optimal weighting- and multiple-tracer techniques to the halos. For our specific simulation setup with $M_{\min} \sim 10^{12} h^{-1} \mathrm{M}_\odot$, we reach almost 1 order of magnitude improvements in $f_{\mathrm{NL}}$-constraints at $z = 0$, even if the dark matter density field is not available. The absolute constraints on $f_{\mathrm{NL}}$ depend on the effective volume and the minimal halo mass that is resolved in the simulations, or observed in the data, and are expected to improve further when higher redshifts or lower-mass halos are considered.

(iii) We confirm the existence of a suppression factor (denoted $q$-factor in the literature) in the amplitude of the linear theory correction to the non-Gaussian halo bias. We argue that this only holds for halos generated with a friends-of-friends finding algorithm and depends on the specified linking length between halo particles. For a linking length of 20% of the mean interparticle distance, our simulations yield $q \simeq 0.8$. For halos generated with a spherical overdensity finder, we demonstrate that the best-fit values of $f_{\mathrm{NL}}$ measured from the simulations are fairly consistent with the input values, i.e., $q \simeq 1$.

(iv) We calculate the Fisher information content from the two-point statistics of halos and dark matter in Fourier space, both analytically and numerically, and express the results in terms of an effective bias, a shot noise matrix and the dark matter power spectrum. In the case of a single mass bin and assuming knowledge of the dark matter density field, the Fisher information is inversely proportional to the shot noise and, therefore, not bounded from above if the shot noise vanishes. However, when only the halo distribution is available, the Fisher

information remains finite even in the limit of zero shot noise. In this case, the amount of information on $f_{\rm NL}$ can only be increased by dividing the halos into multiple mass bins (multiple tracers).

(v) Utilizing the halo model we calculate $\sigma_{f_{\rm NL}}$ and find a remarkable agreement with our simulation results. We show that in the continuous limit of infinite mass bins, optimal constraints on $f_{\rm NL}$ can in principle be achieved even in the case where dark matter observations are not available. With an effective survey volume of $\simeq 50h^{-3}{\rm Gpc}^3$ out to scales of $k_{\rm min} \simeq 0.004h{\rm Mpc}^{-1}$ this means $\sigma_{f_{\rm NL}} \sim 1$ when halos down to $M_{\rm min} \sim 10^{11}h^{-1}{\rm M}_\odot$ are observed at $z = 0$. In comparison to this, a single-tracer method yields $f_{\rm NL}$-constraints that are weaker by about 1 order of magnitude. Further improvements are expected at higher redshifts and lower $M_{\rm min}$, potentially reaching the level of $\sigma_{f_{\rm NL}} \lesssim 0.1$.

(vi) In realistic applications, additional sources of noise, such as a scatter in halo mass will have to be considered. We test the impact of adding a log-normal scatter of $\sigma_{\ln M} = 0.5$ to our halo masses and find our results to be relatively unaffected. Assuming the dark matter to be available to correlate against halos is even more uncertain. Weak-lensing tomography can only measure the dark matter over a broad radial projection and more work is needed to see how far this approach can be pushed. Moreover, one would also need to include weak-lensing ellipticity noise into the analysis, which we have not done here.

We conclude that the shot noise suppression method (modified mass weighting) as presented in [14] when the dark matter density field is available, and the sampling variance cancellation technique (multiple tracers) as proposed in [9] when it is not, have the potential to significantly improve the constraints on primordial non-Gaussianity from current and future large-scale structure data. In [16] it was found (their Fig. 15) that

while the power spectrum analysis of a single tracer with $M_{\rm min} \sim 10^{14}h^{-1}{\rm M}_\odot$ (close to our optimal mass for a single tracer without the dark matter) predicts $\sigma_{f_{\rm NL}} \sim 10$ for $V_{\rm eff} \simeq 50h^{-3}{\rm Gpc}^3$, in good agreement with our results, the bispectrum analysis improves this to $\sigma_{f_{\rm NL}} \sim 5$. Our results suggest that the multitracer analysis of the halo power spectrum can improve upon a single-tracer bispectrum analysis, potentially reaching significantly smaller errors on $f_{\rm NL}$. In principle the multitracer approach can also be applied to the halo bispectrum, but it is not clear how much one can benefit from it, since the dominant terms in the bispectrum do not feature any additional scale dependence that changes with tracer-mass.

In this paper we only focused on primordial non-Gaussianity of the local type and the two-point correlation analysis. Yet, our techniques can be applied to some, but not all, other models of primordial non-Gaussianity, which have only recently been studied in simulations [82–87]. Theoretical calculations of the non-Gaussian halo bias generally suggest different degrees of scale dependence and amplitudes depending on the model [88–92]. Our methods may help to test those various classes of primordial non-Gaussianity and thus provide a tool to probe the physics of the very early Universe.

### Appendix A: FISHER INFORMATION ON PRIMORDIAL NON-GAUSSIANITY FROM THE COVARIANCE OF HALOS

Plugging Eq. (27) into Eq. (26) and using the cyclicity of the trace yields

$$F_{f_{\rm NL}f_{\rm NL}} = \frac{1}{2}{\rm Tr}\left(\frac{\partial \mathbf{C}_{\rm h}}{\partial f_{\rm NL}}\mathbf{C}_{\rm h}^{-1}\frac{\partial \mathbf{C}_{\rm h}}{\partial f_{\rm NL}}\mathbf{C}_{\rm h}^{-1}\right) = \frac{1}{2}{\rm Tr}\left[\left(\boldsymbol{b}'\boldsymbol{b}^{\mathsf{T}}\mathbf{C}_{\rm h}^{-1}P + \boldsymbol{b}\boldsymbol{b}'^{\mathsf{T}}\mathbf{C}_{\rm h}^{-1}P + \boldsymbol{\mathcal{E}}'\mathbf{C}_{\rm h}^{-1}\right)^2\right] =$$

$$= \boldsymbol{b}^{\mathsf{T}}\mathbf{C}_{\rm h}^{-1}\boldsymbol{b}\boldsymbol{b}'^{\mathsf{T}}\mathbf{C}_{\rm h}^{-1}\boldsymbol{b}'P^2 + \boldsymbol{b}^{\mathsf{T}}\mathbf{C}_{\rm h}^{-1}\boldsymbol{b}'\boldsymbol{b}^{\mathsf{T}}\mathbf{C}_{\rm h}^{-1}\boldsymbol{b}'P^2 + 2\boldsymbol{b}^{\mathsf{T}}\mathbf{C}_{\rm h}^{-1}\boldsymbol{\mathcal{E}}'\mathbf{C}_{\rm h}^{-1}\boldsymbol{b}'P + \frac{1}{2}{\rm Tr}\left(\boldsymbol{\mathcal{E}}'\mathbf{C}_{\rm h}^{-1}\boldsymbol{\mathcal{E}}'\mathbf{C}_{\rm h}^{-1}\right). \quad (A1)$$

Applying Eq. (28) yields

$$\boldsymbol{b}^{\intercal}\mathbf{C}_{\mathrm{h}}^{-1}\boldsymbol{b}P = \alpha - \frac{\alpha^2}{1+\alpha} = \frac{\alpha}{1+\alpha} \; , \tag{A2}$$

$$\boldsymbol{b}^{\intercal}\mathbf{C}_{\mathrm{h}}^{-1}\boldsymbol{b}'P = \beta - \frac{\beta\alpha}{1+\alpha} = \frac{\beta}{1+\alpha} \; , \tag{A3}$$

$$\boldsymbol{b}'^{\intercal}\mathbf{C}_{\mathrm{h}}^{-1}\boldsymbol{b}'P = \gamma - \frac{\beta^2}{1+\alpha} = \frac{\gamma + \alpha\gamma - \beta^2}{1+\alpha} \; , \tag{A4}$$

$$\boldsymbol{b}^{\intercal}\mathbf{C}_{\mathrm{h}}^{-1}\boldsymbol{\mathcal{E}}'\mathbf{C}_{\mathrm{h}}^{-1}\boldsymbol{b}'P = \nu - \frac{\alpha\nu + \beta\mu}{1+\alpha} + \frac{\alpha\beta\mu}{(1+\alpha)^2} \; , \tag{A5}$$

$$\frac{1}{2}\mathrm{Tr}\Big(\boldsymbol{\mathcal{E}}'\mathbf{C}_{\mathrm{h}}^{-1}\boldsymbol{\mathcal{E}}'\mathbf{C}_{\mathrm{h}}^{-1}\Big) = \tau + \frac{\rho}{1+\alpha} + \frac{\mu^2/2}{(1+\alpha)^2} \; , \tag{A6}$$

where

$$\alpha \equiv \boldsymbol{b}^{\intercal}\boldsymbol{\mathcal{E}}^{-1}\boldsymbol{b}P \; , \; \beta \equiv \boldsymbol{b}^{\intercal}\boldsymbol{\mathcal{E}}^{-1}\boldsymbol{b}'P \; , \; \gamma \equiv \boldsymbol{b}'^{\intercal}\boldsymbol{\mathcal{E}}^{-1}\boldsymbol{b}'P \; , \tag{A7}$$

$$\mu \equiv -\boldsymbol{b}^{\intercal}\left(\boldsymbol{\mathcal{E}}^{-1}\right)'\boldsymbol{b}P \; , \; \nu \equiv -\boldsymbol{b}^{\intercal}\left(\boldsymbol{\mathcal{E}}^{-1}\right)'\boldsymbol{b}'P \; , \tag{A8}$$

$$\rho \equiv \boldsymbol{b}^{\intercal}\left(\boldsymbol{\mathcal{E}}^{-1}\right)'\boldsymbol{\mathcal{E}}\left(\boldsymbol{\mathcal{E}}^{-1}\right)'\boldsymbol{b}P \; , \tag{A9}$$

$$\tau \equiv \frac{1}{2}\mathrm{Tr}\left(\boldsymbol{\mathcal{E}}'\boldsymbol{\mathcal{E}}^{-1}\boldsymbol{\mathcal{E}}'\boldsymbol{\mathcal{E}}^{-1}\right) \; . \tag{A10}$$

Finally, we get

$$F_{f_{\mathrm{NL}}f_{\mathrm{NL}}} = \frac{(1+\alpha)\,(\alpha\gamma + 2\nu - \rho) + (1-\alpha)\,\beta^2 + (\mu/2 - 2\beta)\,\mu}{(1+\alpha)^2} + \tau \; . \tag{A11}$$

For a single mass bin we have $\alpha\gamma = \beta^2$, $\alpha\nu = \beta\mu$, $\alpha\rho = \mu^2$, $\gamma\rho = \nu^2$ and $\alpha\tau = \rho/2$. In this case, Eq. (A11) becomes

$$F_{f_{\mathrm{NL}}f_{\mathrm{NL}}} = 2\left(\frac{\beta + \sqrt{\tau/2}}{1+\alpha}\right)^2 = 2\left(\frac{bb'P + \mathcal{E}'/2}{b^2P + \mathcal{E}}\right)^2 \; . \tag{A12}$$

## Appendix B: FISHER INFORMATION ON PRIMORDIAL NON-GAUSSIANITY FROM THE COVARIANCE OF HALOS AND DARK MATTER

Now we need to work out Eq. (26) by plugging in Eq. (37) and (38). Let us first note that

$$\frac{\partial \mathbf{C}}{\partial f_{\mathrm{NL}}}\mathbf{C}^{-1} = \begin{pmatrix} -\beta & \boldsymbol{b}'^{\intercal}\boldsymbol{\mathcal{E}}^{-1}P \\ \boldsymbol{b}' - \beta\boldsymbol{b} - \boldsymbol{\mathcal{E}}'\boldsymbol{\mathcal{E}}^{-1}\boldsymbol{b} & \boldsymbol{b}\boldsymbol{b}'^{\intercal}\boldsymbol{\mathcal{E}}^{-1}P + \boldsymbol{\mathcal{E}}'\boldsymbol{\mathcal{E}}^{-1} \end{pmatrix} \; . \tag{B1}$$

This yields

$$\begin{aligned}
F_{f_{\mathrm{NL}}f_{\mathrm{NL}}} = \frac{1}{2}\mathrm{Tr}\big[ & \beta^2 + \boldsymbol{b}'^{\intercal}\boldsymbol{\mathcal{E}}^{-1}\boldsymbol{b}'P - \beta\boldsymbol{b}'^{\intercal}\boldsymbol{\mathcal{E}}^{-1}\boldsymbol{b}P - \boldsymbol{b}'^{\intercal}\boldsymbol{\mathcal{E}}^{-1}\boldsymbol{\mathcal{E}}'\boldsymbol{\mathcal{E}}^{-1}\boldsymbol{b}P + \boldsymbol{b}'\boldsymbol{b}'^{\intercal}\boldsymbol{\mathcal{E}}^{-1}P - \beta\boldsymbol{b}\boldsymbol{b}'^{\intercal}\boldsymbol{\mathcal{E}}^{-1}P \\
& -\boldsymbol{\mathcal{E}}'\boldsymbol{\mathcal{E}}^{-1}\boldsymbol{b}\boldsymbol{b}'^{\intercal}\boldsymbol{\mathcal{E}}^{-1}P + \boldsymbol{b}\boldsymbol{b}'^{\intercal}\boldsymbol{\mathcal{E}}^{-1}\boldsymbol{b}\boldsymbol{b}'^{\intercal}\boldsymbol{\mathcal{E}}^{-1}P^2 + \boldsymbol{b}\boldsymbol{b}'^{\intercal}\boldsymbol{\mathcal{E}}^{-1}\boldsymbol{\mathcal{E}}'\boldsymbol{\mathcal{E}}^{-1}P + \boldsymbol{\mathcal{E}}'\boldsymbol{\mathcal{E}}^{-1}\boldsymbol{b}\boldsymbol{b}'^{\intercal}\boldsymbol{\mathcal{E}}^{-1}P + \boldsymbol{\mathcal{E}}'\boldsymbol{\mathcal{E}}^{-1}\boldsymbol{\mathcal{E}}'\boldsymbol{\mathcal{E}}^{-1}\big] = \\
& = \frac{1}{2}\left(\beta^2 + \gamma - \beta^2 - \nu + \gamma - \beta^2 - \nu + \beta^2 + \nu + \nu + 2\tau\right) = \gamma + \tau \; . \tag{B2}
\end{aligned}$$

## Appendix C: CANCELLATION OF DARK MATTER DENSITY AND COSMIC VARIANCE

In the case where the dark matter density field is known, one can immediately see from the first term in the chi-square of Eq. (35), that with the model $\boldsymbol{\delta}_{\mathrm{h}} = \boldsymbol{b}\delta + \boldsymbol{\epsilon}$ from Eq. (7), the underlying density field $\delta$ is completely canceled (including its sampling variance) and the residual is

$$\langle\chi^2\rangle = \langle\boldsymbol{\epsilon}^{\intercal}\boldsymbol{\mathcal{E}}^{-1}\boldsymbol{\epsilon}\rangle = \mathrm{Tr}\left(\boldsymbol{\mathcal{E}}^{-1}\langle\boldsymbol{\epsilon}\boldsymbol{\epsilon}^{\intercal}\rangle\right) = N \; , \tag{C1}$$

where $N$ is the number of halo bins. If we only consider halos, the first term from Eq. (23) reads

$$\chi^2 = \boldsymbol{\delta}_{\mathrm{h}}^{\mathsf{T}} \mathbf{C}_{\mathrm{h}}^{-1} \boldsymbol{\delta}_{\mathrm{h}} = \boldsymbol{\delta}_{\mathrm{h}}^{\mathsf{T}} \boldsymbol{\mathcal{E}}^{-1} \boldsymbol{\delta}_{\mathrm{h}} - \frac{P}{1+\alpha} \left( \boldsymbol{\delta}_{\mathrm{h}}^{\mathsf{T}} \boldsymbol{\mathcal{E}}^{-1} \boldsymbol{b} \right)^2 \;, \tag{C2}$$

where we used Eq. (28) in the second equality. Plugging in the model $\boldsymbol{\delta}_{\mathrm{h}} = \boldsymbol{b}\delta + \boldsymbol{\epsilon}$, we get

$$\chi^2 = \boldsymbol{b}^{\mathsf{T}} \boldsymbol{\mathcal{E}}^{-1} \boldsymbol{b} \delta^2 + 2\boldsymbol{b}^{\mathsf{T}} \boldsymbol{\mathcal{E}}^{-1} \boldsymbol{\epsilon} \delta + \boldsymbol{\epsilon}^{\mathsf{T}} \boldsymbol{\mathcal{E}}^{-1} \boldsymbol{\epsilon} - \frac{P}{1+\alpha} \left( \boldsymbol{b}^{\mathsf{T}} \boldsymbol{\mathcal{E}}^{-1} \boldsymbol{b} \delta + \boldsymbol{b}^{\mathsf{T}} \boldsymbol{\mathcal{E}}^{-1} \boldsymbol{\epsilon} \right)^2 =$$
$$\left( \alpha - \frac{\alpha^2}{1+\alpha} \right) \frac{\delta^2}{P} + 2\boldsymbol{b}^{\mathsf{T}} \boldsymbol{\mathcal{E}}^{-1} \boldsymbol{\epsilon} \left( 1 - \frac{\alpha}{1+\alpha} \right) \delta + \boldsymbol{\epsilon}^{\mathsf{T}} \boldsymbol{\mathcal{E}}^{-1} \boldsymbol{\epsilon} - \frac{P}{1+\alpha} \left( \boldsymbol{b}^{\mathsf{T}} \boldsymbol{\mathcal{E}}^{-1} \boldsymbol{\epsilon} \right)^2 \;. \tag{C3}$$

A large fraction of the first two terms in the last expression obviously cancel when $\alpha \gg 1$. The quantity $\alpha$, also denoted as *signal-to-noise ratio* in [14], monotonically increases with the number of halo bins $N$. In [14] it was shown to reach $\mathcal{O}(10^2)$ in the continuous limit. Even higher values can be reached when the mass resolution of the simulation is increased [15]. Hence, in the limit $\alpha \gg 1$ the residual of the chi-square in Eq. (C3) becomes

$$\langle \chi^2 \rangle = \frac{\langle \delta^2 \rangle}{P} + 2\boldsymbol{b}^{\mathsf{T}} \boldsymbol{\mathcal{E}}^{-1} \boldsymbol{\epsilon} \frac{\langle \delta \rangle}{\alpha} + \langle \boldsymbol{\epsilon}^{\mathsf{T}} \boldsymbol{\mathcal{E}}^{-1} \boldsymbol{\epsilon} \rangle - \frac{P}{\alpha} \langle \left( \boldsymbol{b}^{\mathsf{T}} \boldsymbol{\mathcal{E}}^{-1} \boldsymbol{\epsilon} \right)^2 \rangle = 1 + N - \frac{\boldsymbol{b}^{\mathsf{T}} \boldsymbol{\mathcal{E}}^{-1} \langle \boldsymbol{\epsilon} \boldsymbol{\epsilon}^{\mathsf{T}} \rangle \boldsymbol{\mathcal{E}}^{-1} \boldsymbol{b}}{\boldsymbol{b}^{\mathsf{T}} \boldsymbol{\mathcal{E}}^{-1} \boldsymbol{b}} = N \;, \tag{C4}$$

the same as in Eq. (C1) with knowledge of the dark matter. Note that in the case of one single halo bin as in Eq. (25), a cancellation neither of the underlying dark matter field, nor of the sampling variance is possible.

## Appendix D: HALO MODEL PREDICTION FOR ALPHA, BETA AND GAMMA

In the halo model the shot noise matrix is given by Eq. (47). In order to invert $\boldsymbol{\mathcal{E}}$, we write $\boldsymbol{\mathcal{E}} = \boldsymbol{\mathcal{A}} - \boldsymbol{\mathcal{M}} \boldsymbol{b}^{\mathsf{T}}$ with $\boldsymbol{\mathcal{A}} \equiv \bar{n}^{-1} \mathbf{I} - \boldsymbol{b} \boldsymbol{\mathcal{M}}^{\mathsf{T}}$ and apply the Sherman-Morrison formula:

$$\boldsymbol{\mathcal{E}}^{-1} = \boldsymbol{\mathcal{A}}^{-1} + \frac{\boldsymbol{\mathcal{A}}^{-1} \boldsymbol{\mathcal{M}} \boldsymbol{b}^{\mathsf{T}} \boldsymbol{\mathcal{A}}^{-1}}{1 - \boldsymbol{b}^{\mathsf{T}} \boldsymbol{\mathcal{A}}^{-1} \boldsymbol{\mathcal{M}}} \;. \tag{D1}$$

Likewise, we apply the Sherman-Morrison formula to invert $\boldsymbol{\mathcal{A}}$:

$$\boldsymbol{\mathcal{A}}^{-1} = \bar{n} \mathbf{I} + \frac{\boldsymbol{b} \boldsymbol{\mathcal{M}}^{\mathsf{T}} \bar{n}}{\bar{n}^{-1} - \boldsymbol{\mathcal{M}}^{\mathsf{T}} \boldsymbol{b}} \;. \tag{D2}$$

With

$$\alpha \equiv \boldsymbol{b}^{\mathsf{T}} \boldsymbol{\mathcal{E}}^{-1} \boldsymbol{b} P = \frac{\boldsymbol{b}^{\mathsf{T}} \boldsymbol{\mathcal{A}}^{-1} \boldsymbol{b}}{1 - \boldsymbol{b}^{\mathsf{T}} \boldsymbol{\mathcal{A}}^{-1} \boldsymbol{\mathcal{M}}} P \;, \tag{D3}$$

$$\beta \equiv \boldsymbol{b}^{\mathsf{T}} \boldsymbol{\mathcal{E}}^{-1} \boldsymbol{b}' P = \frac{\boldsymbol{b}^{\mathsf{T}} \boldsymbol{\mathcal{A}}^{-1} \boldsymbol{b}'}{1 - \boldsymbol{b}^{\mathsf{T}} \boldsymbol{\mathcal{A}}^{-1} \boldsymbol{\mathcal{M}}} P \;, \tag{D4}$$

$$\gamma \equiv \boldsymbol{b}'^{\mathsf{T}} \boldsymbol{\mathcal{E}}^{-1} \boldsymbol{b}' P = \frac{\boldsymbol{b}'^{\mathsf{T}} \boldsymbol{\mathcal{A}}^{-1} \boldsymbol{b}' \left( 1 - \boldsymbol{b}^{\mathsf{T}} \boldsymbol{\mathcal{A}}^{-1} \boldsymbol{\mathcal{M}} \right) + \boldsymbol{b}'^{\mathsf{T}} \boldsymbol{\mathcal{A}}^{-1} \boldsymbol{\mathcal{M}} \boldsymbol{b}^{\mathsf{T}} \boldsymbol{\mathcal{A}}^{-1} \boldsymbol{b}'}{1 - \boldsymbol{b}^{\mathsf{T}} \boldsymbol{\mathcal{A}}^{-1} \boldsymbol{\mathcal{M}}} P \;, \tag{D5}$$

and

$$\boldsymbol{b}^{\mathsf{T}} \boldsymbol{\mathcal{A}}^{-1} \boldsymbol{b} = \frac{\boldsymbol{b}^{\mathsf{T}} \boldsymbol{b}}{\bar{n}^{-1} - \boldsymbol{\mathcal{M}}^{\mathsf{T}} \boldsymbol{b}} \;, \tag{D6}$$

$$\boldsymbol{b}^{\mathsf{T}} \boldsymbol{\mathcal{A}}^{-1} \boldsymbol{\mathcal{M}} = \frac{\boldsymbol{\mathcal{M}}^{\mathsf{T}} \boldsymbol{b} \left( \bar{n}^{-1} - \boldsymbol{\mathcal{M}}^{\mathsf{T}} \boldsymbol{b} \right) + \boldsymbol{b}^{\mathsf{T}} \boldsymbol{b} \boldsymbol{\mathcal{M}}^{\mathsf{T}} \boldsymbol{\mathcal{M}}}{\bar{n}^{-1} - \boldsymbol{\mathcal{M}}^{\mathsf{T}} \boldsymbol{b}} \bar{n} \;, \tag{D7}$$

$$\boldsymbol{b}^{\mathsf{T}} \boldsymbol{\mathcal{A}}^{-1} \boldsymbol{b}' = \frac{\boldsymbol{b}^{\mathsf{T}} \boldsymbol{b}' \left( \bar{n}^{-1} - \boldsymbol{\mathcal{M}}^{\mathsf{T}} \boldsymbol{b} \right) + \boldsymbol{b}^{\mathsf{T}} \boldsymbol{b} \boldsymbol{\mathcal{M}}^{\mathsf{T}} \boldsymbol{b}'}{\bar{n}^{-1} - \boldsymbol{\mathcal{M}}^{\mathsf{T}} \boldsymbol{b}} \bar{n} \;, \tag{D8}$$

$$\boldsymbol{b}'^{\mathsf{T}} \boldsymbol{\mathcal{A}}^{-1} \boldsymbol{\mathcal{M}} = \frac{\boldsymbol{\mathcal{M}}^{\mathsf{T}} \boldsymbol{b}' \left( \bar{n}^{-1} - \boldsymbol{\mathcal{M}}^{\mathsf{T}} \boldsymbol{b} \right) + \boldsymbol{b}^{\mathsf{T}} \boldsymbol{b}' \boldsymbol{\mathcal{M}}^{\mathsf{T}} \boldsymbol{\mathcal{M}}}{\bar{n}^{-1} - \boldsymbol{\mathcal{M}}^{\mathsf{T}} \boldsymbol{b}} \bar{n} \;, \tag{D9}$$

$$\boldsymbol{b}'^{\mathsf{T}} \boldsymbol{\mathcal{A}}^{-1} \boldsymbol{b}' = \frac{\boldsymbol{b}'^{\mathsf{T}} \boldsymbol{b}' \left( \bar{n}^{-1} - \boldsymbol{\mathcal{M}}^{\mathsf{T}} \boldsymbol{b} \right) + \boldsymbol{b}^{\mathsf{T}} \boldsymbol{b}' \boldsymbol{\mathcal{M}}^{\mathsf{T}} \boldsymbol{b}'}{\bar{n}^{-1} - \boldsymbol{\mathcal{M}}^{\mathsf{T}} \boldsymbol{b}} \bar{n} \;, \tag{D10}$$

after some algebra we get

$$\alpha = \frac{\boldsymbol{b}^{\mathsf{T}}\boldsymbol{b}}{\lambda_+\lambda_-}\bar{n}^{-1}P \,, \tag{D11}$$

$$\beta = \frac{\boldsymbol{b}^{\mathsf{T}}\boldsymbol{b}'\left(\bar{n}^{-1} - \boldsymbol{\mathcal{M}}^{\mathsf{T}}\boldsymbol{b}\right) + \boldsymbol{b}^{\mathsf{T}}\boldsymbol{b}\boldsymbol{\mathcal{M}}^{\mathsf{T}}\boldsymbol{b}'}{\lambda_+\lambda_-}P \,, \tag{D12}$$

$$\gamma = \boldsymbol{b}'^{\mathsf{T}}\boldsymbol{b}'\bar{n}P + \frac{\boldsymbol{b}^{\mathsf{T}}\boldsymbol{b}\left(\boldsymbol{\mathcal{M}}^{\mathsf{T}}\boldsymbol{b}'\right)^2 + \boldsymbol{\mathcal{M}}^{\mathsf{T}}\boldsymbol{\mathcal{M}}\left(\boldsymbol{b}^{\mathsf{T}}\boldsymbol{b}'\right)^2 + 2\boldsymbol{b}^{\mathsf{T}}\boldsymbol{b}'\boldsymbol{\mathcal{M}}^{\mathsf{T}}\boldsymbol{b}'\left(\bar{n}^{-1} - \boldsymbol{\mathcal{M}}^{\mathsf{T}}\boldsymbol{b}\right)}{\lambda_+\lambda_-}\bar{n}P \,, \tag{D13}$$

with $\lambda_+\lambda_- = \left(\bar{n}^{-1} - \boldsymbol{\mathcal{M}}^{\mathsf{T}}\boldsymbol{b}\right)^2 - \boldsymbol{b}^{\mathsf{T}}\boldsymbol{b}\boldsymbol{\mathcal{M}}^{\mathsf{T}}\boldsymbol{\mathcal{M}}$. According to Eq. (3) we can write $\boldsymbol{b}' = (\boldsymbol{b} - \mathbb{1})\,u$. Moreover, in the continuous limit we can exchange the vector products by integrals as in Eq. (55). This finally yields

$$\alpha = \frac{\langle b^2\rangle}{\left(\bar{n}_{\mathrm{tot}}^{-1} - \langle\mathcal{M}b\rangle\right)^2 - \langle b^2\rangle\langle\mathcal{M}^2\rangle}\bar{n}_{\mathrm{tot}}^{-1}P \,, \tag{D14}$$

$$\beta = \frac{\left(\langle b^2\rangle - \langle b\rangle\right)\left(\bar{n}_{\mathrm{tot}}^{-1} - \langle\mathcal{M}b\rangle\right) + \langle b^2\rangle\left(\langle\mathcal{M}b\rangle - \langle\mathcal{M}\rangle\right)}{\left(\bar{n}_{\mathrm{tot}}^{-1} - \langle\mathcal{M}b\rangle\right)^2 - \langle b^2\rangle\langle\mathcal{M}^2\rangle}uP \,, \tag{D15}$$

$$\begin{aligned}\gamma = {}&\left(\langle b^2\rangle - 2\langle b\rangle + 1\right)\bar{n}_{\mathrm{tot}}u^2P \\ &+ \frac{\langle b^2\rangle\left(\langle\mathcal{M}b\rangle - \langle\mathcal{M}\rangle\right)^2 + \langle\mathcal{M}^2\rangle\left(\langle b^2\rangle - \langle b\rangle\right)^2 + 2\left(\langle b^2\rangle - \langle b\rangle\right)\left(\langle\mathcal{M}b\rangle - \langle\mathcal{M}\rangle\right)\left(\bar{n}_{\mathrm{tot}}^{-1} - \langle\mathcal{M}b\rangle\right)}{\left(\bar{n}_{\mathrm{tot}}^{-1} - \langle\mathcal{M}b\rangle\right)^2 - \langle b^2\rangle\langle\mathcal{M}^2\rangle}\bar{n}_{\mathrm{tot}}u^2P \,.\end{aligned} \tag{D16}$$

[1] E. Komatsu, Classical and Quantum Gravity **27**, 124010 (2010), 1003.6097.

[2] N. Bartolo, S. Matarrese, and A. Riotto, Advances in Astronomy **2010** (2010), 1001.3957.

[3] M. Liguori, E. Sefusatti, J. R. Fergusson, and E. P. S. Shellard, Advances in Astronomy **2010** (2010), 1001.4707.

[4] A. P. S. Yadav and B. D. Wandelt, Advances in Astronomy **2010** (2010), 1006.0275.

[5] E. Komatsu, K. M. Smith, J. Dunkley, C. L. Bennett, B. Gold, G. Hinshaw, N. Jarosik, D. Larson, M. R. Nolta, L. Page, et al., ApJS **192**, 18 (2011), 1001.4538.

[6] V. Desjacques and U. Seljak, Classical and Quantum Gravity **27**, 124011 (2010), 1003.5020.

[7] L. Verde, Advances in Astronomy **2010** (2010), 1001.5217.

[8] N. Dalal, O. Doré, D. Huterer, and A. Shirokov, Phys. Rev. D **77**, 123514 (2008), 0710.4560.

[9] U. Seljak, Physical Review Letters **102**, 021302 (2009), 0807.1770.

[10] A. Slosar, J. Cosmology Astropart. Phys. **3**, 4 (2009), 0808.0044.

[11] P. McDonald and U. Seljak, J. Cosmology Astropart. Phys. **10**, 7 (2009), 0810.0323.

[12] H. Gil-Marín, C. Wagner, L. Verde, R. Jimenez, and A. F. Heavens, MNRAS **407**, 772 (2010), 1003.3238.

[13] U. Seljak, N. Hamaus, and V. Desjacques, Phys. Rev. Lett. **103**, 091303 (2009), 0904.2963.

[14] N. Hamaus, U. Seljak, V. Desjacques, R. E. Smith, and T. Baldauf, Phys. Rev. D **82**, 043515 (2010), 1004.5377.

[15] Y. Cai, G. Bernstein, and R. K. Sheth, MNRAS **412**, 995 (2011), 1007.3500.

[16] T. Baldauf, U. Seljak, and L. Senatore, J. Cosmology Astropart. Phys. **4**, 6 (2011), 1011.1513.

[17] D. S. Salopek and J. R. Bond, Phys. Rev. D **42**, 3936 (1990).

[18] A. Gangui, F. Lucchin, S. Matarrese, and S. Mollerach, ApJ **430**, 447 (1994), arXiv:astro-ph/9312033.

[19] E. Komatsu and D. N. Spergel, Phys. Rev. D **63**, 063002 (2001), arXiv:astro-ph/0005036.

[20] N. Bartolo, E. Komatsu, S. Matarrese, and A. Riotto, Phys. Rep. **402**, 103 (2004), arXiv:astro-ph/0406398.

[21] S. Matarrese and L. Verde, ApJ **677**, L77 (2008), 0801.4826.

[22] A. Slosar, C. Hirata, U. Seljak, S. Ho, and N. Padmanabhan, J. Cosmology Astropart. Phys. **8**, 31 (2008), 0805.3580.

[23] T. Giannantonio and C. Porciani, Phys. Rev. D **81**, 063530 (2010), 0911.0017.

[24] D. Jeong and E. Komatsu, ApJ **703**, 1230 (2009), 0904.0497.

[25] E. Sefusatti, Phys. Rev. D **80**, 123002 (2009), 0905.0717.

[26] P. McDonald, Phys. Rev. D **78**, 123519 (2008), 0806.1061.

[27] L. Gao, V. Springel, and S. D. M. White, MNRAS **363**, L66 (2005), arXiv:astro-ph/0506510.

[28] L. Gao and S. D. M. White, MNRAS **377**, L5 (2007), arXiv:astro-ph/0611921.

[29] B. A. Reid, L. Verde, K. Dolag, S. Matarrese, and L. Moscardini, J. Cosmology Astropart. Phys. **7**, 13 (2010), 1004.1637.

[30] M. Manera and E. Gaztañaga, MNRAS **415**, 383 (2011), 0912.0446.

[31] V. Desjacques, U. Seljak, and I. T. Iliev, MNRAS **396**, 85 (2009), 0811.2748.

[32] A. Pillepich, C. Porciani, and O. Hahn, MNRAS **402**, 191 (2010), 0811.4176.

[33] R. E. Smith, V. Desjacques, and L. Marian, Phys. Rev. D **83**, 043526 (2011), 1009.5085.

[34] J. N. Fry and E. Gaztanaga, ApJ **413**, 447 (1993), arXiv:astro-ph/9302009.

[35] H. J. Mo and S. D. M. White, MNRAS **282**, 347 (1996), arXiv:astro-ph/9512127.

[36] P. McDonald, Phys. Rev. D **74**, 103512 (2006), arXiv:astro-ph/0609413.

[37] K. M. Smith and M. LoVerde, J. Cosmology Astropart. Phys. **11**, 9 (2011), 1010.0055.

[38] U. Seljak, MNRAS **318**, 203 (2000), arXiv:astro-ph/0001493.

[39] M. Crocce and R. Scoccimarro, Phys. Rev. D **77**, 023533 (2008), 0704.2783.

[40] R. K. Sheth and G. Tormen, MNRAS **308**, 119 (1999), arXiv:astro-ph/9901122.

[41] R. Scoccimarro, R. K. Sheth, L. Hui, and B. Jain, ApJ **546**, 20 (2001), arXiv:astro-ph/0006319.

[42] A. F. Heavens, S. Matarrese, and L. Verde, MNRAS **301**, 797 (1998), arXiv:astro-ph/9808016.

[43] C. Carbone, L. Verde, and S. Matarrese, ApJ **684**, L1 (2008), 0806.1950.

[44] N. Afshordi and A. J. Tolley, Phys. Rev. D **78**, 123507 (2008), 0806.1046.

[45] R. A. Fisher, Roy. Stat. Soc. **98**, 39 (1935).

[46] M. Tegmark, A. N. Taylor, and A. F. Heavens, ApJ **480**, 22 (1997), arXiv:astro-ph/9603021.

[47] A. Heavens, ArXiv e-prints (2009), 0906.0664.

[48] J. Sherman and W. J. Morrison, Ann. Math. Stat. **21**, 124 (1950).

[49] M. S. Bartlett, Ann. Math. Stat. **22**, pp. 107 (1951), ISSN 00034851.

[50] U. Pen, MNRAS **350**, 1445 (2004), arXiv:astro-ph/0402008.

[51] E. Komatsu, J. Dunkley, M. R. Nolta, C. L. Bennett, B. Gold, G. Hinshaw, N. Jarosik, D. Larson, M. Limon, L. Page, et al., ApJS **180**, 330 (2009), 0803.0547.

[52] V. Springel, MNRAS **364**, 1105 (2005), arXiv:astro-ph/0505010.

[53] M. Davis, G. Efstathiou, C. S. Frenk, and S. D. M. White, ApJ **292**, 371 (1985).

[54] S. P. D. Gill, A. Knebe, and B. K. Gibson, MNRAS **351**, 399 (2004), arXiv:astro-ph/0404258.

[55] C. Lacey and S. Cole, MNRAS **271**, 676 (1994), arXiv:astro-ph/9402069.

[56] V. R. Eke, S. Cole, and C. S. Frenk, MNRAS **282**, 263 (1996), arXiv:astro-ph/9601088.

[57] R. W. Hockney and J. W. Eastwood, *Computer simulation using particles* (1988).

[58] A. Knebe, S. R. Knollmann, S. I. Muldrew, F. R. Pearce, M. A. Aragon-Calvo, Y. Ascasibar, P. S. Behroozi, D. Ceverino, S. Colombi, J. Diemand, et al., MNRAS **415**, 2293 (2011), 1104.0949.

[59] M. Grossi, L. Verde, C. Carbone, K. Dolag, E. Branchini, F. Iannuzzi, S. Matarrese, and L. Moscardini, MNRAS **398**, 321 (2009), 0902.2013.

[60] A. A. Berlind and D. H. Weinberg, ApJ **575**, 587 (2002), arXiv:astro-ph/0109001.

[61] U. Maio and F. Iannuzzi, MNRAS **415**, 3021 (2011), 1103.3183.

[62] R. K. Sheth, H. J. Mo, and G. Tormen, MNRAS **323**, 1 (2001), arXiv:astro-ph/9907024.

[63] P. Valageas, A&A **514**, A46+ (2010), 0906.1042.

[64] S. More, A. V. Kravtsov, N. Dalal, and S. Gottlöber, ApJS **195**, 4 (2011), 1103.0005.

[65] V. Desjacques and U. Seljak, Advances in Astronomy **2010**, 908640 (2010), 1006.4763.

[66] C. Carbone, O. Mena, and L. Verde, J. Cosmology Astropart. Phys. **7**, 20 (2010), 1003.0456.

[67] J. Yoo, Phys. Rev. D **79**, 023517 (2009), 0808.3138.

[68] J. Yoo, A. L. Fitzpatrick, and M. Zaldarriaga, Phys. Rev. D **80**, 083514 (2009), 0907.0707.

[69] J. Yoo, Phys. Rev. D **82**, 083508 (2010), 1009.3021.

[70] P. McDonald, J. Cosmology Astropart. Phys. **11**, 26 (2009), 0907.5220.

[71] C. Bonvin and R. Durrer, Phys. Rev. D **84**, 063505 (2011), 1105.5280.

[72] A. Challinor and A. Lewis, Phys. Rev. D **84**, 043516 (2011), 1105.5292.

[73] T. Baldauf, U. Seljak, L. Senatore, and M. Zaldarriaga, J. Cosmology Astropart. Phys. **10**, 31 (2011), 1106.5507.

[74] D. Wands and A. Slosar, Phys. Rev. D **79**, 123507 (2009), 0902.1084.

[75] M. Bruni, R. Crittenden, K. Koyama, R. Maartens, C. Pitrou, and D. Wands, Phys. Rev. D **85**, 041301 (2012), 1106.3999.

[76] D. Jeong, F. Schmidt, and C. M. Hirata, Phys. Rev. D **85**, 023504 (2012), 1107.5427.

[77] J. Yoo, N. Hamaus, U. Seljak, and M. Zaldarriaga, ArXiv e-prints (2011), 1109.0998.

[78] A. Kiessling, A. N. Taylor, and A. F. Heavens, MNRAS **416**, 1045 (2011), 1103.3245.

[79] A. V. Kravtsov, A. Vikhlinin, and D. Nagai, ApJ **650**, 128 (2006), arXiv:astro-ph/0603205.

[80] D. Fabjan, S. Borgani, E. Rasia, A. Bonafede, K. Dolag, G. Murante, and L. Tornatore, MNRAS **416**, 801 (2011), 1102.2903.

[81] E. Rozo, E. S. Rykoff, A. Evrard, M. Becker, T. McKay, R. H. Wechsler, B. P. Koester, J. Hao, S. Hansen, E. Sheldon, et al., ApJ **699**, 768 (2009), 0809.2794.

[82] A. Taruya, K. Koyama, and T. Matsubara, Phys. Rev. D **78**, 123534 (2008), 0808.4085.

[83] N. Bartolo, J. P. Beltrán Almeida, S. Matarrese, M. Pietroni, and A. Riotto, J. Cosmology Astropart. Phys. **3**, 11 (2010), 0912.4276.

[84] V. Desjacques and U. Seljak, Phys. Rev. D **81**, 023006 (2010), 0907.2257.

[85] C. Wagner, L. Verde, and L. Boubekeur, J. Cosmology Astropart. Phys. **10**, 22 (2010), 1006.5793.

[86] C. Fedeli, C. Carbone, L. Moscardini, and A. Cimatti, MNRAS **414**, 1545 (2011), 1012.2305.

[87] C. Wagner and L. Verde, J. Cosmology Astropart. Phys. **3**, 2 (2012), 1102.3229.

[88] L. Verde and S. Matarrese, ApJ **706**, L91 (2009), 0909.3224.

[89] E. Sefusatti, M. Liguori, A. P. S. Yadav, M. G. Jackson, and E. Pajer, J. Cosmology Astropart. Phys. **12**, 22 (2009), 0906.0232.

[90] F. Schmidt and M. Kamionkowski, Phys. Rev. D **82**, 103002 (2010), 1008.0638.

[91] S. Shandera, N. Dalal, and D. Huterer, J. Cosmology Astropart. Phys. **3**, 17 (2011), 1010.3722.

[92] A. Becker, D. Huterer, and K. Kadota, J. Cosmology Astropart. Phys. **1**, 6 (2011), 1009.4189.

# 5

## PAPER IV

**Summary**    Another application for the methods developed above is the analysis of redshift-space distortions (RSD) in spectroscopic galaxy surveys. It has been demonstrated that the use of multiple tracers allows to measure the RSD parameter $\beta$ without cosmic variance limitation. The accuracy to determine $\beta$ is then only limited by the shot noise of the tracers, which can be reduced through optimal weighting. On the basis of $N$-body simulations, the following article investigates the combination of optimal weights and multiple tracers to improve constraints on the RSD parameter. By means of a Fisher analysis it is shown that the best constraints can be achieved when the two principal components of the clustering signal-to-noise ratio of halos are considered only. These two principal components correspond to the two non-Poisson eigenmodes of the shot noise matrix found in paper II. Although one of them exhibits a super-Poissonian shot noise level, a combination of the two eigenmodes is beneficial due to their large relative bias. The inclusion of three-dimensional dark matter maps into the analysis breaks the degeneracy between halo bias, normalization of the power spectrum and growth rate. Using optimal weights, it is demonstrated that the gains in the accuracy on the growth rate can potentially be even much higher.

The contributions of the three authors of this paper are as follows: Uroš Seljak motivated the RSD analysis as a possible application of the methods described above. I conducted the numerical analysis using $N$-body simulations provided by Vincent Desjacques, and composed the manuscript in consultation with Uroš Seljak. It has been submitted to *Physical Review D* in July 2012 and is currently under review.

# Optimal Weighting in Galaxy Surveys:
## Application to Redshift-Space Distortions

Nico Hamaus,[1, *] Uroš Seljak,[1, 2, 3] and Vincent Desjacques[4]

[1] *Institute for Theoretical Physics, University of Zurich, 8057 Zurich, Switzerland*
[2] *Physics Department, Astronomy Department and Lawrence Berkeley National Laboratory,*
*University of California, Berkeley, California 94720, USA*
[3] *Ewha University, Seoul 120-750, S. Korea*
[4] *Département de Physique Théorique & Center for Astroparticle Physics,*
*Université de Genève, 24 Quai Ernest Ansermet, 1211 Genève 4, Switzerland*
(Dated: July 4, 2012)

Using multiple tracers of large-scale structure allows to evade the limitations imposed by sampling variance for some parameters of interest in cosmology. We demonstrate the optimal way of carrying out a multitracer analysis in a galaxy redshift survey by considering the principal components of the shot noise matrix from two-point clustering statistics. We show how to construct two tracers that maximize the benefits of sampling variance and shot noise cancellation using optimal weights. On the basis of high-resolution $N$-body simulations of dark matter halos we apply this technique to the analysis of redshift-space distortions and demonstrate how constraints on the growth rate of structure formation can be substantially improved. The primary limitations are nonlinear effects, which cause significant biases in the method already at scales of $k < 0.1h\mathrm{Mpc}^{-1}$, suggesting the need to develop nonlinear models of redshift-space distortions in order to extract the maximum information from future redshift surveys. Nonetheless we find gains of a factor of a few in constraints on the growth rate achievable when merely the linear regime of a galaxy survey like EUCLID is considered.

## I. INTRODUCTION

One of the deepest mysteries of contemporary cosmology is the nature of the observed accelerated expansion of the Universe. So far, its evolution can be described remarkably well by Einstein's theory of gravitation including a nonzero cosmological constant $\Lambda$. However, in order to fit the astronomical observations (e.g., [1]), $\Lambda$ must be many orders of magnitude smaller than what our standard model of particle physics would expect. This *hierarchy problem* inspired various departures from the cosmological standard model, such as modifications of Einstein's field equations or the introduction of exotic forms of matter.

A particularly sensitive probe of cosmology is the large-scale structure (LSS) of the Universe. Galaxy redshift surveys map out large fractions of its observable volume and thereby reconstruct a three-dimensional map of density fluctuations whose statistical properties directly relate to fundamental cosmological parameters [2–4]. Unfortunately, this reconstruction is hampered by the fact that galaxies are *biased* and *stochastic* tracers of the dominating dark matter density field. Even if the density field could be inferred perfectly well, the finite number $N_k$ of independent Fourier modes in the survey sets a fundamental lower limit on the achievable uncertainty, which is known as *sampling variance* (or *cosmic variance*, in case the survey size is the whole observable Universe). For example, in a measurement of the dark matter power spectrum $P$, the sampling variance limit is given by $\sigma_P/P \geq \sqrt{2/N_k}$, an uncertainty floor that propagates into all the parameters one wants to infer from $P$. This limit decreases towards smaller scales as more and more Fourier modes can be sampled, but at the same time linear theory starts to break down and higher-order perturbation theory has to be adopted to model $P$ (see, e.g., [5–8]). Further complication arises in relating the observed galaxy power spectrum to the latter, as galaxy bias becomes nonlinear and nonlocal [9, 10].

An alternative approach to accurately probe cosmological parameters is to consider multiple tracers of the density field within the well-understood linear regime. The relative clustering amplitude between multiple tracers can be inferred without sampling variance limitation because the underlying density fluctuations cancel out in taking ratios [11, 12]. Therefore, any cosmological information that remains in the relative clustering amplitude between different tracers can potentially be inferred with a much higher accuracy.

In this paper we focus on a particular contribution to the clustering amplitude of galaxies coming from redshift-space distortions (RSD). These are caused by peculiar velocities along the line of sight, causing their clustering statistics to become anisotropic. First treated as a contamination, this effect has been realized to be a powerful probe of cosmology, as an understanding of RSD allows to infer the growth rate of structure formation, which is directly tied to the expansion history of the Universe as well as the theory of gravity (e.g., [13–23]).

After recapping the fundamentals of RSD and introducing a general formalism for the multitracer analysis

* hamaus@physik.uzh.ch

in Sec. II, we present our results on the RSD analysis from $N$-body simulations in Sec. III. Finally we draw our conclusions in Sec. IV.

## II. FORMALISM

### A. Galaxies in redshift space

In galaxy surveys, radial distances are inferred via the individual redshift of objects, assuming they follow the Hubble flow. Due to gravitational attraction, however, galaxies (respectively, their host halos) build up peculiar velocities $\mathbf{v}$ which contribute to their redshift via the Doppler effect. Hence, the real-space and redshift-space locations $\mathbf{r}$ and $\mathbf{s}$ of a galaxy are related as

$$\mathbf{s} = \mathbf{r} + \frac{\mathbf{v} \cdot \hat{\mathbf{r}}}{H(z)} \hat{\mathbf{r}} \, , \tag{1}$$

where $\hat{\mathbf{r}}$ is the unit vector along the line of sight and $H(z)$ is the Hubble constant as a function of redshift $z$. On large scales, gravity causes coherent infall of test particles into the potential wells of the dark matter. Thus, galaxies are moving towards overdense regions in the Universe, resulting in an enhancement of their inferred overdensity along the line of sight. According to linear perturbation theory, the redshift-space and real-space galaxy overdensities are related as

$$\delta_{\mathrm{g}}^{(s)}(\mathbf{k}, \mu) = \delta_{\mathrm{g}}^{(r)}(\mathbf{k}) + f\mu^2 \delta(\mathbf{k}) \, , \tag{2}$$

where $\mu$ the cosine of the angle between any wave vector $\mathbf{k}$ in the survey and the line of sight, $\delta$ the dark matter overdensity field and $f$ the *growth rate* of structure. This well-known result [24] further makes use of the plane-parallel approximation, assuming the separation of any galaxy pair to be much smaller than their distance to the observer. On nonlinear scales, random motions are generated in the process of virialization, which causes a damping in the clustering amplitude of galaxies along the line of sight. This so-called Finger-of-God effect is often modeled phenomenologically by an additional Gaussian damping factor in Eq. (2) [25], but more elaborate schemes have been developed (e.g., [26–34]). We will neglect nonlinear corrections in this paper and focus on the large linear scales.

The growth rate $f$ is the logarithmic derivative of the growth factor $D$ with respect to the scale factor $a$. In linear theory, it can be expressed as

$$f \equiv d\ln D / d\ln a \simeq \Omega_{\mathrm{m}}^{\gamma} \, , \tag{3}$$

with the matter density parameter $\Omega_{\mathrm{m}}$ and the *growth index* $\gamma$ [35]. In Einstein gravity the value of $\gamma$ is about 0.55, but can take on distinctly different values in modified gravity scenarios [36]. Therefore, constraints on the

growth rate can provide viable tests on the theory of gravitation.

Galaxies only form in specific, discrete locations of the density field; they are referred to as *biased* and *stochastic* tracers of the dark matter. On linear scales, this relation can be described locally by

$$\delta_{\mathrm{g}}^{(r)}(\mathbf{r}) = b_{\mathrm{g}}\delta(\mathbf{r}) + \epsilon \, , \tag{4}$$

where the factor $b_{\mathrm{g}}$ is the *linear galaxy bias* and $\epsilon$ a random variable denoted as *shot noise*, describing the stochastic nature of this relation. Both $b_{\mathrm{g}}$ and $\epsilon$ depend on redshift, as well as various properties of the type of galaxies one is considering (e.g., luminosity, color, host-halo mass).

Together with Eq. (2) this yields a model for the overdensity field of galaxies in redshift space,

$$\delta_{\mathrm{g}}^{(s)}(\mathbf{k}, \mu) = \left( b_{\mathrm{g}} + f\mu^2 \right) \delta(\mathbf{k}) + \epsilon \, . \tag{5}$$

Since the phenomena of galaxy biasing and RSD are to multiply the density field $\delta$ by some factor, we can simply define a more general *effective bias* parameter $b$ that contains both contributions,

$$b \equiv b_{\mathrm{g}} + f\mu^2 \, . \tag{6}$$

In the following, we will drop the superscript that distinguishes between real-space and redshift-space quantities for clarity. If not explicitly mentioned otherwise, all symbols should be understood as given in redshift space.

### B. Multiple tracers

In order to exploit the gains of sampling variance and shot noise cancellation, we need to consider multiple tracers of the dark matter density field [11, 12]. One way to achieve this is splitting some galaxy catalog into bins of a certain observable property of the galaxies (like luminosity, color, host-halo mass, etc.). However, the following framework is not limited to galaxies and may be adopted for other tracers of the dark matter density field as well.

#### 1. Covariance matrix

We start by writing the density fields of $N$ tracers as a vector $\boldsymbol{\delta}_{\mathrm{g}} \equiv (\delta_{\mathrm{g}_1}, \delta_{\mathrm{g}_2}, \ldots, \delta_{\mathrm{g}_N})$. The outer product of this vector, once ensemble averaged within a $k$-shell in Fourier space, yields the covariance matrix $\mathbf{C} \equiv \langle \boldsymbol{\delta}_{\mathrm{g}} \boldsymbol{\delta}_{\mathrm{g}}^{\dagger} \rangle$, where the $^{\dagger}$ symbol denotes the Hermitian conjugate (transpose and complex conjugation). Plugging in the model for galaxy overdensities in redshift space from Eq. (5), it reads

$$\mathbf{C} = \boldsymbol{b}\boldsymbol{b}^{\dagger}P + \boldsymbol{\mathcal{E}} \, , \tag{7}$$

with the effective bias vector $\boldsymbol{b} = \boldsymbol{b}_{\mathrm{g}} + f\mu^2\mathbf{I}$, the dark matter power spectrum $P \equiv \langle\delta\delta^*\rangle$ and the *shot noise matrix* $\boldsymbol{\mathcal{E}} \equiv \langle\boldsymbol{\epsilon}\boldsymbol{\epsilon}^\dagger\rangle$ (by definition $\langle\boldsymbol{\epsilon}\delta^*\rangle = 0$). The covariance matrix contains all auto-power and cross-power spectra of the considered tracers, so in total $N(N-1)/2$ independent elements per $k$-shell. However, since all tracers follow the same dark matter density distribution, these elements are correlated.

Let us compare the analysis for a single tracer with the one for two tracers. From a single tracer we can only observe an estimator of its auto-power spectrum

$$C(k,\mu) = \left(1 + \beta\mu^2\right)^2 b_{\mathrm{g}}^2 P(k) + \mathcal{E} \ , \qquad (8)$$

where we define $\beta \equiv f/b_{\mathrm{g}}$. In this parametrization it is obvious to see that $b_{\mathrm{g}}$ is degenerate with the power spectrum $P$; respectively, its normalization $\sigma_8$ defined via

$$P \equiv \sigma_8^2 P_0 \ , \qquad (9)$$

where $P_0$ describes the shape of the power spectrum and is assumed to be known, at least up to linear order. From Eq. (8), only the combination $b_{\mathrm{g}}^2 P$ can be determined at $\mu = 0$ (usually, the shot noise is assumed to be Poissonian, meaning it is scale independent and given by the inverse number density of galaxies $\bar{n}^{-1}$). The same is true for the growth rate $f$, we can only determine the product

$$f^2 P = \frac{C(k,\mu) - \mathcal{E} - [C(k,0) - \mathcal{E}]\left(1 + 2\beta\mu^2\right)}{\mu^4} \ , \quad (10)$$

but this does not apply for $\beta$, which can be extracted directly from observations of $C$ where $\mu \neq 0$ (e.g., [37]). Note, however, that in this case the achievable error on $\beta$ is limited by the sampling variance inherent to $P$.

In case two distinct tracers of the density field with biases $b_{\mathrm{g}}$ and $\alpha b_{\mathrm{g}}$ are observed, where $\alpha$ is their relative galaxy bias, we obtain the three following power spectra:

$$C_{11}(k,\mu) = \left(1 + \beta\mu^2\right)^2 b_{\mathrm{g}}^2 P(k) + \mathcal{E}_{11} \ , \qquad (11)$$

$$C_{22}(k,\mu) = \left(\alpha + \beta\mu^2\right)^2 b_{\mathrm{g}}^2 P(k) + \mathcal{E}_{22} \ , \qquad (12)$$

$$C_{12}(k,\mu) = \left(1 + \beta\mu^2\right)\left(\alpha + \beta\mu^2\right) b_{\mathrm{g}}^2 P(k) + \mathcal{E}_{12} \ . \quad (13)$$

The degree to how well they are correlated is quantified by the cross-correlation coefficient $r^2 \equiv C_{12}^2/C_{11}C_{22}$, so in the idealistic case of no shot noise ($\boldsymbol{\mathcal{E}} = 0$), $r = 1$ and the ratios

$$C_{12}/C_{11} = C_{22}/C_{12} = \sqrt{C_{22}/C_{11}} = \frac{\alpha + \beta\mu^2}{1 + \beta\mu^2} \qquad (14)$$

all yield the same expression, which is independent of $P$. Hence, a combination of observations at different $\mu$ yields $\alpha$ and $\beta$ without sampling variance [12]. Unfortunately, in realistic surveys $\boldsymbol{\mathcal{E}} \neq 0$, so $P$ will not

cancel out completely and the three ratios will be different and scale dependent. This gives rise to residual sampling variance inherent to a measurement of $\alpha$ and $\beta$, which in general can be much smaller than in the single-tracer case. In turn, a better measurement of $\beta$ allows a more precise estimate on $f^2 P$ [see Eq. (10)]. However, the accuracy on $f^2 P$ is still limited by sampling variance, yielding $\sigma_{f^2 P}/f^2 P \geq \sqrt{2/N_k}$, respectively $\sigma_{f\sigma_8}/f\sigma_8 \geq \sqrt{1/2N_k}$ [12].

If both $\boldsymbol{\delta}_{\mathrm{g}}$ *and* $\delta$ are known, we can simply add the dark matter overdensity mode $\delta$ to the overdensities of the tracers and write $\boldsymbol{\delta} \equiv (\delta, \boldsymbol{\delta}_{\mathrm{g}})$. In this case, the effective bias can be obtained directly by taking the ratio $\langle\boldsymbol{\delta}_{\mathrm{g}}\delta^*\rangle/\langle\delta\delta^*\rangle$. The covariance matrix then becomes

$$\mathbf{C} = \begin{pmatrix} \langle\delta\delta^*\rangle & \langle\delta\boldsymbol{\delta}_{\mathrm{g}}^\dagger\rangle \\ \langle\boldsymbol{\delta}_{\mathrm{g}}\delta^*\rangle & \langle\boldsymbol{\delta}_{\mathrm{g}}\boldsymbol{\delta}_{\mathrm{g}}^\dagger\rangle \end{pmatrix} = \begin{pmatrix} P & \boldsymbol{b}^\dagger P \\ \boldsymbol{b}P & \boldsymbol{b}\boldsymbol{b}^\dagger P + \boldsymbol{\mathcal{E}} \end{pmatrix} \ , \quad (15)$$

with $N(N+1)/2$ independent elements. Now the degeneracy between $b_{\mathrm{g}}$, $\sigma_8$ and $f$ is lifted because $P$ is known separately. Considering the cross-correlation coefficient of a tracer $\delta_{\mathrm{g}}$ with the dark matter $\delta$, we find

$$r^2 = \frac{\langle\delta_{\mathrm{g}}\delta^*\rangle^2}{\langle\delta_{\mathrm{g}}\delta_{\mathrm{g}}^*\rangle\langle\delta\delta^*\rangle} = \left(1 + \frac{\mathcal{E}}{\left(b_{\mathrm{g}} + f\mu^2\right)^2 P}\right)^{-1} \ , \quad (16)$$

so the deviation of $r$ from unity is only controlled by the shot noise of the tracer. Again, if $\mathcal{E} = 0$, the dark matter power spectrum disappears completely, so that $b_{\mathrm{g}}$ and $f$ can be determined without sampling variance.

### 2. Fisher information

In order to determine more quantitatively how much information on cosmology is buried in the clustering statistics of biased tracers and the dark matter, we have to compute the Fisher information matrix [38], a derivation of which is presented in the following: we start with a multivariate Gaussian likelihood of the data vector $\boldsymbol{\delta}_{\mathrm{g}}$

$$\mathscr{L} = \frac{1}{(2\pi)^{N/2}\sqrt{\det \mathbf{C}}} \exp\left(-\frac{1}{2}\boldsymbol{\delta}_{\mathrm{g}}^\dagger \mathbf{C}^{-1}\boldsymbol{\delta}_{\mathrm{g}}\right) \ , \qquad (17)$$

which is a reasonable assumption on large scales, where $\delta \ll 1$. The Fisher information matrix for the parameters $\theta_i$ and $\theta_j$ is obtained by ensemble averaging over the Hessian of the log-likelihood [39, 40],

$$F_{ij} \equiv -\left\langle\frac{\partial^2 \ln \mathscr{L}}{\partial\theta_i\partial\theta_j}\right\rangle = \frac{1}{2}\mathrm{Tr}\left(\frac{\partial\mathbf{C}}{\partial\theta_i}\mathbf{C}^{-1}\frac{\partial\mathbf{C}}{\partial\theta_j}\mathbf{C}^{-1}\right) \ . \quad (18)$$

According to the model from Eq. (7), the derivative of the halo covariance matrix with respect to the parameters is

$$\frac{\partial\mathbf{C}}{\partial\theta_i} = \left(\boldsymbol{b}\boldsymbol{b}_i^\dagger + \boldsymbol{b}_i\boldsymbol{b}^\dagger\right) P + \boldsymbol{b}\boldsymbol{b}^\dagger P_i \ , \qquad (19)$$

where $\boldsymbol{b}_i \equiv \partial\boldsymbol{b}/\partial\theta_i$, $P_i \equiv \partial P/\partial\theta_i$ and we assume $\partial\boldsymbol{\mathcal{E}}/\partial\theta_i = 0$. Utilizing the *Sherman-Morrison* formula [41, 42], the inverse of the covariance matrix becomes

$$\mathbf{C}^{-1} = \boldsymbol{\mathcal{E}}^{-1} - \frac{\boldsymbol{\mathcal{E}}^{-1}\boldsymbol{b}\boldsymbol{b}^\dagger\boldsymbol{\mathcal{E}}^{-1}P}{1 + \boldsymbol{b}^\dagger\boldsymbol{\mathcal{E}}^{-1}\boldsymbol{b}P} \; , \qquad (20)$$

provided the shot noise matrix is not singular (e.g., with vanishing $\boldsymbol{\mathcal{E}}$ also $\mathbf{C}$ becomes singular by construction). The full Fisher matrix for this case is calculated in Appendix A. The result is

$$F_{ij} = \left[ \Sigma^{-1}\left(\Sigma_{ij} + \frac{\Sigma_i\Sigma_j}{\Sigma}\right) + \left(\Sigma_{ij} - \frac{\Sigma_i\Sigma_j}{\Sigma}\right) \right.$$
$$\left. + \frac{\Sigma_i}{\Sigma}\frac{P_j}{P} + \frac{\Sigma_j}{\Sigma}\frac{P_i}{P} + \frac{P_iP_j}{2P^2} \right] \left(1 + \Sigma^{-1}\right)^{-2} \; , \quad (21)$$

where

$$\Sigma_{ij} \equiv \boldsymbol{b}_i^\dagger\boldsymbol{\mathcal{E}}^{-1}\boldsymbol{b}_j P \; , \qquad (22)$$

and $\Sigma_i$ as well as $\Sigma$ are defined accordingly by simply omitting the corresponding indices (derivatives). We can identify the first two terms in the square brackets as a *single-tracer* and a *multitracer* term, respectively. The single-tracer term is suppressed by a factor $\Sigma^{-1}$ as compared to the multitracer term. By definition, the latter vanishes for the case of only one tracer, since then $\Sigma\Sigma_{ij} = \Sigma_i\Sigma_j$ and Eq. (21) simplifies to

$$F_{ij} = \left(2\frac{b_ib_j}{b^2} + \frac{b_i}{b}\frac{P_j}{P} + \frac{b_j}{b}\frac{P_i}{P} + \frac{P_iP_j}{2P^2}\right)\left(1 + \frac{\mathcal{E}}{b^2P}\right)^{-2} . \tag{23}$$

While the Fisher information for multiple tracers can in principle become infinite in the limit of no shot noise, Eq. (23) reaches a finite limit when $\mathcal{E} \to 0$.

We consider two sets of parameters separately: the ones that influence only the effective bias,

$$\boldsymbol{\theta}^{(b)} \equiv (\boldsymbol{b}_{\mathrm{g}}, f) \tag{24}$$

and the ones that go into the matter power spectrum,

$$\boldsymbol{\theta}^{(P)} \equiv (\sigma_8, n_s, h, \Omega_\Lambda, \Omega_\mathrm{m}, \Omega_\mathrm{b}, \Omega_\mathrm{k}) \; . \tag{25}$$

The elements of the shot noise matrix are usually not considered as quantities of interest, but as nuisance parameters that can be marginalized over. From Eq. (21) it is evident that there are degeneracies between $\boldsymbol{\theta}^{(b)}$ and $\boldsymbol{\theta}^{(P)}$ due to mixed terms of the form $\Sigma_iP_j$. However, if $\Sigma$ is sufficiently large, those terms are suppressed in comparison to the term $\Sigma_{ij}$.

In case the dark matter density field is known in addition to the galaxies, the derivative of $\mathbf{C}$ from Eq. (15) becomes

$$\frac{\partial\mathbf{C}}{\partial\theta_i} = \begin{pmatrix} P_i & \boldsymbol{b}_i^\dagger P + \boldsymbol{b}^\dagger P_i \\ \boldsymbol{b}_iP + \boldsymbol{b}P_i & \boldsymbol{b}\boldsymbol{b}_i^\dagger P + \boldsymbol{b}_i\boldsymbol{b}^\dagger P + \boldsymbol{b}\boldsymbol{b}^\dagger P_i \end{pmatrix} \; . \tag{26}$$

Furthermore, a block inversion of $\mathbf{C}$ yields

$$\mathbf{C}^{-1} = \begin{pmatrix} (1+\Sigma)P^{-1} & -\boldsymbol{b}^\dagger\boldsymbol{\mathcal{E}}^{-1} \\ -\boldsymbol{\mathcal{E}}^{-1}\boldsymbol{b} & \boldsymbol{\mathcal{E}}^{-1} \end{pmatrix} \; , \qquad (27)$$

and the Fisher information becomes (see Appendix A)

$$F_{ij} = \Sigma_{ij} + \frac{P_iP_j}{2P^2} \; . \tag{28}$$

For a single tracer this further simplifies to

$$F_{ij} = \frac{b_ib_jP}{\mathcal{E}} + \frac{P_iP_j}{2P^2} \; . \tag{29}$$

This expression may increase indefinitely for sufficiently small $\mathcal{E}$. In the limit $\mathcal{E} \to 0$, the effective bias can be determined exactly, allowing an exact measurement of the parameters $\boldsymbol{\theta}^{(b)}$ [12, 43]. On the other hand, constraints on the parameters $\boldsymbol{\theta}^{(P)}$ are always limited by the variance of the power spectrum $\mathrm{Var}(P) = 2P^2$. Here, there are no mixed terms depending both on the effective bias and the power spectrum, so parameter degeneracies between $\boldsymbol{\theta}^{(b)}$ and $\boldsymbol{\theta}^{(P)}$ are absent. We note that in the limit of small $\Sigma_i/\Sigma$, Eq. (21) reduces to Eq. (28).

### 3. Reparametrization

As mentioned above, the growth rate $f$ cannot be determined from a galaxy redshift survey alone, since its degenerate with the power spectrum $P$, respectively its normalization $\sigma_8$. This degeneracy can only be broken with knowledge of the dark matter density field, or other prior constraints. For this reason it is sometimes convenient to reparametrize by the mapping

$$\tilde{\boldsymbol{\theta}}^{(b)} = \boldsymbol{\theta}^{(b)}/b_\mathrm{g}^\mathrm{ref} = (\boldsymbol{b}_\mathrm{g}, f)/b_\mathrm{g}^\mathrm{ref} \equiv (\boldsymbol{\alpha}, \beta) \; , \qquad (30)$$
$$\tilde{\sigma}_8 = \sigma_8 b_\mathrm{g}^\mathrm{ref} \; , \qquad (31)$$

where $b_\mathrm{g}^\mathrm{ref}$ is an arbitrary reference galaxy bias so that $\boldsymbol{\alpha}$ is the relative galaxy bias of all considered tracers to this reference. This mapping leaves the covariance matrix from Eq. (7) unchanged. We can conveniently choose the lowest bias of all tracers as the reference, $b_\mathrm{g}^\mathrm{ref} = b_{\mathrm{g}_1}$, such that $\boldsymbol{\alpha} = (1, b_{\mathrm{g}_2}/b_{\mathrm{g}_1}, \ldots, b_{\mathrm{g}_N}/b_{\mathrm{g}_1})$ is always larger than unity and $\beta = f/b_{\mathrm{g}_1}$. Another popular parametrization is

$$\tilde{\boldsymbol{\theta}}^{(b)} = \boldsymbol{\theta}^{(b)}\sigma_8^\mathrm{ref} = \left(\boldsymbol{b}_\mathrm{g}\sigma_8^\mathrm{ref}, f\sigma_8^\mathrm{ref}\right) \; , \qquad (32)$$
$$\tilde{\sigma}_8 = \sigma_8/\sigma_8^\mathrm{ref} \; , \qquad (33)$$

with $\sigma_8^\mathrm{ref}$ being some arbitrary reference normalization of the power spectrum, which we choose to be identical with our simulation input value of $\sigma_8 = 0.81$. In this paper we will quote constraints on both $\beta$ and $f\sigma_8$ when considering a galaxy redshift survey only, and on $f$ when the latter is combined with dark matter observations.

## III.   ANALYSIS

### A.   Numerical setup

Our numerical analysis is based on a high-resolution $N$-body simulation performed at the University of Zürich supercomputer zBox3 with the GADGET-2 code [44]. It contains $1536^3$ particles of mass $4.7 \times 10^{10} h^{-1} M_\odot$ in a box of $1.3 h^{-1}$Gpc a side. We chose our fiducial cosmology to match the WMAP5 best fit with $\sigma_8 = 0.81$, $n_s = 0.96$, $h = 0.7$, $\Omega_\Lambda = 0.721$, $\Omega_{\rm m} = 0.279$, $\Omega_{\rm b} = 0.046$, $\Omega_{\rm k} = 0$ [45]. We further employ a friends-of-friends algorithm [46] with a linking length of 20% of the mean interparticle distance to generate halo catalogs at different redshifts. With a minimum of 20 dark matter particles per halo we resolve halo masses down to $M_{\rm min} \simeq 9.4 \times 10^{11} h^{-1} M_\odot$, resulting in a mean halo number density of $\bar{n} \simeq 4.0 \times 10^{-3} h^3 {\rm Mpc}^{-3}$ at $z = 0$ and $\bar{n} \simeq 3.3 \times 10^{-3} h^3 {\rm Mpc}^{-3}$ at $z = 1$.

In order to transform the real-space halo catalog into redshift space, we apply Eq. (1) using the velocities of the halos along the three independent directions of the box ($x$, $y$ and $z$ axis). Thus, three independent redshift-space catalogs can be constructed from a single real-space catalog, yielding a total effective volume of $V_{\rm eff} \simeq 6.6 h^{-3} {\rm Gpc}^3$. Density fields are created by cloud-in-cell interpolation [47] onto a mesh of $1024^3$ grid points, and the Fourier modes are obtained using a FFT algorithm.

We utilize the IDL algorithm MPFIT [48] to fit our models to the numerical data and find the best-fit parameters including their uncertainties. It is based on the MINPACK distribution by [49] and uses the Levenberg-Marquardt technique to find the minimum of a multidimensional nonlinear least-squares problem. Parameter uncertainties are calculated via the Jacobian of the chi square, which is determined numerically using finite-difference derivatives.

### B.   Optimal tracer selection

In order to fully exploit the benefits of the multitracer approach, the question remains on how to ideally construct different tracers from a given galaxy catalog. In this section we will derive the answer to that question and test it on the basis of $N$-body simulations.

#### 1.   Principal components of the signal-to-noise ratio

A quantity that plays a crucial role for the cosmological information content contained in the two-point clustering statistics of LSS is the clustering signal-to-noise ratio $\Sigma \equiv \boldsymbol{b}^\dagger \boldsymbol{\mathcal{E}}^{-1} \boldsymbol{b} P$. For dark matter halos, it has been
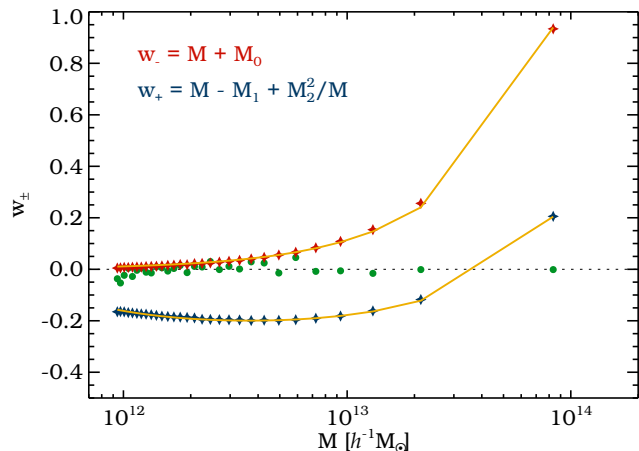


FIG. 1. Three different eigenvectors of the shot noise matrix obtained from a halo catalog that has been split into 30 mass bins of equal number density. The two non-Poisson eigenvectors (upper red and lower blue stars) are overplotted with their best-fit weighting functions $w_\pm$ as solid lines with functional form given in the top left of the panel in corresponding colors. One representative Poisson eigenvector is shown as green circles; when used as a weighting function it yields a very low clustering signal-to-noise ratio $\Sigma$, due to its oscillatory behavior.

demonstrated on the basis of numerical $N$-body simulations that $\Sigma$ is dominated by only two *principal components* corresponding to the two nontrivial (non-Poisson) eigenvectors of the shot noise matrix $\boldsymbol{\mathcal{E}}$ (see Fig. 6 in [50]). We denote these components with a plus and a minus subscript, according to their super- and sub-Poissonian shot noise levels, respectively. In this manner we can expand the clustering signal-to-noise ratio as

$$\Sigma \equiv \boldsymbol{b}^\dagger \boldsymbol{\mathcal{E}}^{-1} \boldsymbol{b} P = \sum_{i=0}^{N} \frac{(\boldsymbol{V}_i^\intercal \boldsymbol{b})^2}{\lambda_i} P \simeq \frac{b_-^2}{\mathcal{E}_-} P + \frac{b_+^2}{\mathcal{E}_+} P \,, \quad (34)$$

where $\boldsymbol{V}_i^\intercal$ and $\lambda_i$ are the $N$ eigenvectors and eigenvalues of the shot noise matrix $\boldsymbol{\mathcal{E}}$, and $b_\pm$ and $\mathcal{E}_\pm$ are the effective bias and shot noise of the two principal components of the tracer density field,

$$\delta_\pm \equiv \frac{\sum_i w_\pm(M_i) \delta_{\rm g}(M_i)}{\sum_i w_\pm(M_i)} \,, \quad (35)$$

where the summation runs over all individual objects in the volume. The $w_\pm(M)$ are weighting functions corresponding to the two non-Poisson eigenvectors of the shot noise matrix, as depicted in Fig. 1. Equation (34) states that a splitting of the tracer density field into $N$ mass bins yields, in the limit $N \to \infty$, about the same clustering signal-to-noise ratio as simply considering the two weighted fields $\delta_+$ and $\delta_-$. Therefore, these are the most promising candidates to carry out a multitracer analysis with.

In [50] the functional form of $w_-(M)$ was found to be well described by

$$w_-(M) = M + M_0 \,, \tag{36}$$

where $M_0$ is about three times the minimum halo mass resolved in the simulation, $M_0 \simeq 3M_{\mathrm{min}}$. For the second weighting function we find

$$w_+(M) = M - M_1 + M_2^2/M \tag{37}$$

to be a good fit to the second eigenvector of the shot noise matrix, as shown in Fig. 1. For the constants $M_1$ and $M_2$ we find $M_1 \simeq 1 \times 10^{14} h^{-1}\mathrm{M}_\odot$, $M_2 \simeq 3 \times 10^{13} h^{-1}\mathrm{M}_\odot$ at $z = 0$ and $M_1 \simeq 1 \times 10^{14} h^{-1}\mathrm{M}_\odot$, $M_2 \simeq 1 \times 10^{15} h^{-1}\mathrm{M}_\odot$ at $z = 1$.

The physical origin of the first principal component is related to halo exclusion effects [51]. The sampling of the density field with halos is less stochastic than Poisson sampling (sampling with points) due their finite extension. Since the exclusion volume of halos is proportional to their mass, this effect is strongest at the high mass end [50]. The second principal component can be interpreted as a loop correction to the galaxy bias [52], coming from the second-order term in a local bias expansion model [53]. Due to its nonlinear character, it adds a super-Poissonian shot noise contribution to the two-point clustering statistics of halos, originating from the squared density field [54, 55]. However, through mode coupling it also yields a second-order clustering signal that originates from the bispectrum (three-point function) and adds valuable information coming from smaller scales.

Figure 2 displays the three covariance matrix elements $C_{++} = \langle \delta_+ \delta_+^* \rangle$, $C_{+-} = \langle \delta_+ \delta_-^* \rangle$ and $C_{--} = \langle \delta_- \delta_-^* \rangle$ in real space ($\mu = 0$) at redshift $z = 0$, extracted from our simulation. The three power spectra are obviously highly correlated and closely follow the shape of the estimated dark matter power spectrum up to $k \simeq 0.1 h\mathrm{Mpc}^{-1}$. By construction, the shot noises of the two fields are not correlated, i.e., $\langle \epsilon_- \epsilon_+ \rangle = 0$. Taking the ratios as in Eq. (14) yields three possible estimators for the relative galaxy bias $\alpha \equiv b_{g_-}/b_{g_+} \simeq 1.6$. In the following two subsections, we will provide evidence for the claim that the fields $\delta_+$ and $\delta_-$ are indeed the optimal choice for a multitracer analysis.

### 2. Sampling variance cancellation

The idea of utilizing multiple tracers is to cancel sampling variance from the underlying density field $\delta$. To quantify the magnitude of cancellation between any two tracers $\delta_{g_1}$ and $\delta_{g_2}$, we define the following statistic:

$$\sigma_{\mathrm{SV}}^2 \equiv \frac{\langle |b_2 \delta_{g_1}(\mathbf{k}, \mu) - b_1 \delta_{g_2}(\mathbf{k}, \mu)|^2 \rangle}{\langle |b_2 \delta_{g_1}(\mathbf{k}, \mu)|^2 \rangle + \langle |b_1 \delta_{g_2}(\mathbf{k}, \mu)|^2 \rangle} \,. \tag{38}$$
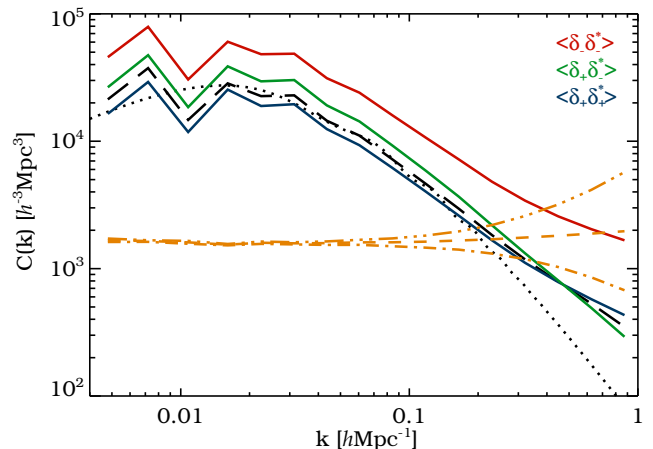


FIG. 2. Real-space auto-power and cross-power spectra of the two fields $\delta_+$ and $\delta_-$ (as indicated), obtained through weighting the halo catalog by the two non-Poisson eigenvectors of the shot noise matrix $w_+$ and $w_-$. The long-dashed black line shows the dark matter power spectrum from the simulation and the dotted line its linear theory prediction. The three different estimators for the relative bias $\alpha$ between $\delta_+$ and $\delta_-$, as defined in Eq. (14), are depicted in dot-dashed ($C_{+-}/C_{++}$), dot-dot-dot-dashed ($C_{--}/C_{+-}$) and dashed ($\sqrt{C_{--}/C_{++}}$). For visibility, they were shifted upwards by a factor of $10^3$.

Here, $b_1$ and $b_2$ is the effective bias as defined in Eq. (6). If the two tracers are completely uncorrelated ($r = 0$), there is no cancellation and $\sigma_{\mathrm{SV}} = 1$. Yet, if they are perfectly correlated ($r = 1$), $\sigma_{\mathrm{SV}} = 0$. Because the real and imaginary parts of any given Fourier mode are uncorrelated, we can swap them for one of the tracers to mimic the case of no correlation.

We consider the following selection criteria for two tracers from our halo catalog:

20/80: lightest 20% vs heaviest 80% of all halos,

50/50: lightest 50% vs heaviest 50% of all halos,

80/20: lightest 80% vs heaviest 20% of all halos,

$u/w_-$: all uniformly weighted vs all $w_-$-weighted halos,

$w_+/w_-$: all $w_+$-weighted vs all $w_-$-weighted halos.

The first three are simply obtained via cutting the halo catalog in two at different mass thresholds $M_{\mathrm{cut}}$ to yield the indicated abundances in each bin. The fourth selection utilizes the whole uniform halo catalog (not weighted) and its $w_-$-weighted form, while the last one uses both weighting functions $w_\pm$ to construct two tracers from one and the same halo catalog. Further details about the tracers with these selection criteria can be found in Table I.

Figure 3 shows $\sigma_{\mathrm{SV}}$ for the different tracer pairs; on large scales they all exhibit significant cancellation of

TABLE I. Details of the tracer selection.

| Selection | $M_{\rm cut}$ $[h^{-1}{\rm M}_\odot]$ | $\bar{M}_1$ $[h^{-1}{\rm M}_\odot]$ | $\bar{M}_2$ $[h^{-1}{\rm M}_\odot]$ | $\bar{n}_1$ $[h^3{\rm Mpc}^{-3}]$ | $\bar{n}_2$ $[h^3{\rm Mpc}^{-3}]$ | $\mathcal{E}_{11}$ $[h^{-3}{\rm Mpc}^3]$ | $\mathcal{E}_{22}$ $[h^{-3}{\rm Mpc}^3]$ | $\mathcal{E}_{12}$ $[h^{-3}{\rm Mpc}^3]$ | $b_{{\rm g}_1}$ | $b_{{\rm g}_2}$ | $\Sigma_{\rm max}$ |
|---|---|---|---|---|---|---|---|---|---|---|---|
| 20/80 | $1.20 \times 10^{12}$ | $1.04 \times 10^{12}$ | $7.72 \times 10^{12}$ | $8.50 \times 10^{-4}$ | $3.15 \times 10^{-3}$ | 1432 | 964 | 448 | 0.899 | 0.988 | 74 |
| 50/50 | $2.00 \times 10^{12}$ | $1.33 \times 10^{12}$ | $1.13 \times 10^{13}$ | $2.00 \times 10^{-3}$ | $2.00 \times 10^{-3}$ | 911 | 1243 | 547 | 0.896 | 1.042 | 73 |
| 80/20 | $5.00 \times 10^{12}$ | $1.97 \times 10^{12}$ | $2.22 \times 10^{13}$ | $3.15 \times 10^{-3}$ | $8.50 \times 10^{-4}$ | 854 | 1770 | 606 | 0.901 | 1.217 | 73 |
| $u/w_-$ | - | $6.30 \times 10^{12}$ | $6.76 \times 10^{13}$ | $4.00 \times 10^{-3}$ | $4.00 \times 10^{-3}$ | 812 | 51 | 53 | 0.969 | 1.457 | 2067 |
| $w_+/w_-$ | - | $2.29 \times 10^{12}$ | $6.76 \times 10^{13}$ | $4.00 \times 10^{-3}$ | $4.00 \times 10^{-3}$ | 804 | 51 | 7 | 0.902 | 1.457 | 2098 |
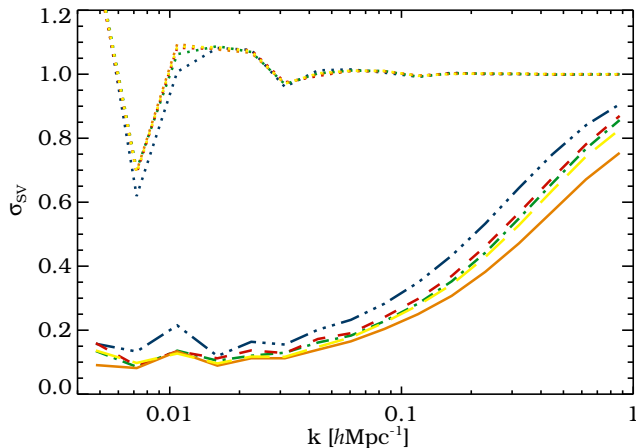


FIG. 3. Sampling variance statistic $\sigma_{\rm SV}$ for five different tracer selections at $z = 0$ as described in the text, 20/80 (dot-dot-dot-dashed, blue), 50/50 (dot-dashed, green), 80/20 (dashed, red), $u/w_-$ (solid, orange) and $w_+/w_-$ (long-dashed, yellow). Dotted lines show the corresponding results for uncorrelated modes by swapping the real and imaginary parts of one of the tracer's Fourier modes.

sampling variance as compared to the reference case with switched real and imaginary parts (dotted lines). Towards smaller scales this effect is deteriorated due to the onset of nonlinearities and velocity dispersion (Finger-of-God effects) [26]. As evident from the plot, a combination of the uniform with the $w_-$-weighted halos yields the highest cancellation of sampling variance. However, the combination of $w_+$-weighted and $w_-$-weighted halos shows a comparable suppression, as opposed to cutting the halo catalog in two, which yields less cancellation, especially for a low mass cut. If a mass cut is imposed to construct two tracers, the highest sampling variance cancellation is achieved when the same abundance of objects in each of the resulting catalogs is chosen (50/50), which is in agreement with the findings of [56].

### 3. Fisher information

Cancellation of sampling variance alone is not a sufficient indicator on how well cosmological parameters can be constrained in a multitracer analysis. This is because one is looking for relative changes in the clustering signal from multiple tracers, and not for the absolute clustering amplitude in each tracer. In this paragraph we will show that it is desirable to have tracers with a high relative galaxy bias ratio $\alpha$.

Quantitatively, the achievable accuracy on a given cosmological parameter $\theta$ is determined by the inversion of the Fisher matrix of Eq. (21). For the sake of simplicity, let us consider only the $f$-$f$ element,

$$F_{ff} = \frac{\Sigma\Sigma_{ff} + \Sigma_f^2 + \Sigma\left(\Sigma\Sigma_{ff} - \Sigma_f^2\right)}{1 + \Sigma^2} \ . \tag{39}$$

In the high signal-to-noise regime, $\Sigma \gg 1$, and expressing $\Sigma$, $\Sigma_f$, as well as $\Sigma_{ff}$ in terms of the two principal components as in Eq. (34), we get

$$F_{ff} \simeq \frac{2\left(\frac{b_-^2}{\mathcal{E}_-^2} + \frac{b_+^2}{\mathcal{E}_+^2}\right) + \frac{(b_- + b_+)^2}{\mathcal{E}_-\mathcal{E}_+}}{\left(\frac{b_-^2}{\mathcal{E}_-} + \frac{b_+^2}{\mathcal{E}_+}\right)^2}\mu^4 + \frac{\frac{(b_- - b_+)^2}{\mathcal{E}_-\mathcal{E}_+}}{\frac{b_-^2}{\mathcal{E}_-} + \frac{b_+^2}{\mathcal{E}_+}}\mu^4 P \ . \tag{40}$$

As a second approximation, we can make use of the fact that $b_-^2/\mathcal{E}_- \gg b_+^2/\mathcal{E}_+$ and $\mathcal{E}_- \ll \mathcal{E}_+$ (see Table I), which yields

$$F_{ff} \simeq \frac{2\mu^4}{b_-^2} + \left(1 - \frac{b_+}{b_-}\right)^2 \frac{\mu^4 P}{\mathcal{E}_+} =$$
$$= \frac{2\mu^4}{(b_{{\rm g}_-} + f\mu^2)^2} + \left(1 - \frac{1 + \beta\mu^2}{\alpha + \beta\mu^2}\right)^2 \frac{\mu^4 P}{\mathcal{E}_+} \ . \tag{41}$$

The single-tracer term (as derived in [57]) is dominated by the first principal component of $\Sigma$, while the multitracer term depends on the bias ratio $\alpha = b_{{\rm g}_-}/b_{{\rm g}_+}$ of both principal components and the shot noise $\mathcal{E}_+$ of the second principle component. In order to maximize $F_{ff}$, it is thus desirable to have a large $\alpha$ and a low $\mathcal{E}_+$ at the same time. In the special case of uniform Poisson shot noise, Eq. (39) reproduces the expression derived in [58].

If the dark matter density field is known separately, this Fisher matrix element becomes

$$F_{ff} = \Sigma_{ff} \simeq \frac{\mu^4 P}{\mathcal{E}_-} \ , \tag{42}$$
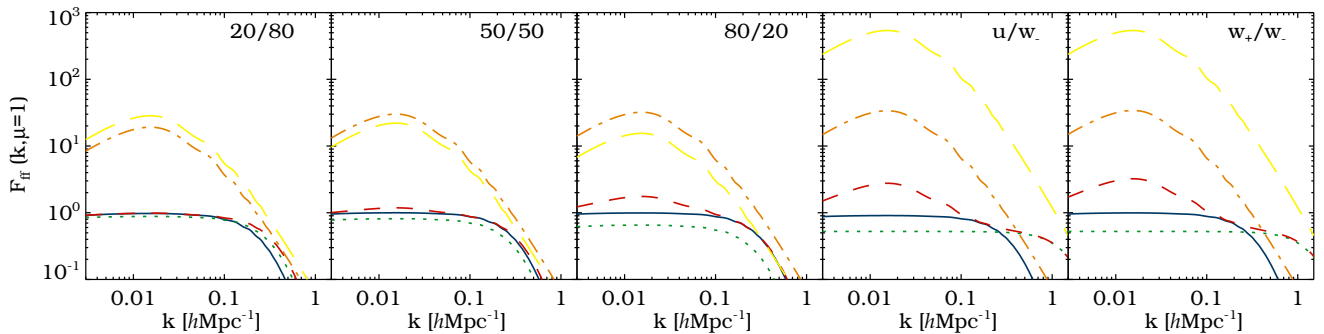
FIG. 4. Fisher matrix element $F_{ff}$ as a function of $k$ at $\mu = 1$ and $z = 0$ for various tracer selections (indicated in the top right of each panel). Results are shown for a single-tracer analysis with the first (solid, blue) and the second tracer (dotted, green) used separately, both of the tracers combined in a multitracer analysis (dashed, red), and each of the tracers combined with idealistic dark matter observations (dot-dashed orange and long-dashed yellow, respectively).

thus independent of the effective bias and limited only by the low shot noise level of the first principal component.

Figure 4 depicts $F_{ff}(k, \mu = 1)$ for all of our five tracer selections. For each case we further distinguish between the following scenarios:

- single-tracer analysis with each of the two tracers taken separately,

- multiple-tracer analysis with both tracers combined,

- combined analysis of each tracer with the dark matter density field.

Clearly, in a single-tracer analysis the tracer with the lowest galaxy bias yields the highest information on the growth rate $f$. This is evident from Eq. (23), where $b_{\rm g}$ enters in the denominator of the first term and the shot noise $\mathcal{E}$ is negligible if $\mathcal{E}/b_{\rm g}^2 P \ll 1$. Since $b_{\rm g_1}$ is very similar in all five cases, the Fisher information from a single tracer cannot be increased much by any particular choice of tracer.

On the contrary, a combination of two tracers can cancel out sampling variance and therefore considerably increase the available information on $f$ if the tracers are selected appropriately. As evident from the dashed red lines in Fig. 4, the multitracer term in Eq. (41) gains importance over the single-tracer term as moving from the left to the right panel. Again, the two tracers obtained by a low mass cut yield the worst results, owing to the fact that the shot noise of both tracers is super-Poissonian in this selection. It is more optimal to impose a high mass cut in order to benefit from the sub-Poissonian shot noise level of the heaviest halos [50]. However, the highest Fisher information content is obtained when correlating the two orthogonally weighted fields $\delta_+$ and $\delta_-$. The main reason for this is the large relative galaxy bias between the two fields and their relatively low shot noise level [see Table I and Eq. (41)].

We have also explored the possibility of splitting the halo catalog into more than two mass bins, considering up to $N = 10$ tracers. We find that the Fisher information from multiple tracers increases with the number of bins $N$ and approaches the result obtained with the two weighted fields $\delta_+$ and $\delta_-$ in the limit of high $N$.

Finally, adding the information from the dark matter density field to each one of the tracers increases the information content on $f$. In this case, sampling variance inherent in the density field $\delta$ is known and can thus be removed from the halo fields directly. According to Eq. (42), the Fisher information is inversely proportional to the shot noise of the tracer, so the lowest stochasticity weight $w_-$ yields the best results.

## C. Multitracer fit

So far we have investigated the Fisher information content on the growth rate using multiple tracers of the LSS. The question of how to actually constrain parameters of interest from a data set in the optimal way will be answered in this section. For this task we want to maximize the likelihood function from Eq. (17), which is equivalent to minimizing its negative logarithm, the chi square

$$\chi^2 \equiv \sum_{\mathbf{k}} \frac{1}{2} \boldsymbol{\delta}_{\rm g}^{\dagger}(\mathbf{k}, \mu) \mathbf{C}^{-1} \boldsymbol{\delta}_{\rm g}(\mathbf{k}, \mu) + \frac{1}{2} \ln (\det \mathbf{C}) . \quad (43)$$

Here, the covariance matrix $\mathbf{C}$ is given by the clustering model of Eq. (7) and we sum over all individual Fourier modes $\boldsymbol{\delta}_{\rm g}(\mathbf{k}, \mu)$ from our halo catalog. When we add the dark matter density field as an observable, we use the model from Eq. (15) and $\boldsymbol{\delta} = (\delta, \boldsymbol{\delta}_{\rm g})$ as our data vector.

Figure 5 presents the fitting results for the RSD parameter $\beta$ and the product of growth rate $f$ with the normalization of the power spectrum $\sigma_8$ from our halo catalogs at redshift $z = 0$. While $\beta$ has been obtained from a single-parameter fit, we have marginalized over
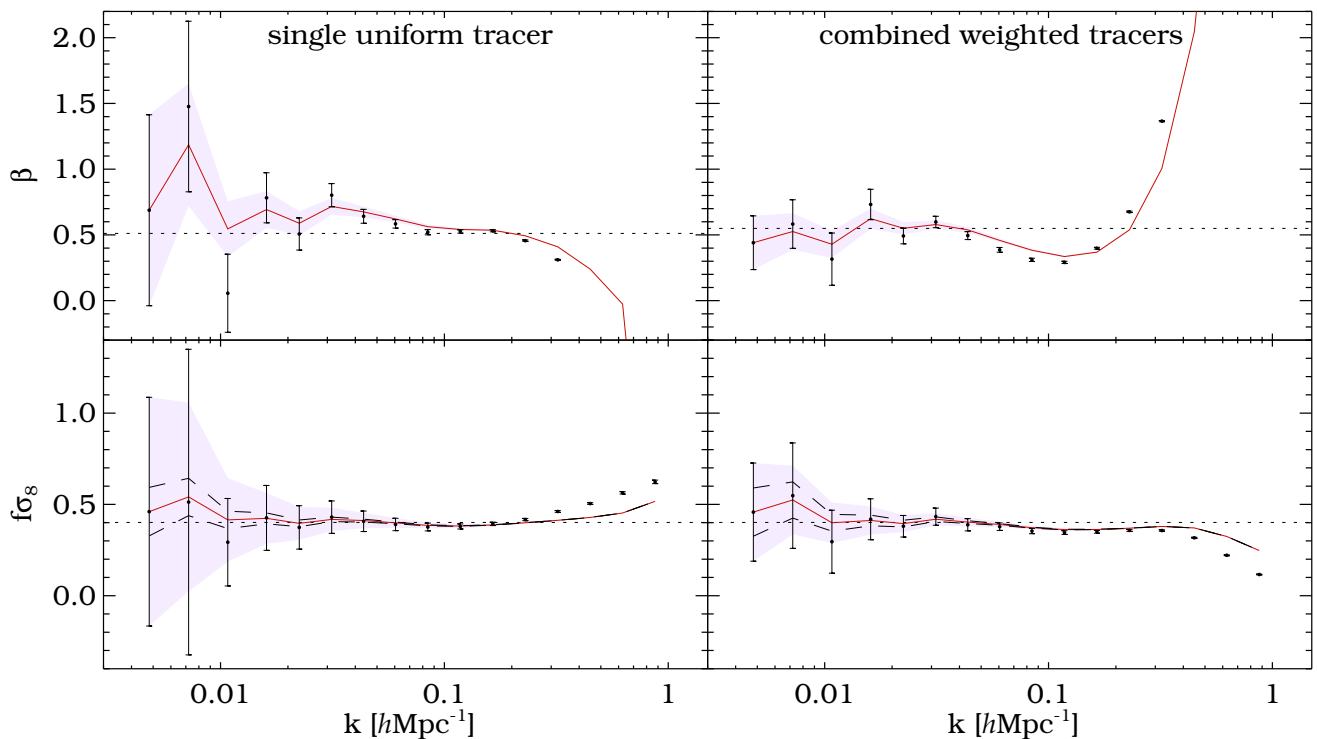
FIG. 5. Fit for the redshift-space distortion parameter $\beta$ (top) and the product $f\sigma_8$ (bottom) from the two-point clustering statistics of halos in an $N$-body simulation with effective volume $V_{\rm eff} \simeq 6.6 h^{-3}{\rm Gpc}^3$ and halo-mass resolution $M_{\rm min} \simeq 9.4 \times 10^{11} h^{-1}{\rm M}_\odot$ at $z = 0$. LEFT: Conventional single-tracer analysis utilizing all halos (not weighted) from the same catalog. RIGHT: Multitracer analysis with the two fields $\delta_+$ and $\delta_-$, obtained through weighting the halo catalog with its principal components $w_+$ and $w_-$. The fitting results are shown in logarithmic bins of $k$ (points with 1-$\sigma$ error bars), as well as cumulative as a function of $k = k_{\rm max}$ with fixed $k_{\rm min} = 0.0048 h{\rm Mpc}^{-1}$ (red solid lines with shaded region). Dotted lines show the linear theory prediction with $f = \Omega_{\rm m}^{0.55}$ and $\sigma_8 = 0.81$, dashed lines the cumulative sampling variance limit.

the galaxy bias of each tracer as a free parameter in the fit for $f\sigma_8$. In the left column, the standard single-tracer analysis utilizing all objects in the halo catalog is performed. The best fits along with their 1$\sigma$-error bars are shown both in $k$ bins (points with error bars), as well as cumulative as a function of $k = k_{\rm max}$ with fixed $k_{\rm min} = 0.0048 h{\rm Mpc}^{-1}$ (solid lines with shaded region).

The constraints on $\beta$ and $f\sigma_8$ are clearly affected by sampling variance, as evident from the large scatter of the points at low $k$. When the number of available Fourier modes grows towards higher $k$, this scatter becomes smaller; however, beyond a scale of $k \simeq 0.2 h{\rm Mpc}^{-1}$, linear theory breaks down and the fits depart from their scale-independent linear value assuming $f = \Omega_{\rm m}^{0.55}$ (dotted line). The cumulative sampling variance limit for the determination of $f\sigma_8$ is shown as a dashed line. Clearly, the single-tracer fit yields a substantially larger uncertainty compared to this limit.

When combining the two $w_+/w_-$-weighted tracers in a multitracer analysis as shown in the right column of Fig. 5, the scatter of the fit is significantly suppressed. On the largest scales, the errors are reduced by up to a factor

of 4 and the constraints on $f\sigma_8$ reach the sampling variance limit closely. However, the fit seems to deviate from the linear theory prediction already at $k \simeq 0.04 h{\rm Mpc}^{-1}$. This is likely due to the high bias of the $w_-$-weighted tracer: as shown in [59], more highly biased halos show a stronger scale dependence in redshift space, invalidating the Kaiser formula on even larger scales. This could be corrected for by nonlinear RSD models, which is beyond the scope of this paper. On the other hand, the apparently more linear behavior of the single-tracer analysis may likely be coincidental at $k > 0.04 h{\rm Mpc}^{-1}$. This is supported by results shown in the left panel of Fig. 6. Here, we combine the uniform halo catalog (without weighting) with the dark matter field from our simulation to fit for $f$ directly. Obviously, sampling variance has decreased even further, but deviations from linear theory already kick in at a scale of $k \simeq 0.04 h{\rm Mpc}^{-1}$.

Most impressive constraints on the growth rate are obtained when we combine the $w_-$-weighted halos with the dark matter density field, as depicted in the right panel of Fig. 6. In this case, sampling variance has almost canceled out completely and the error bars on $f$ have
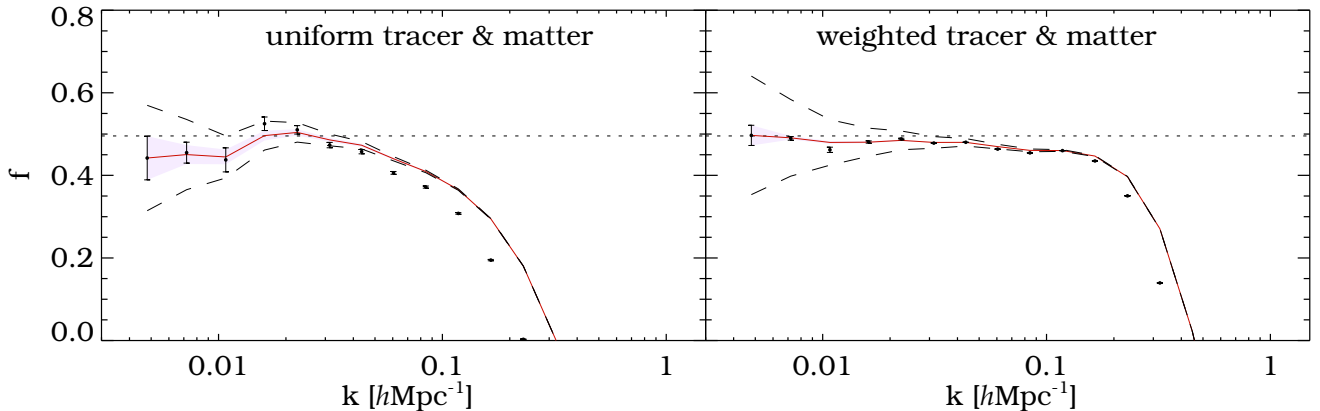
FIG. 6. Fit for the growth rate $f$ from the two-point clustering statistics of halos *and* the dark matter combined. LEFT: All uniform halos (not weighted) and the dark matter. RIGHT: All halos, weighted with the lowest stochasticity weight $w_-$, and the dark matter. The meaning of lines and symbols is the same as in Fig. 5.

diminished by up to a factor of 142 (at the peak of the power spectrum), when compared to the standard single-tracer analysis. Moreover, deviations from linear theory are very small up to scales of $k \sim 0.2h\mathrm{Mpc}^{-1}$, making this kind of experiment the most promising one out of the four considered scenarios.

Methods to combine galaxy clustering and weak lensing data have been studied extensively in the recent literature (e.g., [60–66]), suggesting high improvements for precision cosmology. Unfortunately, obtaining the dark matter density field in 3D from observations is a highly nontrivial problem and is subject of active research. Weak lensing tomography is the technique aiming to achieve this goal (e.g., [67–71]), but the resolution in the radial direction is not expected to be high because of the relatively broad lensing kernels along the line of sight. Moreover, we assume an ideal reconstruction of the dark matter density field without considering additional sources of error involved in the lensing measurement, such as *shape noise* and *intrinsic alignment*, for example.

Without knowledge about $\delta$, in principle we would have to marginalize over all the parameters $\boldsymbol{\theta}^{(P)}$ of the dark matter power spectrum as well. This implies calculating the transfer function in each iteration of the fitting procedure, which goes beyond the scope of this paper. In the high signal-to-noise regime of the multitracer analysis, the degeneracy between the parameters $\boldsymbol{\theta}^{(P)}$ and $\boldsymbol{\theta}^{(b)}$ is expected to be rather weak (except the fundamental degeneracy between $f$ and $\sigma_8$), as the mixed terms between $\Sigma_i$ and $P_j$ in Eq. (21) are suppressed by $\Sigma$. Moreover, in Appendix C of [52] it has been shown that $P(k)$ cancels out to a high degree in the chi square of Eq. (43). Of course, in case the dark matter density field is available, we do not have to worry about those issues, since $b_\mathrm{g}$ and $P$ are directly observable.

In order to quantify the gains in accuracy, we compare the size of the error bars on $\beta$ and $f\sigma_8$ from the multitracer to the single-tracer analysis in Fig. 7 (solid and dashed blue lines, respectively). Obviously, sampling variance mostly cancels on the largest scales, yielding improvements in accuracy of up to a factor of 4. Beyond scales of $k \simeq 0.1h\mathrm{Mpc}^{-1}$, the improvement is deteriorated due to the onset of nonlinear clustering and mode coupling. Deviations from linear theory increase towards smaller scales, making the fit of this model to the data increasingly biased (see Figs. 5 and 6). Therefore, the drop of the curves at $k > 0.3h\mathrm{Mpc}^{-1}$ is likely an artifact of the fitting procedure using an incorrect model and should not be trusted. At redshift $z = 1$ this turnover is moved to smaller scales, the overall improvement in the error ratio is, however, slightly deteriorated. In order to access the cosmological information content buried in the semilinear regime of galaxy clustering in redshift space, one cannot avoid having to invoke more elaborate models involving perturbative methods, such as the ones proposed in [72].

More gains can be achieved when galaxies and ideal dark matter observations are combined, the improvement in the accuracy on $\beta$ compared to the ordinary single-tracer analysis amounts to about a factor of 10 in this case (solid green line). If, additionally, galaxies are weighted optimally, it increases by another factor of 10, two orders of magnitude better than what a single-tracer analysis can achieve. In this case the improvement even persists down to smaller scales of $k \simeq 0.3h\mathrm{Mpc}^{-1}$. However, the effect of optimal weighting is diminished towards higher redshifts.

Unfortunately, the halo masses we used to construct our weighted density fields are not directly observable in reality. Yet, they correlate with many observables, such as X-ray luminosity, galaxy richness, weak lensing shear, velocity dispersion or the thermal Sunyaev-Zel'dovich (SZ) effect (e.g., [73]). Scaling relations between these
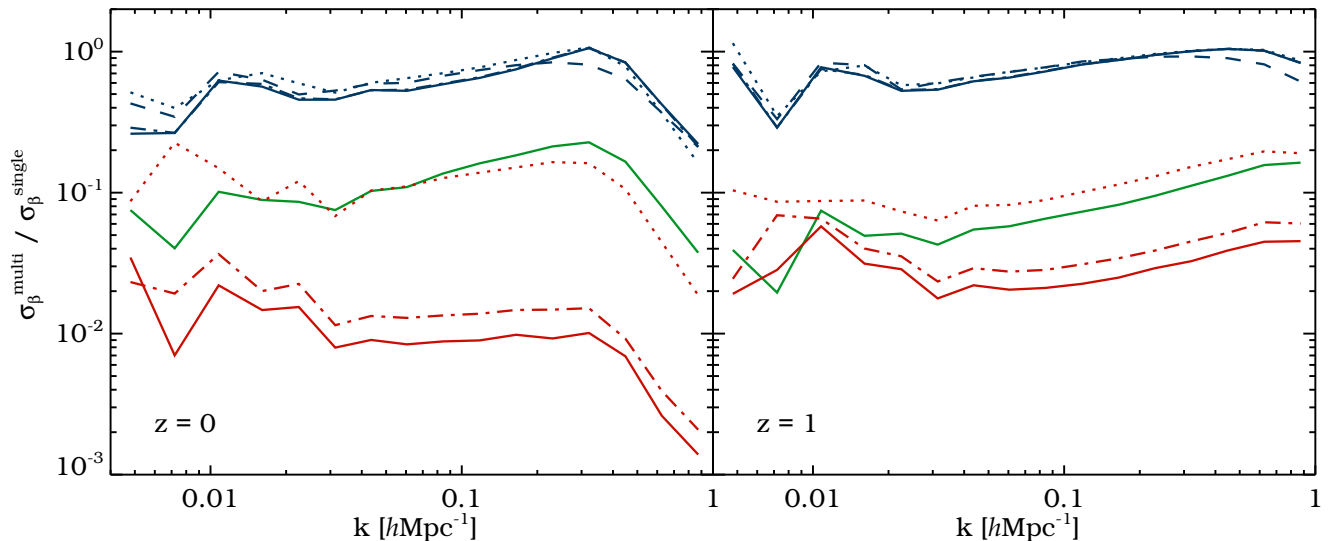
FIG. 7. Ratios of the binned one-sigma error bars (from Fig. 5) on $\beta$ (solid blue) and $f\sigma_8$ (dashed blue) when comparing the optimal multitracer to the single-tracer analysis at $z = 0$ (left panel) and $z = 1$ (right panel). Additionally, the improvement in constraints on $\beta$ from a combined clustering analysis of halos *and* dark matter as compared to the single-tracer case is shown in solid green (no weighting of halos) and in solid red (optimally weighted halos). Adding a log-normal scatter of $\sigma_{\ln M} = 0.1$ (dot-dashed) and $\sigma_{\ln M} = 0.5$ (dotted) to the halo masses results in a degradation of the constraints from the weighted fields.

observables and halo mass can be calibrated with numerical simulations to obtain unbiased mass proxies with minimal scatter (e.g., [74, 75]). While optical methods show a rather large scatter of $\sigma_{\ln M} \simeq 0.45$ [76], X-ray or SZ observations yield tighter relations with $\sigma_{\ln M}$ reaching below 0.1 [77].

We artificially add a constant log-normal scatter to the halo masses of our catalog in order to mimic the observational uncertainties in the mass determination for a rather pessimistic scenario ($\sigma_{\ln M} = 0.5$) and a more optimistic scenario ($\sigma_{\ln M} = 0.1$). The results are depicted in Fig. 7 as dotted and dot-dashed lines, respectively. While the constraints from the multitracer analysis on $\beta$ are only marginally affected for $\sigma_{\ln M} = 0.1$ and degrade by roughly 20–30% for $\sigma_{\ln M} = 0.5$, the combined analysis using optimally weighted halos and the dark matter is more severely deteriorated by mass scatter. Here, even the optimistic scenario increases the uncertainty on the growth rate by roughly 50%, while the benefits from optimal weighting are completely lost when going to $\sigma_{\ln M} = 0.5$.

Clearly, the high level of precision that can be obtained with this kind of experiment demands precise mass estimates. Fortunately, a whole industry of existing and planned experiments devoted to cluster cosmology will provide those high quality data (e.g., [78–83]).

### D. Halo model predictions

In this section we want to investigate how our results depend on the resolution of the simulation; respectively, the minimum resolved halo mass. In a real experiment, this corresponds to the depth of the galaxy survey with a corresponding luminosity threshold. Because $N$-body simulations with a given volume become increasingly expensive with higher resolution, we will turn to theoretical predictions henceforth.

The clustering properties of dark matter and halos can be neatly described by the *halo model* (see, e.g., [84]). The basic idea is to separately describe the clustering within a given halo (one-halo term) and the clustering amongst different halos (two-halo term). In [50] the halo model is utilized to derive an analytical expression for the shot noise matrix. The result can be written as

$$\boldsymbol{\mathcal{E}} = \bar{n}^{-1}\mathbf{I} - \boldsymbol{b}_{\mathrm{g}}\boldsymbol{\mathcal{M}}^\dagger - \boldsymbol{\mathcal{M}}\boldsymbol{b}_{\mathrm{g}}^\dagger \,, \tag{44}$$

where $\bar{n}$ is the number density of halos per bin, $\mathbf{I}$ the identity matrix, $\boldsymbol{\mathcal{M}} \equiv \boldsymbol{M}/\bar{\rho}_{\mathrm{m}} - \boldsymbol{b}_{\mathrm{g}}\langle nM^2\rangle/2\bar{\rho}_{\mathrm{m}}^2$ and $\boldsymbol{M}$ a vector containing the mean halo mass of each bin. In Appendix B we utilize this expression to derive the clustering signal-to-noise ratio $\Sigma$ (as well as $\Sigma_i$ and $\Sigma_{ij}$) from the halo model. With Eq. (39) we can then determine the Fisher information on the growth rate and compare the single-tracer analysis to the multitracer analysis.

Figure 8 displays the same ratio as Fig. 7 for the uncertainty on $\beta$, but now as a function of minimum halo mass $M_{\min}$ at a fixed scale of $k \simeq 0.016h\mathrm{Mpc}^{-1}$ (peak

of the power spectrum). The gains from the multitracer method kick in at $M_{\min} \simeq 10^{14} h^{-1} \mathrm{M}_\odot$, where $\Sigma \simeq 1$, and increase towards lower $M_{\min}$ due to the growing signal-to-noise ratio.

A combination of galaxy and dark matter observations may increase these gains further, especially when the galaxies are weighted optimally. In this case there is no saturation towards lower $M_{\min}$ and the improvement compared to the single-tracer analysis continues to grow. In contrast, the uniform galaxy overdensity field (not weighted) combined with dark matter already shows up a saturation at $M_{\min} \simeq 10^{10} h^{-1} \mathrm{M}_\odot$, so no more information on the growth rate can be gained when even more lighter halos are included in this kind of analysis. Also note that the halo model predictions underestimate the improvements obtained when adding dark matter clustering information, as our $N$-body results with $M_{\min} \simeq 9.4 \times 10^{11} h^{-1} \mathrm{M}_\odot$ yield higher improvements (see Fig. 7).

In the shot noise dominated regime above a minimum mass of $M_{\min} \sim 10^{14} h^{-1} \mathrm{M}_\odot$ the error ratio decreases again towards higher $M_{\min}$ because the Fisher information on $f$ from a single tracer here roughly scales as $\mathcal{E}^{-2}$, while for a tracer combined with dark matter as $\mathcal{E}^{-1}$ [see Eqs. (23) and (29), respectively]. We refer the reader to Figs. 10 and 11 of [52], where a similar plot is shown for the individual error bars on the non-Gaussianity parameter $f_{\mathrm{NL}}$.

## IV. CONCLUSIONS

In this paper we investigated the benefits of using weights in a multitracer analysis of LSS, with a particular focus on constraining the growth rate of structure formation. On the basis of earlier results on the clustering properties of dark matter halos and their stochasticity [50], we argue that the gains from a multitracer analysis in the sense of [12] can be achieved by considering only the two principal components of the clustering signal-to-noise ratio $\Sigma$ (or, equivalently, the two non-Poisson eigenvectors of the shot noise matrix $\mathcal{E}$).

We present their explicit functional forms in terms of weights, showing that the first one coincides with the weighting function explored in previous work [50], giving rise to low stochasticity and high bias. For the second one the weights are also mass dependent, but have a zero crossing, such that the overall bias is low. This yields a high relative galaxy bias $\alpha$ between the two tracers, maximizing the Fisher information content on the cosmological parameters [12]. All of the other eigenvectors oscillate around zero and add very little information. The advantage of reducing the information to two eigenvectors is that all of the objects in a given catalog can be used to construct the two principal components, while in the conventional multitracer analysis the catalog has
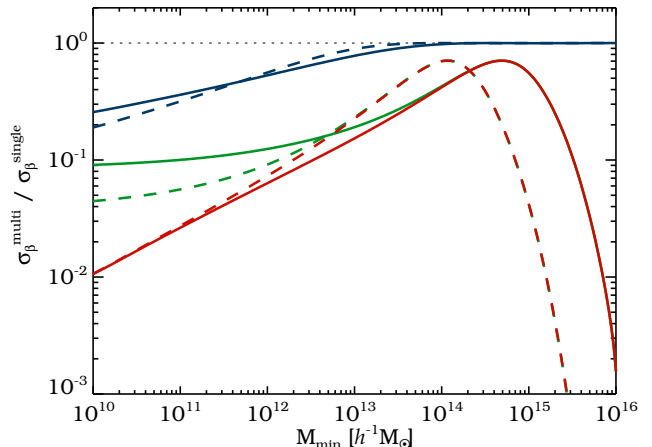


FIG. 8. Halo model prediction for the improvement on $\sigma_\beta$ from the single-tracer analysis to the optimal multitracer analysis (blue) at $k \simeq 0.016 h \mathrm{Mpc}^{-1}$ as a function of the lower halo-mass threshold $M_{\min}$ at $z = 0$ (solid) and $z = 1$ (dashed). The results for the combined analysis of uniform halos (not weighted) and dark matter (green), as well as the combination of optimally weighted halos with the dark matter (red) are also depicted.

to be split into many lower number density subsamples with higher shot noise [56, 58].

On the basis of numerical $N$-body simulations of dark matter halos, we demonstrate that the constraints on $\beta$ and $f\sigma_8$ can be improved by up to a factor of 4 relative to a single-tracer method, but most of the improvement comes from large scales (low $k$), while for higher $k$ the gains are smaller and vanish above $k \sim 0.1 h \mathrm{Mpc}^{-1}$, where nonlinear effects introduce additional stochasticity between the two tracers. This technique is fairly insensitive to the observational uncertainty on the halo masses, as even a 50% log-normal scatter does not degrade the improvements significantly. Halo model considerations suggest even higher gains of the method with increasing mass resolution.

One potential concern for our method is the possibility that galaxies might be bad tracers of their host-halo centers [85] and therefore exhibit less pronounced principal components in the clustering signal-to-noise ratio that are distinct from Poisson sampling. However, there are strong indications that certain types of galaxies do show strong correlations in both position and mass with their host halo, e.g. luminous red galaxies (LRGs) [86]. Techniques to distinguish satellite galaxies from central galaxies have been developed and the satellite fraction can be used as an estimator of the host-halo mass [87]. Mock LRG catalogs obtained from a halo occupation distribution (HOD) model suggest some reduction in stochasticity is possible even without explicit knowledge of halo masses [88]. Therefore, an achievement of the presented gains seems feasible in light of upcoming spectroscopic

galaxy surveys such as EUCLID [3], which will attain galaxy number densities, host-halo mass ranges and a survey volume comparable to the simulations used in this paper [89, 90].

Whether these gains translate into a useful constraint on the final cosmological parameters depends on our ability to model nonlinear RSD effects. We find nonlinear effects are important for $\beta$ already at $k > 0.03h\mathrm{Mpc}^{-1}$, although they appear to be important for $f\sigma_8$ only at $k > 0.1h\mathrm{Mpc}^{-1}$. In the most pessimistic case where the RSD model cannot be trusted for $k > 0.03h\mathrm{Mpc}^{-1}$, the multitracer method provides major gains relative to the single-tracer case, but neither method provides very strong constraints overall because of the limited number of available Fourier modes. In the case where we can use all the modes up to $k \sim 0.1h\mathrm{Mpc}^{-1}$, the overall errors are considerably smaller and the multitracer method provides less of an advantage. It is clear that a better modeling of the nonlinear effects in RSD is needed to understand the ultimate reach of RSD in both single-tracer and multitracer methods.

In a more idealistic scenario, we also consider the joint analysis of halos and the dark matter density field, which in principle is achievable via a combination of spectroscopic redshift surveys and weak lensing tomography. Here, utilizing optimal weights can yield up to two orders of magnitude improvements in constraining $\beta$ as compared to a single-tracer analysis, but the method is more prone to uncertainties in the halo mass estimates. It is unlikely that this gain can be achieved in practice, since it is very difficult to measure dark matter clustering in the radial direction directly.

A further technique to construct differently biased tracers of the density field makes use of nonlinear transformations [91]. Although it is difficult to describe the effects of a nonlinear transformation on both signal and noise in galaxy clustering data, combined with optimal weights this may provide another tool for the multitracer analysis.

In this paper we have focused on the information that can be extracted from RSD, in particular $\beta$ and $f\sigma_8$, but our method is not limited to constraints on the growth rate, but may be applied to the analysis of primordial non-Gaussianity [52], general relativistic corrections in large-scale clustering [92], the Alcock-Paczyński test [12] or any other quantity that influences the effective bias of tracers of the density field. It is possible that a better model of the nonlinear RSD may yield a more efficient multitracer method, where the gains relative to the single-tracer analysis described here on large scales can be extended to smaller scales. We leave these directions for the future.

## ACKNOWLEDGMENTS

## Appendix A: FISHER MATRIX FOR MULTIPLE BIASED TRACERS

With Eqs. (19) and (20) plugged into Eq. (18), we have

$$
\begin{aligned}
F_{ij} &= \frac{1}{2}\mathrm{Tr}\left[\left(\boldsymbol{b}\boldsymbol{b}_i^\dagger + \boldsymbol{b}_i\boldsymbol{b}^\dagger + \boldsymbol{b}\boldsymbol{b}^\dagger\frac{P_i}{P}\right)\mathbf{C}^{-1}\left(\boldsymbol{b}\boldsymbol{b}_j^\dagger + \boldsymbol{b}_j\boldsymbol{b}^\dagger + \boldsymbol{b}\boldsymbol{b}^\dagger\frac{P_j}{P}\right)\mathbf{C}^{-1}\right]P^2 = \\
&= \frac{1}{2}\left(\boldsymbol{b}^\dagger\mathbf{C}^{-1}\boldsymbol{b}\boldsymbol{b}_i^\dagger\mathbf{C}^{-1}\boldsymbol{b}_j + \boldsymbol{b}^\dagger\mathbf{C}^{-1}\boldsymbol{b}\boldsymbol{b}_j^\dagger\mathbf{C}^{-1}\boldsymbol{b}_i + \boldsymbol{b}^\dagger\mathbf{C}^{-1}\boldsymbol{b}_i\boldsymbol{b}^\dagger\mathbf{C}^{-1}\boldsymbol{b}_j + \boldsymbol{b}_i^\dagger\mathbf{C}^{-1}\boldsymbol{b}\boldsymbol{b}_j^\dagger\mathbf{C}^{-1}\boldsymbol{b} + \boldsymbol{b}^\dagger\mathbf{C}^{-1}\boldsymbol{b}\boldsymbol{b}^\dagger\mathbf{C}^{-1}\boldsymbol{b}_i\frac{P_j}{P} + \right. \\
&\quad \left. \boldsymbol{b}^\dagger\mathbf{C}^{-1}\boldsymbol{b}\boldsymbol{b}_i^\dagger\mathbf{C}^{-1}\boldsymbol{b}\frac{P_j}{P} + \boldsymbol{b}^\dagger\mathbf{C}^{-1}\boldsymbol{b}\boldsymbol{b}^\dagger\mathbf{C}^{-1}\boldsymbol{b}_j\frac{P_i}{P} + \boldsymbol{b}^\dagger\mathbf{C}^{-1}\boldsymbol{b}\boldsymbol{b}_j^\dagger\mathbf{C}^{-1}\boldsymbol{b}\frac{P_i}{P} + \boldsymbol{b}^\dagger\mathbf{C}^{-1}\boldsymbol{b}\boldsymbol{b}^\dagger\mathbf{C}^{-1}\boldsymbol{b}\frac{P_iP_j}{P^2}\right)P^2 = \\
&= \frac{\Sigma}{1+\Sigma}\left[\Sigma_{ij} - \frac{\Sigma_i\Sigma_j}{1+\Sigma}\right] + \frac{\Sigma_i\Sigma_j}{(1+\Sigma)^2} + \frac{\Sigma_i\Sigma}{(1+\Sigma)^2}\frac{P_j}{P} + \frac{\Sigma_j\Sigma}{(1+\Sigma)^2}\frac{P_i}{P} + \left(\frac{\Sigma}{1+\Sigma}\right)^2\frac{P_iP_j}{2P^2} = \\
&= \left[\Sigma^{-1}\left(\Sigma_{ij} + \frac{\Sigma_i\Sigma_j}{\Sigma}\right) + \left(\Sigma_{ij} - \frac{\Sigma_i\Sigma_j}{\Sigma}\right) + \frac{\Sigma_i}{\Sigma}\frac{P_j}{P} + \frac{\Sigma_j}{\Sigma}\frac{P_i}{P} + \frac{P_iP_j}{2P^2}\right]\left(1+\Sigma^{-1}\right)^{-2} . \quad \text{(A1)}
\end{aligned}
$$

With additional knowledge about the dark matter density field we need to work out Eq. (18) by plugging in Eqs. (26) and (27). Let us first note that

$$
\frac{\partial\mathbf{C}}{\partial\theta_i}\mathbf{C}^{-1} = \begin{pmatrix} P_i/P - \Sigma_i & \boldsymbol{b}_i^\dagger\boldsymbol{\mathcal{E}}^{-1}P \\ \boldsymbol{b}_i + \boldsymbol{b}\left(P_i/P - \Sigma_i\right) & \boldsymbol{b}\boldsymbol{b}_i^\dagger\boldsymbol{\mathcal{E}}^{-1}P \end{pmatrix} ,
$$

so

$$
\frac{\partial\mathbf{C}}{\partial\theta_i}\mathbf{C}^{-1}\frac{\partial\mathbf{C}}{\partial\theta_j}\mathbf{C}^{-1} =
$$

$$
\begin{pmatrix} \left(P_i/P - \Sigma_i\right)\left(P_j/P - \Sigma_j\right) + \Sigma_{ij} + \Sigma_i\left(P_j/P - \Sigma_j\right) & \left(P_i/P - \Sigma_i\right)\boldsymbol{b}_j^\dagger\boldsymbol{\mathcal{E}}^{-1}P + \Sigma_i\boldsymbol{b}_j^\dagger\boldsymbol{\mathcal{E}}^{-1}P \\ \left[\boldsymbol{b}_i + \boldsymbol{b}\left(P_i/P - \Sigma_i\right)\right]\left(P_j/P - \Sigma_j\right) + \boldsymbol{b}\Sigma_{ij} + \boldsymbol{b}\Sigma_i\left(P_j/P - \Sigma_j\right) & \boldsymbol{b}_i\boldsymbol{b}_j^\dagger\boldsymbol{\mathcal{E}}^{-1}P + \boldsymbol{b}\boldsymbol{b}_j^\dagger\boldsymbol{\mathcal{E}}^{-1}P\left(P_i/P - \Sigma_i\right) + \boldsymbol{b}\Sigma_i\boldsymbol{b}_j^\dagger\boldsymbol{\mathcal{E}}^{-1}P \end{pmatrix}
$$

This yields

$$
F_{ij} = \frac{1}{2}\mathrm{Tr}\left(\frac{\partial\mathbf{C}}{\partial\theta_i}\mathbf{C}^{-1}\frac{\partial\mathbf{C}}{\partial\theta_j}\mathbf{C}^{-1}\right) = \Sigma_{ij} + \frac{P_iP_j}{2P^2} . \quad \text{(A2)}
$$

## Appendix B: HALO MODEL PREDICTION FOR THE CLUSTERING SIGNAL-TO-NOISE RATIO

In the halo model the shot noise matrix is given by Eq. (44). In order to invert $\boldsymbol{\mathcal{E}}$, we write $\boldsymbol{\mathcal{E}} = \boldsymbol{\mathcal{A}} - \boldsymbol{\mathcal{M}}\boldsymbol{b}_\mathrm{g}^\dagger$ with $\boldsymbol{\mathcal{A}} \equiv \bar{n}^{-1}\mathbf{I} - \boldsymbol{b}_\mathrm{g}\boldsymbol{\mathcal{M}}^\dagger$ and apply the Sherman-Morrison formula twice:

$$
\boldsymbol{\mathcal{E}}^{-1} = \boldsymbol{\mathcal{A}}^{-1} + \frac{\boldsymbol{\mathcal{A}}^{-1}\boldsymbol{\mathcal{M}}\boldsymbol{b}_\mathrm{g}^\dagger\boldsymbol{\mathcal{A}}^{-1}}{1 - \boldsymbol{b}_\mathrm{g}^\dagger\boldsymbol{\mathcal{A}}^{-1}\boldsymbol{\mathcal{M}}} \quad , \quad \boldsymbol{\mathcal{A}}^{-1} = \bar{n}\mathbf{I} + \frac{\boldsymbol{b}_\mathrm{g}\boldsymbol{\mathcal{M}}^\dagger\bar{n}}{\bar{n}^{-1} - \boldsymbol{\mathcal{M}}^\dagger\boldsymbol{b}_\mathrm{g}} . \quad \text{(B1)}
$$

With

$$
\Sigma_{ij} \equiv \boldsymbol{b}_i^\dagger\boldsymbol{\mathcal{E}}^{-1}\boldsymbol{b}_jP = \frac{\boldsymbol{b}_i^\dagger\boldsymbol{\mathcal{A}}^{-1}\boldsymbol{b}_j\left(1 - \boldsymbol{b}_\mathrm{g}^\dagger\boldsymbol{\mathcal{A}}^{-1}\boldsymbol{\mathcal{M}}\right) + \boldsymbol{b}_i^\dagger\boldsymbol{\mathcal{A}}^{-1}\boldsymbol{\mathcal{M}}\boldsymbol{b}_\mathrm{g}^\dagger\boldsymbol{\mathcal{A}}^{-1}\boldsymbol{b}_j}{1 - \boldsymbol{b}_\mathrm{g}^\dagger\boldsymbol{\mathcal{A}}^{-1}\boldsymbol{\mathcal{M}}}P , \quad \text{(B2)}
$$

and

$$
\boldsymbol{b}_i^\dagger\boldsymbol{\mathcal{A}}^{-1}\boldsymbol{b}_j = \frac{\boldsymbol{b}_i^\dagger\boldsymbol{b}_j\left(\bar{n}^{-1} - \boldsymbol{\mathcal{M}}^\dagger\boldsymbol{b}_\mathrm{g}\right) + \boldsymbol{b}_i^\dagger\boldsymbol{b}_\mathrm{g}\boldsymbol{\mathcal{M}}^\dagger\boldsymbol{b}_j}{\bar{n}^{-1} - \boldsymbol{\mathcal{M}}^\dagger\boldsymbol{b}_\mathrm{g}}\bar{n} , \quad \text{(B3)}
$$

$$
1 - \boldsymbol{b}_\mathrm{g}^\dagger\boldsymbol{\mathcal{A}}^{-1}\boldsymbol{\mathcal{M}} = \frac{\left(\bar{n}^{-1} - \boldsymbol{\mathcal{M}}^\dagger\boldsymbol{b}_\mathrm{g}\right)^2 - \boldsymbol{b}_\mathrm{g}^\dagger\boldsymbol{b}_\mathrm{g}\boldsymbol{\mathcal{M}}^\dagger\boldsymbol{\mathcal{M}}}{\bar{n}^{-1} - \boldsymbol{\mathcal{M}}^\dagger\boldsymbol{b}_\mathrm{g}}\bar{n} , \quad \text{(B4)}
$$

and similar terms combining $\boldsymbol{b}$, $\boldsymbol{b}_i$, $\boldsymbol{b}_\mathrm{g}$ and $\boldsymbol{\mathcal{M}}$, after some algebra we get

$$\Sigma_{ij} = \boldsymbol{b}_i^\dagger \boldsymbol{b}_j \bar{n} P + \frac{\boldsymbol{b}_i^\dagger \boldsymbol{\mathcal{M}} \boldsymbol{b}_\mathrm{g}^\dagger \boldsymbol{b}_\mathrm{g} \boldsymbol{\mathcal{M}}^\dagger \boldsymbol{b}_j + \left(\boldsymbol{b}_i^\dagger \boldsymbol{b}_\mathrm{g} \boldsymbol{\mathcal{M}}^\dagger \boldsymbol{b}_j + \boldsymbol{b}_i^\dagger \boldsymbol{\mathcal{M}} \boldsymbol{b}_\mathrm{g}^\dagger \boldsymbol{b}_j\right)\left(\bar{n}^{-1} - \boldsymbol{\mathcal{M}}^\dagger \boldsymbol{b}_\mathrm{g}\right) + \boldsymbol{b}_i^\dagger \boldsymbol{b}_\mathrm{g} \boldsymbol{\mathcal{M}}^\dagger \boldsymbol{\mathcal{M}} \boldsymbol{b}_\mathrm{g}^\dagger \boldsymbol{b}_j}{\left(\bar{n}^{-1} - \boldsymbol{\mathcal{M}}^\dagger \boldsymbol{b}_\mathrm{g}\right)^2 - \boldsymbol{b}_\mathrm{g}^\dagger \boldsymbol{b}_\mathrm{g} \boldsymbol{\mathcal{M}}^\dagger \boldsymbol{\mathcal{M}}} \bar{n} P \ . \tag{B5}$$

In the continuous limit ($N \to \infty$), we can exchange the vector products by integrals over the mass function and set $\bar{n}_\mathrm{tot} = \bar{n}N$. This finally yields

$$\Sigma_{ij} = \langle b_i b_j \rangle \bar{n}_\mathrm{tot} P + \frac{\langle b_\mathrm{g}^2 \rangle \langle \mathcal{M} b_i \rangle \langle \mathcal{M} b_j \rangle + \left(\langle b_i b_\mathrm{g} \rangle \langle \mathcal{M} b_j \rangle + \langle \mathcal{M} b_i \rangle \langle b_j b_\mathrm{g} \rangle\right)\left(\bar{n}_\mathrm{tot}^{-1} - \langle \mathcal{M} b_\mathrm{g} \rangle\right) + \langle b_i b_\mathrm{g} \rangle \langle b_j b_\mathrm{g} \rangle \langle \mathcal{M}^2 \rangle}{\left(\bar{n}_\mathrm{tot}^{-1} - \langle \mathcal{M} b_\mathrm{g} \rangle\right)^2 - \langle b_\mathrm{g}^2 \rangle \langle \mathcal{M}^2 \rangle} \bar{n}_\mathrm{tot} P \ .$$
$$\tag{B6}$$

[1] S. Perlmutter, G. Aldering, G. Goldhaber, R. A. Knop, P. Nugent, P. G. Castro, S. Deustua, S. Fabbro, A. Goobar, D. E. Groom, et al., ApJ **517**, 565 (1999), arXiv:astro-ph/9812133.

[2] *BigBOSS*, URL http://bigboss.lbl.gov.

[3] *EUCLID*, URL http://sci.esa.int/euclid.

[4] *SDSS-III*, URL http://www.sdss3.org.

[5] F. Bernardeau, S. Colombi, E. Gaztañaga, and R. Scoccimarro, Phys. Rep. **367**, 1 (2002), arXiv:astro-ph/0112551.

[6] M. Crocce and R. Scoccimarro, Phys. Rev. D **73**, 063519 (2006), arXiv:astro-ph/0509418.

[7] A. Taruya and T. Hiramatsu, ApJ **674**, 617 (2008), 0708.1367.

[8] T. Matsubara, Phys. Rev. D **78**, 083519 (2008), 0807.1733.

[9] K. Chuen Chan and R. Scoccimarro, ArXiv e-prints (2012), 1204.5770.

[10] T. Baldauf, U. Seljak, V. Desjacques, and P. McDonald, ArXiv e-prints (2012), 1201.4827.

[11] U. Seljak, Physical Review Letters **102**, 021302 (2009), 0807.1770.

[12] P. McDonald and U. Seljak, J. Cosmology Astropart. Phys. **10**, 7 (2009), 0810.0323.

[13] L. Guzzo, M. Pierleoni, B. Meneux, E. Branchini, O. Le Fèvre, C. Marinoni, B. Garilli, J. Blaizot, G. De Lucia, A. Pollo, et al., Nature **451**, 541 (2008), 0802.1944.

[14] W. J. Percival and M. White, MNRAS **393**, 297 (2009), 0808.0003.

[15] A. Cabré and E. Gaztañaga, MNRAS **393**, 1183 (2009), 0807.2460.

[16] M. Crocce, E. Gaztañaga, A. Cabré, A. Carnero, and E. Sánchez, MNRAS **417**, 2577 (2011), 1104.5236.

[17] C. Blake, S. Brough, M. Colless, C. Contreras, W. Couch, S. Croom, T. Davis, M. J. Drinkwater, K. Forster, D. Gilbank, et al., MNRAS **415**, 2876 (2011), 1104.2948.

[18] A. J. Ross, W. J. Percival, M. Crocce, A. Cabré, and E. Gaztañaga, MNRAS **415**, 2193 (2011), 1102.0968.

[19] A. Nusser, E. Branchini, and M. Davis, ApJ **744**, 193 (2012), 1106.6145.

[20] F. Beutler, C. Blake, M. Colless, D. H. Jones, L. Staveley-Smith, G. B. Poole, L. Campbell, Q. Parker, W. Saunders, and F. Watson, MNRAS **423**, 3430 (2012), 1204.4725.

[21] B. A. Reid, L. Samushia, M. White, W. J. Percival, M. Manera, N. Padmanabhan, A. J. Ross, A. G. Sánchez, S. Bailey, D. Bizyaev, et al., ArXiv e-prints (2012), 1203.6641.

[22] L. Samushia, B. A. Reid, M. White, W. J. Percival, A. J. Cuesta, L. Lombriser, M. Manera, R. C. Nichol, D. P. Schneider, D. Bizyaev, et al., ArXiv e-prints (2012), 1206.5309.

[23] A. Raccanelli, D. Bertacca, D. Pietrobon, F. Schmidt, L. Samushia, N. Bartolo, O. Doré, S. Matarrese, and W. J. Percival, ArXiv e-prints (2012), 1207.0500.

[24] N. Kaiser, MNRAS **227**, 1 (1987).

[25] J. A. Peacock and S. J. Dodds, MNRAS **267**, 1020 (1994), arXiv:astro-ph/9311057.

[26] R. Scoccimarro, Phys. Rev. D **70**, 083007 (2004), arXiv:astro-ph/0407214.

[27] J. L. Tinker, D. H. Weinberg, and Z. Zheng, MNRAS **368**, 85 (2006), arXiv:astro-ph/0501029.

[28] B. A. Reid and M. White, MNRAS **417**, 1913 (2011), 1105.4165.

[29] E. Jennings, C. M. Baugh, and S. Pascoli, MNRAS **410**, 2081 (2011), 1003.4282.

[30] M. Sato and T. Matsubara, Phys. Rev. D **84**, 043501 (2011), 1105.5007.

[31] J. Kwan, G. F. Lewis, and E. V. Linder, ApJ **748**, 78 (2012), 1105.1194.

[32] L. Samushia, W. J. Percival, and A. Raccanelli, MNRAS **420**, 2102 (2012), 1102.1014.

[33] S. de la Torre and L. Guzzo, ArXiv e-prints (2012), 1202.5559.

[34] D. Bianchi, L. Guzzo, E. Branchini, E. Majerotto, S. de la Torre, F. Marulli, L. Moscardini, and R. E. Angulo, ArXiv e-prints (2012), 1203.1545.

[35] P. J. E. Peebles, *The large-scale structure of the universe* (1980).

[36] E. V. Linder and R. N. Cahn, Astroparticle Physics **28**, 481 (2007), arXiv:astro-ph/0701317.

[37] T. Okumura and Y. P. Jing, ApJ **726**, 5 (2011), 1004.3548.

[38] R. A. Fisher, Roy. Stat. Soc. **98**, 39 (1935).

[39] M. Tegmark, A. N. Taylor, and A. F. Heavens, ApJ **480**, 22 (1997), arXiv:astro-ph/9603021.

[40] A. Heavens, ArXiv e-prints (2009), 0906.0664.

[41] J. Sherman and W. J. Morrison, Ann. Math. Stat. **21**, 124 (1950).

[42] M. S. Bartlett, Ann. Math. Stat. **22**, pp. 107 (1951), ISSN 00034851.

[43] U. Seljak, N. Hamaus, and V. Desjacques, Phys. Rev. Lett. **103**, 091303 (2009), 0904.2963.

[44] V. Springel, MNRAS **364**, 1105 (2005), arXiv:astro-ph/0505010.

[45] E. Komatsu, J. Dunkley, M. R. Nolta, C. L. Bennett, B. Gold, G. Hinshaw, N. Jarosik, D. Larson, M. Limon, L. Page, et al., ApJS **180**, 330 (2009), 0803.0547.

[46] M. Davis, G. Efstathiou, C. S. Frenk, and S. D. M. White, ApJ **292**, 371 (1985).

[47] R. W. Hockney and J. W. Eastwood, *Computer simulation using particles* (1988).

[48] C. B. Markwardt, in *Astronomical Data Analysis Software and Systems XVIII*, edited by D. A. Bohlender, D. Durand, & P. Dowler (2009), vol. 411 of *Astronomical Society of the Pacific Conference Series*, p. 251, 0902.2850.

[49] J. Moré, *The Levenberg-Marquardt algorithm: Implementation and theory*, vol. 630 of *Lecture Notes in Mathematics* (Springer Berlin / Heidelberg, 1978).

[50] N. Hamaus, U. Seljak, V. Desjacques, R. E. Smith, and T. Baldauf, Phys. Rev. D **82**, 043515 (2010), 1004.5377.

[51] R. E. Smith, R. Scoccimarro, and R. K. Sheth, Phys. Rev. D **75**, 063512 (2007), arXiv:astro-ph/0609547.

[52] N. Hamaus, U. Seljak, and V. Desjacques, Phys. Rev. D **84**, 083509 (2011), 1104.2321.

[53] J. N. Fry and E. Gaztañaga, ApJ **413**, 447 (1993), arXiv:astro-ph/9302009.

[54] A. F. Heavens, S. Matarrese, and L. Verde, MNRAS **301**, 797 (1998), arXiv:astro-ph/9808016.

[55] P. McDonald, Phys. Rev. D **74**, 103512 (2006), arXiv:astro-ph/0609413.

[56] H. Gil-Marín, C. Wagner, L. Verde, R. Jimenez, and A. F. Heavens, MNRAS **407**, 772 (2010), 1003.3238.

[57] M. White, Y.-S. Song, and W. J. Percival, MNRAS **397**, 1348 (2009), 0810.1518.

[58] G. M. Bernstein and Y.-C. Cai, MNRAS **416**, 3009 (2011), 1104.3862.

[59] T. Okumura, U. Seljak, and V. Desjacques, ArXiv e-prints (2012), 1206.4070.

[60] T. Baldauf, R. E. Smith, U. Seljak, and R. Mandelbaum, Phys. Rev. D **81**, 063531 (2010), 0911.4973.

[61] E. Gaztañaga, M. Eriksen, M. Crocce, F. J. Castander, P. Fosalba, P. Marti, R. Miquel, and A. Cabré, MNRAS **422**, 2904 (2012), 1109.4852.

[62] Y.-C. Cai and G. Bernstein, MNRAS **422**, 1045 (2012), 1112.4478.

[63] M. Cacciato, O. Lahav, F. C. van den Bosch, H. Hoekstra, and A. Dekel, MNRAS **426**, 566 (2012), 1203.2616.

[64] P. Simon, ArXiv e-prints (2012), 1203.6205.

[65] E. Jullo, J. Rhodes, A. Kiessling, J. E. Taylor, R. Massey, J. Berge, C. Schimd, J.-P. Kneib, and N. Scoville, ApJ **750**, 37 (2012), 1202.6491.

[66] F. van den Bosch, S. More, M. Cacciato, H. Mo, and X. Yang, ArXiv e-prints (2012), 1206.6890.

[67] W. Hu, ApJ **522**, L21 (1999).

[68] U. Pen, MNRAS **350**, 1445 (2004), arXiv:astro-ph/0402008.

[69] R. Massey, J. Rhodes, R. Ellis, N. Scoville, A. Leauthaud, A. Finoguenov, P. Capak, D. Bacon, H. Aussel, J.-P. Kneib, et al., Nature **445**, 286 (2007).

[70] P. Simon, A. N. Taylor, and J. Hartlap, MNRAS **399**, 48 (2009), 0907.0016.

[71] J. T. VanderPlas, A. J. Connolly, B. Jain, and M. Jarvis, ApJ **727**, 118 (2011), 1008.2396.

[72] U. Seljak and P. McDonald, J. Cosmology Astropart. Phys. **11**, 39 (2011), 1109.1888.

[73] S. W. Allen, A. E. Evrard, and A. B. Mantz, ARA&A **49**, 409 (2011), 1103.4829.

[74] R. E. Angulo, V. Springel, S. D. M. White, A. Jenkins, C. M. Baugh, and C. S. Frenk, ArXiv e-prints (2012), 1203.3216.

[75] Y. Noh and J. D. Cohn, ArXiv e-prints (2012), 1204.1577.

[76] E. Rozo, E. S. Rykoff, A. Evrard, M. Becker, T. McKay, R. H. Wechsler, B. P. Koester, J. Hao, S. Hansen, E. Sheldon, et al., ApJ **699**, 768 (2009), 0809.2794.

[77] A. V. Kravtsov, A. Vikhlinin, and D. Nagai, ApJ **650**, 128 (2006), arXiv:astro-ph/0603205.

[78] *ACT*, URL http://physics.princeton.edu/act.

[79] *DES*, URL http://www.darkenergysurvey.org.

[80] *eROSITA*, URL http://mpe.mpg.de/erosita.

[81] *LSST*, URL http://www.lsst.org/lsst.

[82] *SPT*, URL http://pole.uchicago.edu.

[83] *WFXT*, URL http://wfxt.pha.jhu.edu.

[84] U. Seljak, MNRAS **318**, 203 (2000), arXiv:astro-ph/0001493.

[85] R. A. Skibba, F. C. van den Bosch, X. Yang, S. More, H. Mo, and F. Fontanot, MNRAS **410**, 417 (2011), 1001.4533.

[86] Z. Zheng, I. Zehavi, D. J. Eisenstein, D. H. Weinberg, and Y. P. Jing, ApJ **707**, 554 (2009), 0809.1868.

[87] Z. Zheng, A. A. Berlind, D. H. Weinberg, A. J. Benson, C. M. Baugh, S. Cole, R. Davé, C. S. Frenk, N. Katz, and C. G. Lacey, ApJ **633**, 791 (2005), arXiv:astro-ph/0408564.

[88] Y. Cai, G. Bernstein, and R. K. Sheth, MNRAS **412**, 995 (2011), 1007.3500.

[89] R. Laureijs, J. Amiaux, S. Arduini, J. . Auguères, J. Brinchmann, R. Cole, M. Cropper, C. Dabin, L. Duvet, A. Ealet, et al., ArXiv e-prints (2011), 1110.3193.

[90] E. Majerotto, L. Guzzo, L. Samushia, W. J. Percival, Y. Wang, S. de la Torre, B. Garilli, P. Franzetti, E. Rossetti, A. Cimatti, et al., MNRAS **424**, 1392 (2012), 1205.6215.

[91] U. Seljak, J. Cosmology Astropart. Phys. **3**, 4 (2012), 1201.0594.

[92] J. Yoo, N. Hamaus, U. Seljak, and M. Zaldarriaga, Phys. Rev. D **86**, 063514 (2012), 1206.5809.

# 6

## OUTLOOK

In addition to the presented ones, further applications for multitracer analyses utilizing optimal weights are conceivable. One example is the so-called *Alcock-Paczyński* test [1], where the conversion factor between radial and angular coordinates in the universe is determined. Because this factor depends on the cosmic expansion history, it is particularly sensitive to the dark energy at late times. The use of multiple tracers can break degeneracies between various parameters in the model, which, combined with optimal weighting techniques, can potentially be constrained with unprecedented accuracy [30].

Another example deals with general relativistic corrections to the common Newtonian treatment of galaxy clustering [55]. These corrections become important only on very large scales, comparable to the size of the horizon. In a single-tracer analysis their detection is hampered due to cosmic variance, i.e. the limited number of independent Fourier modes available in the observable universe. In a recent study it was demonstrated that the use of multiple tracers and optimal weights can potentially reveal those corrections in the galaxy clustering pattern, opening up the unique possibility to test general relativity on the largest cosmic scales [56]. An extension of this study to modified gravity scenarios is feasible.

The methods developed in this thesis bear promising implications for the attainable precision in cosmological analyses of large-scale structure. However, their performance has only been tested on the basis of dark matter simulations so far. A next step could be the inclusion of baryons using full-fledged hydrodynamic simulations, in order to close the gap between the formation of dark matter halos and galaxies. Unfortunately, due to the enormous range of scales important for galaxy formation, a self-consistent treatment is numerically not achievable yet, and semi-analytic models have to be adopted. HOD-models, for example, are already quite successful in reproducing the observed clustering properties of galaxies [40]. Within this framework, it has been shown that for certain types of galaxies, optimal weighting techniques are still very efficient [7]. The actual benefit of these methods still has to be tested on observational data, taking into account all real-world complications of galaxy surveys, this presents a true challenge for future investigations in this direction.

A further challenge is posed on the theory side. In order to exploit the gains of using optimal weights and multiple tracers beyond the linear regime, it is necessary to consider more elaborate models of large-scale structure. While perturbative approaches for the description of dark matter clustering are already quite successful [3], complications arising due to nonlinear galaxy biasing and redshift-space distortions increasingly impede the practicability of smaller and smaller scales that are available in galaxy surveys. In order for the unused data to be of any value for cosmological inference, new approaches have to be developed towards this direction (e.g., [45]). Conversely, one can think of the inverse approach of nonlinearly transforming the data in order to describe it with a more simple model [44]. Although it is difficult to describe the effects of nonlinear transformations on both signal and noise in galaxy clustering data, combined with optimal weights this may provide another tool for the multitracer analysis. In general, this framework may even be extended to tracers of large-scale structure other than galaxies.

# References

[1] ALCOCK, C., AND PACZYŃSKI, B. An evolution free test for non-zero cosmological constant. Nature *281* (Oct. 1979), 358.

[2] BAYES, M., AND PRICE, M. An Essay towards Solving a Problem in the Doctrine of Chances. *Philosophical Transactions 53* (1763), 370–418.

[3] BERNARDEAU, F., COLOMBI, S., GAZTAÑAGA, E., AND SCOCCIMARRO, R. Large-scale structure of the Universe and cosmological perturbation theory. Phys. Rep. *367* (Sept. 2002), 1–248.

[4] BERTSCHINGER, E. Simulations of Structure Formation in the Universe. ARA&A *36* (1998), 599–654.

[5] BIANCHI, L. On the three-dimensional spaces which admit a continuous group of motions. *Memorie di Matematica e di Fisica della Società Italiana delle Scienze, Serie Terza XI, 267-352 (1898) 11* (1898), 267–352.

[6] BOND, J. R., COLE, S., EFSTATHIOU, G., AND KAISER, N. Excursion set mass functions for hierarchical Gaussian fluctuations. ApJ *379* (Oct. 1991), 440–460.

[7] CAI, Y., BERNSTEIN, G., AND SHETH, R. K. Optimal linear reconstruction of dark matter from halo catalogues. MNRAS *412* (Apr. 2011), 995–1010.

[8] COLE, S., AND KAISER, N. Biased clustering in the cold dark matter cosmogony. MNRAS *237* (Apr. 1989), 1127–1146.

[9] COORAY, A., AND SHETH, R. Halo models of large scale structure. Phys. Rep. *372* (Dec. 2002), 1–129.

[10] DAVIS, M., EFSTATHIOU, G., FRENK, C. S., AND WHITE, S. D. M. The evolution of large-scale structure in a universe dominated by cold dark matter. ApJ *292* (May 1985), 371–394.

[11] DAVIS, M., HUCHRA, J., LATHAM, D. W., AND TONRY, J. A survey of galaxy redshifts. II - The large scale space distribution. ApJ *253* (Feb. 1982), 423–445.

[12] DE SITTER, W. Einstein's theory of gravitation and its astronomical consequences. Third paper. MNRAS *78* (Nov. 1917), 3–28.

[13] DEKEL, A., AND LAHAV, O. Stochastic Nonlinear Galaxy Biasing. ApJ *520* (July 1999), 24–34.

[14] EISENSTEIN, D. J., ZEHAVI, I., HOGG, D. W., SCOCCIMARRO, R., BLAN-
     TON, M. R., NICHOL, R. C., SCRANTON, R., SEO, H.-J., TEGMARK, M.,
     ZHENG, Z., ANDERSON, S. F., ANNIS, J., BAHCALL, N., BRINKMANN, J.,
     BURLES, S., CASTANDER, F. J., CONNOLLY, A., CSABAI, I., DOI, M.,
     FUKUGITA, M., FRIEMAN, J. A., GLAZEBROOK, K., GUNN, J. E., HENDRY,
     J. S., HENNESSY, G., IVEZIĆ, Z., KENT, S., KNAPP, G. R., LIN, H., LOH,
     Y.-S., LUPTON, R. H., MARGON, B., MCKAY, T. A., MEIKSIN, A., MUNN,
     J. A., POPE, A., RICHMOND, M. W., SCHLEGEL, D., SCHNEIDER, D. P.,
     SHIMASAKU, K., STOUGHTON, C., STRAUSS, M. A., SUBBARAO, M., SZA-
     LAY, A. S., SZAPUDI, I., TUCKER, D. L., YANNY, B., AND YORK, D. G.
     Detection of the Baryon Acoustic Peak in the Large-Scale Correlation Function
     of SDSS Luminous Red Galaxies. ApJ*633* (Nov. 2005), 560–574.

[15] FISHER, R. A. *Roy. Stat. Soc. 98* (1935), 39.

[16] FRIEDMAN, A. Über die Krümmung des Raumes. *Zeitschrift fur Physik 10*
     (Dec. 1922), 377–386.

[17] FRY, J. N., AND GAZTAÑAGA, E. Biasing and hierarchical statistics in large-
     scale structure. ApJ*413* (Aug. 1993), 447–452.

[18] GUTH, A. H. Inflationary universe: A possible solution to the horizon and
     flatness problems. Phys. Rev. D*23* (Jan. 1981), 347–356.

[19] HEAVENS, A. Statistical techniques in cosmology. *ArXiv e-prints* (June 2009).

[20] HOCKNEY, R. W., AND EASTWOOD, J. W. *Computer simulation using par-
     ticles.* 1988.

[21] HUBBLE, E. A Relation between Distance and Radial Velocity among Extra-
     Galactic Nebulae. *Proceedings of the National Academy of Science 15* (Mar.
     1929), 168–173.

[22] JING, Y. P. Correcting for the Alias Effect When Measuring the Power Spec-
     trum Using a Fast Fourier Transform. ApJ*620* (Feb. 2005), 559–563.

[23] KAISER, N. Clustering in real space and in redshift space. MNRAS*227* (July
     1987), 1–21.

[24] KNEBE, A., KNOLLMANN, S. R., MULDREW, S. I., PEARCE, F. R.,
     ARAGON-CALVO, M. A., ASCASIBAR, Y., BEHROOZI, P. S., CEVERINO, D.,
     COLOMBI, S., DIEMAND, J., DOLAG, K., FALCK, B. L., FASEL, P., GARD-
     NER, J., GOTTLÖBER, S., HSU, C.-H., IANNUZZI, F., KLYPIN, A., LUKIĆ,
     Z., MACIEJEWSKI, M., MCBRIDE, C., NEYRINCK, M. C., PLANELLES, S.,
     POTTER, D., QUILIS, V., RASERA, Y., READ, J. I., RICKER, P. M., ROY,
     F., SPRINGEL, V., STADEL, J., STINSON, G., SUTTER, P. M., TURCHANI-
     NOV, V., TWEED, D., YEPES, G., AND ZEMP, M. Haloes gone MAD: The
     Halo-Finder Comparison Project. MNRAS*415* (Aug. 2011), 2293–2318.

[25] KOMATSU, E., SMITH, K. M., DUNKLEY, J., BENNETT, C. L., GOLD, B., HINSHAW, G., JAROSIK, N., LARSON, D., NOLTA, M. R., PAGE, L., SPERGEL, D. N., HALPERN, M., HILL, R. S., KOGUT, A., LIMON, M., MEYER, S. S., ODEGARD, N., TUCKER, G. S., WEILAND, J. L., WOLLACK, E., AND WRIGHT, E. L. Seven-year Wilkinson Microwave Anisotropy Probe (WMAP) Observations: Cosmological Interpretation. ApJS*192* (Feb. 2011), 18.

[26] LACEY, C., AND COLE, S. Merger Rates in Hierarchical Models of Galaxy Formation - Part Two - Comparison with N-Body Simulations. MNRAS*271* (Dec. 1994), 676.

[27] LEMAÎTRE, G. Un Univers homogène de masse constante et de rayon croissant rendant compte de la vitesse radiale des nébuleuses extra-galactiques. *Annales de la Societe Scietifique de Bruxelles 47* (1927), 49–59.

[28] LEMAÎTRE, G. Expansion of the universe, A homogeneous universe of constant mass and increasing radius accounting for the radial velocity of extra-galactic nebulae. MNRAS*91* (Mar. 1931), 483–490.

[29] LINDER, E. V., AND CAHN, R. N. Parameterized beyond-Einstein growth. *Astroparticle Physics 28* (Dec. 2007), 481–488.

[30] MCDONALD, P., AND SELJAK, U. How to evade the sample variance limit on measurements of redshift-space distortions. J. Cosmology Astropart. Phys.*10* (Oct. 2009), 7–+.

[31] MO, H. J., AND WHITE, S. D. M. An analytic model for the spatial clustering of dark matter haloes. MNRAS*282* (Sept. 1996), 347–361.

[32] MUKHANOV, V. *Physical Foundations of Cosmology.* Nov. 2005.

[33] MUKHANOV, V. F., FELDMAN, H. A., AND BRANDENBERGER, R. H. Theory of cosmological perturbations. Phys. Rep.*215* (June 1992), 203–333.

[34] PEACOCK, J. A., AND DODDS, S. J. Reconstructing the Linear Power Spectrum of Cosmological Mass Fluctuations. MNRAS*267* (Apr. 1994), 1020.

[35] PEEBLES, P. J. E. *The large-scale structure of the universe.* 1980.

[36] PENZIAS, A. A., AND WILSON, R. W. A Measurement of Excess Antenna Temperature at 4080 Mc/s. ApJ*142* (July 1965), 419–421.

[37] PERLMUTTER, S., ALDERING, G., GOLDHABER, G., KNOP, R. A., NUGENT, P., CASTRO, P. G., DEUSTUA, S., FABBRO, S., GOOBAR, A., GROOM, D. E., HOOK, I. M., KIM, A. G., KIM, M. Y., LEE, J. C., NUNES, N. J., PAIN, R., PENNYPACKER, C. R., QUIMBY, R., LIDMAN, C., ELLIS, R. S., IRWIN, M., MCMAHON, R. G., RUIZ-LAPUENTE, P., WALTON, N., SCHAEFER, B., BOYLE, B. J., FILIPPENKO, A. V., MATHESON, T., FRUCHTER, A. S., PANAGIA, N., NEWBERG, H. J. M., COUCH,

W. J., and Supernova Cosmology Project. Measurements of Omega and Lambda from 42 High-Redshift Supernovae. ApJ*517* (June 1999), 565–586.

[38] Press, W. H., and Schechter, P. Formation of Galaxies and Clusters of Galaxies by Self-Similar Gravitational Condensation. ApJ*187* (Feb. 1974), 425–438.

[39] Radhakrishna Rao, C. Information and the accuracy attainable in the estimation of statistical parameters. *Bull. Calcutta Math. Soc. 37* (1945), 81–91.

[40] Reid, B. A., Percival, W. J., Eisenstein, D. J., Verde, L., Spergel, D. N., Skibba, R. A., Bahcall, N. A., Budavari, T., Frieman, J. A., Fukugita, M., Gott, J. R., Gunn, J. E., Ivezić, Ž., Knapp, G. R., Kron, R. G., Lupton, R. H., McKay, T. A., Meiksin, A., Nichol, R. C., Pope, A. C., Schlegel, D. J., Schneider, D. P., Stoughton, C., Strauss, M. A., Szalay, A. S., Tegmark, M., Vogeley, M. S., Weinberg, D. H., York, D. G., and Zehavi, I. Cosmological constraints from the clustering of the Sloan Digital Sky Survey DR7 luminous red galaxies. MNRAS*404* (May 2010), 60–85.

[41] Robertson, H. P. Kinematics and World-Structure. ApJ*82* (Nov. 1935), 284.

[42] Scoccimarro, R. Transients from initial conditions: a perturbative analysis. MNRAS*299* (Oct. 1998), 1097–1118.

[43] Seljak, U. Analytic model for galaxy and dark matter clustering. MNRAS*318* (Oct. 2000), 203–213.

[44] Seljak, U. Bias, redshift space distortions and primordial nongaussianity of nonlinear transformations: application to Ly-$\alpha$ forest. J. Cosmology Astropart. Phys.*3* (Mar. 2012), 4.

[45] Seljak, U., and McDonald, P. Distribution function approach to redshift space distortions. J. Cosmology Astropart. Phys.*11* (Nov. 2011), 39.

[46] Seljak, U., and Zaldarriaga, M. A Line-of-Sight Integration Approach to Cosmic Microwave Background Anisotropies. ApJ*469* (Oct. 1996), 437.

[47] Sheth, R. K., Mo, H. J., and Tormen, G. Ellipsoidal collapse and an improved model for the number and spatial distribution of dark matter haloes. MNRAS*323* (May 2001), 1–12.

[48] Sheth, R. K., and Tormen, G. Large-scale bias and the peak background split. MNRAS*308* (Sept. 1999), 119–126.

[49] Smith, R. E., Scoccimarro, R., and Sheth, R. K. Scale dependence of halo and galaxy bias: Effects in real space. Phys. Rev. D*75*, 6 (Mar. 2007), 063512.

[50] SMOOT, G. F., BENNETT, C. L., KOGUT, A., WRIGHT, E. L., AYMON, J., BOGGESS, N. W., CHENG, E. S., DE AMICI, G., GULKIS, S., HAUSER, M. G., HINSHAW, G., JACKSON, P. D., JANSSEN, M., KAITA, E., KELSALL, T., KEEGSTRA, P., LINEWEAVER, C., LOEWENSTEIN, K., LUBIN, P., MATHER, J., MEYER, S. S., MOSELEY, S. H., MURDOCK, T., ROKKE, L., SILVERBERG, R. F., TENORIO, L., WEISS, R., AND WILKINSON, D. T. Structure in the COBE differential microwave radiometer first-year maps. ApJ$396$ (Sept. 1992), L1–L5.

[51] SPRINGEL, V. The cosmological simulation code GADGET-2. MNRAS$364$ (Dec. 2005), 1105–1134.

[52] WALKER, A. G. On milne's theory of world-structure. *Proceedings of the London Mathematical Society s2-42*, 1 (1937), 90–127.

[53] WHITE, S. D. M. Formation and Evolution of Galaxies: Les Houches Lectures. *Astronomy* (Oct. 1994).

[54] WHITE, S. D. M., AND REES, M. J. Core condensation in heavy halos - A two-stage theory for galaxy formation and clustering. MNRAS$183$ (May 1978), 341–358.

[55] YOO, J. General relativistic description of the observed galaxy power spectrum: Do we understand what we measure? Phys. Rev. D$82$, 8 (Oct. 2010), 083508–+.

[56] YOO, J., HAMAUS, N., SELJAK, U., AND ZALDARRIAGA, M. Going beyond the Kaiser redshift-space distortion formula: a full general relativistic account of the effects and their detectability in galaxy clustering. *ArXiv e-prints* (June 2012).

[57] ZEL'DOVICH, Y. B. Gravitational instability: An approximate theory for large density perturbations. A&A$5$ (Mar. 1970), 84–89.

[58] ZHENG, Z., BERLIND, A. A., WEINBERG, D. H., BENSON, A. J., BAUGH, C. M., COLE, S., DAVÉ, R., FRENK, C. S., KATZ, N., AND LACEY, C. G. Theoretical Models of the Halo Occupation Distribution: Separating Central and Satellite Galaxies. ApJ$633$ (Nov. 2005), 791–809.